A ROBUST COOPERATIVE LOCALIZATION SYSTEM FOR A HETEROGENEOUS TEAM OF SMALL UNMANNED GROUND VEHICLES

by

VEERA JAWAHAR VIBEESHANAN

Presented to the Faculty of the Graduate School of

The University of Texas at Arlington in Partial Fulfillment

of the Requirements

for the Degree of

DOCTOR OF PHILOSOPHY

THE UNIVERSITY OF TEXAS AT ARLINGTON

August 2007

To my dear mother, father, sister, and wife

ACKNOWLEDGEMENTS

First and foremost, I thank my advisor, Dr. Brian Huff, for his inspiring guidance and enduring support throughout my doctoral work. I also thank Dr. Don Liles, Dr. Sheik Imrhan, Dr. Bill Corley, and Dr. Kamesh Subbarao for reviewing my doctoral research work as members of the supervising committee. Special thanks to Dr. Subbarao for helping me out greatly in Kalman filtering and to Dr. Corley for getting me started on the Dempster-Shafer theory of evidence.

I thank the following people for their invaluable assistance: Dr. V. C. P. Chen, Dr. K. J. Rogers, Mr. R. M. Dumse, Dr. M. Huber, and Dr. D. J. Cook. I also thank my teachers from high school and college who were instrumental in shaping me into who I am today. I wish to acknowledge my former and current student associates in the Manufacturing Lab for having created a symbiotic atmosphere for research activities. I thank “all” my friends who supported and cared for me during my doctoral work.

Last, but not the least, I thank my parents and grandparents who always put my needs above theirs. It is upon their sacrifices that I have come this far. I also thank my wife, sister, aunt, uncle, and the remainder of my well-knit relatives for their unflinching support during this endeavor.

May 14, 2007

ABSTRACT

A ROBUST COOPERATIVE LOCALIZATION SYSTEM FOR A HETEROGENEOUS TEAM OF SMALL UNMANNED GROUND VEHICLES

Publication No. _____

Veera Jawahar Vibeeshanan, Ph.D.

The University of Texas at Arlington, 2007

Supervising Professor: Brian L. Huff

This dissertation presents an organic approach to the cooperative localization problem by sequentially solving the problems of sensor calibration, multi-sensor fusion filtering, and cooperative localization. Successful navigation of unmanned ground vehicles requires accurate localization. Localization refers to the determination of the pose (position and orientation) of an unmanned ground vehicle with respect to a local or a global frame of reference. Cooperative localization is suited to multi-vehicle systems where vehicles with better accuracy in localization can assist those with poor accuracy through communication and relative pose sensing.

A parametric modeling approach is presented for sensor calibration. Designed experiments are conducted with the objective of building parametric models and mass assignment tables. An evidence theoretic adaptive fusion filter, the Eta-Filter, is proposed for multi-sensor fusion filtering. The Eta-Filter leverages the Dempster-Shafer theory of evidence to make a Kalman filter adaptive to operating scenarios and sensor goodness while accounting for the ignorance component of uncertainty. It is composed of an adaptive pre-processing unit, an evidence extraction and combination unit, and a Kalman filter. The evidence extraction and combination unit uses fuzzy-type techniques or rule-based mass assignment tables to compute the mass function. Then, the Dempster's rule for combination is used to combine the disparate evidences for a proposition. Based on the combined evidence, decisions on switching between pre-processing models and between corresponding input noise covariance matrices in the adaptive pre-processing unit are made. Also, the measurement noise covariance matrix of the Kalman filter is varied depending upon the evidence that the sensor is good. Experiments that demonstrate the validity of the Eta-Filter using empirical data are presented. A range-only cooperative localization system that resembles a "star" arrangement is presented. Combination is performed in the minimum variance sense under the assumption of independence of errors between the individual estimates. A statistically designed experiment that demonstrates the merits of the range-only cooperative localization system is presented. An ANOVA F-test, conducted at the one percent significance level, reveals that the range-only cooperative localization system

has a significantly lower mean final position error when compared to a non-cooperative localization system.

TABLE OF CONTENTS

LIST OF ILLUSTRATIONS

LIST OF TABLES

CHAPTER 1

INTRODUCTION

1.1 Statement of the Problem

This dissertation answers the following question posed by Unmanned Ground Vehicles (UGVs): "**where are we?**" "A *UGV* is defined as any piece of mechanized equipment that moves across the surface of the ground and serves as a means of carrying or transporting something, but explicitly does not carry a human being [Gag95]." The realm of UGVs (Figure 1.1) has gained unprecedented attention from the robotic research community over the recent past [Mad04, Rou02, Ryd05, Spl03]. The application areas for UGVs include landmine detection [Rac05], automated highways [Att00], fire-fighting [Saa05], and security [Sai95].

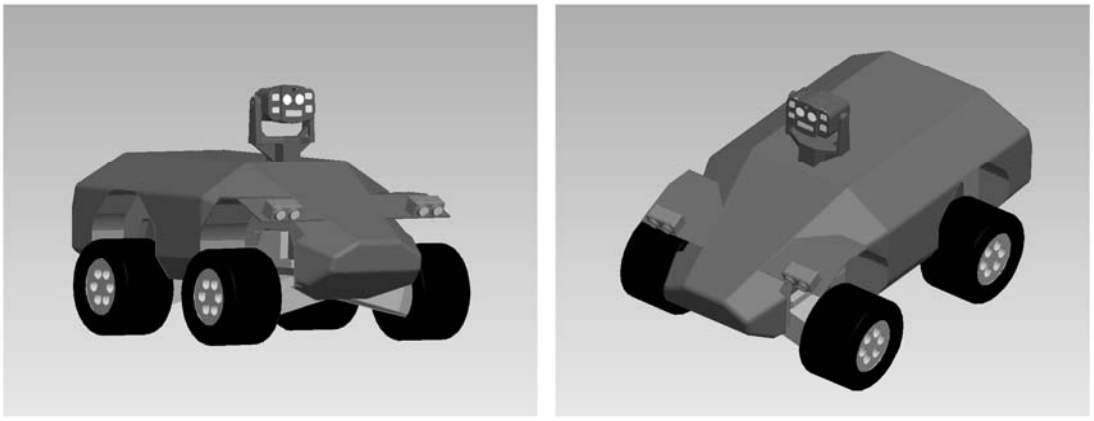

Figure 1.1 A Concept Small UGV: A Computer Aided Design (CAD) rendering using *Pro/ENGINEER*^{TM}.

Localization is defined as the determination of the "*pose*" (the position and the orientation with respect to a local or a global frame of reference) of a UGV and is regarded as a fundamental problem to providing autonomous capability for a UGV [Cox90]. In mathematical parlance, the pose is represented by a vector $\mathbf{x} = [x, y, \psi]^T$, where x represents the position along the x-axis, y represents the position along the y-axis, and ψ represents the orientation about the z-axis. The ability of a UGV to navigate through the environment requires accurate localization [Cro95]. The area of localization has gained considerable attention from researchers over the past few decades [Bal03, Bor96, Cox90, Del99, Fox00, Goe99, Gut98, Reu00, Tsu78, Tsu82]. Within the ambit of localization, there is a specific area known as *Cooperative Localization* (CL) [Rek98] which is geared to multi-robot systems [Fer98, Rek02, Sch98, Spl01]. CL provides an answer to the question: "*where are we*?" Throughout this dissertation, the following systems are also considered as CL systems: mutual positioning [Sug93], cooperative positioning [Kur94], collaborative localization [Fox00], and distributed localization [Rou02].

Cooperation is an interaction that is generally dependent on communication and is classified as [Mat94]: (1) *explicit cooperation*, an interaction that involves exchange of information or actions taken to benefit another agent, and (2) *implicit cooperation*, an action that is taken for the benefit the agent itself but that which results in benefits to other agents as well. Cooperation is also defined as "*doing something together*" with a goal of creating an improvement [Pre90]. Communication can be viewed as the medium

through which cooperation occurs. It is classified as [Bal94]: no communication, state communication, and goal communication.

Multi-robot systems have intrinsic advantages over their single-robot counterparts [Ara02]. The payoff is better for a "*heterogeneous*" (with different capabilities) team of robots [Cao97]. Especially for small UGVs that have a limited payload capability, each member of the team could have different sensing capabilities with different levels of accuracies and sophistication. A CL strategy for such a heterogeneous team of small UGVs would amortize the cost of expensive and accurate sensors across the entire team [Fox00]. The CL problem is a well explored area [Cag06, Fox00, Kur94, Mad04, Rou02, Spl03, Sug93]. Nevertheless, there are a number of challenges that still remain. The use of low-cost and faulty sensors requires a more efficient mechanism for the representation of uncertainty. Probabilistic techniques do not account for the ignorance component of uncertainty. Also, CL systems tend to require expensive relative sensing devices for cooperation to occur.

1.2 Research Objective

The objective of this research work is the development of a robust cooperative localization system for a heterogeneous group of small UGVs that would provide a better accuracy for each individual UGV than would a non-cooperative system. The problem is further decomposed into three sub-problems as follows:

(1) *localization sensor calibration*,

(2) *multi-sensor fusion filtering*, and

(3) *cooperative localization*.

The aforementioned three sub-problems are solved sequentially. This provides an "*organic*" approach to achieving the objective starting from the roots of the problem, *i.e.*, sensor calibration. The rationale behind this sequential approach is that the errors due to improper calibration are difficult to isolate at the cooperative localization stage. The objective must be achieved while meeting constraints such as limited sensor carrying capacity and reduced computational capability that are imposed by the small size of the UGVs. The goal is to build a cooperative localization system that is robust yet simple and low-cost.

1.3 Dissertation Conformance

Throughout this dissertation, unless explicitly stated, the s*ymbolic* notation conforms to the Aerospace Standard-4/Joint Architecture for Unmanned Systems (AS-4/JAUS) specifications [Joi04], and the *units* are the International System of Units (SI units) [Tay01]. According to the AS-4/JAUS specification, the global frame of reference, defined as {northwards (x-axis), eastwards (y-axis), downwards (z-axis)}, follows the mathematical right-hand rule [Joi04]. The global frame of reference used is the World Geodetic System as defined in 1984 (WGS84) [Eva05]. The origin of the local frame of reference is the start position of the UGV. The local frame describes the distance and the angle in meters and radians respectively.

In addition, the terminology used in connection with uncertainty is as defined by the International Organization for Standardization (ISO) vocabulary [Tay94]. For example, the terms such as accuracy and precision are *qualitative* by definition. Therefore, the phrase, "the precision is 10 meters," is not acceptable, whereas the

phrase, “the precision, expressed as the standard deviation under repeatability conditions, is 10 meters,” is acceptable [Tay94]. *Accuracy* represents the “closeness of the agreement between a measurement and the true value [Tay94].” *Precision* is defined as “the closeness of the agreement between independent test results under stipulated conditions [Tay94].” The stipulated conditions may include repeatable and/or reproducible conditions. “*Repeatability* is the closeness of agreement between successive measurements of the same measurand under the same conditions of measurement [Tay94].” “Same conditions” refer to the same measurement procedure, the same observer, the same measurement instrument, the same location, and repetition within a short period of time. *Reproducibility* is similar to repeatability with the exception that the conditions of measurement are different (*e.g.* a different location) [Tay94]. As far as this dissertation is considered, the terms “*UGV*” and “*robot*” are used synonymously. Also, *N* represents north and *E* represents east.

The following convention on notations is adhered to:

(1) *Scalar* variables are represented by small letters in italics.

(2) *Vector* variables are represented by bolded small letters.

(3) *Matrices* are represented by bolded capital letters.

(4) *Superscripts*: transpose of a matrix – ^{T}; inverse of a matrix – $^{-1}$; *a priori* – $^{-}$; *a posteriori* – $^{+}$.

(5) *Subscripts*: discrete time-step number – $_{k}$; global frame of reference – $_{G}$; local frame of reference – $_{L}$; vehicle frame of reference – $_{V}$.

(6) *Accents*: measurement – $\tilde{}$ (tilda); estimate – $\hat{}$ (hat); mean – $\bar{}$ (bar).

The list of units and symbols used is as follows:

(1) *Base units:* length – meter (m); time – second (s).

(2) *Derived units:* speed, velocity – m/s; acceleration – m/s^2; angle – rad (radians); angular velocity – rad/s; frequency – Hz (Hertz).

(3) *Allowed non-SI units:* degree – ^{o}; minute – '; second – ".

(4) *Time reference*: Coordinated Universal Time (UTC).

1.4 Dissertation Outline

The remainder of this dissertation is organized as follows. Chapter 2 presents a review of literature that is related to this research work. The review describes the types of localization sensors that are employed in this research, localization error characteristics, sensor calibration methods, fusion filtering techniques, and existing CL systems. Chapter 3 presents an evidence theoretic fusion filtering approach for localization of single UGVs. It includes descriptions of the methodologies for creating parametric sensor calibration models and for building mass assignment tables that are geared to the requirements of the evidence theoretic fusion filter. In addition, an experimental validation of the fusion filtering approach is detailed. Chapter 4 presents a detailed description of a CL system. It includes a description of sensor modeling and self-localization of individual UGVs. A range-only CL system that resembles a "*star*" arrangement is presented. The merits of the CL system are discussed based on the results of a designed experiment. Chapter 5 provides a conclusion of this research work and includes a brief summary, contributions, and possible future extensions.

CHAPTER 2

LITERATURE REVIEW

This chapter presents a review of the types of localization sensors, error characteristics, sensor calibration methods, fusion filtering techniques, and existing approaches to CL.

2.1 Types of Localization Sensors

Localization sensors for UGVs are classified as [Bor96]: (1) *internal* sensors and (2) *external* sensors (also known as *proprioceptive* sensors and *exteroceptive* sensors respectively [Rou02]). Internal sensors are located within the vehicle and do not require any external sensory stimuli. Examples of this genre are wheel encoders, accelerometers, and gyroscopes. External sensors, on the other hand, depend on external sources of input in order to operate. For example, a digital compass requires an external magnetic field as sensory input. Other external sensors include the Global Positioning System (GPS), ultrasonic sensors, and vision sensors. Sensors are also classified as [Bra03]: (1) *active* sensors, sensors that stimulate the environment prior to making a measurement, and (2) *passive* sensors, sensors that do not stimulate the environment prior to making a measurement. The following sections describe the sensors that are of interest to this work such as wheel encoders, accelerometers, rate-gyros, digital compasses, and GPS units.

2.1.1 Wheel Encoder

The *wheel encoder* measures the distance traveled by each wheel or track [Eve95]. The most commonly used type of wheel encoder is the optical encoder that is generally coupled to the wheel axle of a UGV [Bor96]. The wheel encoders are prone to accumulation of measurement errors due to wheel slippage [Bor96, Suk99].

2.1.2 Inertial Measurement Unit

An Inertial Measurement Unit (IMU) comprises of gyroscopes and accelerometers [Bra03]. A *gyroscope* (a solid-state rate-gyro) measures the angular velocity about an axis of reference [Bor96]. The relative orientation is computed by integrating the rate-gyro measurement with respect to time [Wal03]. Solid-state rate-gyros are used as an inexpensive means for UGV localization [Sol04]. An *accelerometer* measures the acceleration along an axis of reference. Acceleration is subsequently integrated twice with respect to time for computing the displacement [Eve95]. Low-cost solid-state accelerometers exhibit "*drift*" as a function of time and temperature [Liu01, Suk99, Wei98] and contain higher measurement errors at lower magnitudes of acceleration [Neb99]. Misalignment of the axis of the inertial sensors with respect to the vehicle frame contributes to "*bias*" [Suk99]. The process of integration, a requirement for the inertial sensors, leads to an unbounded growth of measurement errors with time [Bar95, Suk99]. A critical advantage of the IMU is the property that it is *non-jammable* by external signals [Dur01].

2.1.3 Digital Compass

A *digital compass* measures the absolute orientation of a robot with respect to the geomagnetic north [Eve95]. The use of magneto-resistive technology for solid-state digital compasses is prevalent [Sto00]. A major shortcoming of the digital compass is the fact that proximity to underground cables or ferrous material can lead to a significant distortion in the measurements [Bor97, Sto00].

2.1.4 Global Positioning System

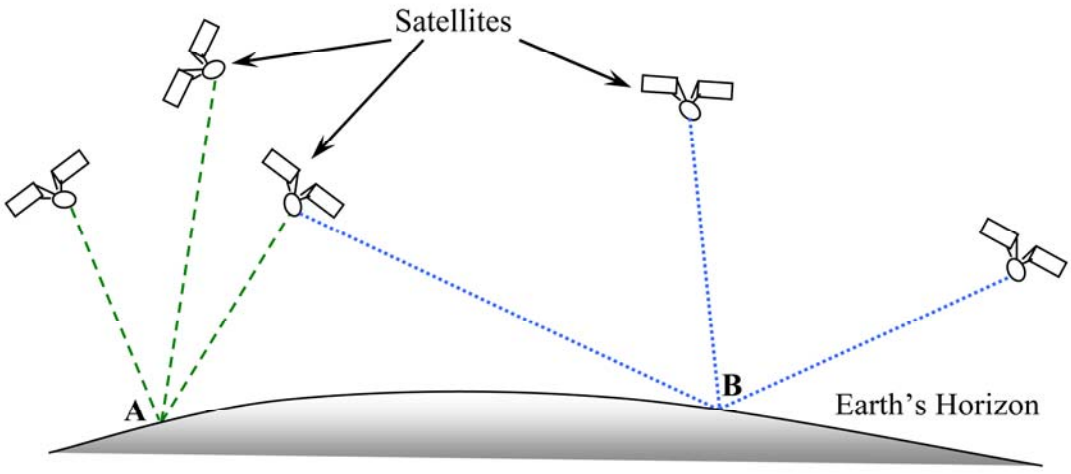

Figure 2.1 Dilution of Precision (DOP): Receiver B has a better DOP than receiver A as the satellites are spaced farther with respect to receiver B.

A GPS system uses satellites in space to determine the location of an object with respect to the WGS84 frame of reference [Eve95]. A minimum of four satellites are required by the GPS system to locate an object in a three-dimensional space [Eve95]. However, an object that is on the surface of the earth can be located with three satellites [Eve95]. The standard error ranges for GPS units with respect to horizontal positioning

are given as follows [ElM00]: GPS – 10 m to 15 m, Differential GPS (DGPS) – 1 m, and Real Time Kinematic GPS (RTK-GPS) – 0.2 m. The *Novatel*^{TM} *RT2* is capable of achieving 0.02 m standard error in position [Suk99]. The RTK-GPS is a differential positioning technique that uses the known coordinates of a reference station (a stationary receiver) to determine the location of a mobile receiver through phase measurements and real-time processing [ElM00].

The two major sources of GPS error are [Neb97]: (1) the Position Dilution of Precision (PDOP), a positive integer that refers to the actual geometry of the relative positions of the satellites and the receiver (Figure 2.1), and (2) the precision in determination of the range due to atmospheric delays and receiver noise. Multiple reflections of a satellite signal, known as "*multipathing*," can lead to erroneous range determination [Neb97]. The GPS sensor has an intermittent characteristic as the availability of satellite signals depends on the environment of the receiver (bridges and skyscrapers may block the satellite signals) [Bon01]. However, a 2001 US Federal Communications Commission (FCC) mandate that required wireless carriers to provide the caller's latitude and longitude within 50 m for 67% of emergency calls has spurred the concept of the Assisted-GPS (AGPS) [Dju01], wherein a GPS receiver is "*assisted*" by a wireless network. The AGPS comprises of a wireless handset, an AGPS server with a reference GPS, and wireless base-stations that coordinate with each other. The accuracy of an AGPS system, expressed as a standard error, is 50 m (*indoors*) and 15 m (*outdoors*) [Dju01].

2.2 Error Characteristics and Calibration Methods

Errors represent the difference between measured values and true values. They are categorized as *systematic* errors and *non-systematic (random)* errors [Bor94, Tay94]. They are also known as "*bias*" and "*noise*" respectively [Fen04]. Under Gaussian assumption, bias refers to the difference between the true value and the mean value, and noise refers to the difference between a measured value and the mean value [Byc03].

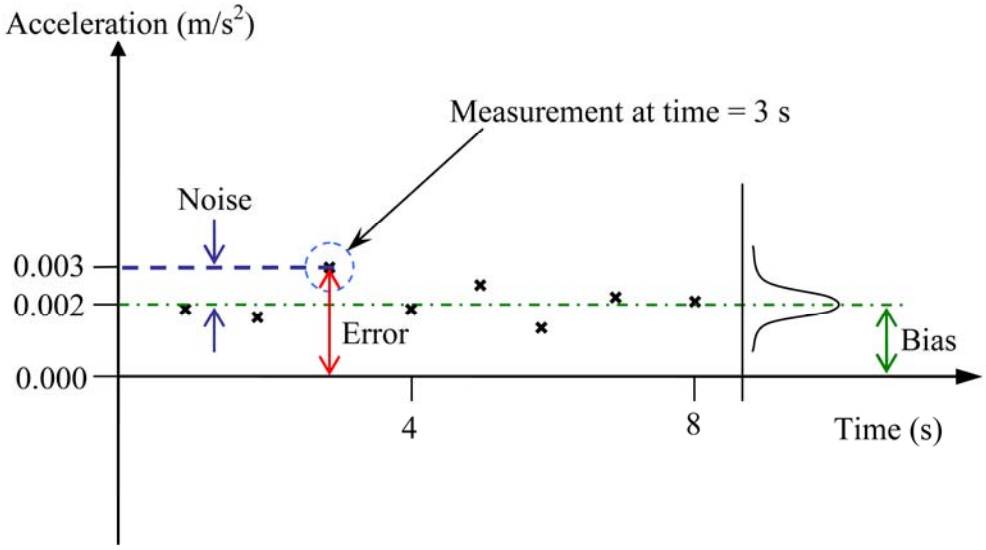

Figure 2.2 Components of Measurement Error: Measurement at time = 3 s shows a bias component (represented by the dashed-dotted line) of 0.002 m/s^2 and a noise component (represented by the distance between the dashed-dotted line and the dashed line) of 0.001 m/s^2 in acceleration, *i.e.*, bias = error – noise.

Calibration is defined as the process of identifying and eliminating systematic errors (biases) from sensor readings [Byc03]. Also, it refers to mapping raw sensor

outputs to standardized units [Fra04]. The uncertainties due to errors are quantified as standard errors (root mean squared errors) and are determined using "Type-A" (statistical) evaluations or "Type-B" (other than statistical) evaluations [Tay94]. In this dissertation, **standard errors are determined using "Type-A" evaluations**. Figure 2.2 illustrates the bias and the noise components of measurement error. A series of accelerometer measurements are recorded from a UGV that is *at rest*, *i.e.*, acceleration = 0.000 m/s^2, and are plotted as a function of time. The figure shows that there is a bias component in the error.

Calibration models are classified as [Vib07a]: (1) *parametric* models, wherein the models are known *a priori*, and (2) *nonparametric* models, wherein the models are determined from empirical data. Though nonparametric models such as the Multivariate Adaptive Regression Splines (MARS) [Fri91] offer the advantage of automatic model identification using empirical data, they are not the only option when calibration models are known *a priori*. As the sensors employed in this research work have known models, **the focus of this work is on parametric modeling**. Parametric calibration can be performed using multivariate regression analysis models [Tri99]. There are several procedures for the parametric calibration of differential drive UGVs: procedures wherein the calibration parameters are a function of wheel radii and track length [Ant05, Bor95], a scheme that involves representation of the variances associated with driver-wheel radius, steering angle, and attitude as a function of "*maneuvers*" (*e.g.* standing, curving, steering, and straight path) [deC03], and an online calibration method that uses redundant information from multiple onboard sensors [von98].

2.3 Fusion Filtering Techniques

The usage of multiple sensors to localize a UGV requires the combination of information from multiple sensors (sensor fusion [Sas00]) in order to produce the "*best*" state estimate (in the minimum error sense). Sensor fusion is a widely researched area [Bor96, Cox91, Dur90, Has88, Kam97, Lop00, Mut00, Wil76]. Multiple sensors are used in both *redundant* and *complementary* ways [Vib07b].

Sensor fusion is classified as [Bar01]: (1) *centralized estimation fusion* and (2) *distributed estimation fusion*. The centralized fusion architecture uses one filter that fuses measurements from all sensors to estimate the state and has a high computational overhead as well as a poor fault tolerance [Bar01]. On the other hand, the distributed architecture (also known as *loosely coupled*) uses multiple filters that run in parallel and offers a significant reduction in computational overhead [Bar01].

The generic fusion formula for a statistical combination of two estimates (under the assumption of independence of errors between the two estimates) is given by [Bar01, Car90, Car96]:

$$\hat{\mathbf{x}}_{c,k} = (\mathbf{P}_{1,k}^{-1} + \mathbf{P}_{2,k}^{-1})^{-1}(\mathbf{P}_{1,k}^{-1}\hat{\mathbf{x}}_{1,k} + \mathbf{P}_{2,k}^{-1}\hat{\mathbf{x}}_{2,k}), \tag{2.1}$$

where $\hat{\mathbf{x}}_{1,k}$ and $\hat{\mathbf{x}}_{2,k}$ are the individual state estimates, $\mathbf{P}_{1,k}$ and $\mathbf{P}_{2,k}$ are the individual error covariance matrices, $\hat{\mathbf{x}}_{c,k}$ is the fused state estimate, and $\mathbf{P}_{c,k} = (\mathbf{P}_{1,k}^{-1} + \mathbf{P}_{2,k}^{-1})^{-1}$ is the fused error covariance matrix.

The estimation of the current dynamical state of a robot is known as *filtering* [Bar01]. Of the statistical filtering techniques that are available, the recursive *Bayesian*

filtering is capable of producing optimal estimates but is computationally intractable [Thr05]. *Particle filtering*, on the other hand, is a version of the recursive Bayesian filtering that uses samples ("*particles*") to represent the posterior distribution [Dou01]. It has a computational time complexity that is directly proportional to the number of samples and has been applied to the UGV localization problem [Del99, Fox00, Gus02, Thr01]. Nevertheless, it is computationally expensive when the number of samples is high. It must be noted, however, that the accuracy of the filter is poor when the number of samples is low. *Kalman filtering* [Kal60] is another derivative of the recursive Bayesian filtering with two underlying assumptions: (1) the prior distribution and the uncertainty in the process and measurement models are independent, white, and zero mean Gaussian processes and (2) the process and measurement models are linear. An exception to the linearity assumption is the Extended Kalman Filter (EKF), wherein a nonlinear model is linearized at the most recent state estimate [May79]. The property of the Kalman Filter (KF) that makes it attractive from the standpoint of implementation is its "*constant-time*" complexity.

Early applications of Kalman filtering include the parallel Kalman filtering method [Wil76] and the decentralized Kalman filter [Has88]. The decentralized architecture was found to be more robust to sensor failures and more flexible to accommodating additional sensors [Dur90]. A version of the decentralized filter known as the federated Kalman filter uses multiple local filters (one for each sensor) that run in parallel and one master filter that generates a globally optimal estimate [Car90]. The decentralized or distributed methods for fusion filtering offer increased efficiencies

[Gao93]. Several applications of Kalman filtering for sensor fusion exist in literature [Car04, Rou97, Sas00].

The statistical and probabilistic techniques discussed in the preceding paragraph depend on the accuracy of the process model and the measurement model. As accurate mathematical modeling of dynamical systems is difficult, the *Dempster-Shafer* (DS) theory of evidence may be leveraged to bolster the state estimation process. Though techniques such as Multiple Model Adaptive Estimation (MMAE) [May85, Han98] offer ways to counter modeling inaccuracies, they do not account for ignorance. The DS theory of evidence, unlike the Bayesian theory, **factors in the "*ignorance*" component of uncertainty leading to a better representation of inaccuracies** [Sha76]. The DS theory of evidence permits the use of heuristic domain knowledge of experts into the fusion process [Mur98] and has been found to be better than the Bayesian process in a vision sensor fusion application [Wu02]. The DS theory has been applied to localization of vehicles using multi-target tracking [Cle02] and road-matching techniques [ElN05].

2.4 Cooperative Localization

For a team of UGVs that have heterogeneous sensing capabilities and also operate under varying environmental conditions, vehicles with better accuracy in localization can assist those with poor accuracy. This is generally known as a CL system [Rek02]. Cooperation is achieved by using relative position and/or relative orientation between the vehicles and estimates of their own position and/or orientation. The CL problem is similar to that of localizing the nodes of a wireless sensor network with the difference being that the nodes of a CL system are mobile and capable of

independent localization [Das02]. By having just few expensive and highly accurate UGVs and many inexpensive but poorly accurate UGVs, CL holds the potential of decreasing the "*per-UGV*" cost [Fox00]. However, additional constraints are posed due to the increase in communication between the vehicles and due to the additional sensors that are required for determining their relative pose. The next section presents the current approaches to CL.

2.4.1 Current Approaches to Cooperative Localization

The earliest published work on CL is a "*leapfrogging*" approach (one UGV is stationary while the other moves and *vice versa*) that employs two cooperating vehicles [Sug93]. The "*portable landmark*" approach is a leapfrogging approach for more than two vehicles wherein the team is divided into two groups [Kur94, Kur98, Kur00].

Geometric CL systems include *triangulation*, a method based on the angles that the UGV makes with the vertices of a triangle, and *trilateration*, a method based on the distance measurements to the vertices of a triangle [Bor96]. But these methods do not take into account the errors associated with individual vehicle estimates. A computationally efficient method for solving the trilateration problem takes into account both measurement noise and system non-linearity [Man96]. Spherical coordinate transforms have also been used in the determination of the relative distance for a CL technique for two vehicles [Hya99]. Geometric techniques that use a triangular constraint method (based on the fact that the angles of a triangle add up to 180 degrees) have been investigated by equipping the UGVs with omni-directional cameras [Kat99]. The computational time was found to be excessive when the number of UGVs exceeded

seven. The use of active stereo vision for tracking a two-robot team has been investigated as a means of collaborative localization [Dav00].

A probabilistic algorithm for collaborative multi-robot localization showed an improvement in localization accuracy [Fox00]. Probabilistic methods such as the maximum likelihood approach have been used in combination with the geometric trilateration technique for teams of small robots [Gra01]. In a distributed multi-robot localization scheme that views the entire team of robots as a *group* "organism" with *multiple* "limbs," each robot is considered as a joint that is capable of three degrees of motion [Rou02]. A reduction in computational overhead is achieved by decomposing a single Kalman filter into multiple filters. In another study, the CL problem is decoupled into two sequential optimization problems as follows [Das02]: (1) estimation of the orientations of the team and (2) estimation of the positions of the team. A completely distributed particle filter, wherein every UGV estimates the relative pose of every other UGV in the team, has been implemented in [How03].

A deterministic method for CL that uses an *unknown-but-bounded* approach to sensor modeling as well as linear programming optimization techniques was presented in [Spl03]. Recently, several EKF based approaches and particle filter based methods have been presented for CL: Rao-Blackwellized particle filter for the estimation of the relative distances and the relative bearings between multiple robots [Lin05], an EKF based cooperative distributed localization method that employs laser rangefinders to obtain the relative pose [Mad04], an EKF that uses relative distance and orientation information to localize seven robots simultaneously [Mar05], a bearing-only CL system

for pairs of robots that includes a comparison of convergence rates between an EKF and a particle filter [Mon05], a distributed particle filter algorithm for the localization of a three robot team wherein the positions of the robots are considered to be the vertices of a triangle with each robot using an identical particle filter to determine the centroid of the triangle [Pea05], an EKF based relative localization system wherein *SICK*^{TM} laser scanners and wheel encoders are employed to measure the distance and the bearing between a stationary observer robot and moving robots [Sch04], and a distributed and a scalable localization system that uses an EKF in conjunction with a minimum entropy criterion for the selection of optimal measurements that minimize the global uncertainty [Cag06].

Other recent methods of CL are as follows: a stereo vision technique [Mil05], a geometric method that employs a laser scanner [Ryd05], a relative position measurement graph based method [Mou06], a *stigmeric* potential field method for simultaneous localization and mapping of a multi-vehicle team [Sti06], and a low-cost method wherein some robots that are equipped with localization sensors localize the other robots [Kou06]. Table 2.1 shows a classification of CL systems based on seven criteria.

On the hardware front for CL, the *Ultra Wide-Band* (UWB) technology can be used for communication as well as ranging [Che04]. A prototype UWB precision asset location system obtained a Root Mean Squared (RMS) error of 0.9 m to 1.5 m and was found to operate even in the presence of heavy multipath [Fon02]. The first FCC certified commercial UWB Precision Asset Location system (PAL650) that comprised

of active tags with radomes, ceiling mounted UWB receivers, and a base processing hub achieved standard errors ranging between 0.1 m and 0.5 m depending on the axis and the algorithm used (steepest descent algorithm or Davidon-Fletcher-Powell quasi-Newton algorithm) for computing the position of the tags [Fon03].

Table 2.1 Classification of CL Systems

Basis Criteria	Classification
Mobility Restrictions	Restricted (*e.g.* leapfrogging)
	Unrestricted
Process Model	Deterministic
	Stochastic
Relative Measurements	Range and bearing
	Bearing only
	Range only
Estimator Type	Centralized
	Decentralized (*e.g.* distributed)
Team Type	Homogeneous
	Heterogeneous
Operating Environment	Indoor
	Outdoor
	Indoor and outdoor
Maximum Team Size	Small (< 10)
	Large (>= 10)

The existing approaches to CL described in the preceding paragraphs require either relative orientation sensing devices or relative distance sensing devices or both relative orientation and relative sensing devices. Devices such as *SICK*^{TM} laser scanners are expensive, and this characteristic may offset the cost advantage of a CL system. The UWB technology, described in the preceding paragraph, is a low-cost communications-cum-ranging device that can achieve standard errors less than 0.15 m [Fon03]. The UWB technology uses the Angle-of-Arrival (AOA) of signals for relative orientation sensing and Time-of-Arrival (TOA) of signals for relative distance sensing. However, the AOA method has two major disadvantages [Pat05]: (1) requirement of an array of sensor elements (that in turn leads to an increase in cost) and (2) sensitivity to higher inter-UGV distances. Therefore, **a range-only CL system has the potential for reaping the cost benefits of a CL system**.

CHAPTER 3

EVIDENCE THEORETIC ADAPTIVE FILTERING

3.1 An Overview of the ***η***-Filter

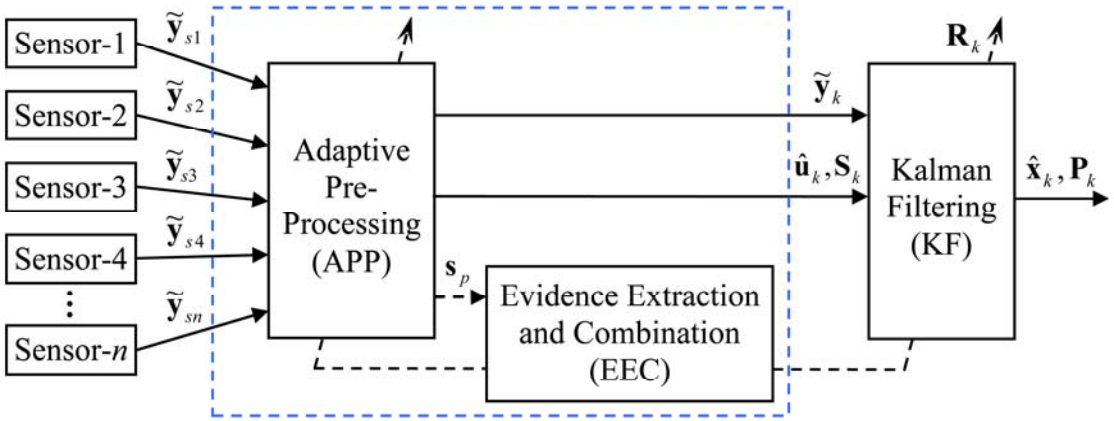

Figure 3.1 The ***η***-Filter Framework: A generic '*n*' sensor fusion filter model showing how the APP and the EEC are "*added on*" to an existing Kalman filter.

An ***e***vidence ***t***heoretic ***a***daptive ("***eta***" or "***η***") filter is essentially an application of the KF that leverages the DS theory of evidence (also known as *belief theory*) [Vib06, Vib07b]. As shown in Figure 3.1, existing KF based fusion filters can be *retrofitted* by "*adding-on*" an Adaptive Pre-Processing (APP) unit and an Evidence Extraction and Combination (EEC) unit. From the standpoint of functionality, the ***η***-Filter adapts to operating scenarios and sensor goodness by means of the DS theory of

evidence. However, parametric models and mass assignment tables are required based on the operating scenarios and the sensors under consideration [Vib07b].

The following sections describe the experimental procedures for creating parametric models of linear velocities, angular velocities, and the orientation (heading) and for building a mass assignment table for a GPS sensor. They also describe the three components of the $\boldsymbol{\eta}$-Filter (APP, EEC, and EKF) and the experimental validation of the $\boldsymbol{\eta}$-Filter.

3.2 Parametric Calibration and Mass Assignment

A set of four designed experiments were performed with the objective of building multiple *parametric models* for linear velocity and angular velocity for two operating scenarios and a *mass assignment table* for GPS sensor goodness. The results of this calibration procedure were subsequently used in the experimental validation of the $\boldsymbol{\eta}$-Filter described in Section 3.4. For these experiments, a car-type UGV – the FHP-4WD-SMP – was used. The *FHP-4WD-SMP* is essentially a *Traxxas E-Maxx* remote-control car chassis (Figure 3.2) that is driven by a *Motorola DSP56F805* based onboard controller, the *IsoPod*^{TM}. Another controller, the *IsoPodX*^{TM}, with a combined memory of 992Kb was used exclusively for data-logging (Figure 3.2). Both relative and absolute localization sensors [Fra04] were used in the experiments. The sensors are listed as follows: six custom-built magnetic encoders in the form of magnetically actuated reed sensors that were chosen due to mechanical constraints in the rear wheels of the UGV (Figure 3.3), an *Analog Devices ADXL202-EB* dual-axis accelerometer (Figure 3.4), a *GWS PG-03* solid-state rate-gyro (Figure 3.4), a *Devantech CMPS03* digital compass

(Figure 3.2), and a *Navman/Jupiter TU10-D007-091 GPS Development Kit* (Figure 3.2). In addition to the aforementioned sensing hardware, a *MaxStream-XTend-PKG*^{TM} wireless unit (Figure 3.2) was employed for broadcasting the logged data to the base station after the completion of each run. Due to hardware memory limitations, the maximum duration of each run was limited to 60 s.

3.2.1 Models for Linear Velocity

Two models for linear velocity are required for the APP: (1) based on all sensors and (2) based on only inertial sensors. An experiment consisting of twenty-one straight-line runs was performed in a parking lot. The runs comprised of seven repetitions each for three throttle settings. The data from the sensors of interest, *i.e.*, the six rear wheel encoder probes (R1, R2, R3, L1, L2, and L3), the accelerometer-x, and the rate-gyro, were logged at a frequency of 20 Hz. Figure 3.7 shows a description of the raw plots. The distance of each run was measured by manually marking the start/stop points and using a *standard* measuring tape. Then, the linear velocity of the UGV was computed by dividing the distance of each run by the preset duration of the run. The following linear regression models [Mas03] are created using the empirical data.

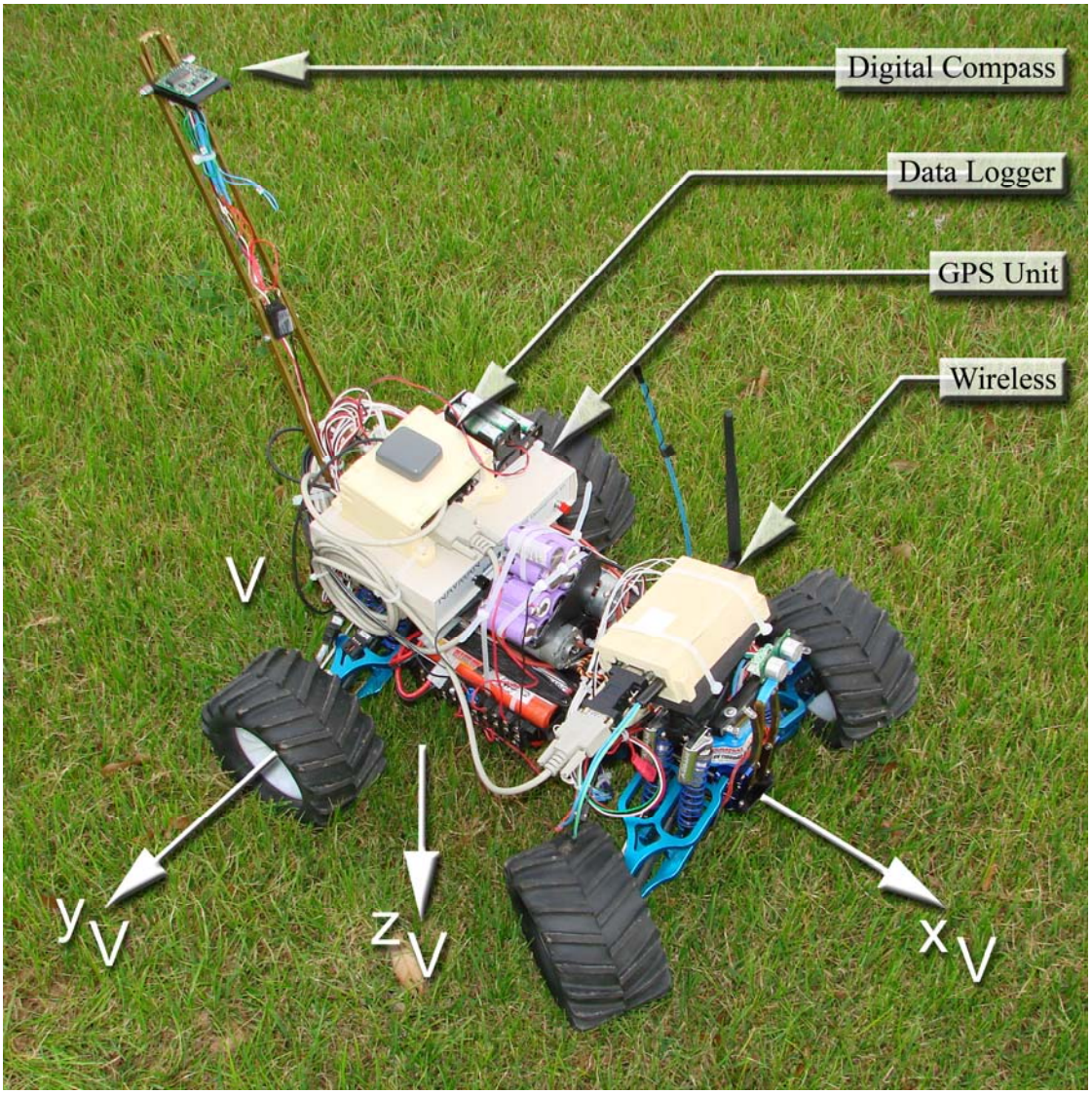

Figure 3.2 An Experimental UGV – The FHP-4WD-SMP: Notice that the axes of the vehicle frame 'V' conform to the AS-4/JAUS specifications.

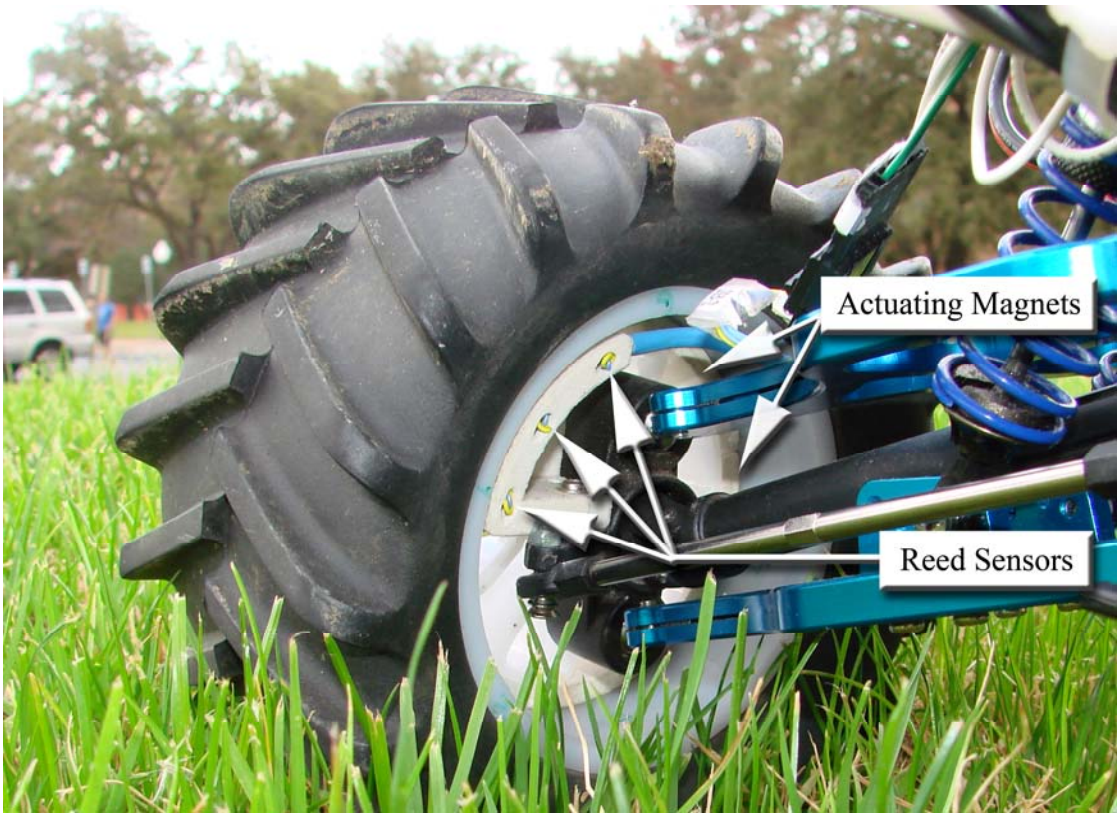

Figure 3.3 The Rear Wheel Encoders: A set of magnets embedded inside the wheel rim actuate the reed sensors (L1, L2, and L3 are shown here) that serve as encoders. In-house rapid prototyping was used in the manufacture of the wheel encoder components.

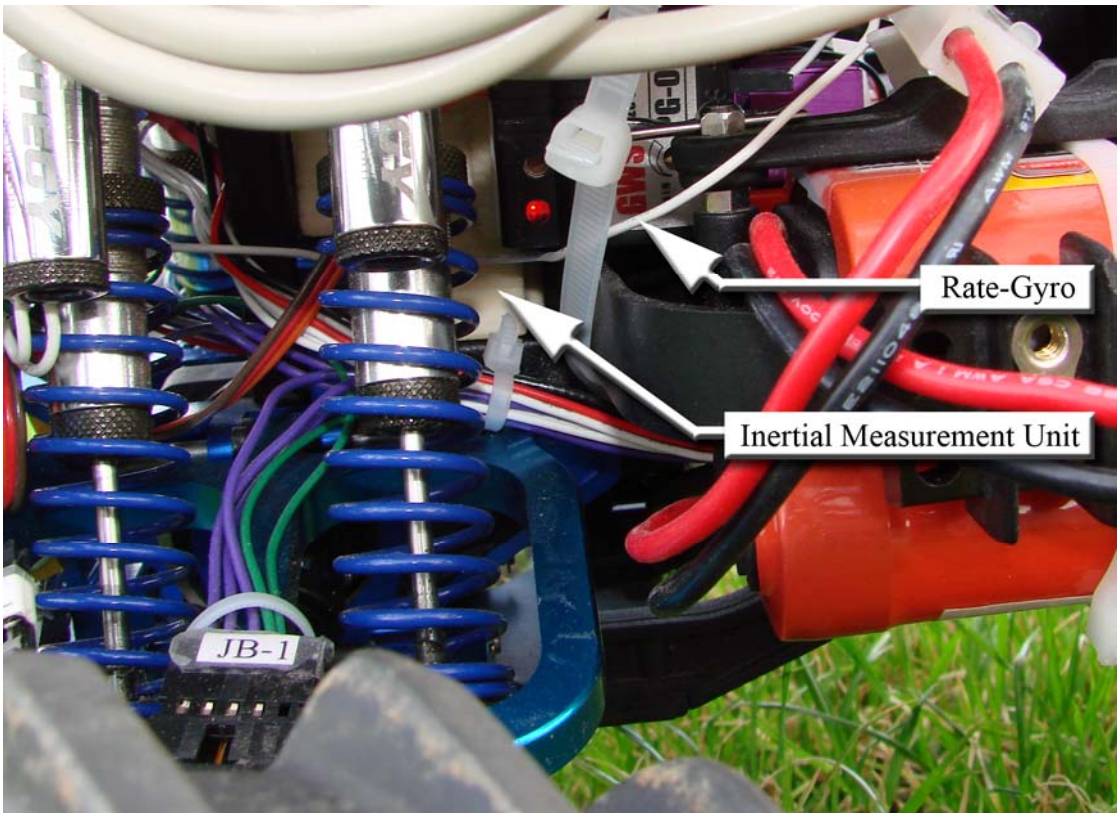

Figure 3.4 The Inertial Measurement Unit: A dual-axis accelerometer is positioned above the center of the rear wheel axle (the origin of the vehicle frame, in two a dimensional sense). A solid-state rate-gyro with its rotation axis aligned to the z_V-axis is strapped on to the accelerometer housing.

Model R*n* (for velocity based on the right rear wheel encoders) is given by the following equation:

$$v_{r,n} = \beta_0 + \beta_1(TPS_{r,n}) + \varepsilon_{vr,n}, \tag{3.1}$$

where v is the velocity, the subscripts r and n represent right and the number of the encoder respectively, *i.e.*, n = 1, 2, 3, β_0 is the intercept, β_1 is the slope, TPS represents the Ticks Per Second, and $\varepsilon_{vr,n}$ is the residual with $\varepsilon_{vr,n} \sim N(0,\sigma_{vr,n})$. Figure 3.5 shows a plot of the velocity model based on rear wheel encoder R3. Table 3.1 shows a listing of parameter estimates, $\hat{\beta}_n$. MSE refers to the Mean Squared Error and R^2 refers to the goodness-of-fit. Further,

$$TPS_{r,n} = \left[\frac{ticks_{r,n}}{(\Delta t)}\right], \tag{3.2}$$

where $ticks_{r,n}$ represents the number of ticks of the n^{th} right encoder and Δt is the time between sampling.

Model L*n* (for velocity based on the left rear wheel encoders) is given by the following equation:

$$v_{l,n} = \beta_0 + \beta_1(TPS_{l,n}) + \varepsilon_{vl,n}, \tag{3.3}$$

where the subscript l represents left, n = 1, 2, 3, and $\varepsilon_{vl,n}$ is the residual with $\varepsilon_{vl,n} \sim N(0,\sigma_{vl,n})$. Further,

$$TPS_{l,n} = \left[\frac{ticks_{l,n}}{(\Delta t)}\right], \tag{3.4}$$

where $ticks_{l,n}$ represents the number of ticks of the n^{th} left encoder.

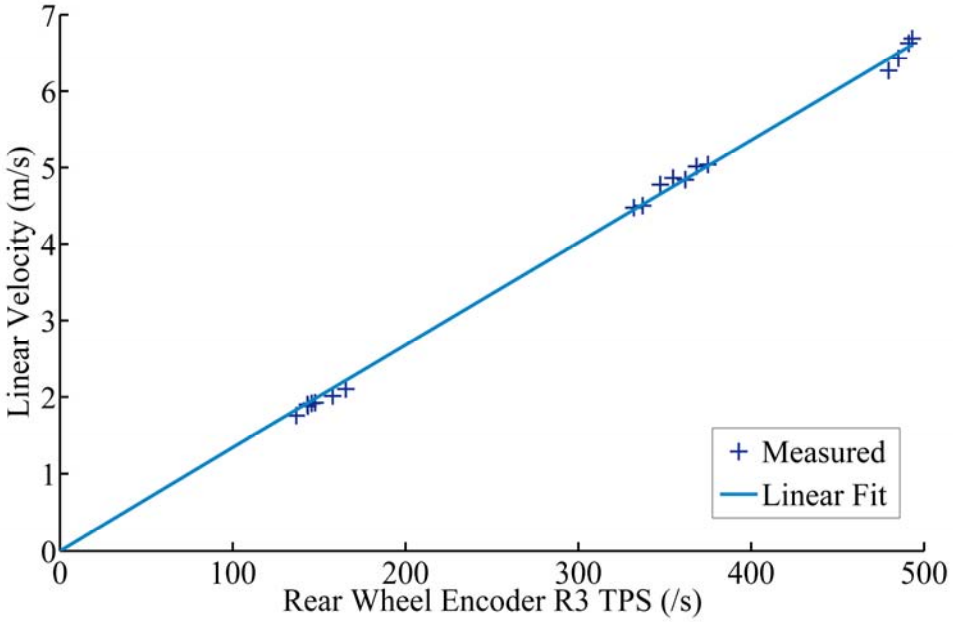

Figure 3.5 Linear Velocity from Rear Wheel Encoder R3: Notice that the y-intercept for this linear model is pegged at zero.

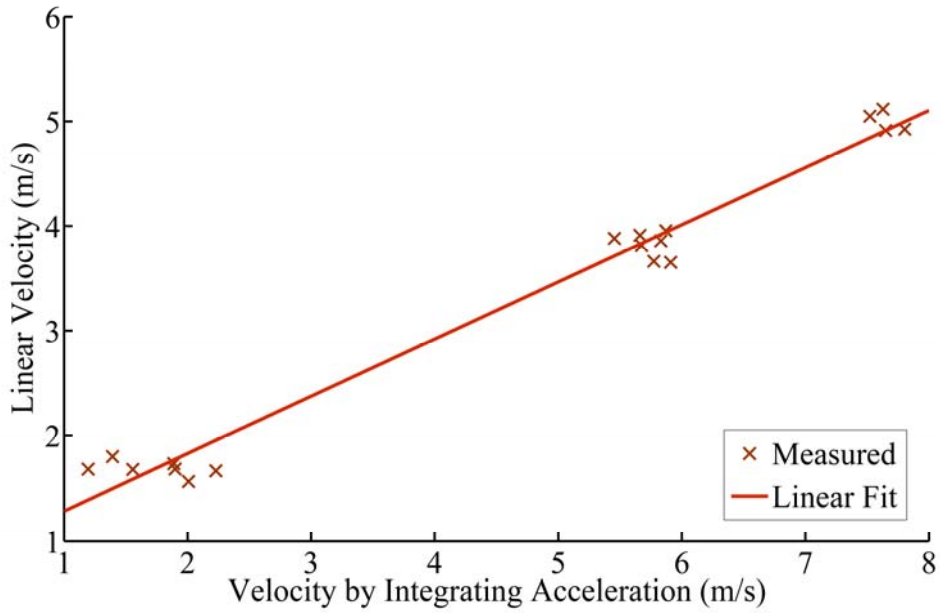

Figure 3.6 Linear Velocity from Accelerometer Measurements: The velocity as integrated from the acceleration along the x_V-axis shows a bias (indicated by a non-zero y-intercept) as well as a scale factor (slope $\neq 1$).

Table 3.1 Model Parameter Estimates and Goodness-of-Fits

Model	$\hat{\beta}_0$	$\hat{\beta}_1$	$\hat{\beta}_2$	$\hat{\beta}_3$	$\hat{\beta}_4$	$\hat{\beta}_5$	MSE	R^2
R1	0.000	0.011					0.16	0.9921
R2	0.000	0.113					0.54	0.9642
R3	0.000	0.013					0.01	0.9997
L1	0.000	0.014					0.03	0.9987
L2	0.000	0.013					0.03	0.9984
L3	0.000	0.019					0.03	0.9984
C1	0.736	0.546					0.04	0.9802
W1	0.996	-0.589					0.10	0.8296
W2	-0.338	-0.016					0.01	0.9987
D1	-0.070	1.151	-0.004	2.77E-5	-5.9E-8	4.3E-11	3.73	0.9998
D2	-0.002	1.136	-0.005	3.63E-5	-9.4E-8	8.3E-11	2.76	0.9998

Model C1 (for velocity based on accelerometer-x) is given by the following equation:

$$v_{ax} = \beta_0 + \beta_1 \sum_{i=0}^{k} (a_x \cdot \Delta t) + \varepsilon_{vax}, \tag{3.5}$$

where v_{ax} is the velocity along vehicle x-axis (x_V) based on the accelerometer-x, k is the time-step, a_x is the measured acceleration along the x_V-axis, and ε_{vax} is the residual with $\varepsilon_{vax} \sim N(0, \sigma_{vax})$. Figure 3.6 shows a plot of model C1.

Model C2 (for velocity based on accelerometer-y) is given by the following equation:

$$v_{ay} = \beta_0 + \beta_1 \sum_{i=0}^{k} (a_y \cdot \Delta t) + \varepsilon_{vay}, \tag{3.6}$$

where v_{ay} is the velocity along vehicle y-axis (y_V) based on accelerometer-y, a_y is the measured acceleration along the y_V-axis, and ε_{vay} is the residual with $\varepsilon_{vay} \sim N(0, \sigma_{vay})$.

The linear velocities of the right and the left wheels, as determined by the individual encoders using Equations (3.1) and (3.3), are fused by taking weighted averages. The weights are set as the inverse of the error variances using the generic fusion equation under the assumption of independence of errors between the encoders, *i.e.*, Equation (2.1). The resulting velocity models are given as follows.

Model R (for fused velocity of the right rear wheel) is given by the following equation:

$$v_r = \left[\frac{\sum_{n=1}^{3} (\sigma_{vr,n}^2)^{-1} (v_{r,n})}{\sum_{n=1}^{3} (\sigma_{vr,n}^2)^{-1}} \right] + \varepsilon_{vr}, \tag{3.7}$$

where ε_{vr} is the residual with $\varepsilon_{vr} \sim N(0, \sigma_{vr})$. Further,

$$\sigma_{vr}^2 = \left(\sum_{n=1}^{3} (\sigma_{vr,n}^2)^{-1} \right)^{-1}. \tag{3.8}$$

Model L (for fused velocity of the left rear wheel) is given by the following equation:

$$v_l = \left[\frac{\sum_{n=1}^{3} (\sigma_{vl,n}^2)^{-1} (v_{l,n})}{\sum_{n=1}^{3} (\sigma_{vl,n}^2)^{-1}} \right] + \varepsilon_{vl}, \tag{3.9}$$

where ε_{vl} is the residual with $\varepsilon_{vl} \sim N(0, \sigma_{vl})$. Further,

$$\sigma_{vl}^2 = (\sum_{n=1}^{3} (\sigma_{vl,n}^2)^{-1})^{-1}. \tag{3.10}$$

Based on the requirements of the ***η***-Filter, velocity models are built for the two operating scenarios by taking weighted averages, as in the case of Equation (3.7).

Model A1 (for fused velocity of the UGV for "*normal*" scenario) is given by the following equation:

$$v_{x1} = \left[\frac{(\sigma_{vr}^2)^{-1} v_r + (\sigma_{vl}^2)^{-1} v_l + (\sigma_{vax}^2)^{-1} v_{ax}}{(\sigma_{vr}^2)^{-1} + (\sigma_{vl}^2)^{-1} + (\sigma_{vax}^2)^{-1}} \right] + \varepsilon_{vx1}, \tag{3.11}$$

where v_{x1} is the fused velocity along the x_V-axis and ε_{vx1} is the residual with $\varepsilon_{vx1} \sim N(0, \sigma_{vx1})$. Further,

$$\sigma_{vx1}^2 = ((\sigma_{vr}^2)^{-1} + (\sigma_{vl}^2)^{-1} + (\sigma_{vax}^2)^{-1})^{-1}. \tag{3.12}$$

Equation (3.11) is valid only for straight-line trajectories. For arbitrary trajectories, the average of v_r and v_l is computed and then combined with v_{ax} in the minimum variance sense, as in the case of Equation (3.7).

Model A2 (for fused velocity of the UGV for "*trapped*" scenario) is given by the following equation:

$$v_{x2} = v_{ax} + \varepsilon_{vx2}, \tag{3.13}$$

where v_{x2} is the fused velocity along the x_V-axis and ε_{vx2} is the residual with $\varepsilon_{vx2} \sim N(0, \sigma_{vx2})$. Further,

$$\sigma_{vx2}^2 = \sigma_{vax}^2. \tag{3.14}$$

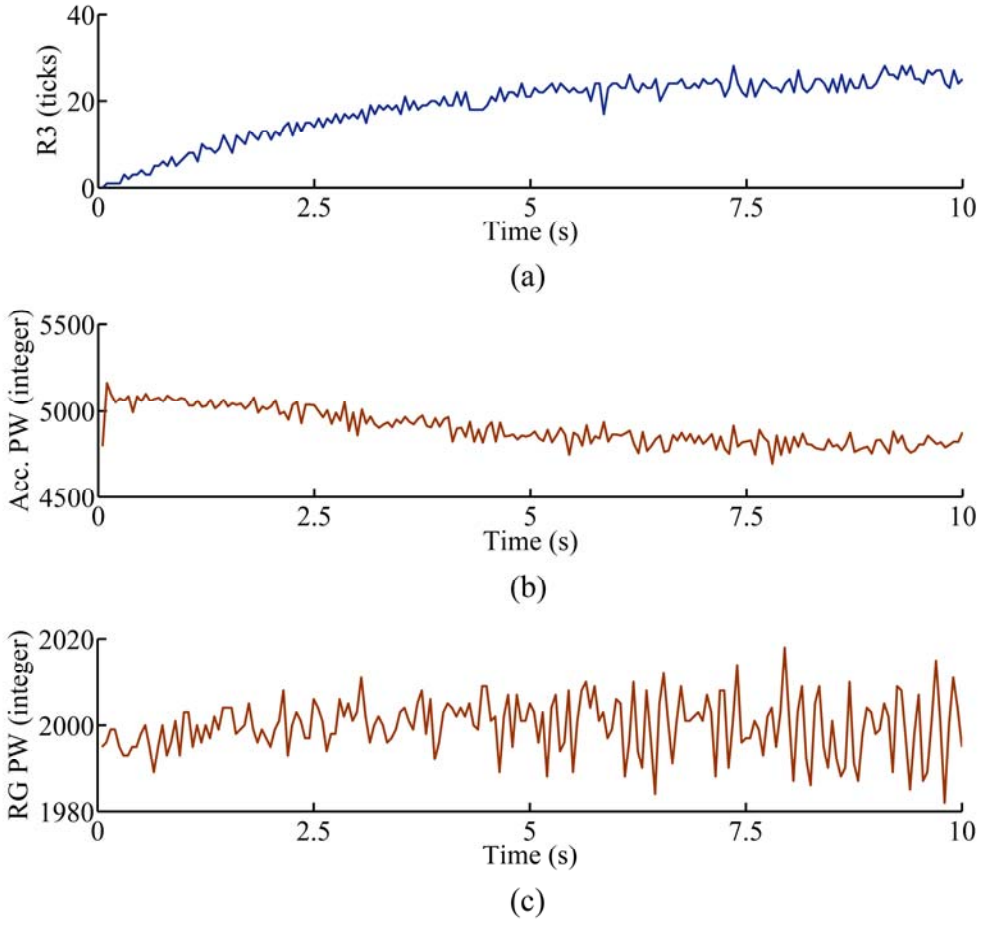

Figure 3.7 The Raw Measurements for a Straight Line Run: Measurement from the rear wheel encoder R3 (a), accelerometer-x Pulse Width (PW) measurement (b), and the Rate-Gyro (RG) PW measurement (c). The high-frequency noise visible in these plots is mainly due to vibrations. It is countered by using low-pass filters.

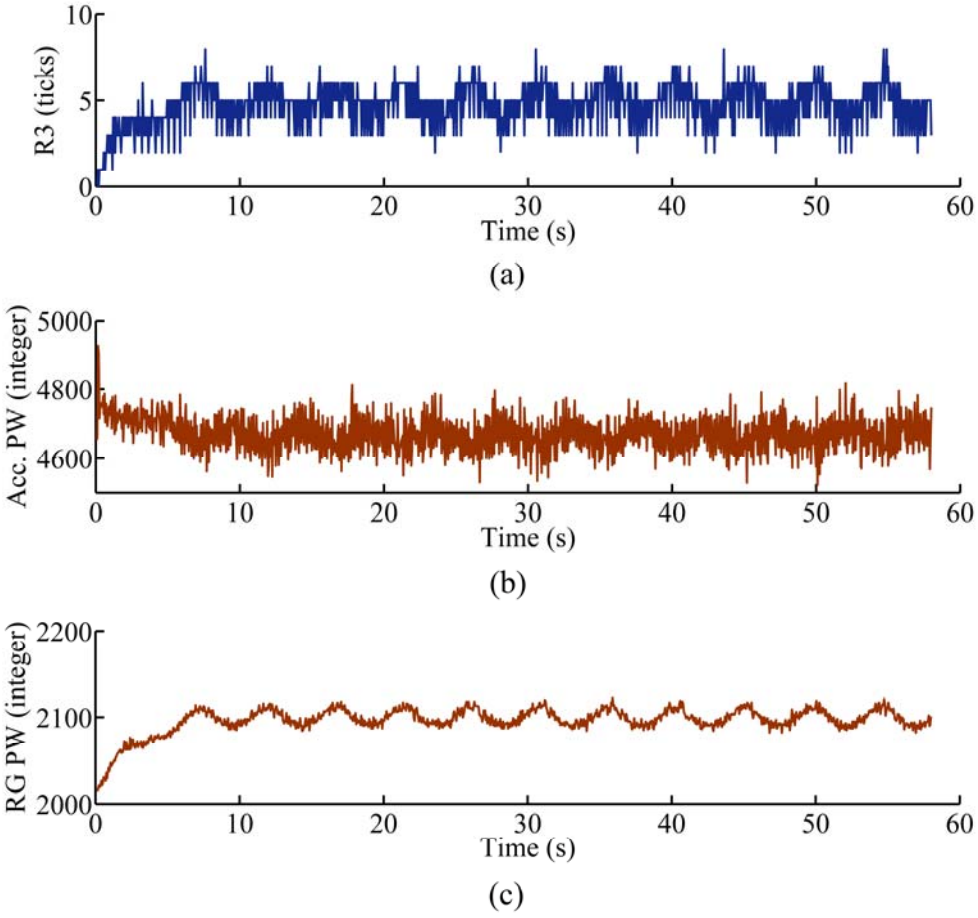

Figure 3.8 The Raw Measurements for a Curve Run: Measurements from the rear wheel encoder R3 (a), accelerometer-x PW measurement (b), and the RG PW measurement (c). The fluctuations (low-frequency noise) are caused due to the inclined surface on which the experiment was conducted.

3.2.2 Models for Angular Velocity

An experiment consisting of thirty-three runs was conducted with the objective of creating two models for angular velocity, *i.e.*, one for each scenario. The runs included three repetitions each for eleven steering-angle settings. Data from the six rear wheel encoders, the rate-gyro, and the compass were logged at a frequency of 20 Hz. Figure 3.8 shows the raw measurement plots. The compass data was logged in order to compute the angular velocity of the UGV. The angular velocity was computed by dividing the total angle turned, as determined by the compass, by the preset duration of the run. The following models are built using the empirical data.

Model W1 (for angular velocity based on the rear wheel encoders) is given by the following equation:

$$\omega_{rl} = \beta_0 + \beta_1 (TPS_{r,n} - TPS_{l,n}) + \varepsilon_{\omega rl}, \tag{3.15}$$

where ω_{rl} is the angular velocity measured by the right-left encoder difference, n = 3 (for this work), and $\varepsilon_{\omega rl}$ is the residual with $\varepsilon_{\omega rl} \sim N(0, \sigma_{\omega rl})$. Table 3.1 shows a listing of the parameter estimates, $\hat{\beta}_n$. The relatively lower value of R^2 for model W1 can be inferred from Table 3.1. Figure 3.9 shows a plot of Model W1. The poor goodness-of-fit is noticeable. This indicates that the wheel encoders are less reliable in estimating the angular velocity of the UGV under consideration.

Model W2 (for angular velocity based on the rate-gyro) is given by the following equation:

$$\omega_{rg} = \beta_0 + \beta_1 (pulse_{rg}) + \varepsilon_{\omega rg}, \tag{3.16}$$

where ω_{rg} is the angular velocity measured by the rate-gyro, $pulse_{rg}$ is the pulse width difference integer measured from the rate-gyro, *i.e.*, the difference between the pulse width integer while the UGV is stationary (*at rest*) and the measured pulse width integer, and $\varepsilon_{\omega rg}$ is the residual with $\varepsilon_{\omega rg} \sim N(0, \sigma_{\omega rg})$. Figure 3.10 shows a plot of model W2.

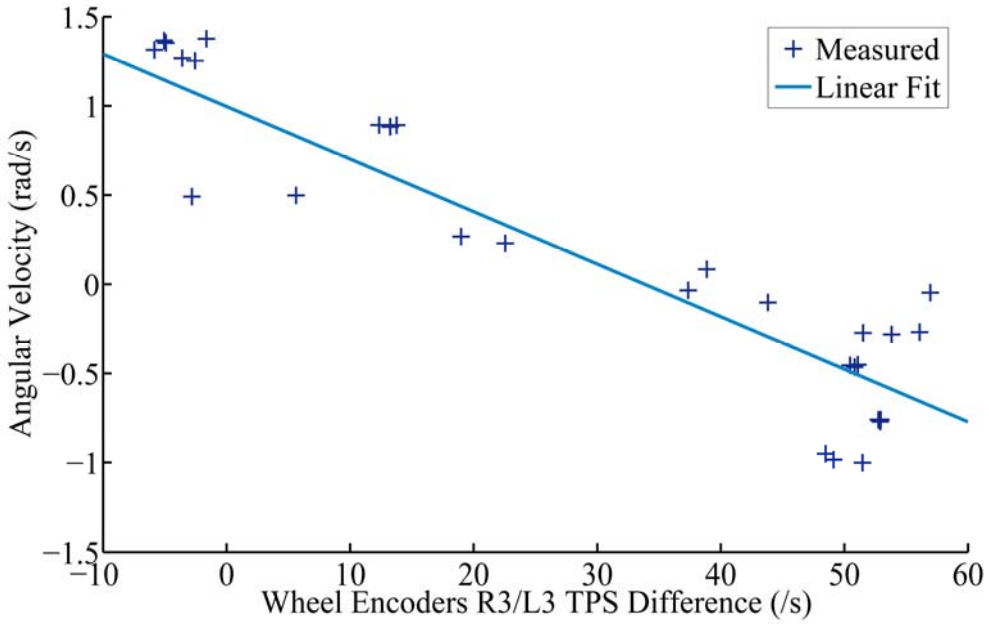

Figure 3.9 Angular Velocity from Rear Wheel Encoder R3/L3 TPS Difference: The difference between the right wheel encoder R3 TPS and the left wheel encoder L3 TPS shows a linear relationship with the angular velocity.

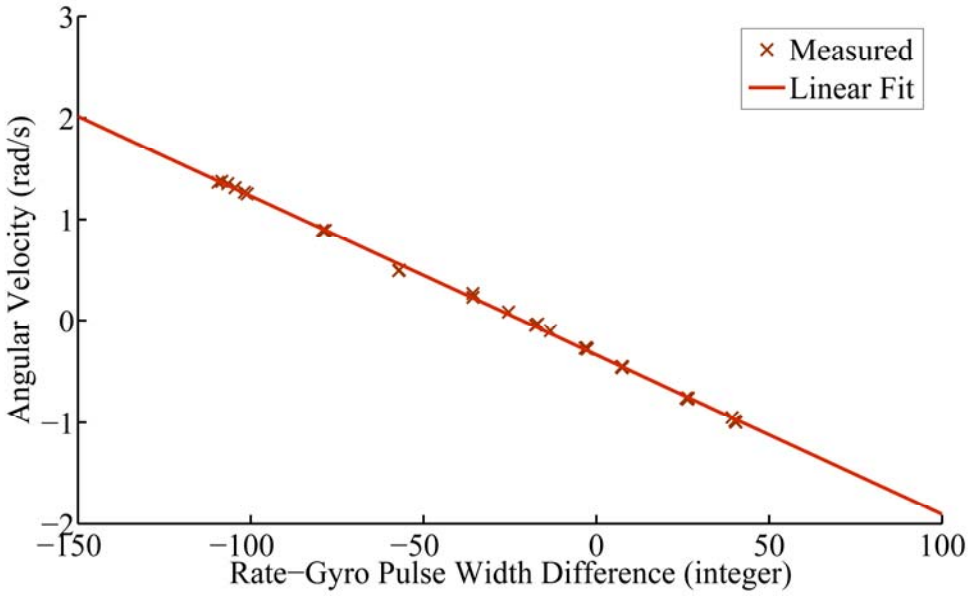

Figure 3.10 Angular Velocity from the Rate-Gyro: The difference between the "*at rest*" pulse width and the measured pulse width shows a linear relationship with the angular velocity.

The angular velocity models for the trapped and the normal operating scenarios are created by taking weighted averages, as in the case of Equation (3.7).

Model B1 (for fused angular velocity for the "*normal*" scenario) is given by the following equation:

$$\omega_{z1} = \left[\frac{(\sigma^2_{\omega rl})^{-1}\omega_{rl} + (\sigma^2_{\omega rg})^{-1}\omega_{rg}}{(\sigma^2_{\omega rl})^{-1} + (\sigma^2_{\omega rg})^{-1}} \right] + \varepsilon_{\omega z1}, \tag{3.17}$$

where ω_{zl} is the fused angular velocity about the z_V-axis (Figure 3.2) and $\varepsilon_{\omega z1}$ is the residual with $\varepsilon_{\omega z1} \sim N(0, \sigma_{\omega z1})$. Further,

$$\sigma_{\omega z1} = ((\sigma^2_{\omega rl})^{-1} + (\sigma^2_{\omega rg})^{-1})^{-1}. \tag{3.18}$$

Model B2 (for fused angular velocity for the "*trapped*" scenario) is given by the following equation:

$$\omega_{z2} = \omega_{rg} + \varepsilon_{\omega z2}, \tag{3.19}$$

where ω_{z2} is the fused angular velocity about the z_V-axis and $\varepsilon_{\omega z2}$ is the residual with $\varepsilon_{\omega z2} \sim N(0, \sigma_{\omega z2})$. Further,

$$\sigma^2_{\omega z2} = \sigma^2_{\omega rg}. \tag{3.20}$$

3.2.3 Models for Orientation

The inclination of the surface is considered as a factor that could impact the measurements from the digital compass. Two models are required for the two "*test*" surfaces, *i.e.*, one parking lot with a level surface and another with an inclined surface. Figure 3.19 shows the inclined surface. The methodology for modeling the compass is similar to the procedure presented in [Oje00]. The compass was mounted on the UGV at a location that was free of magnetic interference (Figure 3.1). In order to prevent errors due to magnetic storms [McL04], a check was made with a local observatory to confirm the absence of magnetic storms. The UGV was first mounted on an aluminum fixture and aligned to the geomagnetic north. Then, the entire setup was indexed in clockwise and counter-clockwise directions at 45 degree increments from the geomagnetic north. A measurement was recorded at each index point. The procedure was performed twice for each of the two test surfaces.

A fifth degree polynomial model appears to offer the best fit for the two test surfaces based on a qualitative assessment of the residual plots (Figure 3.11). The

standard error for a fifth degree model is 34% less than that for a third degree model and is 65% less than that for a linear model. The goodness-of-fit is greater than 0.99 for all the three models. The *declination* (or magnetic variation), which is defined as the difference between the true north and the geomagnetic north, depends on the location as well as the time of measurement [McL04]. This value (4.7333º for the current validation experiment location and time) is to be "*added*" to the fitted model while computing the absolute orientation [McL04].

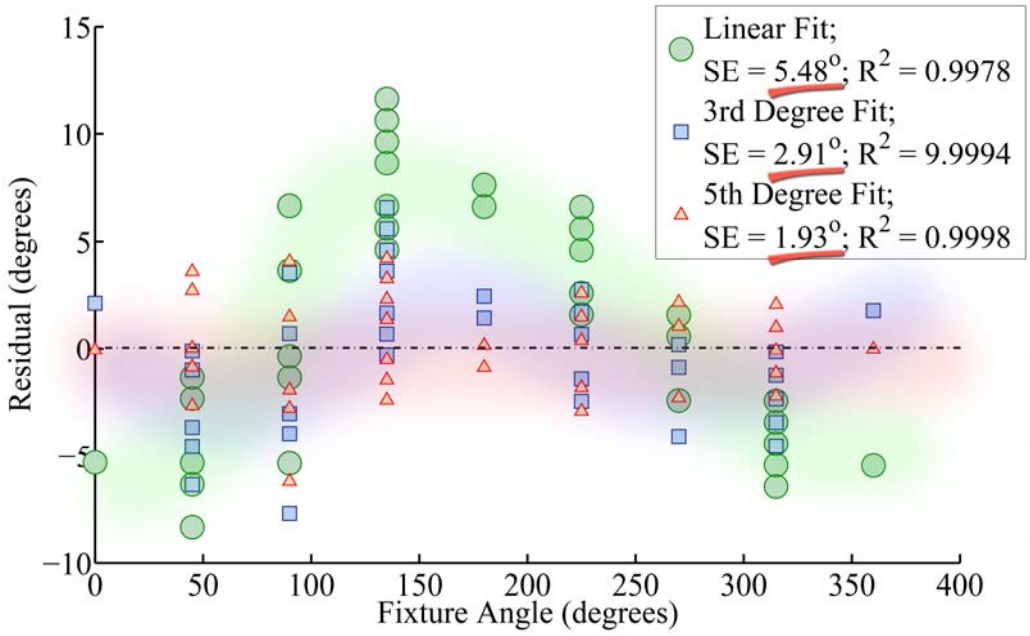

Figure 3.11 The Compass Residual Plots for Three Types of Fits: Residuals of the linear fit and the third degree fit show nonlinear trends. Residuals of the fifth degree fit do not exhibit any trend. They also have the least Standard Error (SE) and the highest goodness-of-fit. A sixth degree fit tends to *over-fit*. It is therefore not considered.

Model D*n* (for orientation based on the compass, *n* = location = 1, 2) is given by the following equation:

$$\psi_k = \beta_0 + \beta_1\psi_{co} + \beta_2\psi_{co}^2 + \beta_3\psi_{co}^3 + \beta_4\psi_{co}^4 + \beta_5\psi_{co}^5 + \varepsilon_\psi, \tag{3.21}$$

where ψ is the orientation (heading), subscript *co* refers to the compass, and ε_ψ is the residual with $\varepsilon_\psi \sim N(0, \sigma_\psi)$. Figure 3.12 shows the fifth degree compass curve for a *level* surface.

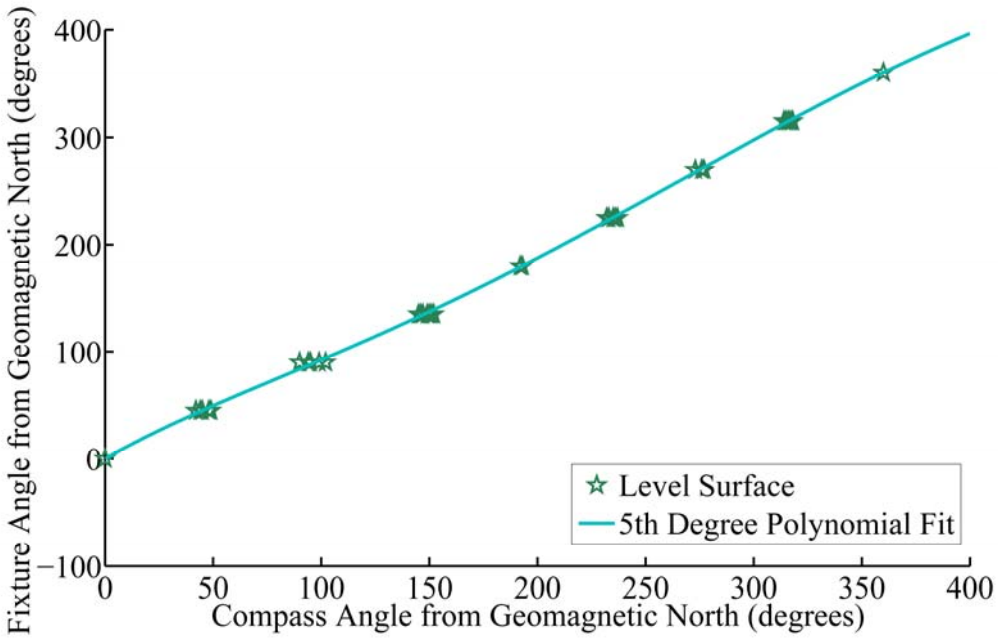

Figure 3.12 The Compass Curve for Level Surface: A fifth degree polynomial model is selected based on an assessment of the residual plots and goodness-of-fit.

3.2.4 Mass Assignment Table for GPS

A mass assignment table that contains the required mass functions is created based on the factors that influence the GPS reading. Two hundred readings were logged in five locations and in two staggered time windows. The geographic coordinates (latitude, longitude) for the five locations are as follows: (32.7263639°, −97.1128827°), (32.7298098°, −97.1200778°), (32.7321189°, −97.1126556°), (32.7320419°, −97.1119642°), and (32.7301885°, −97.1106639°). The staggering of the data-logging time windows was done keeping in mind the approximately 12-hour period of the satellites and the equal spacing of the 4 satellites in each of the 6 orbits of the GPS constellation [Dju01]. The receiver was manually *reset* prior to each measurement in order to ensure a fresh position fix. Based on the results of the Analysis of Variance (ANOVA) F-test, it "*cannot*" be concluded, at the 5% significance level (α), that the position errors depend on the *time* or the *location* of measurement [Vib07a]. However, the GPS position error shows a dependence on the number of satellites (#*Sat*) and the Horizontal Dilution of Precision (*HDOP*). Three discrete levels for the #*Sat* and the *HDOP* criteria are created. Figure 3.13 shows a scatter-plot of the errors for the three levels of the #*Sat* and the *HDOP* criteria.

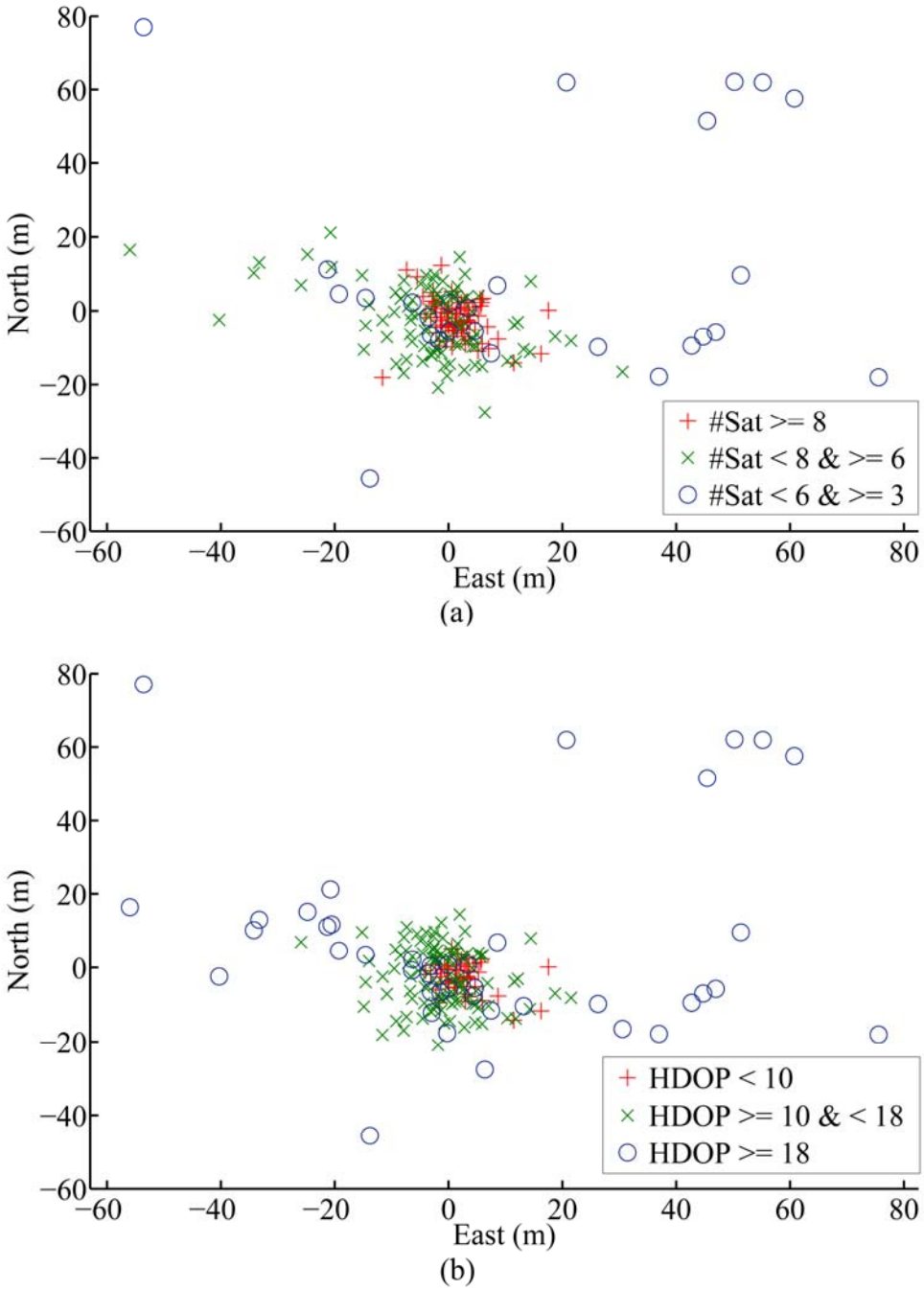

Figure 3.13 Error Plots of the GPS as a Function of *#Sat* (a) and *HDOP* (b): The measurements have a higher precision when *#Sat* >= 8 and when *HDOP* < 10.

Table 3.2 Mass Assignment Table for GPS Sensor Goodness

Criteria	Value	Axis (a)	${}^{a}m_s(yes)$	${}^{a}m_s(no)$	${}^{a}m_s(yes, no)$
#Sat (s=1)	*>= 8*	*N*	0.95	0.00	0.05
		E	0.91	0.00	0.09
	< 8 & >= 6	*N*	0.75	0.10	0.15
		E	0.69	0.03	0.28
	< 6 & >= 3	*N*	0.33	0.57	0.10
		E	0.53	0.30	0.17
HDOP (s=2)	*< 10*	*N*	0.94	0.00	0.06
		E	0.96	0.00	0.04
	>= 10 & < 18	*N*	0.88	0.02	0.10
		E	0.77	0.01	0.22
	>= 18	*N*	0.36	0.56	0.08
		E	0.44	0.24	0.32

Therefore, a mass assignment table (Table 3.2) is created based on the following two criteria: *#Sat* and *HDOP*. Within each criteria instance, the mass functions ${}^{a}m_s(U)$ are computed using the empirical data based on the fraction of occurrence and the following rule:

IF $|error| < 10\ m$ THEN $U = \{yes\}$

ELSE IF $|error| >= 20\ m$ THEN $U = \{no\}$

ELSE $U = \{yes, no\}$.

The error variances along the north and the east axes are computed using the same rule as above [Vib07a]. Table 3.2 is subsequently used in the computation of the values of the **R** matrix in Equations (3.44) and (3.45).

3.3 Components of the $\boldsymbol{\eta}$-Filter

3.3.1 Adaptive Pre-Processing

The APP unit uses multiple models for processing raw sensor measurements, and adapts to operating scenarios by "*switching*" between models. Figure 3.14 shows the components of the APP for the UGV localization problem. With the exception of the GPS measurements, all measurements ($\tilde{\mathbf{y}}_{s1},\ldots,\tilde{\mathbf{y}}_{sn}$) are first processed by Low Pass Filters (LPFs) that take the form of moving average filters. The LPFs are effective in reducing vibration-induced noise. Two models for linear velocity (A1 and A2) and two models for angular velocity (B1 and B2) are created as described in Section 3.2. The EEC unit performs the switching between the two sets of models and is described in next section. The *source-of-evidence* vector for UGV localization is defined as

$$\mathbf{s}_p = [HDOP,\ \#Sat,\ a_x,\ v_l,\ \ v_r]^T, \tag{3.22}$$

where the subscript *p* refers to APP.

The input noise covariance matrix (**S**) depends on the position of the switch, *i.e.*, it depends on whether the models used are (A1 and B1) or (A2 and B2). The corresponding error variances of the models are used as the diagonal elements of the matrix **S**.

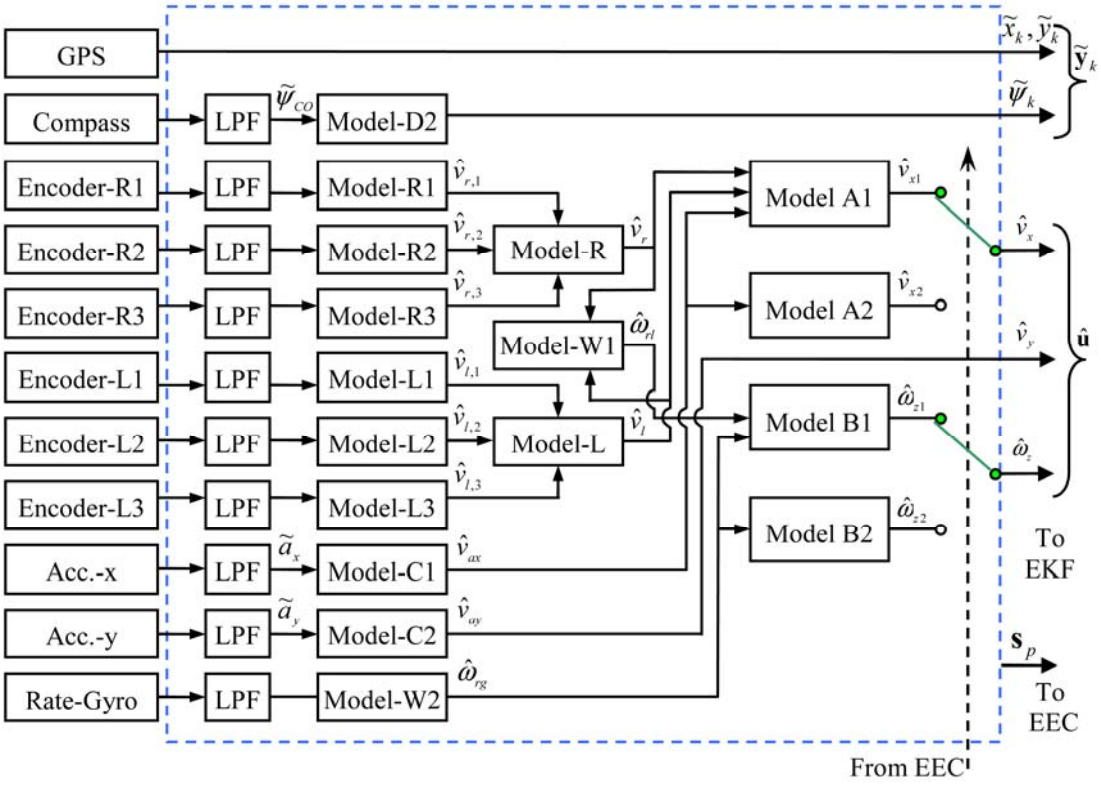

Figure 3.14 The Adaptive Pre-Processing Framework: The raw sensor measurements are adaptively pre-processed by switching between models.

3.3.2 Evidence Extraction and Combination

The EEC forms the "*crux*" of the ***η***-Filter framework and relies on the DS theory of evidence. The first step in the application of the *DS theory* [Sha76] is the definition of the *frame of discernment*, *W*, which represents the set of all possible worlds the UGV or the sensor can be in. Thereafter, the subsets of importance are identified. Evidence is quantified as a continuous or as a discrete value depending on the source of the evidence. In the evidence extraction stage, mass functions are assigned

based on the components of the source-of-evidence vector. Either a *fuzzy-type* method or a rule-based *mass assignment table* is used depending on whether the evidence is continuous or discrete. *Mass function* (or basic probability assignment) indicates the degree of support that a body of evidence provides for "*exactly*" one proposition, *i.e.*, the degree of belief one should accord exactly that proposition on the basis of the evidence [Sha76]. It is a number between zero and one and is defined by the following equation [Hal03]:

$$m(U): 2^W \rightarrow [0..1] \text{ and } U \in W, \tag{3.23}$$

where the subset U represents a proposition.

The two properties of a mass function are follows [Hal03]:

$$m(\varnothing) = 0. \tag{3.24}$$

$$\sum_{U \subseteq W} m(U) = 1. \tag{3.25}$$

Once evidence extraction is completed, the *Dempster's rule for combination* is applied in order to fuse the disparate pieces of evidences that contribute to a proposition (Figure 3.16). The combined degree of support for a proposition is described by the following equation [Hal03]:

$$(m_1 \oplus m_2)(U) = \sum_{U_1 \cap U_2 = U} m_1(U_1) m_2(U_2) / c, \tag{3.26}$$

where

$$c = \sum_{U_1 \cap U_2 \neq \varnothing} m_1(U_1) m_2(U_2). \tag{3.27}$$

Equation (3.26) represents the "*pooling*" of evidence and is also known as the *orthogonal sum*. It deals "*symmetrically*" with the evidences, *i.e.*, the result of the combination does not depend on the order in which the evidence arrives. This is in contrast to the Bayesian theory, where the order in which the evidence arrives impacts the outcome of the combination [Sha76].

Finally, the belief function (also known as support function) is computed. The *belief function* represents the "*total*" degree of support provided by a body evidence for a proposition [Sha76] and is defined by the following equation [Hal03]:

$$Bel(U): 2^W \rightarrow [0..1] \text{ and } W = \{w_1, w_2, ..., w_n\}. \tag{3.28}$$

It is computed using the following relationship [Hal03]:

$$Bel_m(U) = \sum_{U' \subseteq U} m(U'). \tag{3.29}$$

The three properties of a belief function are as follows [Hal03]:

$$Bel(\varnothing) = 0. \tag{3.30}$$

$$Bel(W) = 1. \tag{3.31}$$

$$Bel(\cup_{i=1}^{n} U_i) \geq \sum_{i=1}^{n} \sum_{\{I \subseteq \{1,...,n\}: |I|=i\}} (-1)^{i+1} Bel(\cap_{j \in I} U_j). \tag{3.32}$$

Definition: A car-type UGV with differentials is said to be "*trapped*" if at least one wheel is spinning but there is no displacement of the UGV.

The following sections describe a *two-pronged* approach: (1) for the "trapped robot" scenario and (2) for GPS sensor goodness.

3.3.2.1 The "Trapped Robot" Scenario

The frame of discernment, W, for operating scenarios is given by:

$$W = \{norm,\ trap\}, \tag{3.33}$$

where *norm* = normal and *trap* = trapped. The subsets of localization importance are

$$\{norm\},\ \{trap\},\ \{norm,\ trap\}. \tag{3.34}$$

The subset $\{norm,\ trap\}$ corresponds to the "*ignorance*" component of uncertainty. A set of two criteria contribute evidence to a proposition (scenario in this case) and are given as follows: (1) the magnitude of velocity difference between the right and the left rear wheels, *i.e.*, $|v_r - v_l|$, and (2) the magnitude of acceleration of the UGV, *i.e.*, $|a_x|$. As the system is dependent on the information from only the rear wheel encoders, a trapped robot scenario that involves a front wheel spin *is not detected*. As the evidences are continuous variables, a "*fuzzy-type*" method for mass assignment is used (Figure 3.15) [Car04]. The combined mass function for $U = \{trap\}$ is computed using Equation (3.26). The belief function, $Bel(trap)$, is computed using Equation (3.29). Based on the value of $Bel(trap)$, switching between models is performed, *i.e.*, if the belief exceeds a preset *threshold* value (a value of 0.5 is considered here). Hence, the APP adapts to the changing operating scenarios of the UGV by switching between models for linear and angular velocities.

3.3.2.2 GPS Sensor Goodness

The frame of discernment for GPS sensor goodness is defined by the following equation:

$$W = \{yes,\ no\}\,, \tag{3.35}$$

where *yes* and *no* are answers to the following question: *is the sensor reading good?* The subsets of importance for sensor goodness are

$$\{yes\},\ \{no\},\ \{yes,\ no\}\,. \tag{3.36}$$

In this case, the subset $\{yes, no\}$ corresponds to the "*ignorance*" component of uncertainty. As the evidences are discrete variables (*#Sat* and *HDOP*), a rule-based "*mass assignment table*" (Table 3.2) is used. Like in the previous case, the combined mass functions are computed using Equation (3.26). The combined mass functions are subsequently used in the computation of the components of the measurement error covariance matrix in Equations (3.44) and (3.45). In this way, the fusion filtering system adapts to the quality of the GPS measurements, *i.e.*, the measurement noise covariance matrix (**R**) adapts to sensor goodness depending on *#Sat* and *HDOP*.

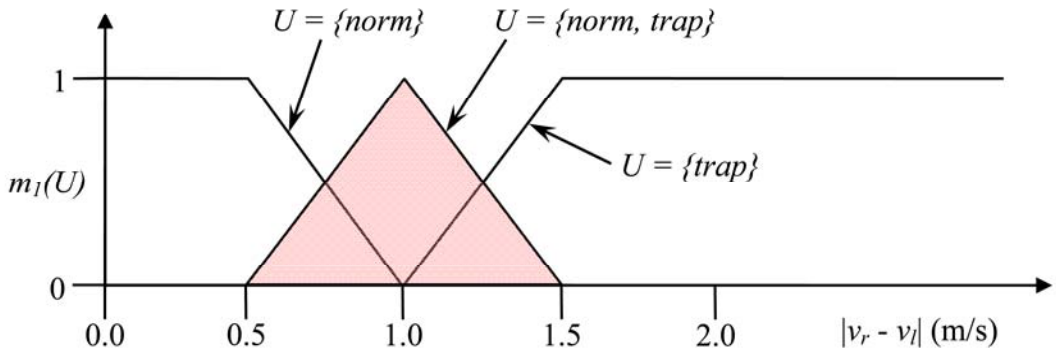

(a)

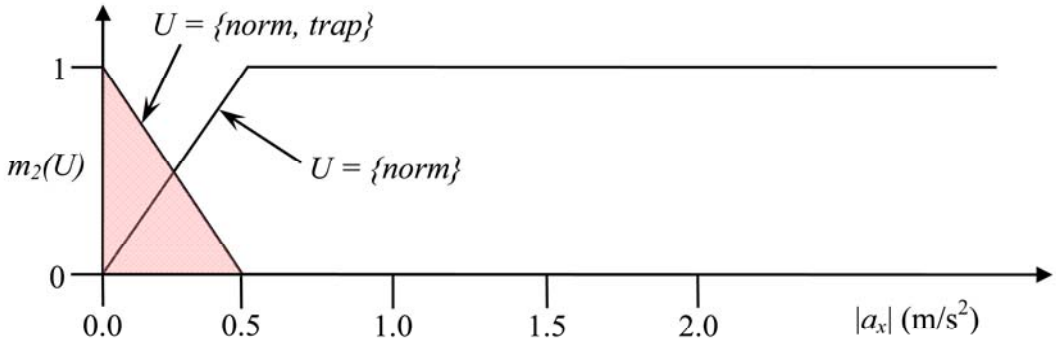

(b)

Figure 3.15 Fuzzy-Type Mass Assignment for the Trapped Robot Scenario: The velocity difference magnitude criterion (a) and the acceleration magnitude criterion (b). The shaded regions represent the "*ignorance*" component.

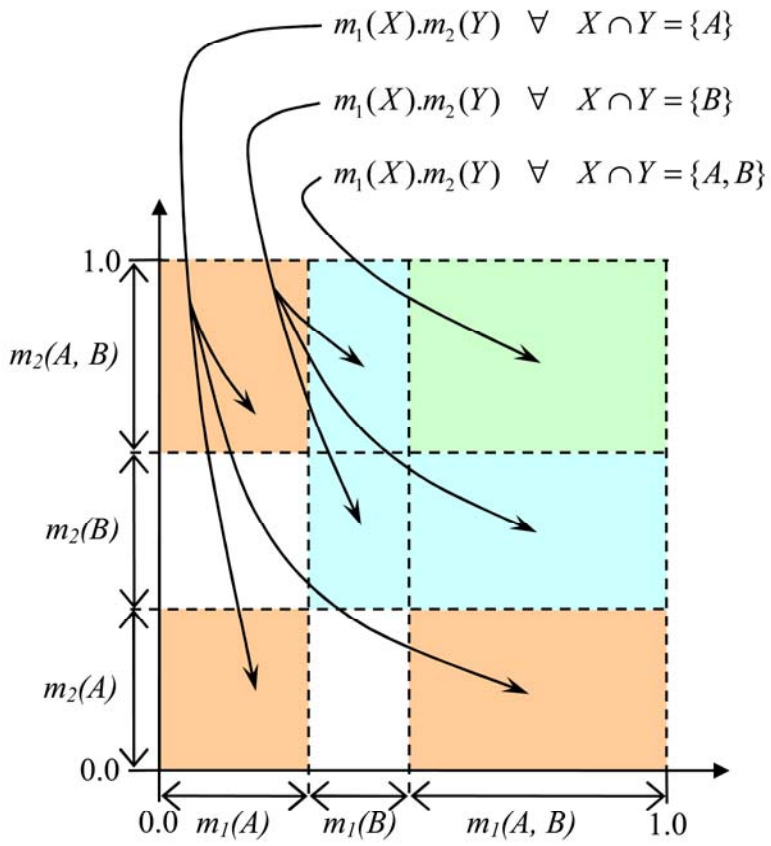

Figure 3.16 A Geometric Interpretation of Dempster's Rule for Combination: {*A*, *B*} represents {*norm*, *trap*} and {*yes*, *no*} for the trapped robot scenario and GPS sensor goodness respectively.

3.3.3 Extended Kalman Filtering

As the UGV localization process model is *nonlinear*, an EKF is developed [Cra04, May79]. Despite the existence of dynamical models for UGVs [Eco00], a kinematic (constant velocity) model is used with the intention of keeping it simple. As the symbolic notation conforms to the AS-4/JAUS convention [Joi04], the x-axis points towards the north, the y-axis points towards the east, and the z-axis points towards the earth, *i.e.*, "*downwards*" (Figures 3.2 and 3.17). Platforms with the following steering mechanisms are considered [Bra03]: *differential* steering (wheeled or tracked) and *Ackermann* steering.

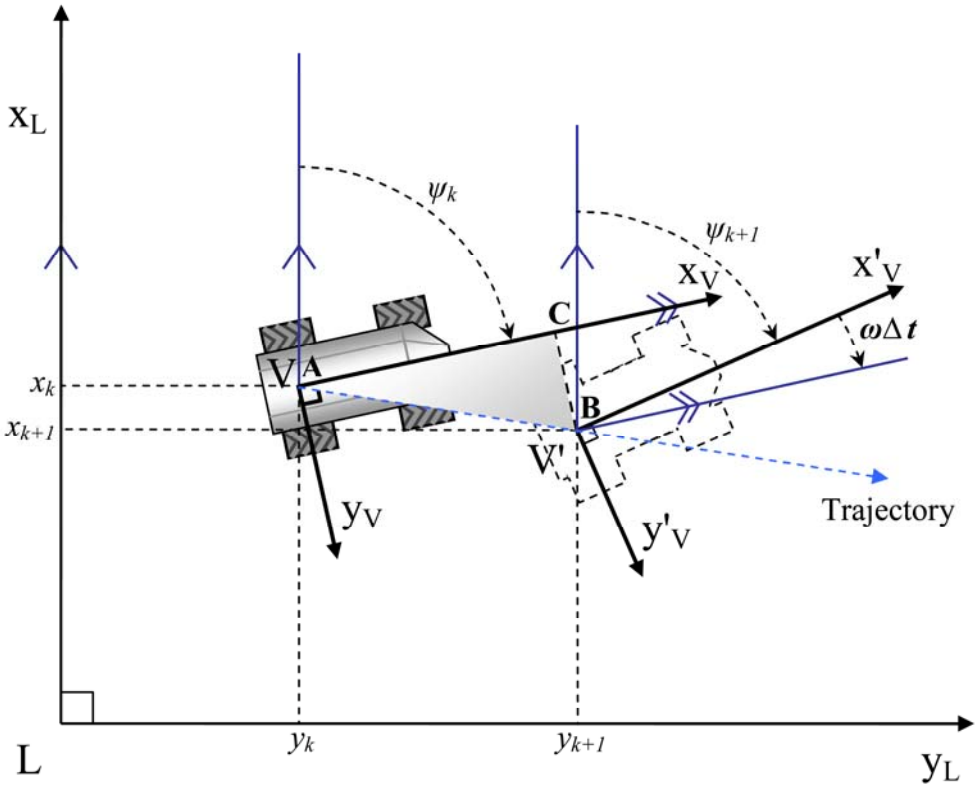

Figure 3.17 The Kinematic Process Description: A geometric description of the pose transition of the UGV from time-step *k* to time-step *k+1*.

3.3.3.1 Process and Measurement Models

The nonlinear *process model* is a difference equation that propagates the state of the system from the current discrete time-step (k) to the next discrete time-step (k+1) and is defined as follows:

$$\mathbf{x}_{k+1} = \boldsymbol{\varphi}(\mathbf{x}_k, \mathbf{u}_k) + \mathbf{w}_k, \tag{3.37}$$

where $\mathbf{x} = [x, y, \psi]^T$ is the state vector, x is the position along the x_L-axis in meters, y is the position along the y_L-axis in meters, and ψ is the orientation about the z_L-axis in radians, $\mathbf{u} = [v_x, v_y, \omega_z]^T$ is the input vector, v_x is the velocity along the x_V-axis, v_y is the velocity along the y_V-axis, ω_z is angular velocity about the z_V-axis, $\boldsymbol{\varphi}(\mathbf{x}_k, \mathbf{u}_k)$ is a nonlinear function of $\mathbf{x}$ and $\mathbf{u}$, and $\mathbf{w} = [w_x, w_y, w_\psi]^T$ is the error with $\mathbf{w}_k \sim N(0, \mathbf{Q}_k)$. $\mathbf{Q}$ is the process noise covariance matrix. "*Tuning*" of the Kalman filter refers to the adjustment of the elements of the matrix $\mathbf{Q}$ in order to achieve the required performance. An increase in the values of the elements of matrix $\mathbf{Q}$ results in a corresponding increase in the weighting of the measurements. Therefore, the values of $\mathbf{Q}$ should be on the lower side when the sensors are noisy or faulty.

After the application of homogeneous transformation [Cra89], the nonlinear process model is represented by the following three equations:

$$x_{k+1} = x_k + v_x \Delta t(\cos \psi_k) - v_y \Delta t(\sin \psi_k) + w_x, \tag{3.38}$$

$$y_{k+1} = y_k + v_x \Delta t(\sin \psi_k) + v_y \Delta t(\cos \psi_k) + w_y, \text{ and} \tag{3.39}$$

$$\psi_{k+1} = \psi_k + \omega_z \Delta t + w_\psi. \tag{3.40}$$

The input covariance matrix depends on the switch position of the APP and is given by

$$\mathbf{S}_k = diag(\sigma_{vx}^2, \sigma_{vy}^2, \sigma_{\omega z}^2), \tag{3.41}$$

where σ_{vx}^2 is the variance of velocity along axis x_v, σ_{vy}^2 is the variance of velocity along axis y_v, and $\sigma_{\omega z}^2$ is the variance of angular velocity attributed to the rate-gyro. Here, we assume that there is no cross-correlation between the errors in angular and linear velocities.

The linear *measurement model* that relates the state of the system to the measurement vector is given by equation

$$\tilde{\mathbf{y}}_k = \mathbf{H}_k \mathbf{x}_k + \mathbf{v}_k, \tag{3.42}$$

where $\tilde{\mathbf{y}}$ is the measurement vector, **H** is the measurement matrix (an identity matrix in this case), and **v** is the measurement error with $\mathbf{v}_k \sim N(0, \mathbf{R}_k)$.

The measurement noise covariance matrix depends on the available evidence (*#Sat* and *HDOP*) and is given by

$$\mathbf{R}_k = diag(\sigma_{xx}^2, \sigma_{yy}^2, \sigma_{\psi\psi}^2), \tag{3.43}$$

where

$$\sigma_{xx}^2 = {}^{N}m(yes).\sigma_{x,yes}^2 + {}^{N}m(yes,no).\sigma_{x,yes,no}^2 + {}^{N}m(no).\sigma_{x,no}^2, \tag{3.44}$$

$$\sigma_{yy}^2 = {}^{E}m(yes).\sigma_{y,yes}^2 + {}^{E}m(yes,no).\sigma_{y,yes,no}^2 + {}^{E}m(no).\sigma_{y,no}^2, \tag{3.45}$$

and

$$\sigma_{\psi\psi}^2 = \sigma_{\psi}^2. \tag{3.46}$$

The prefixed superscripts *N* and *E* refer to north and east respectively. The values for the variances on the right hand side of Equations (3.44) and (3.45) are selected from Table III in [Vib07a]. The value for the variance on the right hand side of Equation (3.46) is selected from Table 3.1. The mass functions ${}^{a}m(U)$ are drawn from the mass assignment table (Table 3.2). The weighting of the variances are performed on the basis of the second property of mass functions as stated in Equation (3.25), *i.e.*, $\sum_{U \subseteq W} m(U) = 1$. In other words, further normalization is not required.

3.3.3.2 Measurement Update and Propagation Cycle

If viewed as a finite state machine, a Kalman filter would have three states as shown in Figure 3.18, *i.e.*, initialization, measurement update, and propagation.

Figure 3.18 The Discrete Kalman Filter Cycle: The cycle starts at the initialization state and then transitions to the measurement update state after the initialization of the state estimate and its error covariance. If there is a valid measurement based on the squared Mahalanobis distance criterion, then measurement update is performed. If there is no valid measurement or no measurement at all, there is a transition to the propagation state. Propagation is performed as per the process model, and the cycle transitions back to the measurement update state.

The *initialization* step assigns the initial state estimate and its error covariance as the *a priori* state estimate and the *a priori* error covariance respectively. It is formulated as follows.

The *a priori* state estimate at time-step $k = 0$ is given by

$$\hat{\mathbf{x}}_0^- = \hat{\mathbf{x}}(t_0), \tag{3.47}$$

and the *a priori* estimation error covariance matrix $\mathbf{P}_0^-$ is given by

$$\mathbf{P}_0^- = E\{(\mathbf{x}(t_0) - \hat{\mathbf{x}}(t_0))(\mathbf{x}(t_0) - \hat{\mathbf{x}}(t_0))^T\}, \tag{3.48}$$

where $E\{.\}$ represents the expected value.

The *measurement update* step is performed in three steps as follows: (1) computation of gain, (2) measurement validation, and (3) update.

The first step involves the computation of the *Kalman gain*, a weighting factor that determines the proportion of the measurement that should be added to the *a priori* state estimate. It is given by the following equation:

$$\mathbf{K}_k = \mathbf{P}_k^- \mathbf{H}_k^T [\mathbf{H}_k \mathbf{P}_k^- \mathbf{H}_k^T + \mathbf{R}_k]^{-1}, \tag{3.49}$$

where **K** is the Kalman gain.

Then the measurement is "validated" using the squared *Mahalanobis distance* ($^M d_k$) criterion and is given by the following condition [Bou00]:

$$^M d_k^2 = \mathbf{e}_k^T [\mathbf{H}_k \mathbf{P}_k^- \mathbf{H}_k^T + \mathbf{R}_k]^{-1} \mathbf{e}_k < \chi^2_{3,0.05}, \tag{3.50}$$

where $\mathbf{e}_k = [\tilde{\mathbf{y}}_k - \mathbf{H}_k \hat{\mathbf{x}}_k^-]$ is the innovation vector and $\chi^2_{3,0.05} = 7.815$ is obtained from a Chi-squared distribution table for degrees of freedom (dimension of the state vector) = 3

and p-value = 0.05. The validation step ensures that the ${}^{M}d_k^2$ value for measurement updates is bounded within its 95% confidence limits.

The final step is the computation of the update where the *a priori* state estimate is combined with the weighted innovation vector in order to obtain the *a posteriori* state estimate. The corresponding *a posteriori* error covariance is also computed. The equations are given by

$$\hat{\mathbf{x}}_k^+ = \hat{\mathbf{x}}_k^- + \mathbf{K}_k[\tilde{\mathbf{y}}_k - \mathbf{H}_k\hat{\mathbf{x}}_k^-] \tag{3.51}$$

and

$$\mathbf{P}_k^+ = [\mathbf{I} - \mathbf{K}_k\mathbf{H}_k]\mathbf{P}_k^- . \tag{3.52}$$

The *propagation* step propagates the state of the system and its error covariance from the current time-step to the next time-step. As the process model is nonlinear, *linearization* is performed at the most recent state estimate, *i.e.*, the *a posteriori* state estimate. The corresponding equations are given as follows:

$$\hat{\mathbf{x}}_{k+1}^- = \boldsymbol{\varphi}(\hat{\mathbf{x}}_k^+, \hat{\mathbf{u}}_k) \tag{3.53}$$

and

$$\mathbf{P}_{k+1}^- = \boldsymbol{\Phi}_k(\hat{\mathbf{x}}_k^+)\mathbf{P}_k^+\boldsymbol{\Phi}_k^T(\hat{\mathbf{x}}_k^+) + \boldsymbol{\Gamma}_k(\hat{\mathbf{x}}_k^+)\mathbf{S}_k\boldsymbol{\Gamma}_k^T(\hat{\mathbf{x}}_k^+) + \mathbf{Q}_k , \tag{3.54}$$

where the Jacobian matrices $\boldsymbol{\Phi}_k(\hat{\mathbf{x}}_k^+)$ and $\boldsymbol{\Gamma}_k(\hat{\mathbf{x}}_k^+)$ are the partial derivatives of $\boldsymbol{\varphi}$ with respect to $\mathbf{x}$ and $\mathbf{u}$ respectively at the point $\hat{\mathbf{x}}_k^+$. Thus,

$$\boldsymbol{\Phi}_k(\hat{\mathbf{x}}_k^+) = \frac{d\boldsymbol{\phi}(\hat{\mathbf{x}}_k^+)}{dx} = \begin{bmatrix} 1 & 0 & -\hat{v}_x\Delta t(\sin\hat{\psi}_k^+) + \hat{v}_y\Delta t(\cos\hat{\psi}_k^+) \\ 0 & 1 & \hat{v}_x\Delta t(\cos\hat{\psi}_k^+) - \hat{v}_y\Delta t(\sin\hat{\psi}_k^+) \\ 0 & 0 & 1 \end{bmatrix} \tag{3.55}$$

and

$$\boldsymbol{\Gamma}_k(\hat{\mathbf{x}}_k^+) = \frac{d\boldsymbol{\phi}(\hat{\mathbf{x}}_k^+)}{du} = \begin{bmatrix} \Delta t(\cos\hat{\psi}_k^+) & -\Delta t(\sin\hat{\psi}_k^+) & 0 \\ \Delta t(\sin\hat{\psi}_k^+) & \Delta t(\cos\hat{\psi}_k^+) & 0 \\ 0 & 0 & \Delta t \end{bmatrix}. \tag{3.56}$$

3.4 Results of Experimental Validation

3.4.1 "Trapped Robot" Scenario

An experiment was performed to check the validity of the ***η***-Filter. In particular, the ***η***-Filter is compared with the EKF and the Dead Reckoning (DR) techniques for state estimation when the UGV operating scenario is *trapped* and GPS sensor goodness is *poor*, *i.e.*, when *#Sat* is "low" and *HDOP* is "high." As the factors such as operating scenario and GPS sensor goodness depend on the environment and cannot be controlled during the experiment, a statistically designed experiment is not feasible. So, the validation experiment was performed by artificially creating the "*trapped*" robot scenario and varying GPS sensor goodness using the following procedure. The UGV was remote-controlled to follow an approximately circular path in an open parking lot. Figure 3.19 shows the location of the experiment, with the UGV at its start/stop position. In the midst of the run, one wheel was forcibly raised causing the UGV to become "*trapped*," *i.e.*, all the power from the motors was transmitted through the differentials to the raised wheel. This caused the UGV to stop. Simultaneously, the GPS antenna was covered. This led to a drop in *#Sat* and an increase in *HDOP*. After 5 to 10 seconds, the UGV was released. Thereafter, the "*normal*" scenario resumed. The UGV was then driven back to the start/stop position (a 1 m by 1 m box). The data logged

during the run was transmitted to the ground station (a laptop computer) through the wireless unit. Then, *MATLAB*^{TM} (version 7.0 R14) was used to implement the filter using the empirical data.

The actual start/stop position was measured from known landmarks such as the edges of the parking lot using a *standard* measuring tape. These distances were then added to the geographic coordinates of the landmarks that were extracted from a 0.3048 m resolution *United States Geological Survey* (USGS) geographic information systems database by using the *ArcMap*^{TM} software. The geographic coordinates of the start/stop position L2 (32.7257531°, −97.1122750°) in the global frame of reference refers to the (0, 0) point in the local frame of reference. Figure 3.20 shows plots of the position and the orientation estimates of the UGV. The DR method shows a steady drift from the estimates of both the $\boldsymbol{\eta}$-Filter and the EKF. The following *position errors* were found at the end of the approximately 60 meter run: 1.58 m for $\boldsymbol{\eta}$-Filter, 3.70 m for GPS, 4.67 m for EKF, and 7.41 m for DR. Thus, the $\boldsymbol{\eta}$-Filter performs better than the EKF or DR with respect to the final position estimates.

The validity of the $\boldsymbol{\eta}$-Filter may not be judged on the basis of the final position error alone. As shown in Figure 3.22, a high Velocity Difference (VD) and a near-zero acceleration cause a high *Bel*(*trap*) value (between the 20th and the 25th second). The "*switching*" takes place when the *Bel*(*trap*) value exceeds the preset threshold value of 0.5. Thereafter, the APP unit switches to an inertial model for the computation of linear and angular velocities.

At the same time, a low *#Sat* value and a high *HDOP* lead to a low *Bel*(*yes*) value (Figure 3.23). Consequently, the EEC increases the values of the *xx* (north) and *yy* (east) components of the measurement noise covariance matrix thereby causing the ***η***-Filter to adapt to GPS sensor goodness, *i.e.*, the GPS measurements are weighted less during the measurement update. In this experimental run, there is no noticeable increase in the residuals along the north and the east directions (Figures 3.21 (a) and (b)). Therefore, the ***η***-Filter performs only as good as the EKF with respect to GPS sensor goodness. However, the ***η***-Filter would perform better than the EKF with respect to GPS sensor goodness in the event of larger residuals due to low *#Sat* and high *HDOP*. Figure 3.13 shows the variation of GPS error versus *#Sat* and *HDOP*.

The path-plot (Figure 3.20 (a)) clearly indicates that the ***η***-Filter performs better than the EKF "*after*" a point where the UGV was *trapped*. As the true path is unknown, it is difficult to make an assessment of this improvement. However, a reasonable assessment can be made that there is an improvement in the case of the ***η***-Filter in the trapped robot scenario with respect to the true start/stop position.

Thus, the performance of the ***η***-Filter leads to an improvement in the accuracy. Figure 3.21 describes the consistency of the ***η***-Filter, *i.e.*, the residuals are within their $\pm 2\sigma$ bounds.

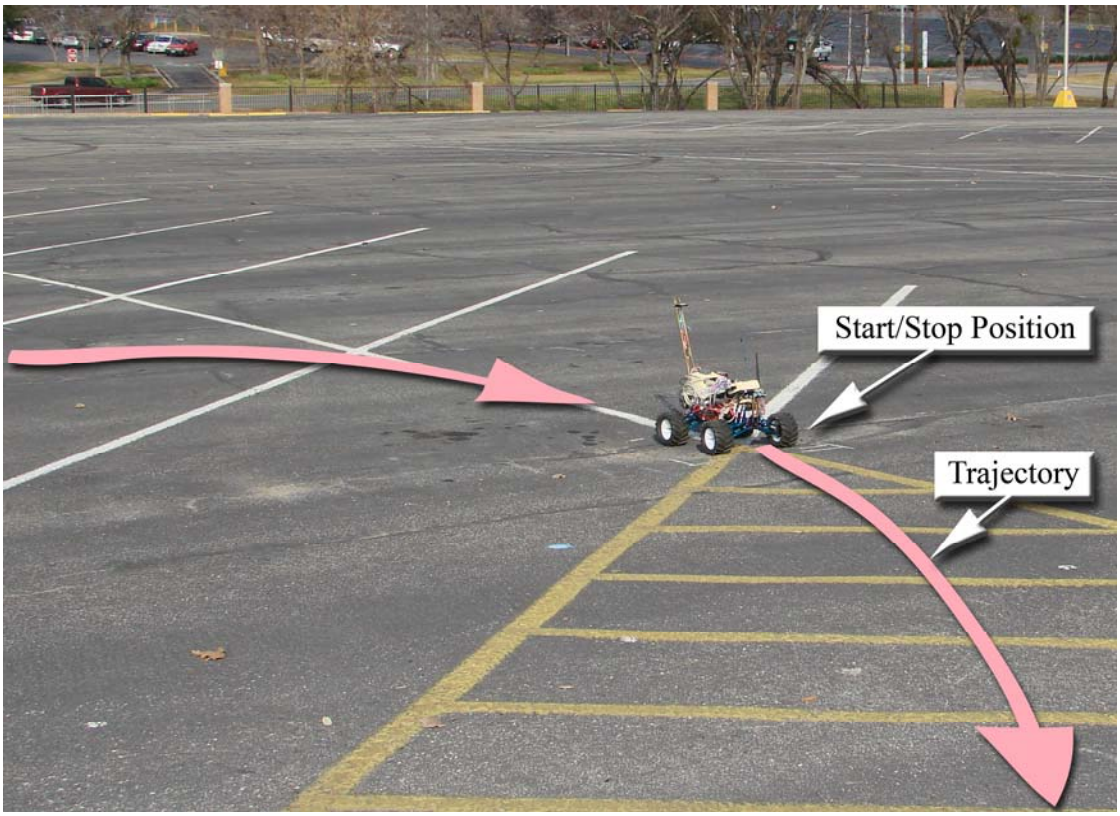

Figure 3.19 The Validation Experiment: The UGV at its start/stop position (marked by a 1 m by 1 m square box) prior to the validation trials. An approximately circular trajectory was used.

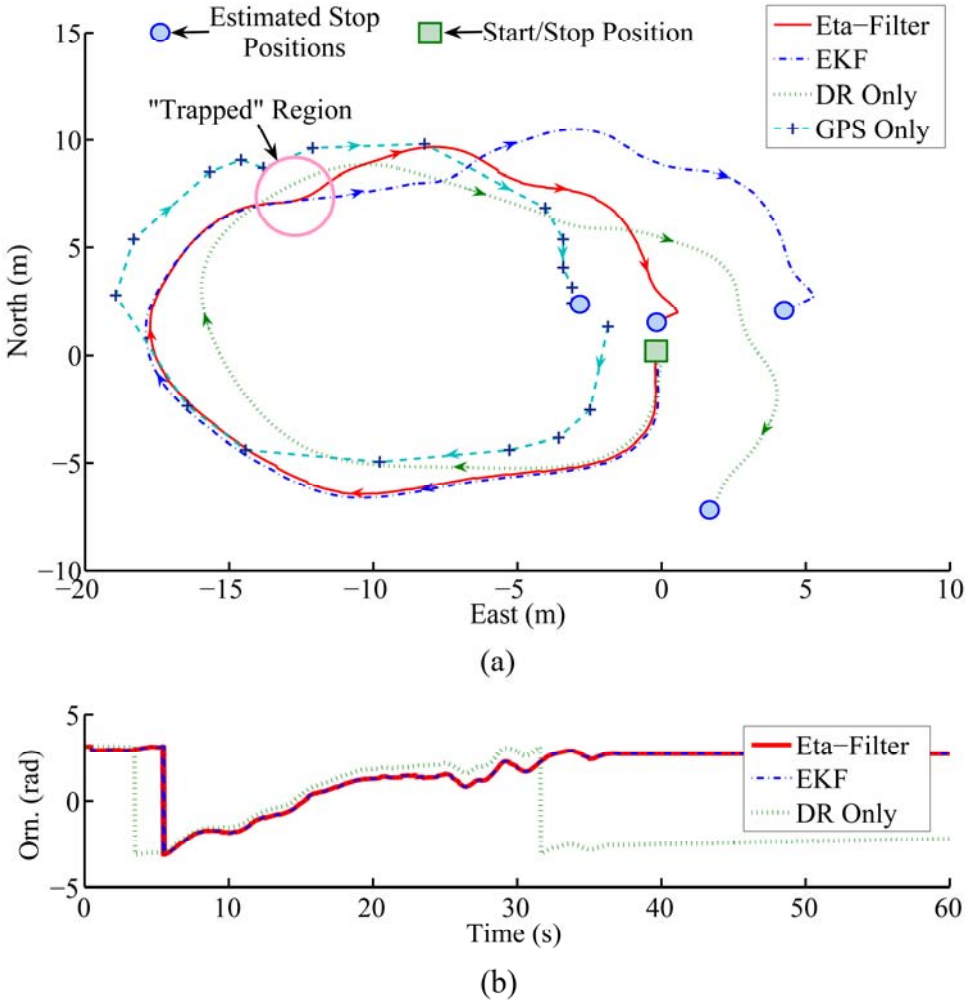

Figure 3.20 The Path Plot (a) and the Orientation Plot (b): The path plots indicate that the η-Filter has a better final estimate than the EKF and DR Only. There is a steady accumulation of error with DR Only.

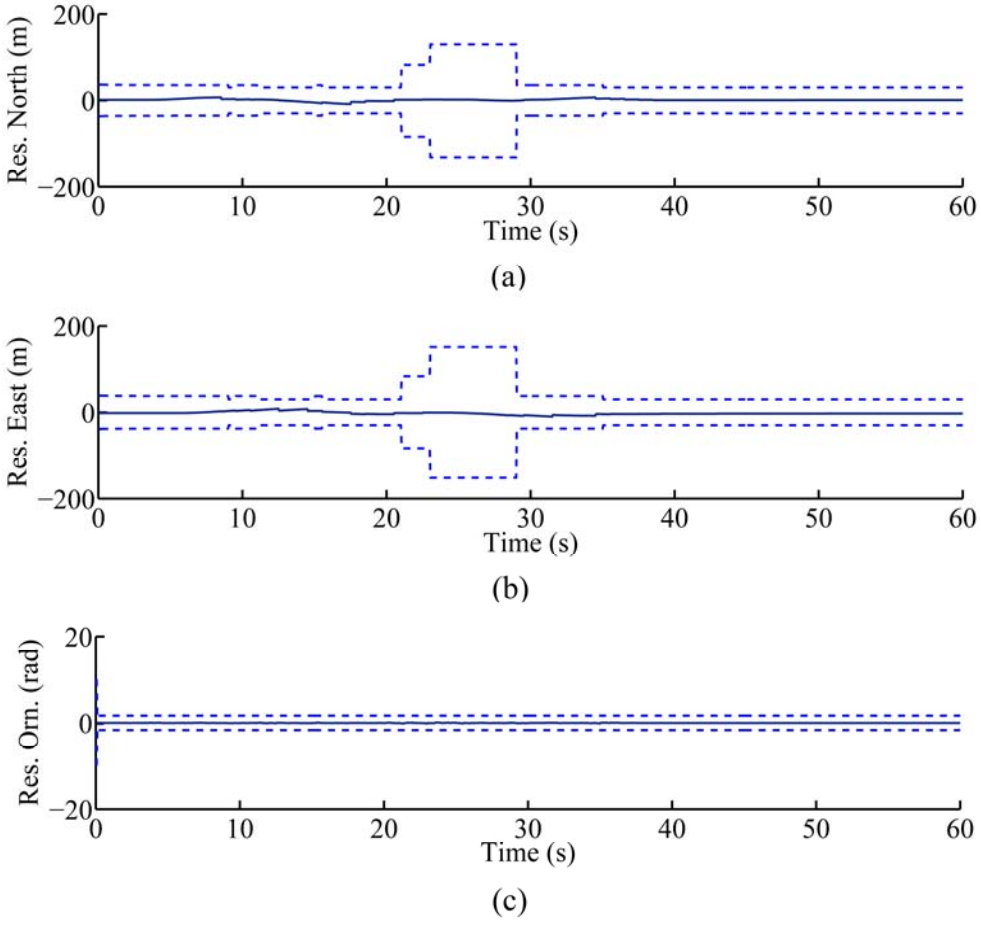

Figure 3.21 The Residual Plots of North (a), East (b), and Orientation (c): The residuals, marked as solid lines, are within their ±2σ bounds (95% confidence bounds), marked as dashed lines.

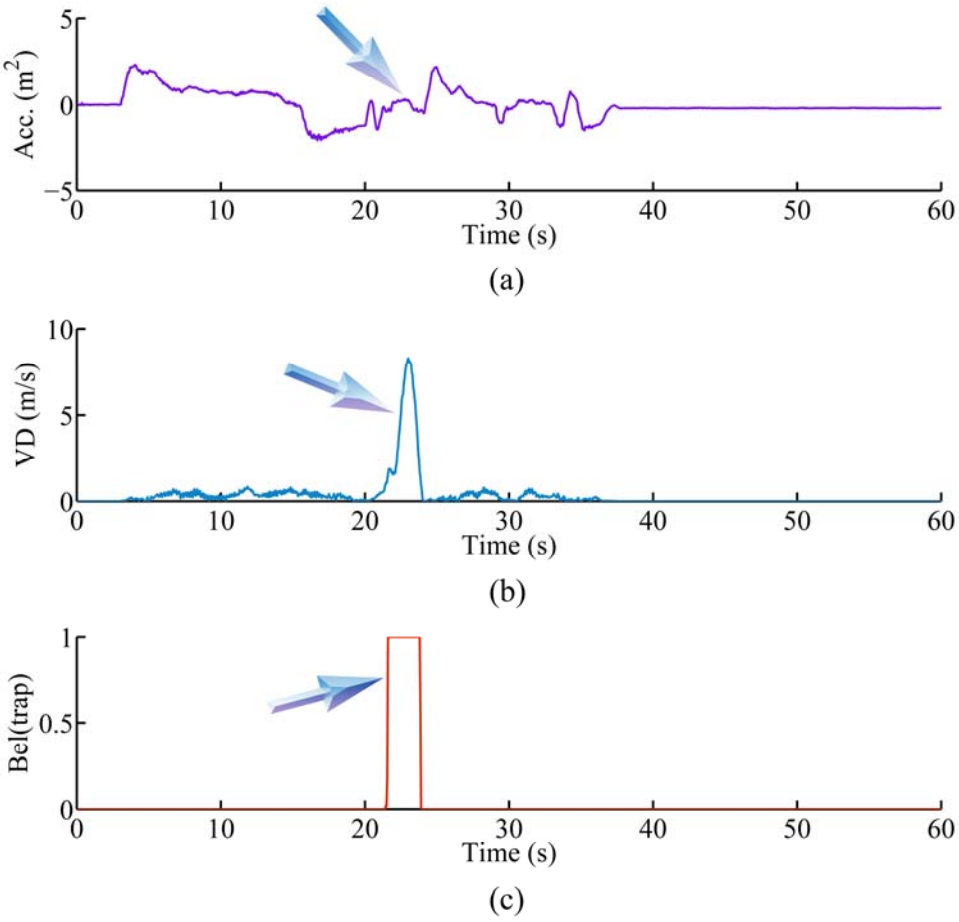

Figure 3.22 The Operating Scenario Belief Plots: The arrows point to the low magnitude of acceleration (a), high Velocity Difference (VD) (b), and the consequent high belief values (c) for the *trap* scenario. This indicates that the robot is "*trapped.*"

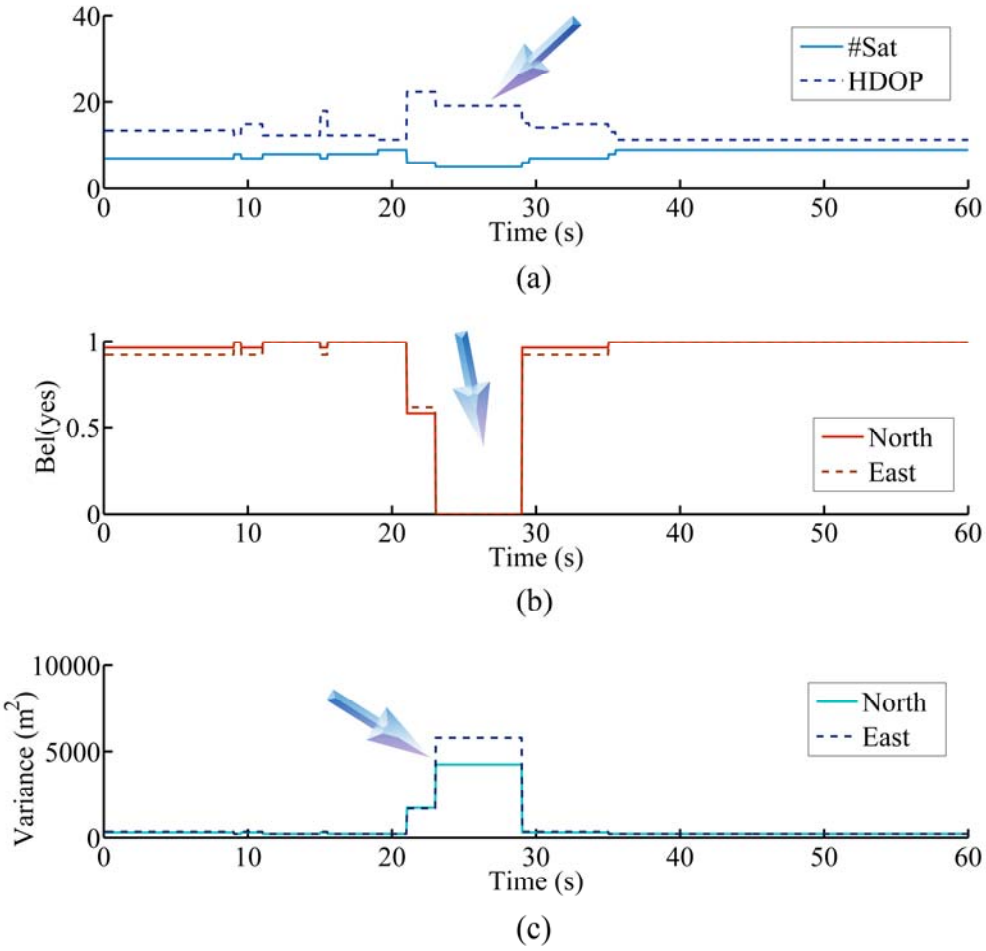

Figure 3.23 GPS Sensor Goodness Plots: The arrows point to the increase in HDOP and decrease in #Sat (a), a decrease in the belief value for *yes* (GPS is good) (b), and an increase in the *xx* and *yy* components of the measurement error covariance matrix **R** (c). Also, *Bel*(*yes*) = *m*(*yes*) for GPS sensor goodness.

3.4.2 "Normal" Scenario

After the validation experiment of the $\boldsymbol{\eta}$-Filter, a designed experiment was conducted to analyze the variation in final position error under the "*normal*" operating scenario, *i.e.*, when the UGV is not trapped. In such a scenario, assuming that the UGV is "not" trapped, the only source of improvement would be the variation in GPS sensor goodness. It must be mentioned that the $\boldsymbol{\eta}$-Filter was "*tuned*" to rely more on the wheel encoders and the digital compass than the GPS and the inertial sensors. Hence, the $\boldsymbol{\eta}$-Filter would show only a marginal improvement over the EKF under the normal operating scenario.

The experiment consisted of sixteen "*figure-8*" runs (8 repetitions each for two locations). Figure 3.24 shows the start/stop position L1 with geographical coordinates (32.7253688°, −97.1115144°). The second location is L2 (defined in Section 3.4.1). The first four and the last four runs were conducted at location L1, while the remaining eight runs were conducted at location L2. This ordering was planned ahead of the experiment in order to prevent the effect of time on measurements. The data logged during the run was transmitted to the ground station through the wireless unit. Figures A.1 through A.48 (in Appendix A) show the graphical descriptions of the results for the sixteen runs. Appendix B presents the results of the designed experiment.

Based on the results of the ANOVA F-test, it "*cannot*" be concluded, at the 5% significance level, that the mean final position errors are different for the $\boldsymbol{\eta}$-Filter and the EKF. So, the 11.17% improvement in the average position error is not statistically significant. However, violations of the *normality-of-errors* and the *absence-of-outliers*

assumptions of the ANOVA F-test render the aforementioned conclusion less powerful. Data transformation techniques [Pel98] to alleviate the violation of assumptions problem is not obvious due to the absence of a clear relationship between the variance and the treatment means (Figure B.4). Trial and error methods for the identification of appropriate transforms are time-consuming, and are hence not performed. Also, a high type II error of 0.9 implies a high probability of failing to reject the null hypothesis when in fact it is false, *i.e.*, there is a good chance that an improvement in the final position estimates is "*not*" detected when in fact there is an improvement. A remedial measure to decrease the high type II error is to increase the number of repetitions.

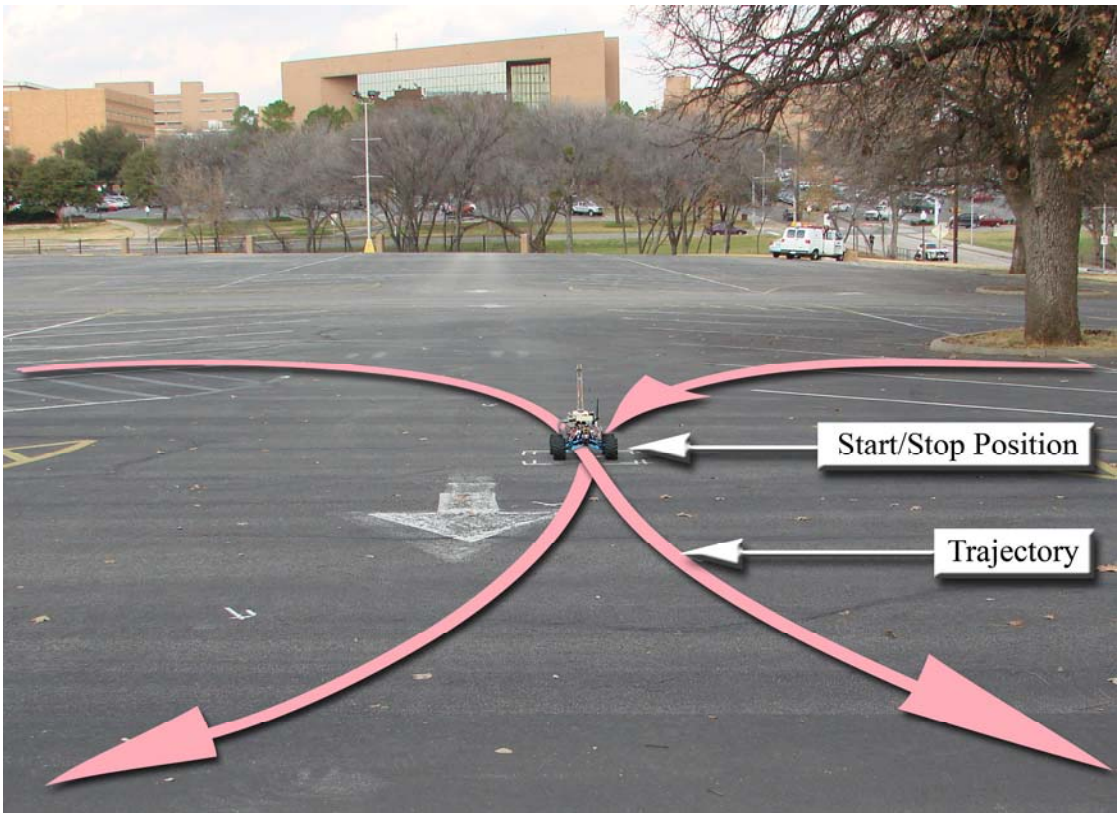

Figure 3.24 The Experiment for "*normal*" Scenario: The UGV at its start/stop position at location L1. A figure-8 trajectory was used.

CHAPTER 4

MULTI-UGV COOPERATIVE LOCALIZATION

4.1 Overview of the Cooperative Schema

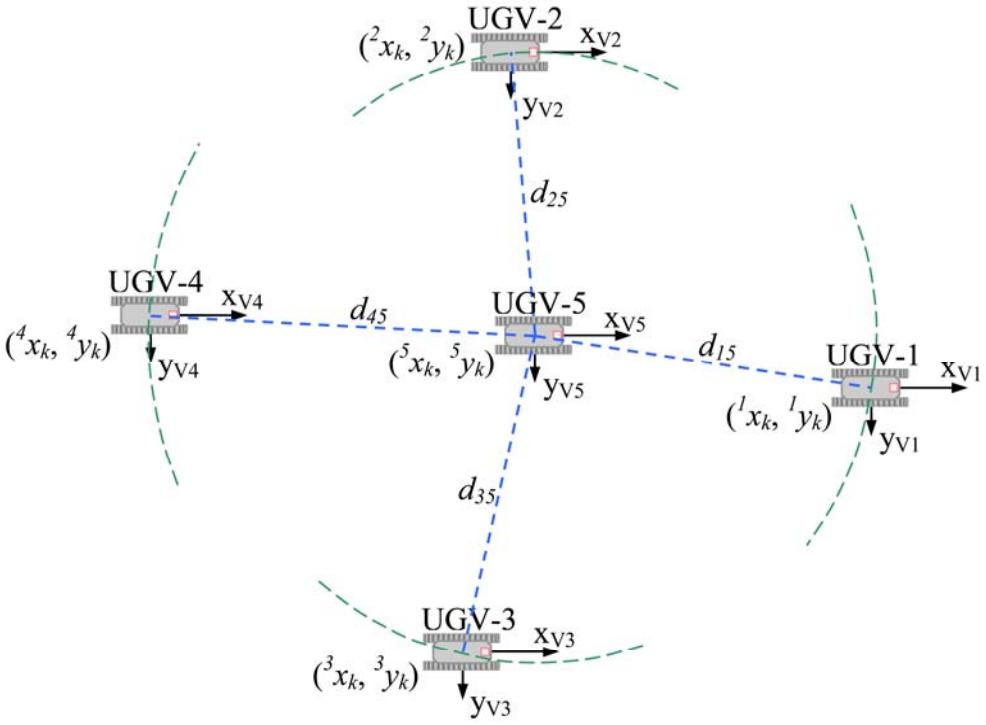

Figure 4.1 Five UGVs in a "Star" Arrangement: The center UGV (marked as UGV-5) acts as a mobile beacon and broadcasts its estimated pose and estimation error covariance matrix to the peripheral UGVs. The peripheral UGVs cooperatively fuse their own pose estimates with the pose estimates of the mobile beacon. The symbol d_{ij} represents the relative distance between the i^{th} and the j^{th} UGV.

A *range-only* CL architecture that resembles a "*star*" arrangement (Figure 4.1) is developed for a team of UGVs. One UGV that has a better accuracy and precision than the remainder of the team serves as a *mobile beacon* that broadcasts its position estimate and the estimation error covariance to the remainder of the team. The other members of the team estimate their own positions by fusing the information received from the mobile beacon, the relative distances between them, and their own position estimates, in a minimum variance sense.

4.2 Self-Localization of UGVs

Self-localization refers to the localization of the individual UGVs using only onboard sensors and without any cooperation with other UGVs. The individual UGVs employ the $\boldsymbol{\eta}$-Filter for self-localization. As five differential-steer UGVs were to be employed for validation trials, designed experiments were conducted with the objective of building models for linear and angular velocities and creating mass assignment tables for the GPS units of the five UGVs. Each differential-steer UGV is built on a low-cost *Commercially-Off-the-Shelf* (COTS) platform and is driven by a *Motorola DSP56F803* based onboard controller, the *PlugaPodS*^{TM}. An *XBee-PRO*^{TM} (v1.xAx - 802.15.4 wireless protocol) wireless module and a *SiRF Star III* chipset based *EM-406* GPS receiver are "*stacked*" on to the *PlugaPodS*^{TM} microcontroller. Two optical encoders are employed by each UGV for determining the linear and the angular velocities. A *Devantech CMPS03* digital compass was mounted on one of the UGVs that served as a mobile beacon.

4.2.1 Experiments for Parametric Modeling and Mass Assignment

A series of three experiments were conducted for building *parametric models* and *mass assignment tables* for each of the five UGVs. In the first experiment, ten straight-line runs were performed for each of the five UGVs in laboratory environment (vinyl flooring). Data from the right and the left optical encoders were logged at the end of each run. The distance of each run was measured using a *standard* measuring tape. The velocity was computed from the distance of each run and the preset duration of the run. The following linear models are created based on the empirical data.

Model A*u* (for linear velocity based on the encoders) is given by the following equation:

$$v_{x1,u} = \beta_0 + \beta_1 (ATPS_u) + \varepsilon_{vx1,u}, \tag{4.1}$$

where the subscript *u* represents the number of the UGV, *i.e.*, *u* = 1, 2, 3, 4, 5, *ATPS* is the Average Ticks Per Second (of the left and the right encoders), and $\varepsilon_{vx1,u}$ is the residual with $\varepsilon_{vx1,u} \sim N(0, \sigma_{vx1,u})$. Table 4.1 shows the parameter estimates, $\hat{\beta}_n$. Further,

$$ATPS_u = \left[\frac{ticks_{r,u} + ticks_{l,u}}{2.(\Delta t)} \right]. \tag{4.2}$$

The same compass used for the single-UGV localization was used for multi-UGV localization. Therefore, the model presented in Section 3.2.3 (represented by Equation (3.21)) is used.

Table 4.1 Linear and Angular Velocity Model Parameter Estimates

Model	$\hat{\beta}_0$	$\hat{\beta}_1$	MSE	R^2
A1	0.000000	0.001150	3.67E-06	0.99996
A2	0.000000	0.001068	1.13E-06	0.99998
A3	0.000000	0.001053	5.85E-07	0.99999
A4	0.000000	0.001071	1.14E-06	0.99997
A5	0.000000	0.001049	4.39E-07	0.99999
B1	0.012242	0.002778	0.000693	0.99960
B2	-0.000490	0.002455	0.000523	0.99958
B3	0.017243	0.002582	0.000407	0.99952
B4	-0.008660	0.002550	0.000774	0.99941
B5	-0.013540	0.002573	0.000120	0.99987

In another experiment, fifty runs, consisting of five repetitions each for two steering angle settings, were performed for each of the five UGVs. The angle turned by the UGV was measured using a *standard* protractor. The angular velocity of the UGV was computed by dividing the total angle turned by the preset duration of the run. The following models are created for angular velocities based on the empirical data.

Model B*u* (for angular velocity based on the encoders) is given by the following equation:

$$\omega_{z1,u} = \beta_0 + \beta_1(DTPS_u) + \varepsilon_{\omega z1,u}, \tag{4.3}$$

where $\omega_{z1,u}$ is the angular velocity measured by the right-left encoder difference, u = 1, 2, 3, 4, 5, *DTPS* is the Difference in Ticks Per Second (between the left and the right encoders), and $\varepsilon_{\omega z1,u}$ is the residual with $\varepsilon_{\omega z1,u} \sim N(0, \sigma_{\omega z1,u})$. Table 4.1 shows a listing of parameter estimates, $\hat{\beta}_n$. Further,

$$DTPS_u = \left[\frac{ticks_{l,u} - ticks_{r,u}}{\Delta t} \right]. \tag{4.4}$$

The third experiment comprised of logging GPS data for creating mass assignment tables for the five UGVs. A total of two thousand readings were logged in two locations and in two staggered time windows. The geographic coordinates for the two locations are as follows: (32.7301862°, −97.1106639°) and (32.7263060°, −97.1129139°). Base on an ANOVA F-test, conducted at the 5% significance level using *SAS*^{TM} (version 9.1), it was found that the GPS error varied significantly between the receivers of the five UGVs. A *Tukey's* pairwise comparison test was performed, at a

significance level of 0.05, to identify the GPS receiver means that were significantly different from others. As can be inferred from Table 4.2, "*zero*" does not belong to the 95% confidence intervals of all pairs except pairs (1, 4) and (2, 5). So it *cannot* be statistically concluded that the means of pairs (1, 4) and (2, 5) are different (Figure 4.2). Based on this conclusion, receivers with similar error means are grouped together with common mass functions, *i.e.*, the data logged by receivers with similar means are "*pooled*" together while creating the mass assignment table. Figures 4.3 through 4.5 show scatter-plots of the errors for the three levels of the *#Sat* and the *HDOP* criteria.

Figure 4.2 Ordered Means for Tukey's Pairwise Comparison Test: The solid line connects the receivers whose means are not statistically different.

Table 4.2 Least Squares Means (LSMs) for Receiver Effect.

Receiver A	Receiver B	Difference Between Means	Simultaneous 95% Confidence Limits for LSM(A) – LSM(B)
1	2	-8.460518	(-10.891688, -6.029349)
1	3	-3.574777	(-6.005946, -1.143607)
1	4	0.484023	(-1.947146, 2.915193)
1	5	-6.118244	(-8.549413, -3.687075)
2	3	4.885741	(2.454572, 7.316911)
2	4	8.944542	(6.513372, 11.375711)
2	5	2.342274	(-0.088895, 4.773443)
3	4	4.058800	(1.627631, 6.489970)
3	5	-2.543467	(-4.974637, -0.112298)
4	5	-6.602268	(-4.974637, -0.112298)

Table 4.3 Mass Assignment Table for the Five *EM-406* GPS Receivers

Criteria	Value	Axis (a)	Receivers 1, 4			Receivers 2, 5			Receiver 3		
			${}^{a}m_s(yes)$	${}^{a}m_s(no)$	${}^{a}m_s(yes,no)$	${}^{a}m_s(yes)$	${}^{a}m_s(no)$	${}^{a}m_s(yes,no)$	${}^{a}m_s(yes)$	${}^{a}m_s(no)$	${}^{a}m_s(yes,no)$
#Sat (s=1)	*>= 9*	*N*	1.00	0.00	0.00	1.00	0.00	0.00	1.00	0.00	0.00
		E	1.00	0.00	0.00	1.00	0.00	0.00	1.00	0.00	0.00
	< 9 & >= 6	*N*	0.45	0.36	0.19	0.56	0.25	0.19	0.27	0.62	0.11
		E	0.78	0.02	0.20	0.54	0.03	0.43	0.80	0.00	0.20
	< 6 & >= 3	*N*	0.43	0.11	0.46	0.13	0.53	0.34	0.25	0.13	0.62
		E	0.78	0.00	0.22	0.22	0.54	0.24	0.25	0.13	0.62
HDOP (s=2)	*< 10*	*N*	1.00	0.00	0.00	0.99	0.00	0.01	1.00	0.00	0.00
		E	1.00	0.00	0.00	0.95	0.00	0.05	1.00	0.00	0.00
	>= 10 & < 18	*N*	0.47	0.34	0.19	0.44	0.25	0.31	0.20	0.71	0.09
		E	0.80	0.02	0.18	0.58	0.02	0.40	0.91	0.01	0.08
	>= 18	*N*	0.40	0.20	0.40	0.11	0.59	0.31	0.65	0.00	0.35
		E	0.72	0.00	0.28	0.15	0.60	0.25	0.00	1.00	0.00

Table 4.4 Error Variances for the Five *EM-406* GPS Receivers

U	Receivers 1, 4		Receivers 2, 5		Receiver 3	
	$\sigma_{x,U}$ (m^2)	$\sigma_{y,U}$ (m^2)	$\sigma_{x,U}$ (m^2)	$\sigma_{y,U}$ (m^2)	$\sigma_{x,U}$ (m^2)	$\sigma_{y,U}$ (m^2)
{yes}	3.78	4.03	2.37	6.72	2.03	4.82
{no}	529.79	4377.36	947.58	695.66	449.09	398.62
{yes, no}	65.45	51.76	125.56	87.21	92.83	104.34

A mass assignment table (Table 4.3) is built using the same method adopted in Section 3.2.4. However, the rule to compute the mass functions *m(U)* for each criteria instance based on the fraction of occurrence is modified in order to account for the better precision of the five *EM-406* GPS receivers when compared to the *TU10-D007-091* GPS receiver. The rule is given as

IF |*error*| < *5 m* THEN *U* = *{yes}*

ELSE IF |*error*| >= *15 m* THEN *U* = *{no}*

ELSE *U* = *{yes,no}*.

The aforementioned rule is also applied to compute the error variances along the north and the east axes (Table 4.4).

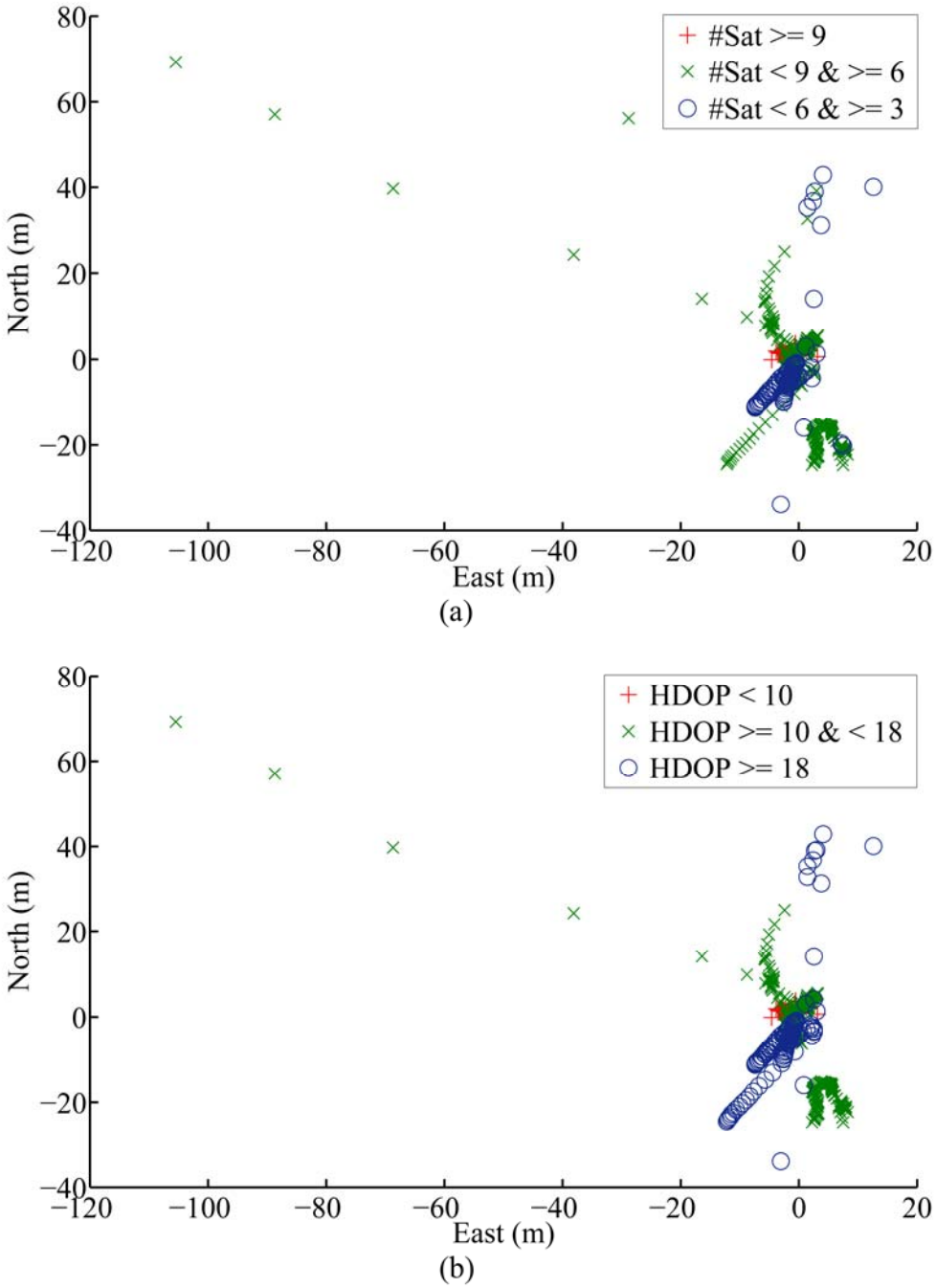

Figure 4.3 Error Plots of the GPS Receivers 1 and 4 as a Function of *#Sat* (a) and *HDOP* (b): The errors appear to be auto-correlated due to the possible presence of filters within the receivers.

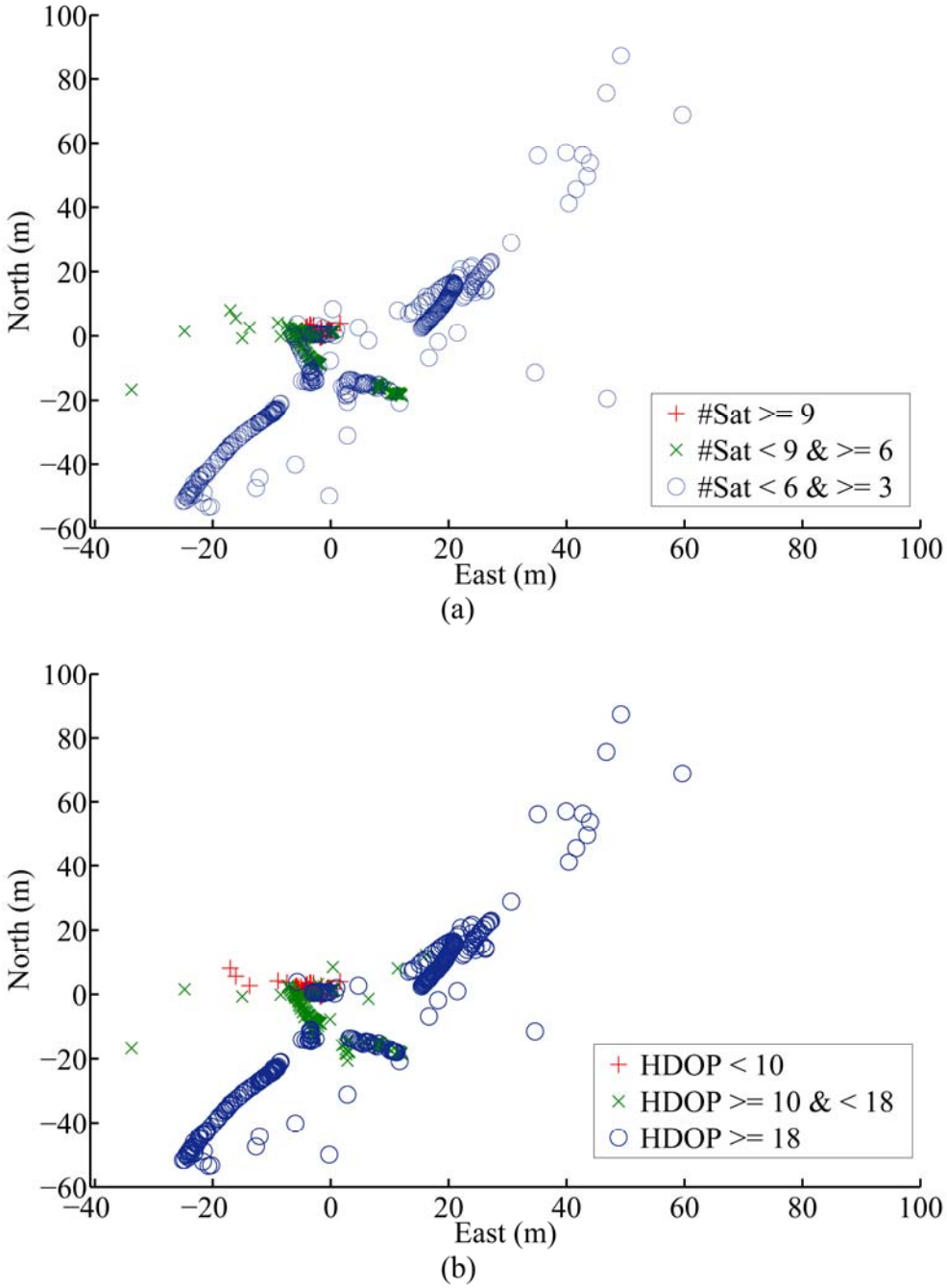

Figure 4.4 Error Plots of the GPS Receivers 2 and 5 as a Function of *#Sat* (a) and *HDOP* (b): The errors appear to be auto-correlated due to the possible presence of filters within the receivers.

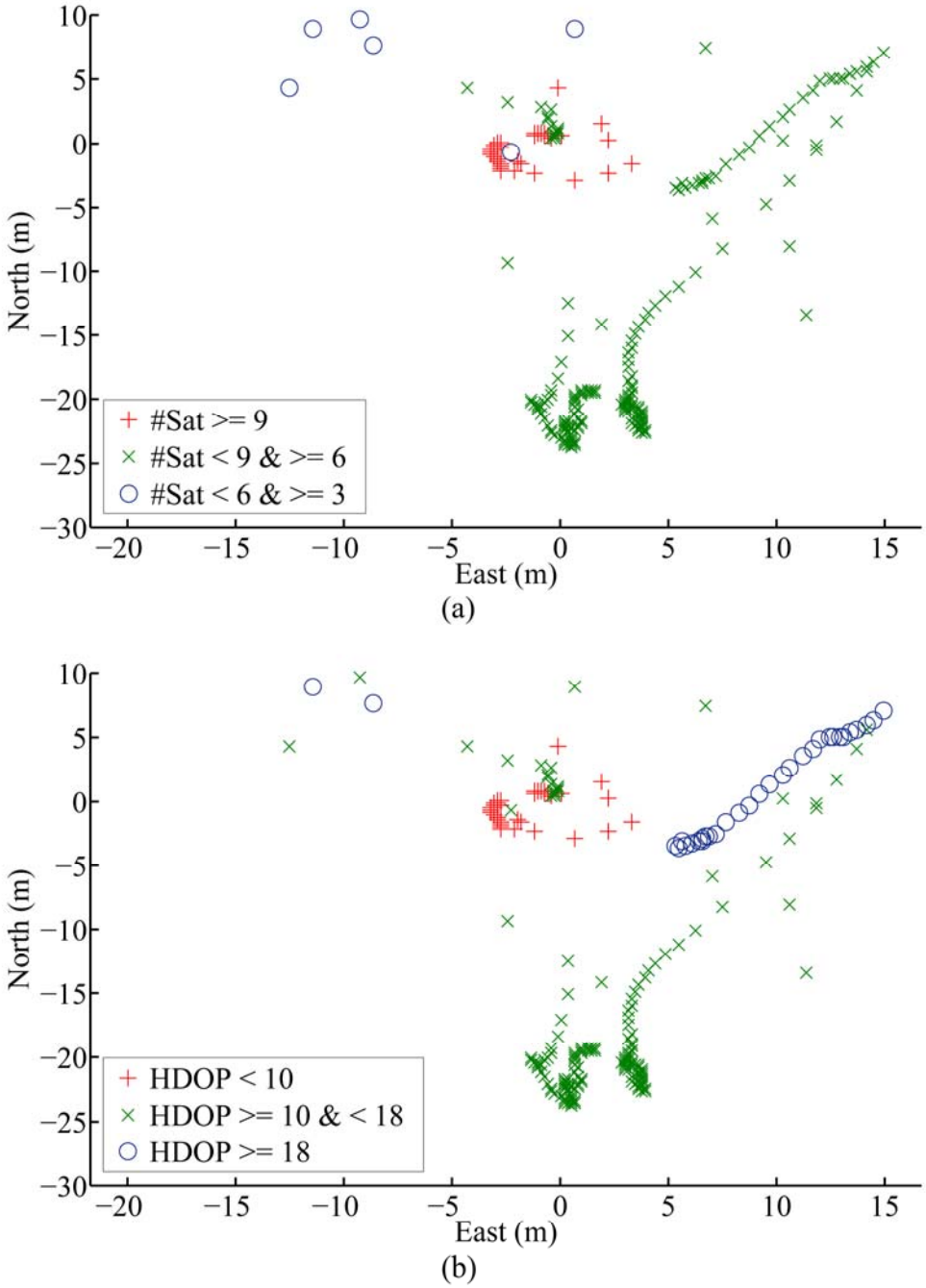

Figure 4.5 Error Plots of the GPS Receiver 3 as a Function of *#Sat* (a) and *HDOP* (b): The errors appear to be auto-correlated due to the possible presence of filters within the receivers.

4.3 Range-Only Cooperative Fusion

The state estimates determined by the self-localization system are fused with those that are determined by the information from the mobile beacon and corresponding relative distances using Equation (4.11). The combined estimate thus obtained is then fed back into the $\boldsymbol{\eta}$-Filter for a measurement update. Figure 4.6 shows the CL schema.

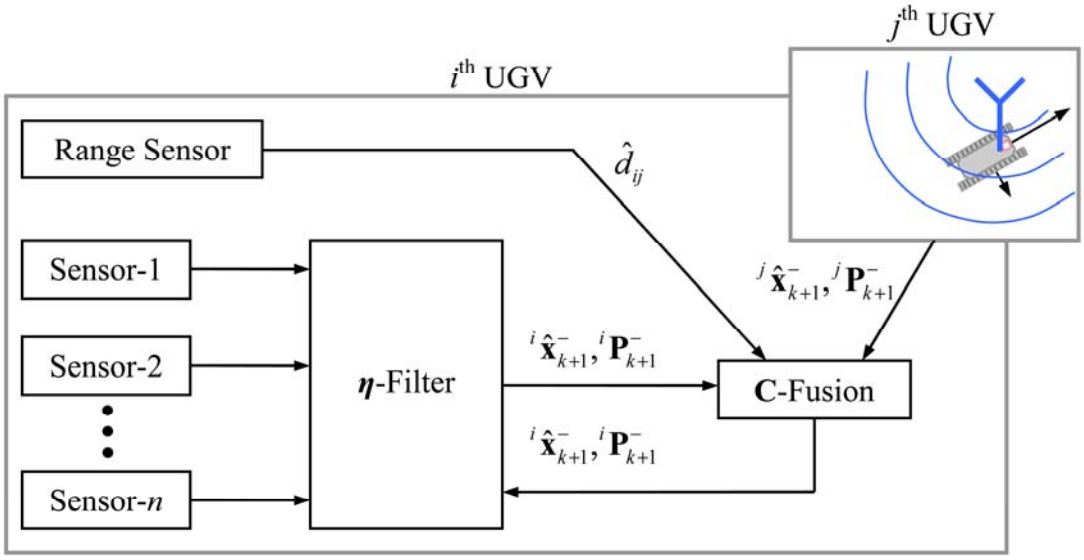

Figure 4.6 The Cooperative Localization Schema: The state estimate of the i^{th} UGV is fused with that of the j^{th} UGV which serves as a mobile beacon.

Cooperation occurs intermittently after each leg of the entire duration of the run. The process for mobile beacon positioning using relative distance is as follows:

$$ {}^{i}_{j}\hat{x}_{k+1} = {}^{j}\hat{x}_{k} + \hat{d}_{ij}.\cos(\hat{\psi}_{ij}) + \varepsilon_{{}^{i}_{j}x_{k+1}} \tag{4.5} $$

and

$$ {}^{i}_{j}\hat{y}_{k+1} = {}^{j}\hat{y}_{k} + \hat{d}_{ij}.\sin(\hat{\psi}_{ij}) + \varepsilon_{{}^{i}_{j}y_{k+1}}. \tag{4.6} $$

where ${}^{i}_{j}\hat{\mathbf{x}}^{-}_{k+1} = [{}^{i}_{j}\hat{x}_{k+1}, {}^{i}_{j}\hat{y}_{k+1}]^{T}$ is the state estimate of the i^{th} UGV based on the estimate of the j^{th} UGV, d_{ij} is the range of the j^{th} UGV (the mobile beacon) from the i^{th} UGV, and $\hat{\psi}_{ij}$ is the estimated relative angle between the i^{th} UGV and the j^{th} UGV. Further,

$$\hat{\mathbf{q}} = \begin{bmatrix} \hat{d}_{ij} \\ \hat{\psi}_{ij} \end{bmatrix} \tag{4.7}$$

and

$$\hat{\boldsymbol{\xi}} = \begin{bmatrix} \hat{d}_{ij}.\cos(\hat{\psi}_{ij}) \\ \hat{d}_{ij}.\sin(\hat{\psi}_{ij}) \end{bmatrix}. \tag{4.8}$$

The position of the i^{th} UGV based on the information from the j^{th} UGV and d_{ij} is given as

$${}^{i}_{j}\hat{\mathbf{x}}^{-}_{k+1} = {}^{j}\hat{\mathbf{x}}^{-}_{k+1} + \begin{bmatrix} \hat{d}_{ij}.\cos(\hat{\psi}_{ij}) \\ \hat{d}_{ij}.\sin(\hat{\psi}_{ij}) \end{bmatrix}. \tag{4.9}$$

Further,

$$\hat{\psi}_{ij} = \tan^{-1}\left[\frac{{}^{i}\hat{y}^{-}_{k+1} - {}^{j}\hat{y}^{-}_{k+1}}{{}^{i}\hat{x}^{-}_{k+1} - {}^{j}\hat{x}^{-}_{k+1}} \right]. \tag{4.10}$$

Using the generic fusion formula (Equation (2.1)), the fused cooperative localization estimate is given as follows:

$${}^{i}\hat{\mathbf{x}}^{-}_{k+1} = (({}^{i}\mathbf{P}^{-}_{k+1})^{-1} + ({}^{i}_{j}\mathbf{P}^{-}_{k+1})^{-1})^{-1}.(({}^{i}\mathbf{P}^{-}_{k+1})^{-1}.{}^{i}\hat{\mathbf{x}}^{-}_{k+1} + ({}^{i}_{j}\mathbf{P}^{-}_{k+1})^{-1}.{}^{i}_{j}\hat{\mathbf{x}}^{-}_{k+1}), \tag{4.11}$$

where the prefixed superscripts represent "*of the UGV*" and the prefixed subscripts represent "*by the UGV*." Further, under the assumption of independence of errors between the mobile beacon position and the relative position,

$$ {}_{j}^{i}\mathbf{P}_{k+1}^{-} = {}^{j}\mathbf{P}_{k+1}^{-} + \mathbf{\Xi}_{k+1}({}_{j}^{i}\hat{\mathbf{x}}_{k+1}^{-}) E\{\mathbf{c}_{k+1}\mathbf{c}_{k+1}{}^{T}\} \mathbf{\Xi}_{k+1}({}_{j}^{i}\hat{\mathbf{x}}_{k+1}^{-})^{T}, \tag{4.12} $$

where

$$ \mathbf{c}_{k+1} = \begin{bmatrix} \varepsilon_{{}_{j}^{i}x_{k+1}} \\ \varepsilon_{{}_{j}^{i}y_{k+1}} \end{bmatrix} \tag{4.13} $$

and the Jacobian $\mathbf{\Xi}_{k+1}({}_{j}^{i}\hat{\mathbf{x}}_{k+1}^{-})$ is the partial derivative of ξ with respect to $\mathbf{q}$ at the point ${}_{j}^{i}\hat{\mathbf{x}}_{k+1}^{-}$. Thus,

$$ \mathbf{\Xi}_{k+1}({}_{j}^{i}\hat{\mathbf{x}}_{k+1}^{-}) = \frac{d\xi({}_{j}^{i}\hat{\mathbf{x}}_{k+1}^{-})}{d\mathbf{q}} = \begin{bmatrix} \cos(\hat{\psi}_{ij}) & -\hat{d}_{ij}.\sin(\hat{\psi}_{ij}) \\ \sin(\hat{\psi}_{ij} & \hat{d}_{ij}.\cos(\hat{\psi}_{ij}) \end{bmatrix}. \tag{4.14} $$

From Equation (4.12),

$$ {}_{j}^{i}\mathbf{P}_{k+1}^{-} = {}^{j}\mathbf{P}_{k+1}^{-} + \mathbf{\Xi}\mathbf{C}\mathbf{\Xi}^{T}, \tag{4.15} $$

where $\mathbf{C}$ is the covariance matrix associated with relative position information between the i^{th} and the j^{th} UGV, *i.e.*, $\mathbf{C}_k = diag(\sigma_{d_{ij}}^2, \sigma_{\psi_{ij}}^2)$.

From Equation (4.15),

$$ {}_{j}^{i}\mathbf{P}_{k+1}^{-} = {}^{j}\mathbf{P}_{k+1}^{-} + \begin{bmatrix} \sigma_{d_{ij}}^2.\cos^2(\hat{\psi}_{ij}) + \sigma_{\psi_{ij}}^2.\hat{d}_{ij}^2.\sin^2(\hat{\psi}_{ij}) & \cos(\hat{\psi}_{ij}).\sin(\hat{\psi}_{ij})(\sigma_{d_{ij}}^2 - \hat{d}_{ij}^2.\sigma_{\psi_{ij}}^2) \\ \cos(\hat{\psi}_{ij}).\sin(\hat{\psi}_{ij})(\sigma_{d_{ij}}^2 - \hat{d}_{ij}^2.\sigma_{\psi_{ij}}^2) & \sigma_{d_{ij}}^2.\sin^2(\hat{\psi}_{ij}) + \sigma_{\psi_{ij}}^2.\hat{d}_{ij}^2.\cos^2(\hat{\psi}_{ij}) \end{bmatrix}. \tag{4.16} $$

The estimation error covariance of the fused cooperative localization estimate is given as follows:

$$ {}^{i}\mathbf{P}_{k+1}^{-} = (({}^{i}\mathbf{P}_{k+1}^{-})^{-1} + ({}_{j}^{i}\mathbf{P}_{k+1}^{-})^{-1})^{-1}. \tag{4.17} $$

4.4 Experimental Results

A designed experiment [Che05] was conducted to validate the *range-only* CL algorithm. Of the five differential-steering UGVs used, one UGV that had a better sensing capability than the remainder of the team served as a mobile beacon, *i.e.*, it was equipped with a digital compass in addition to the wheel encoders and the GPS. All UGVs were equipped with wheel encoders. The experiment was conducted on cement surface on campus. The following trajectory sequence was used (Figure 4.7): (1) Leg-1: go ahead 5 m, turn left 90°; (2) Leg-2: go ahead 2 m, turn right 90°; and (3) Leg-3: go ahead 3 m. Data was logged at 10 Hz from all the five UGVs through an *XBee-PRO*^{TM} wireless module. The data included left encoder ticks, right encoder ticks, latitude, longitude, UTC time, #Sat, HDOP, and orientation from the digital compass of the mobile beacon (UGV-5).

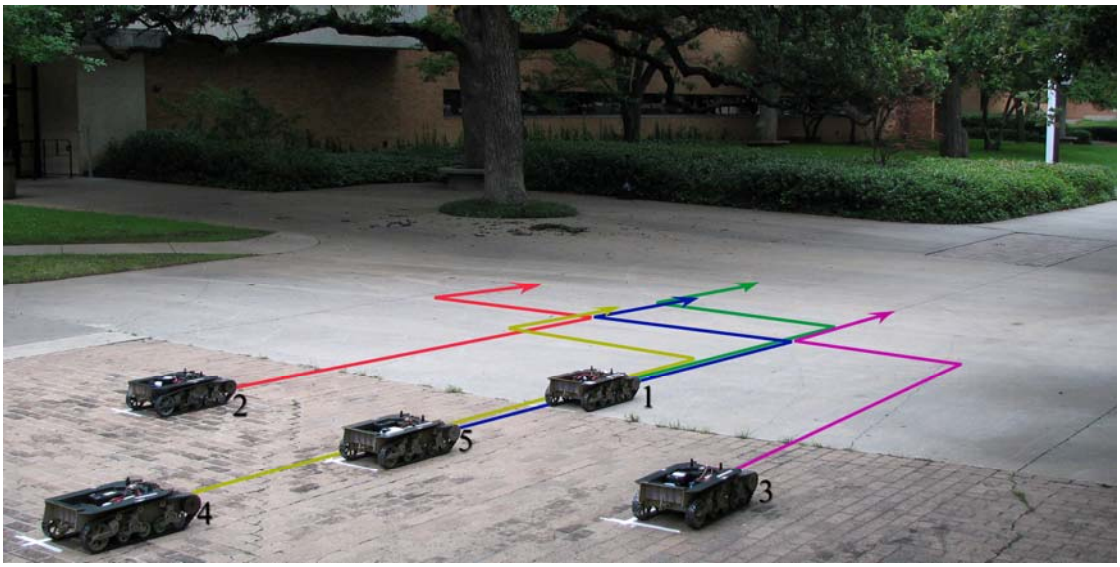

Figure 4.7 The Five UGVs at their Start Positions: The trajectories include one left turn and one right turn. The solid lines represent the approximate trajectories.

The start position of UGV-1 is the origin (0, 0) of the local frame of reference (Figure 4.8). The geographic coordinates of the origin of the local frame (32.7313167°, –97.1121583°) are extracted from a 0.3048 m resolution USGS geographic information systems database using the *ArcMap*^{TM} software. The starting formation of the five UGVs resembles a *star* arrangement with UGV-5 in the center position of the formation (Figure 4.7). The distances between the center UGV and the peripheral UGVs were measured at the end of each leg of the run by using a *standard* measuring tape. Consequently, three sets of range measurements were recorded for each run. Hence, cooperation between the UGVs takes place intermittently at the end of each leg.

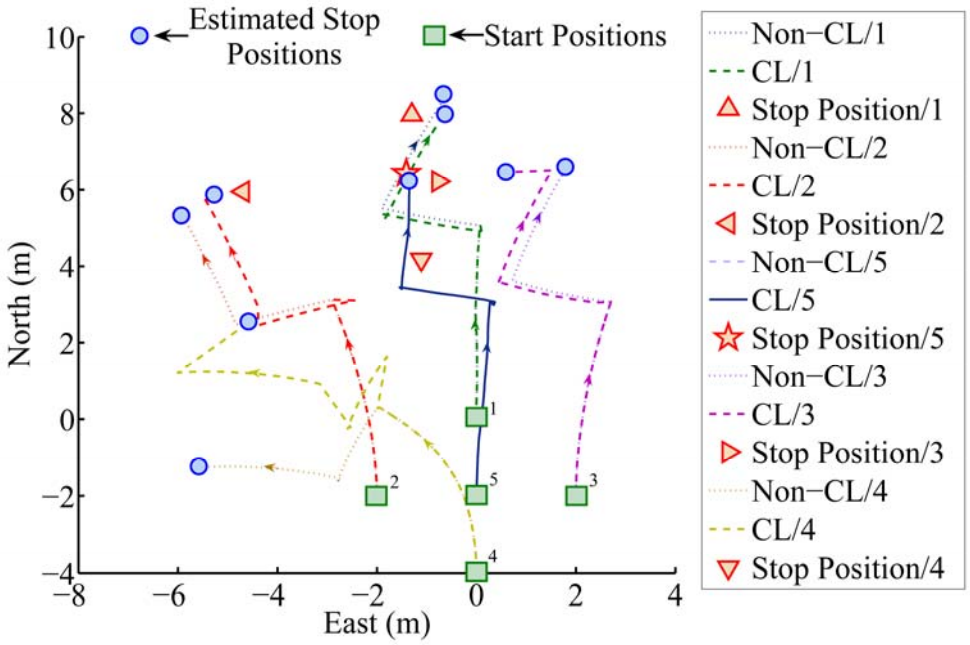

Figure 4.8 The Estimated Path Plots of the Five UGVs for Repetition One: The numbers following the slash symbol represent the UGV numbers. The final position estimates of a CL system are closer to the actual final positions than that of a non-CL system for the four peripheral UGVs.

Then, *MATLAB*^{TM} (version 7.0 R14) was used to implement the range-only CL system using the empirical data, offline. Figures 4.8 through 4.12 show a comparison of the state estimates based on the range-only CL system with that based on a non-CL system for all the five repetitions. Figure 4.8 shows that the estimates of the CL system are better than those of the non-CL system for all four UGVs. Also, UGV-4 shows a systematic error in position for all the five repetitions. This is consistent with the "*improper*" calibration of UGV-4. During a *pilot* experiment, a faulty gear-box/encoder assembly of UGV-4 was replaced. After the replacement of the gear-box/encoder assembly of UGV-4, a re-calibration was *not* performed. Thus, improper calibration impacts the localization accuracy for both CL as well as non-CL systems.

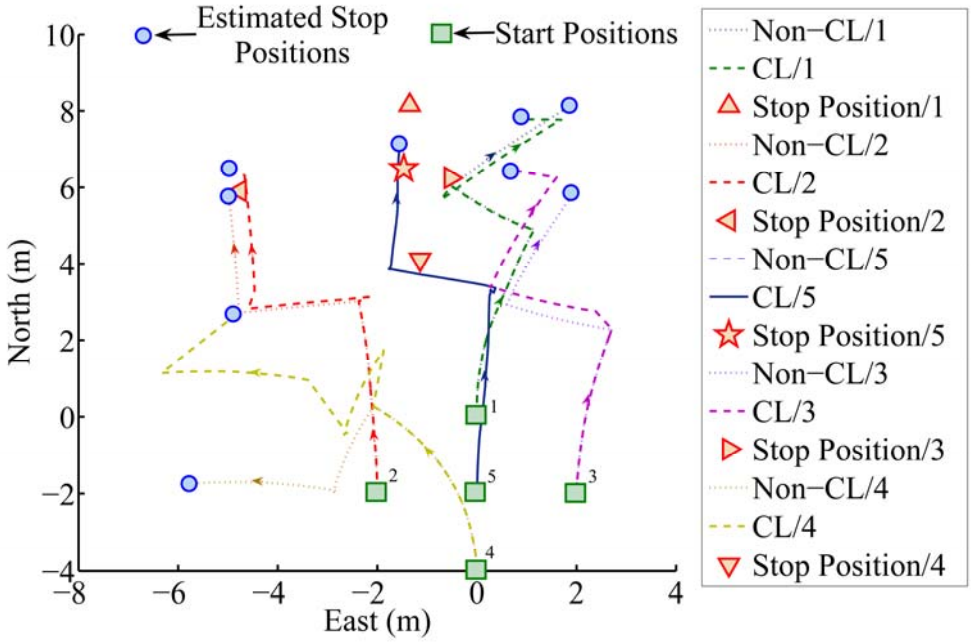

Figure 4.9 The Estimated Path Plots of the Five UGVs for Repetition Two: The numbers following the slash symbol represent the UGV numbers. The final position estimates of a CL system are closer to the actual final positions than that of a non-CL system for the peripheral UGVs 1, 3, and 4.

There are two factors of interest. Factor A is "*CL*" with levels 1 = CL system (there is cooperative localization) and 2 = non-CL system (there is no cooperative localization). Factor B is "*UGV*" with levels 1 = UGV-1, 2 = UGV-2, 3 = UGV-3, and 4 = UGV-4. UGV-5 is not considered for statistical testing. It only serves as a mobile beacon. Five repetitions were performed for each of the eight treatment combinations.

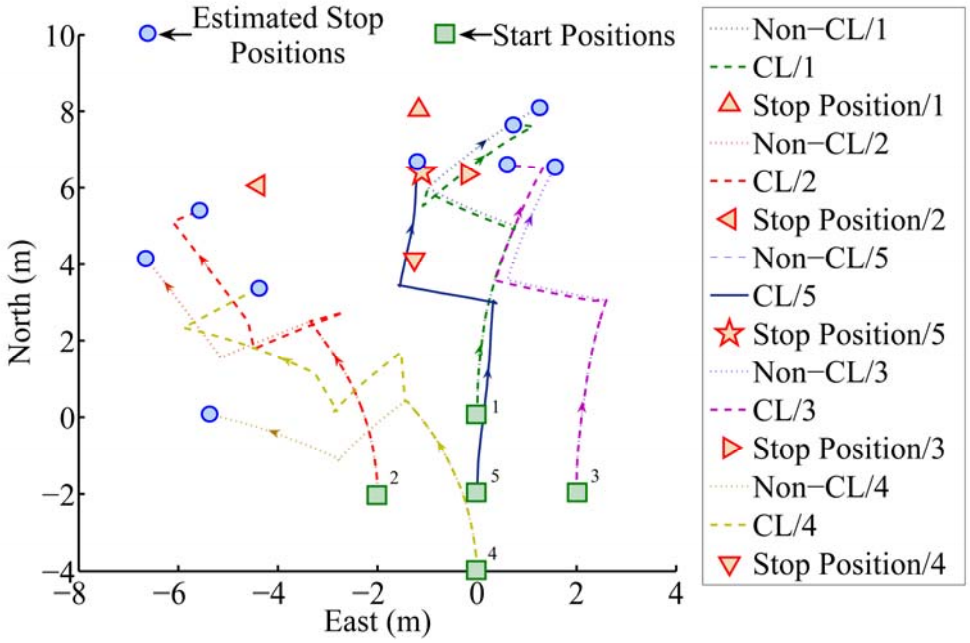

Figure 4.10 The Estimated Path Plots of the Five UGVs for Repetition Three: The numbers following the slash symbol represent the UGV numbers. The final position estimates of a CL system are closer to the actual final positions than that of a non-CL system for the four peripheral UGVs.

Based on the results of the ANOVA F-test, it can be concluded, at the 1% significance level, that the mean final position error of a CL system is significantly less than that of a non-CL system and that the mean final position errors of the five UGVs are not the same. No significant violations of the ANOVA assumptions were found. Appendix C presents a detailed description of the designed experiment. The mean final

position errors are computed as follows: 1.7317 m (for a CL system) and 2.8941 m (for a non-CL system). Thus, the range-only CL system shows a 40% improvement in the mean final position error over a non-CL system.

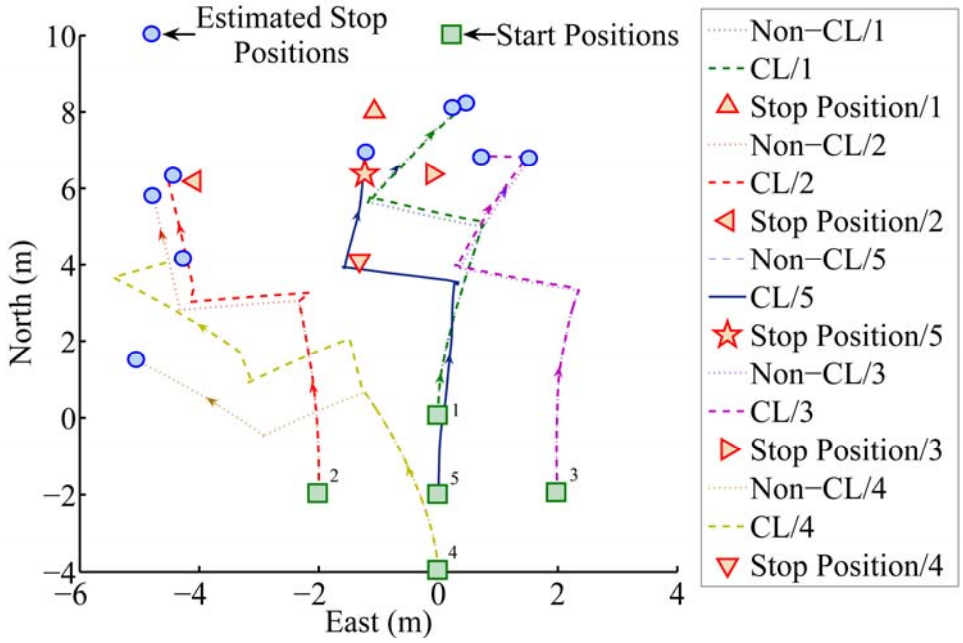

Figure 4.11 The Estimated Path Plots of the Five UGVs for Repetition Four: The numbers following the slash symbol represent the UGV numbers. The final position estimates of a CL system are closer to the actual final positions than that of a non-CL system for the four peripheral UGVs.

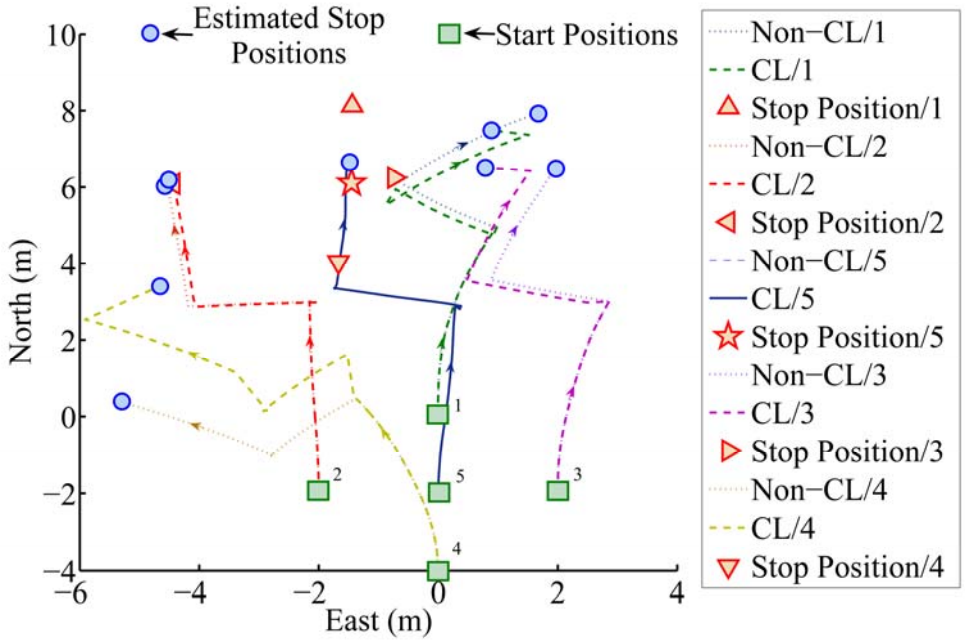

Figure 4.12 The Estimated Path Plots of the Five UGVs for Repetition Five: The numbers following the slash symbol represent the UGV numbers. The final position estimates of a CL system are closer to the actual final positions than that of a non-CL system for the four peripheral UGVs.

CHAPTER 5

CONCLUSION

5.1 Summary of the Research Work

In this dissertation, novel approaches for single-UGV localization and multi-UGV CL were presented. They included methodologies for creating parametric calibration models and mass assignment tables. The "*theoretical*" aspects of the techniques and their validation using "*empirical*" data were described.

In Chapter 1, an introduction to the CL problem, a tripartite research objective, conformance of this dissertation, and a brief outline of the chapters were described. In Chapter 2, a detailed review of literature that is related to this research work was presented. The review described the different types of localization sensors that were employed in this research, the fundamentals of error characteristics with respect to localization, existing methods for localization sensor calibration, current fusion filtering techniques, and an extensive report of the current approaches to CL.

In Chapter 3, the $\boldsymbol{\eta}$-Filter as a technique for single-UGV localization was explained in detail. It included methodologies for creating parametric sensor calibration models and for building a mass assignment table that is suited to the requirements of the $\boldsymbol{\eta}$-Filter. An experimental validation of the $\boldsymbol{\eta}$-Filter including a designed experiment was described. A definite improvement in the accuracy of localization in the *trapped*

scenario was noticed (Figure 5.1). However, no definite improvement was noticed in the mean final position error in the *normal* scenario, at the 5% significance level. On the average, the ***η***-Filter performed better than the EKF by 11.17% (Figure 5.1).

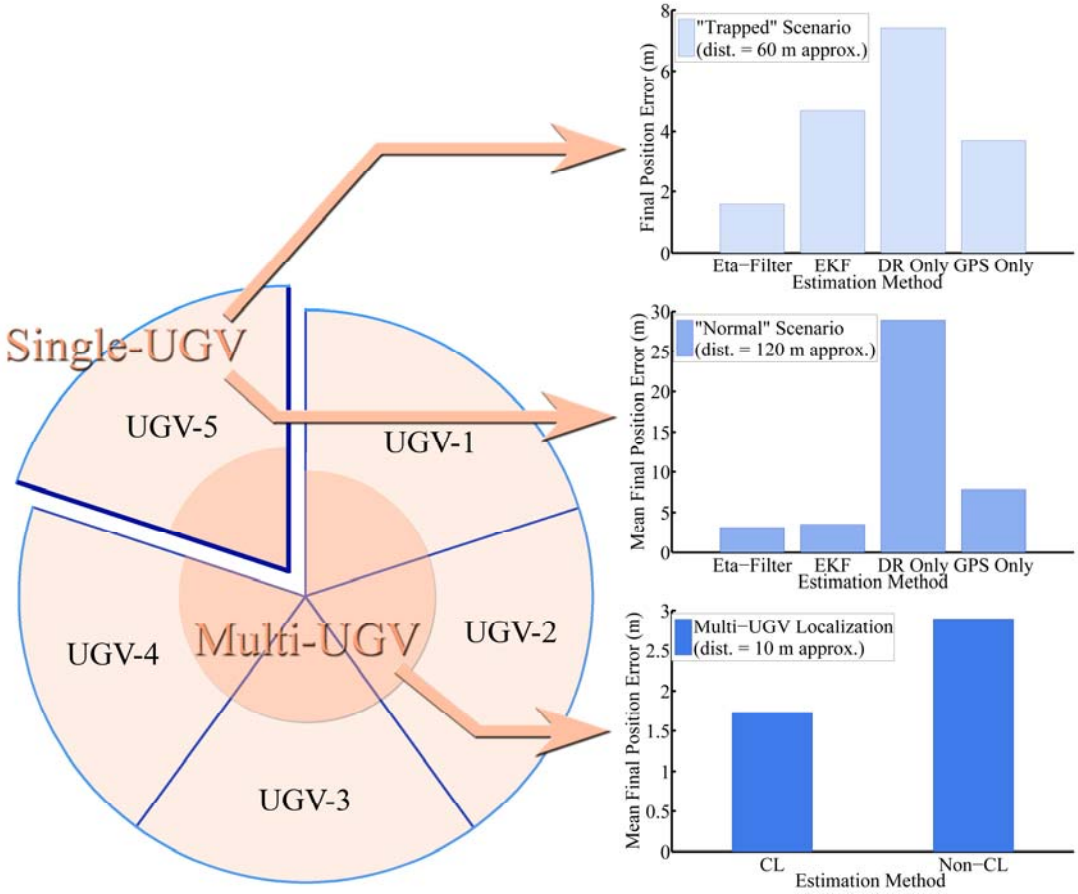

Figure 5.1 The Performance Charts: A comparison of the methodologies for single-UGV and multi-UGV localization. The ***η***-Filter and the range-only CL system have a relatively low mean final position error.

In Chapter 4, the range-only CL system that resembles a "*star*" arrangement was presented. It included descriptions of sensor modeling and self-localization of single UGVs. The chapter also described the theory behind the cooperative fusion process and a statistically designed experiment for testing the performance of the range-

only CL system. The experiment indicated that the range-only CL system consistently performed better than the non-CL system with a 40% improvement in the mean final position error, at the 1% significance level (Figure 5.1).

5.2 Contributions

A parametric calibration procedure that relates the sensor outputs directly to the requirements of the $\boldsymbol{\eta}$-Filter such as linear velocity, angular velocity, and orientation was presented. Linear regression models were used for linear and angular velocities, and a fifth degree polynomial model was used for the orientation. Also, a procedure for the creation of mass assignment tables for the GPS was described.

The methodology presented for single-UGV localization has enhanced existing KF based approaches to localization. The pitfalls of modeling inaccuracies that stem from environmental changes and ignorance were accounted for by the $\boldsymbol{\eta}$-Filter. This led to an improvement in accuracy and an increase in "*robustness*." In particular, a two-pronged approach was advocated for dealing with "*changes*" in operating scenarios and sensor goodness. For operating scenarios, adaptive switching was performed between multiple parametric models for KF inputs and between corresponding input noise covariance matrices. For sensor goodness, a variable measurement noise covariance matrix was used.

The technique for multi-UGV CL that uses a range-only system provided for a low-cost and a "*heterogeneous*" multi-UGV system. By having one UGV with a full suite of localization sensors and four UGVs with only wheel encoders, the per-UGV

cost was decreased. This decrease in the per-UGV cost for a CL system was obtained while maintaining a better accuracy in comparison to a non-CL system.

Designed experiments were employed for testing the accuracy of localization systems. This provided a more precise comparison of localization systems by taking into account the possible factors that cause variability, *i.e.*, the *location* factor in the case of the $\boldsymbol{\eta}$-Filter and the *UGV* factor in the case of the CL system.

On the whole, an organic approach has been presented as an answer to the question posed by multi-UGV systems: "*where are we?*"

5.3 Future Extensions

In future, models for more operating scenarios such as the "*kidnapped robot*" scenario and mass assignment tables for more sensors (for goodness) such as the digital compass or vision sensors may be formulated. The $\boldsymbol{\eta}$-Filter may be applied to multi-sensor fusion filtering problems that fall outside the domain of UGV localization starting with the basic framework shown in Figure 3.1.

The *range-only* CL system can be extended to more than five UGVs and also have multiple mobile beacons. The presence of multiple mobile beacons would improve the accuracy in position. The CL system may be extended to three dimensions and include Unmanned Aerial Vehicles (UAVs) in the team.

The $\boldsymbol{\eta}$-Filter and the *range-only* CL system serve as base-level capabilities for future activities such as speed and heading control, environmental mapping, waypoint navigation, and a host of other higher level tasks.

APPENDIX A

GRAPHS FOR η-FILTER EXPERIMENTS

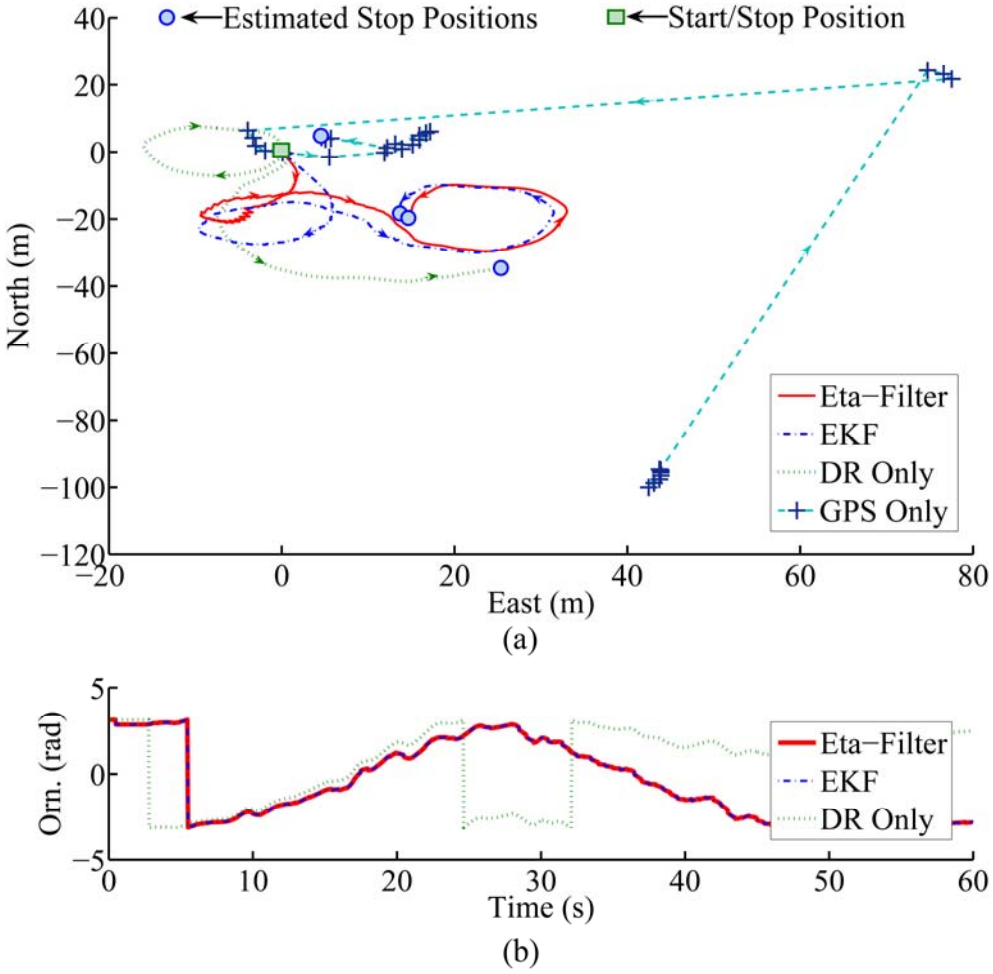

Figure A.1 The Path (a) and Orientation (b) Plots for Run One in the "normal" Scenario: Erratic GPS measurements are present. There is no significant difference between the $\boldsymbol{\eta}$-Filter and the EKF.

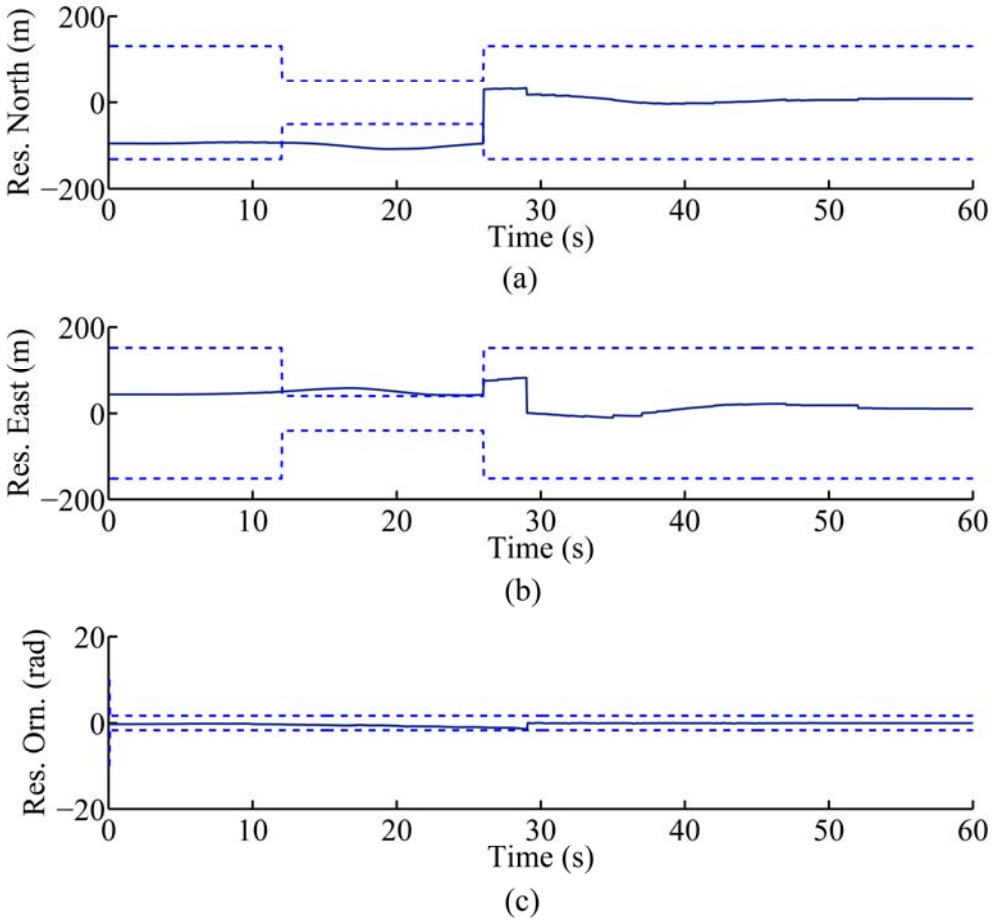

Figure A.2 The Residual Plots of North (a), East (b), and Orientation (c) for Run One: The residuals, marked as solid lines, are within their ±2σ bounds (95% confidence bounds), marked as dashed lines, for most of the time.

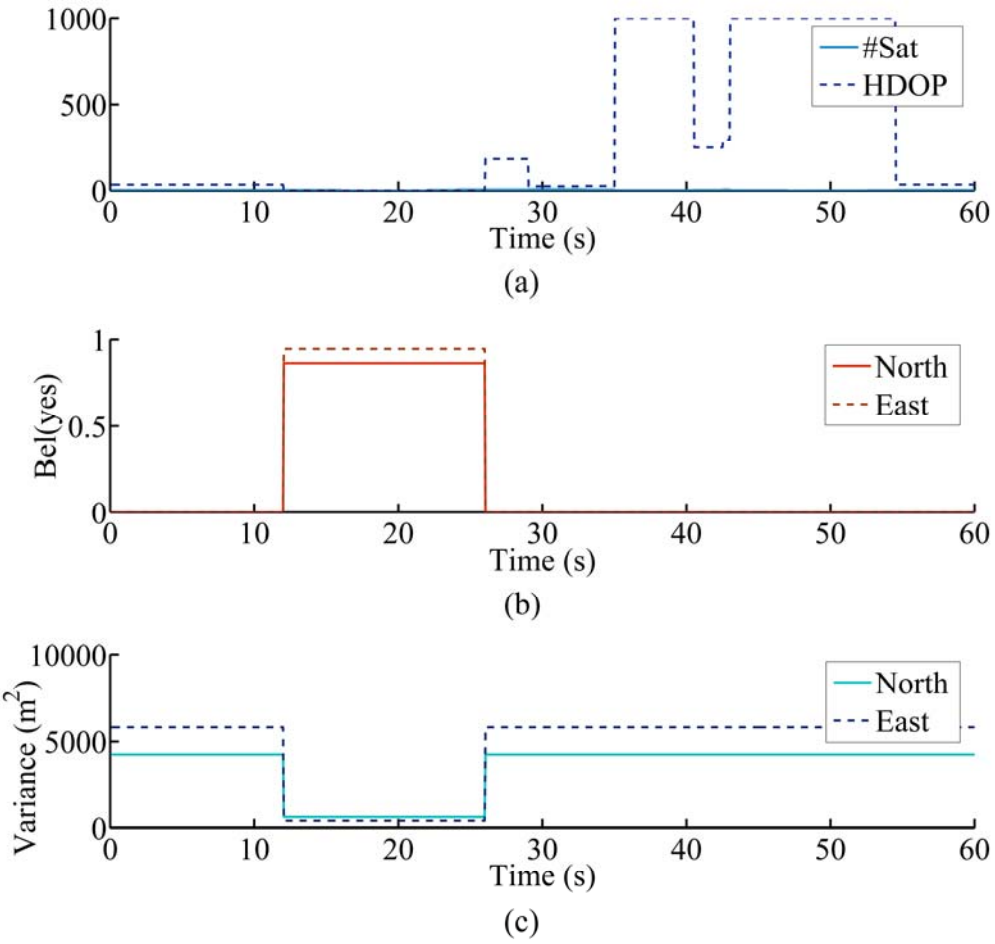

Figure A.3 GPS Sensor Goodness Plots for Run One: An increase in HDOP and a decrease in #Sat (though not clearly visible in this graph) (a) lead to a decrease in the belief value for *yes* (the GPS is good) (b) and an increase in the north (*xx*) and the east (*yy*) components of the measurement error covariance matrix **R** (c).

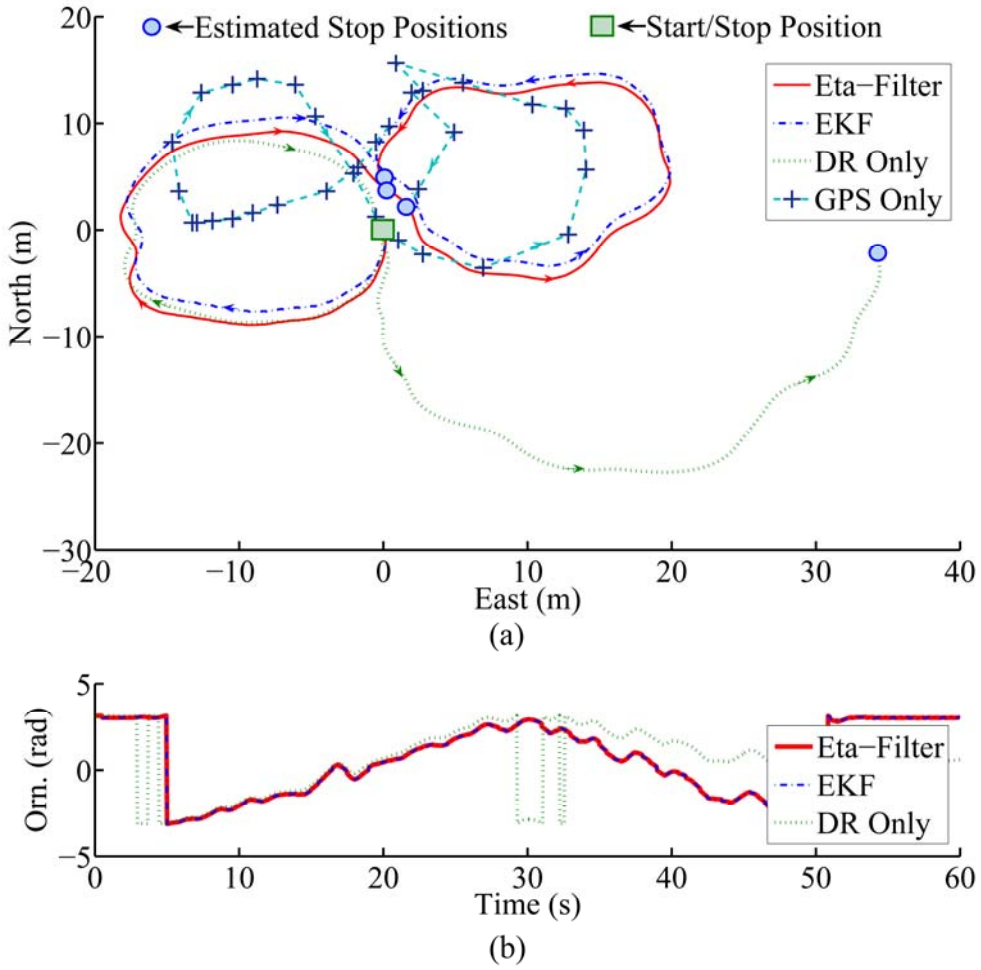

Figure A.4 The Path (a) and Orientation (b) Plots for Run Two in the "normal" Scenario: There is no significant difference between the $\boldsymbol{\eta}$-Filter and the EKF.

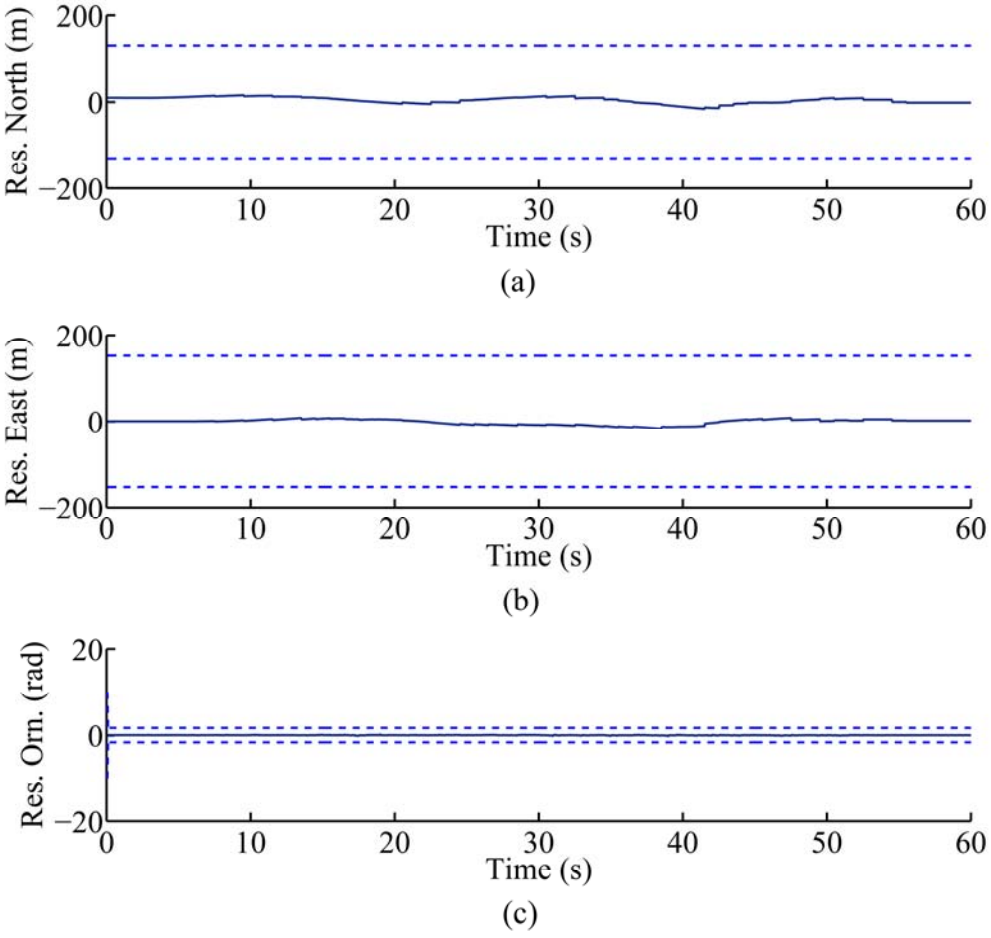

Figure A.5 The Residual Plots of North (a), East (b), and Orientation (c) for Run Two: The residuals, marked as solid lines, are within their ±2σ bounds (95% confidence bounds), marked as dashed lines.

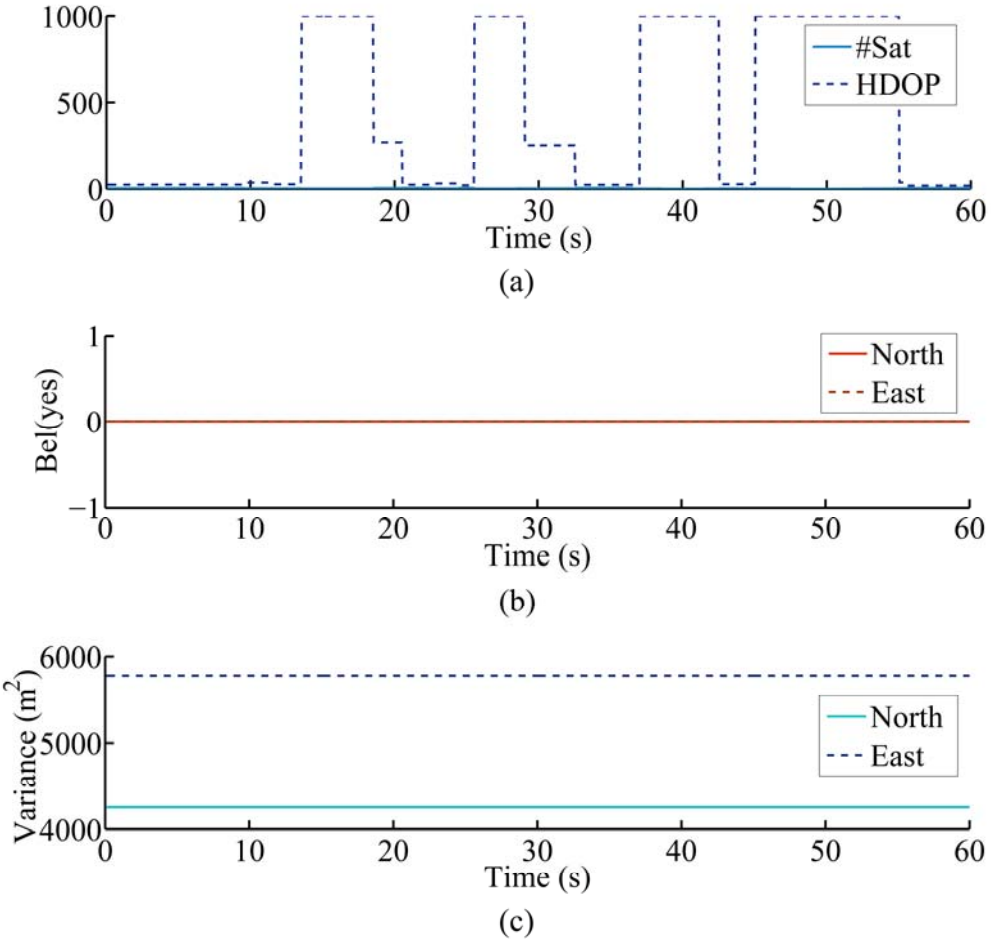

Figure A.6 GPS Sensor Goodness Plots for Run Two: A very high HDOP and a low #Sat (though not clearly visible in this graph) (a) lead to a "zero" belief value for *yes* (the GPS is good) (b) and constantly high north (*xx*) and east (*yy*) components of the measurement error covariance matrix **R** (c).

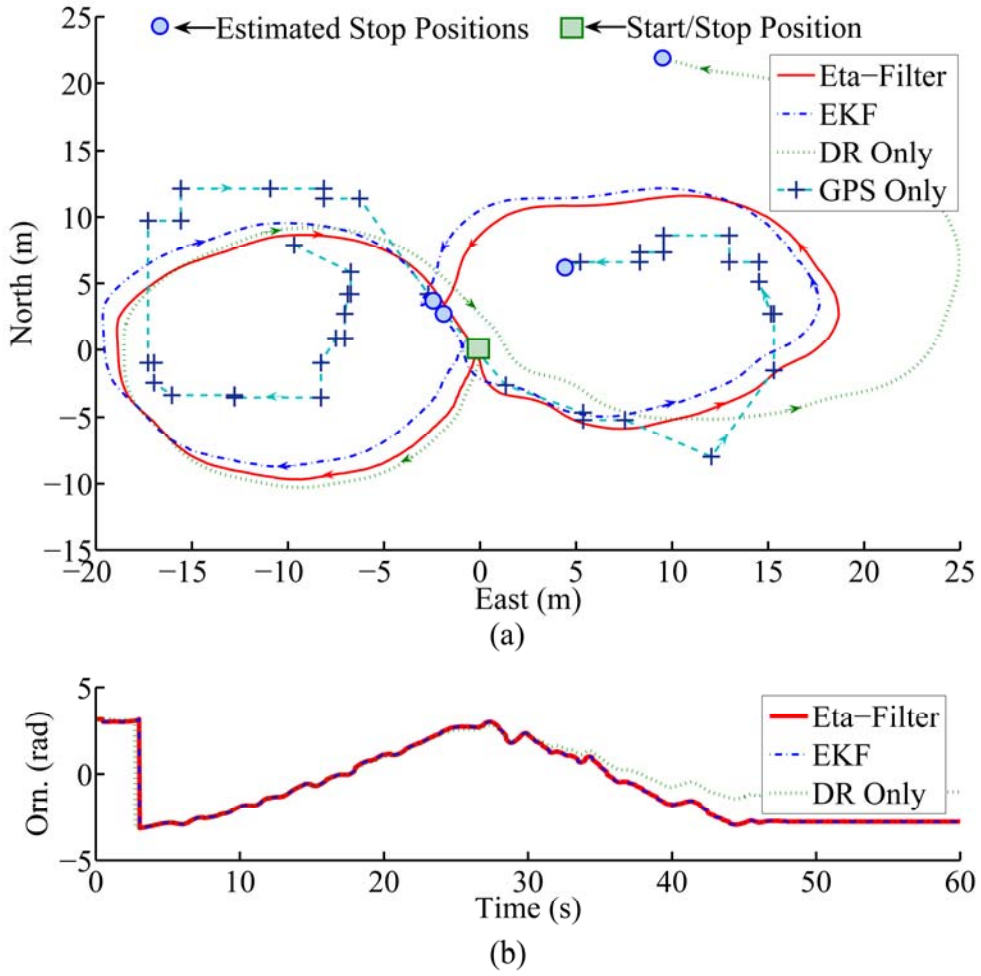

Figure A.7 The Path (a) and Orientation (b) Plots for Run Three in the "normal" Scenario: There is no significant difference between the ***η***-Filter and the EKF.

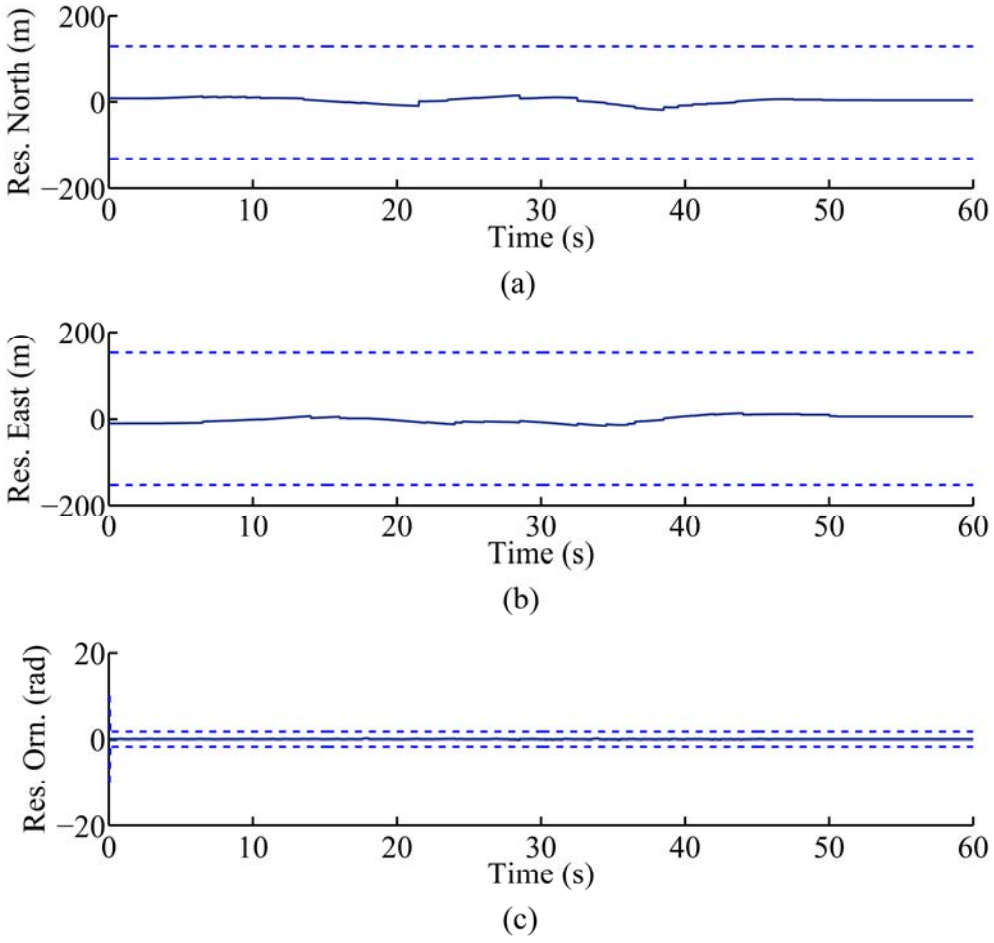

Figure A.8 The Residual Plots of North (a), East (b), and Orientation (c) for Run Three: The residuals, marked as solid lines, are within their ±2σ bounds (95% confidence bounds), marked as dashed lines.

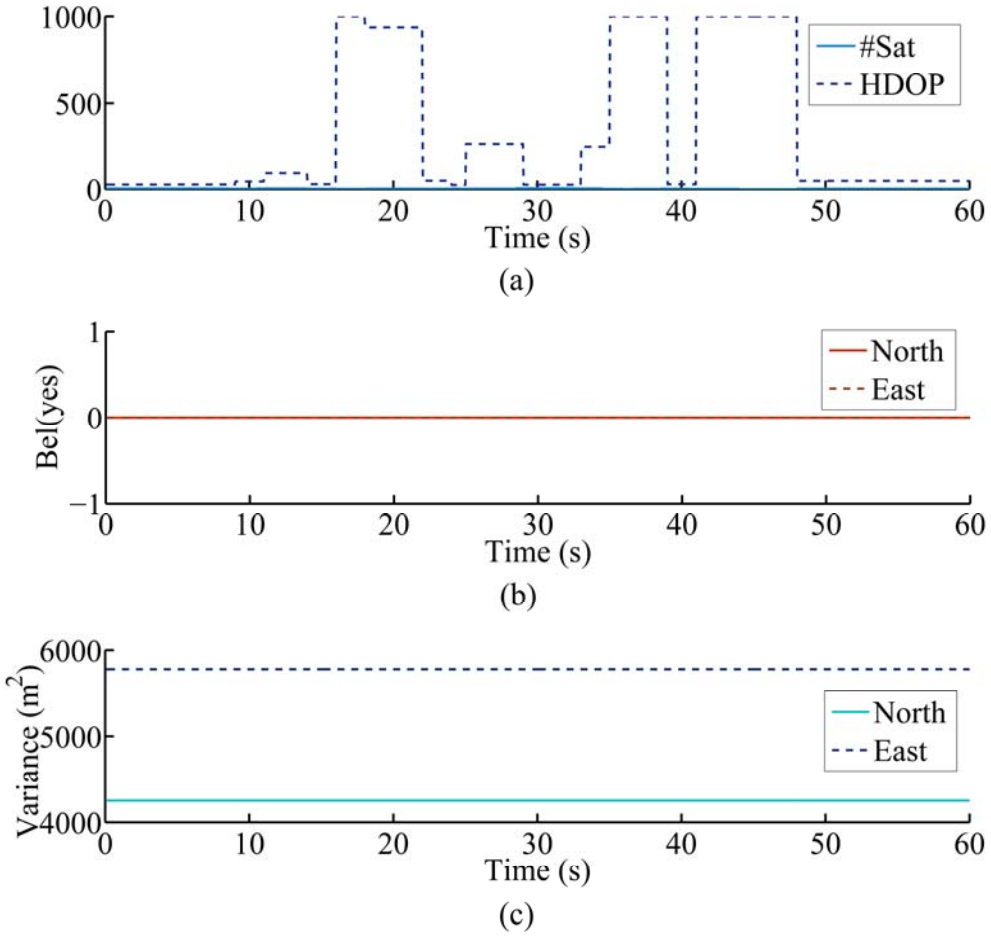

Figure A.9 GPS Sensor Goodness Plots for Run Three: A very high HDOP and a low #Sat (though not clearly visible in this graph) (a) lead to a "zero" belief value for *yes* (the GPS is good) (b) and constantly high north (*xx*) and east (*yy*) components of the measurement error covariance matrix **R** (c).

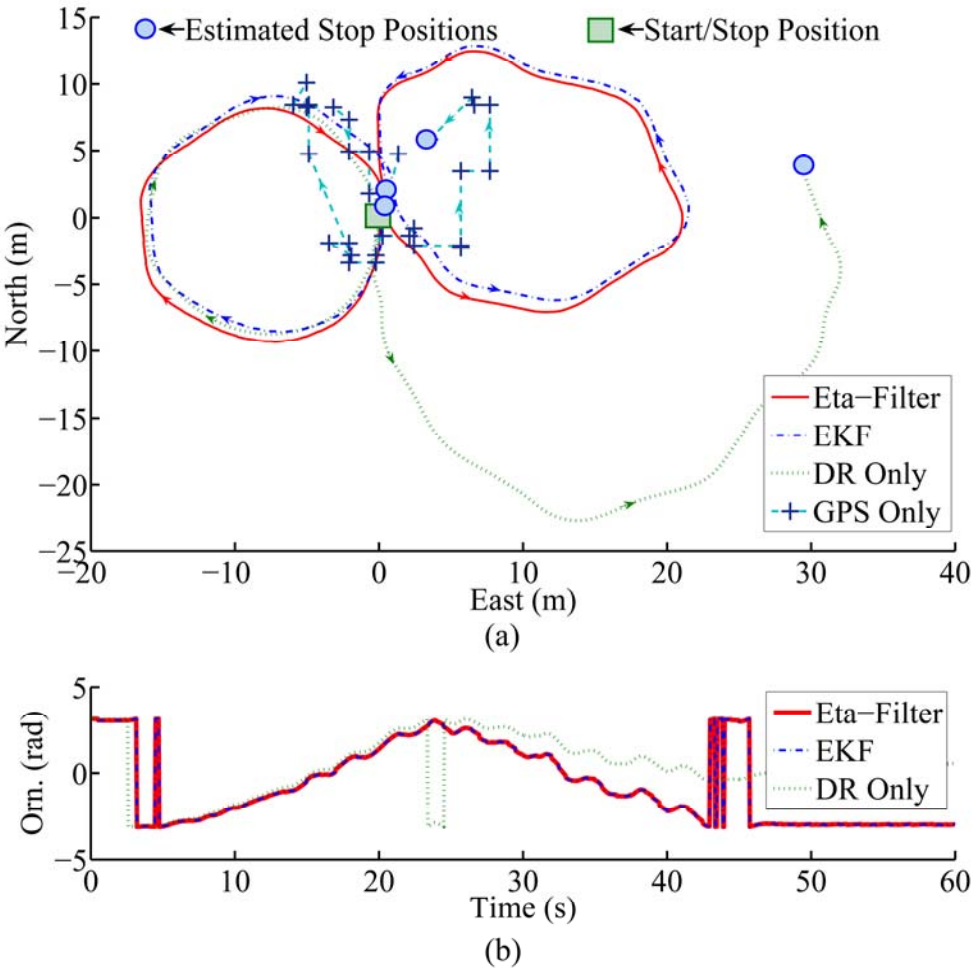

Figure A.10 The Path (a) and Orientation (b) Plots for Run Four in the "normal" Scenario: There is no significant difference between the $\boldsymbol{\eta}$-Filter and the EKF.

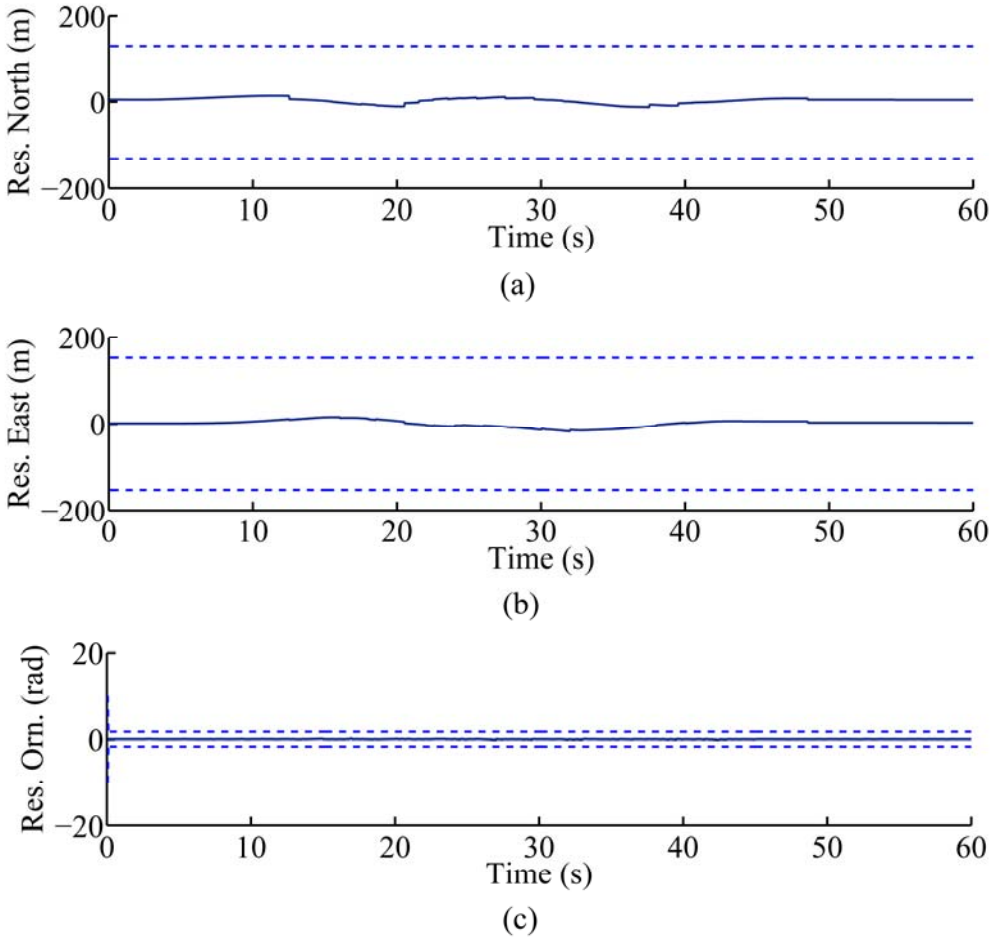

Figure A.11 The Residual Plots of North (a), East (b), and Orientation (c) for Run Four: The residuals, marked as solid lines, are within their ±2σ bounds (95% confidence bounds), marked as dashed lines.

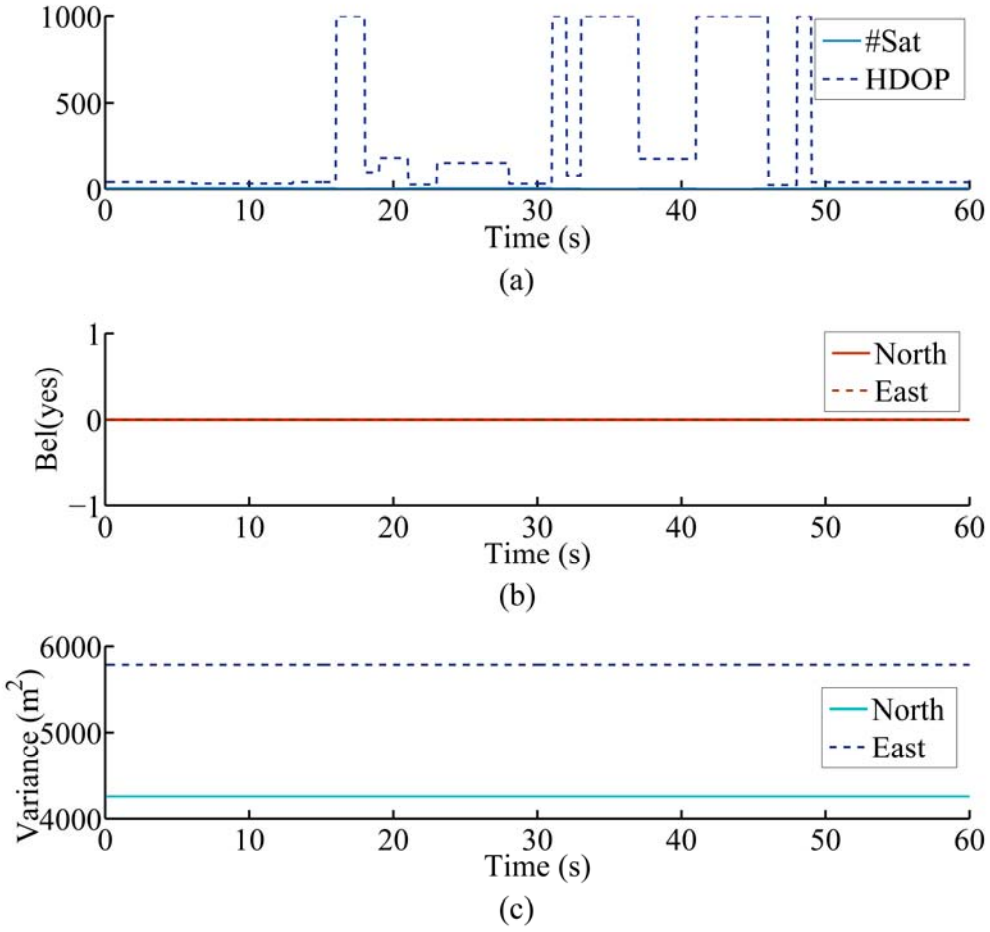

Figure A.12 GPS Sensor Goodness Plots for Run Four: A very high HDOP and a low #Sat (though not clearly visible in this graph) (a) lead to a "zero" belief value for *yes* (the GPS is good) (b) and constantly high north (*xx*) and east (*yy*) components of the measurement error covariance matrix **R** (c).

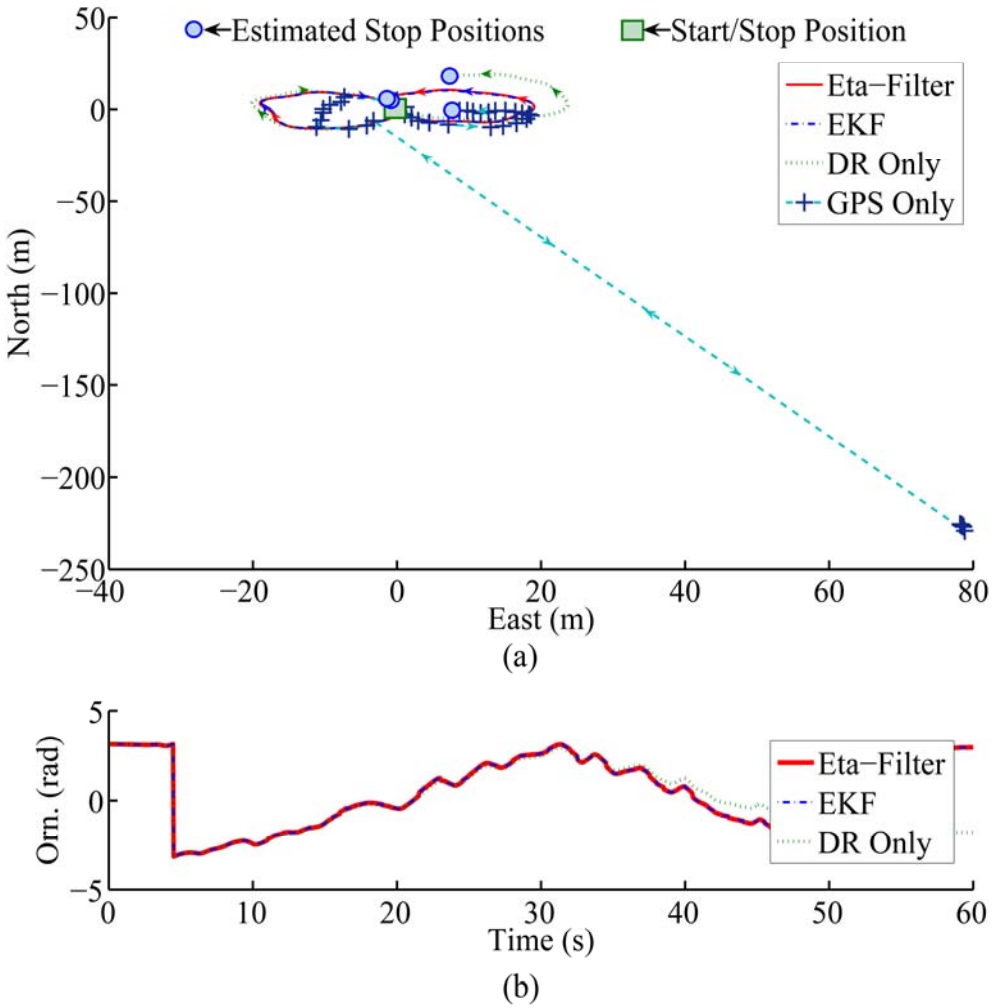

Figure A.13 The Path (a) and Orientation (b) Plots for Run Five in the "normal" Scenario: "Invalid" GPS measurements are present. There is no significant difference between the $\boldsymbol{\eta}$-Filter and the EKF.

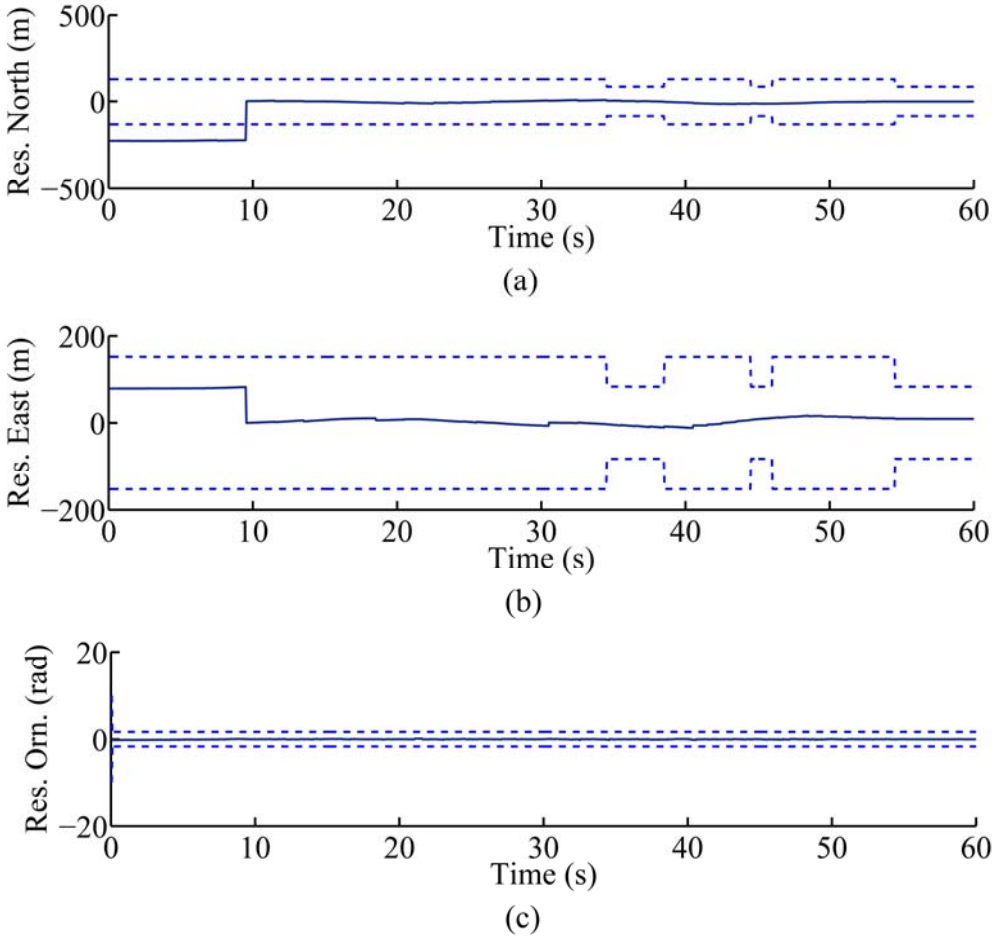

Figure A.14 The Residual Plots of North (a), East (b), and Orientation (c) for Run Five: The residuals, marked as solid lines, are within their ±2σ bounds (95% confidence bounds), marked as dashed lines, for most of the time.

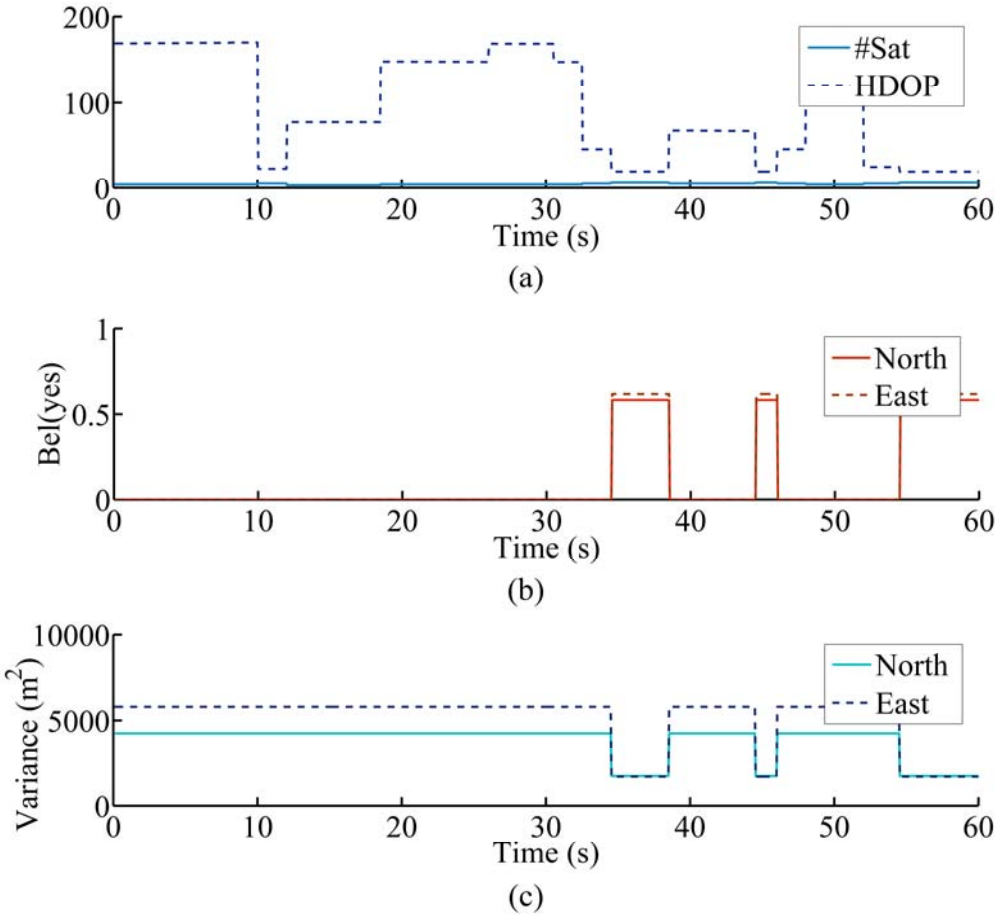

Figure A.15 GPS Sensor Goodness Plots for Run Five: An increase in HDOP and a decrease in #Sat (though not clearly visible in this graph) (a) lead to a decrease in the belief value for *yes* (the GPS is good) (b) and an increase in the north (*xx*) and the east (*yy*) components of the measurement error covariance matrix **R** (c).

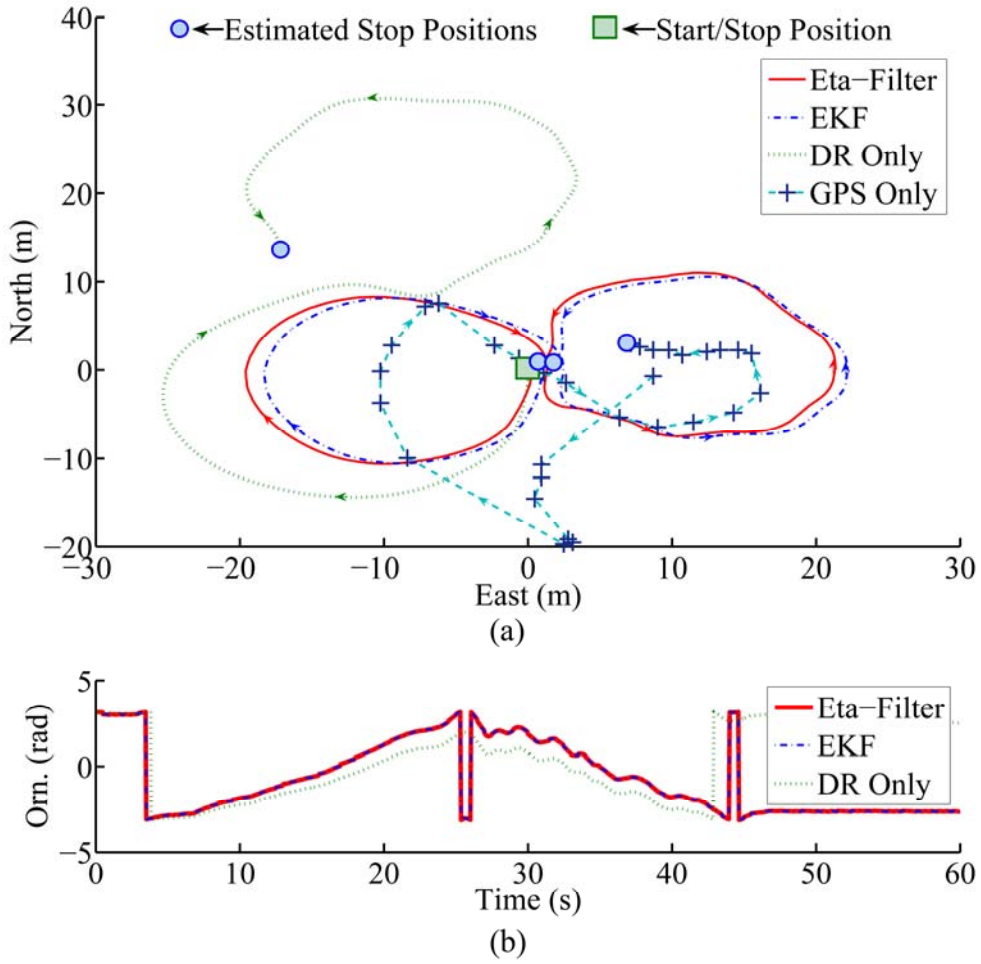

Figure A.16 The Path (a) and Orientation (b) Plots for Run Six in the "normal" Scenario: Erratic GPS measurements are present. There is no significant difference between the $\boldsymbol{\eta}$-Filter and the EKF.

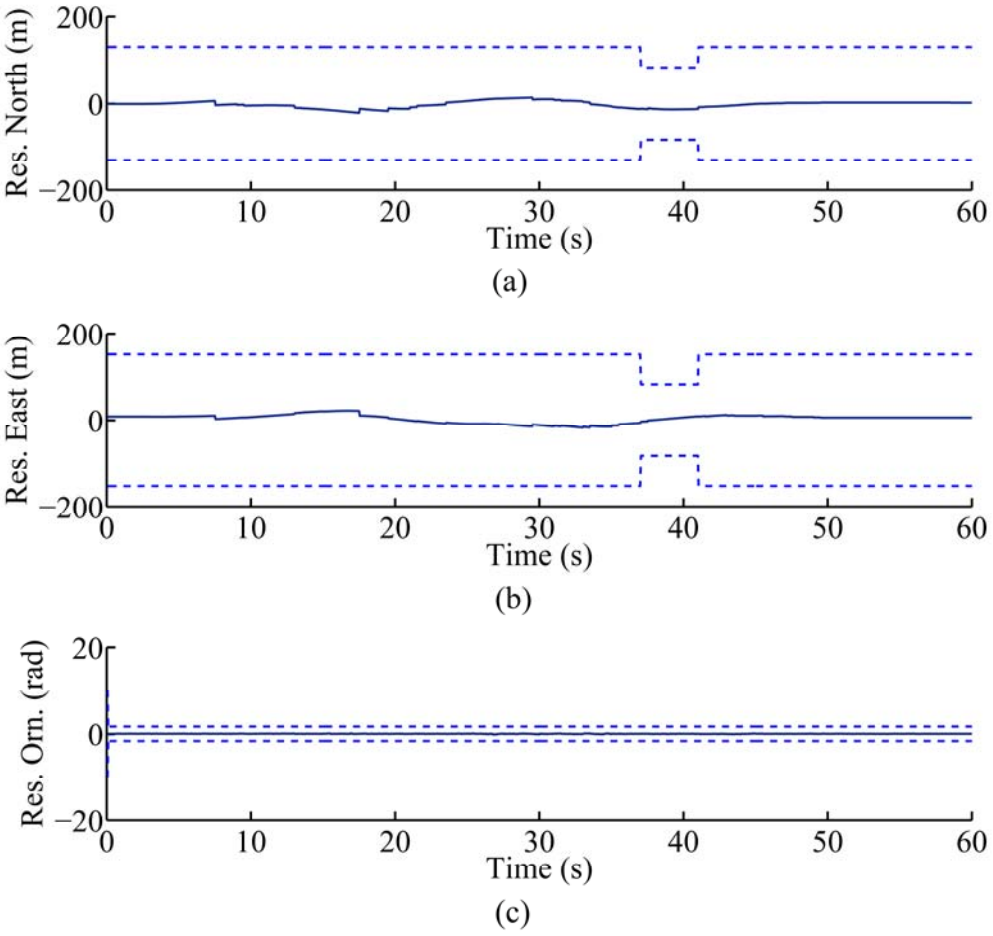

Figure A.17 The Residual Plots of North (a), East (b), and Orientation (c) for Run Six: The residuals, marked as solid lines, are within their ±2σ bounds (95% confidence bounds), marked as dashed lines.

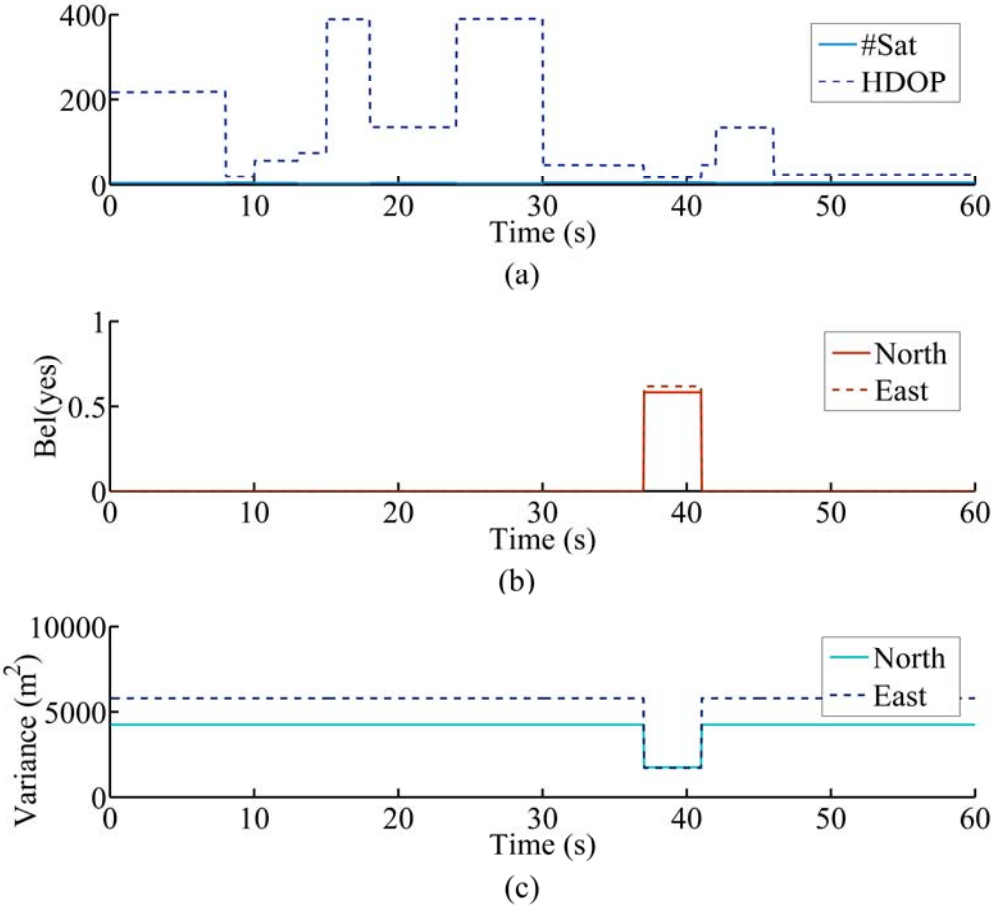

Figure A.18 GPS Sensor Goodness Plots for Run Six: A decrease in HDOP and an increase in #Sat (though not clearly visible in this graph) (a) lead to an increase in the belief value for *yes* (the GPS is good) (b) and an increase in the north (*xx*) and the east (*yy*) components of the measurement error covariance matrix **R** (c).

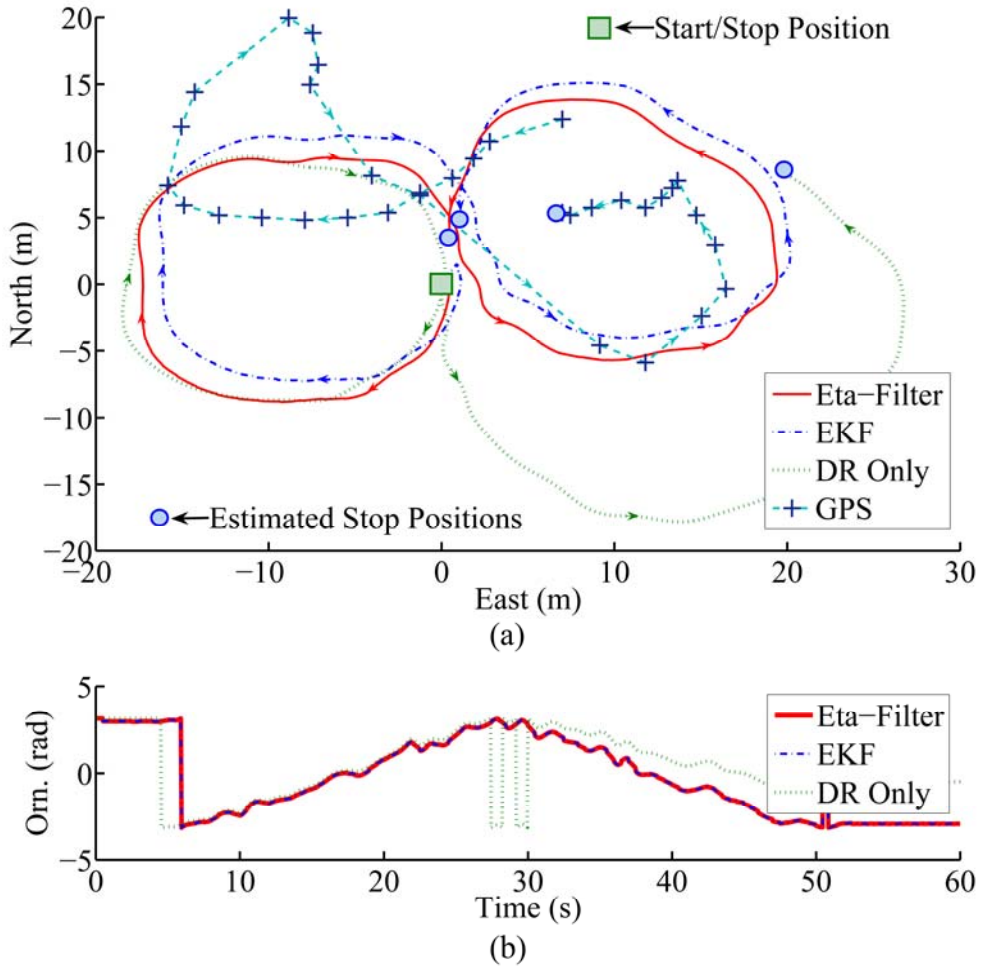

Figure A.19 The Path (a) and Orientation (b) Plots for Run Seven in the "normal" Scenario: There is no significant difference between the $\boldsymbol{\eta}$-Filter and the EKF.

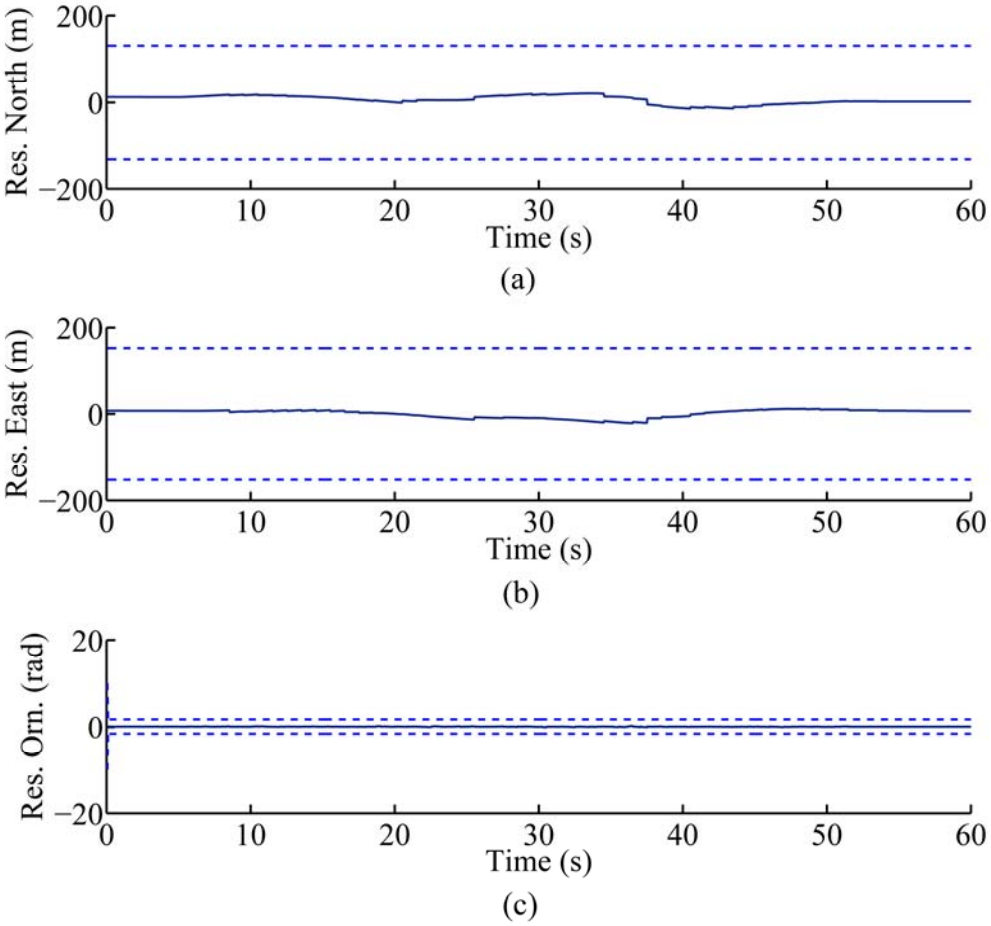

Figure A.20 The Residual Plots of North (a), East (b), and Orientation (c) for Run Seven: The residuals, marked as solid lines, are within their ±2σ bounds (95% confidence bounds), marked as dashed lines.

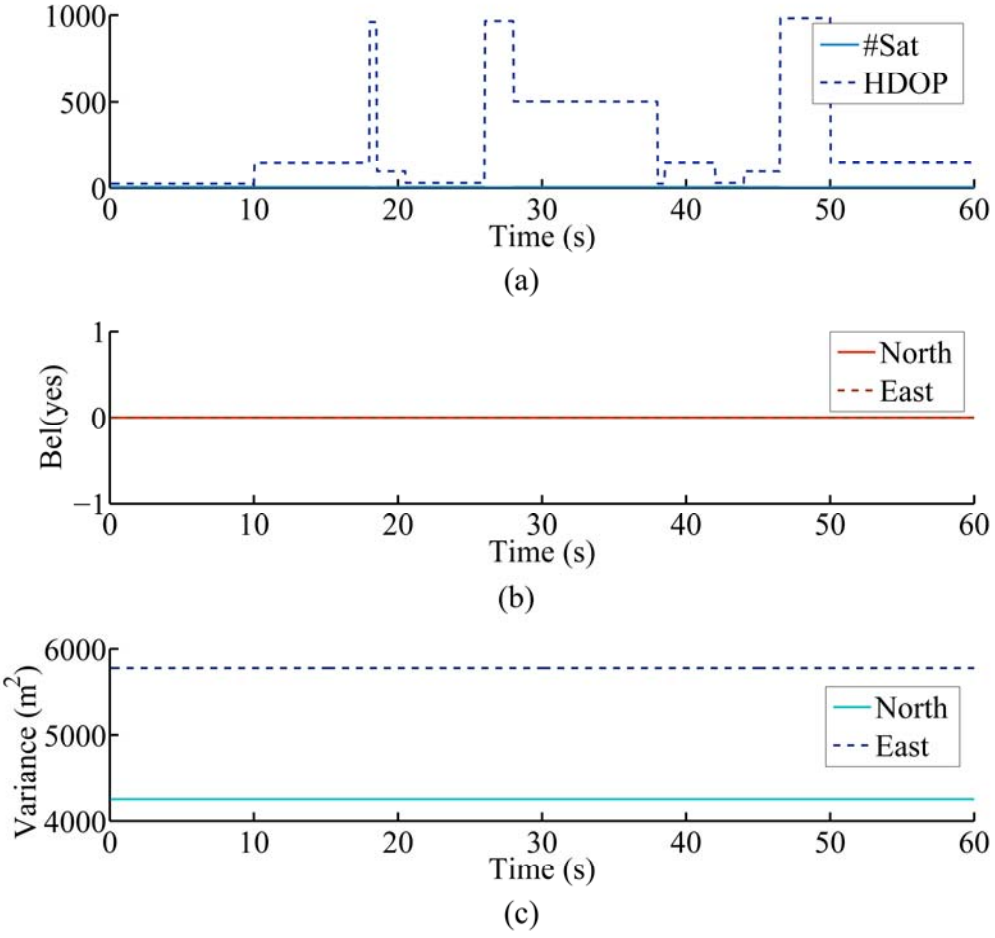

Figure A.21 GPS Sensor Goodness Plots for Run Seven: A very high HDOP and a low #Sat (though not clearly visible in this graph) (a) lead to a "zero" belief value for *yes* (the GPS is good) (b) and constantly high north (*xx*) and east (*yy*) components of the measurement error covariance matrix **R** (c).

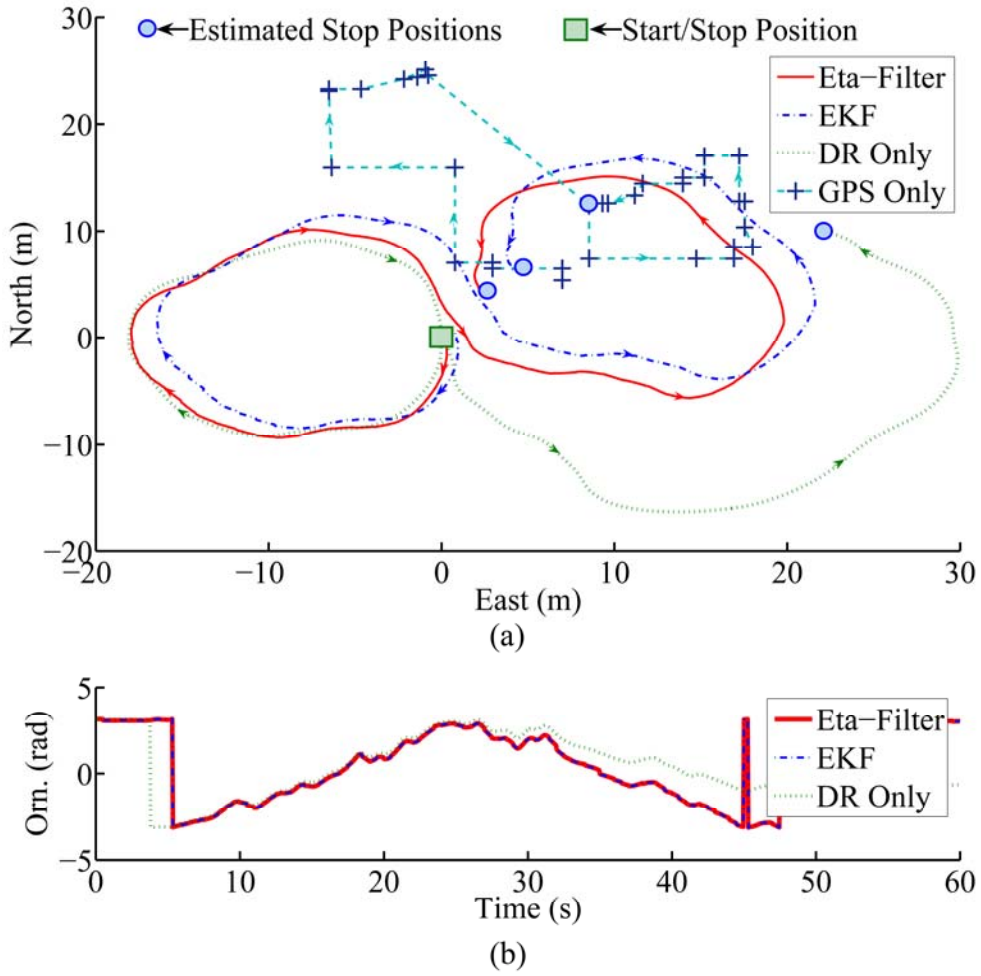

Figure A.22 The Path (a) and Orientation (b) Plots for Run Eight in the "normal" Scenario: Erratic GPS measurements are present. There is no significant difference between the ***η***-Filter and the EKF.

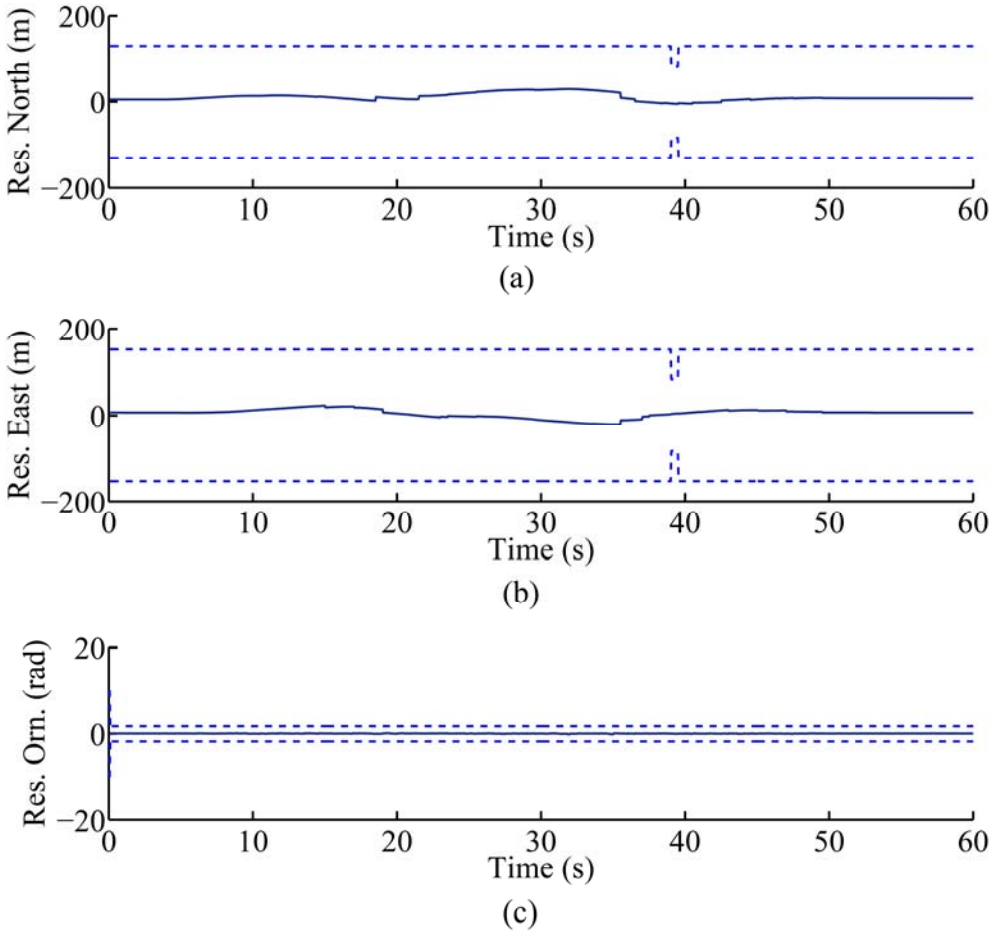

Figure A.23 The Residual Plots of North (a), East (b), and Orientation (c) for Run Eight: The residuals, marked as solid lines, are within their ±2σ bounds (95% confidence bounds), marked as dashed lines.

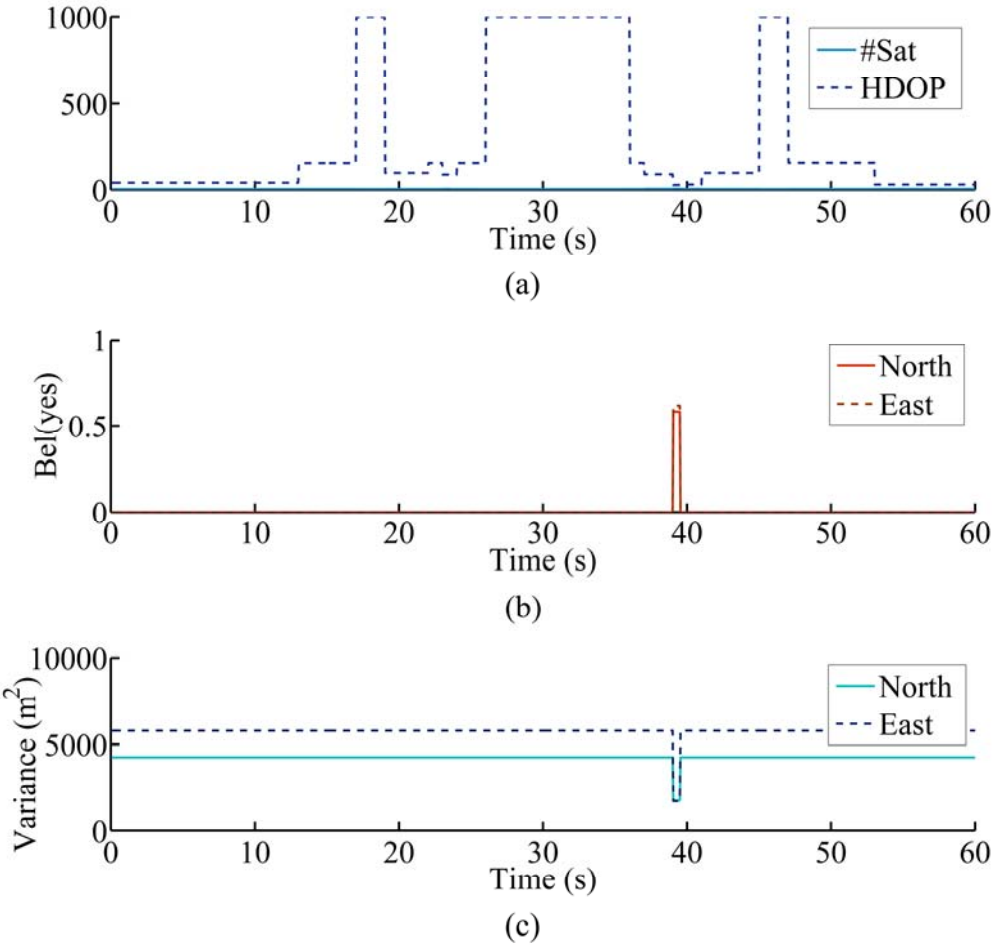

Figure A.24 GPS Sensor Goodness Plots for Run Eight: An increase in HDOP and a decrease in #Sat (though not clearly visible in this graph) (a) lead to a decrease in the belief value for *yes* (the GPS is good) (b) and an increase in the north (*xx*) and the east (*yy*) components of the measurement error covariance matrix **R** (c).

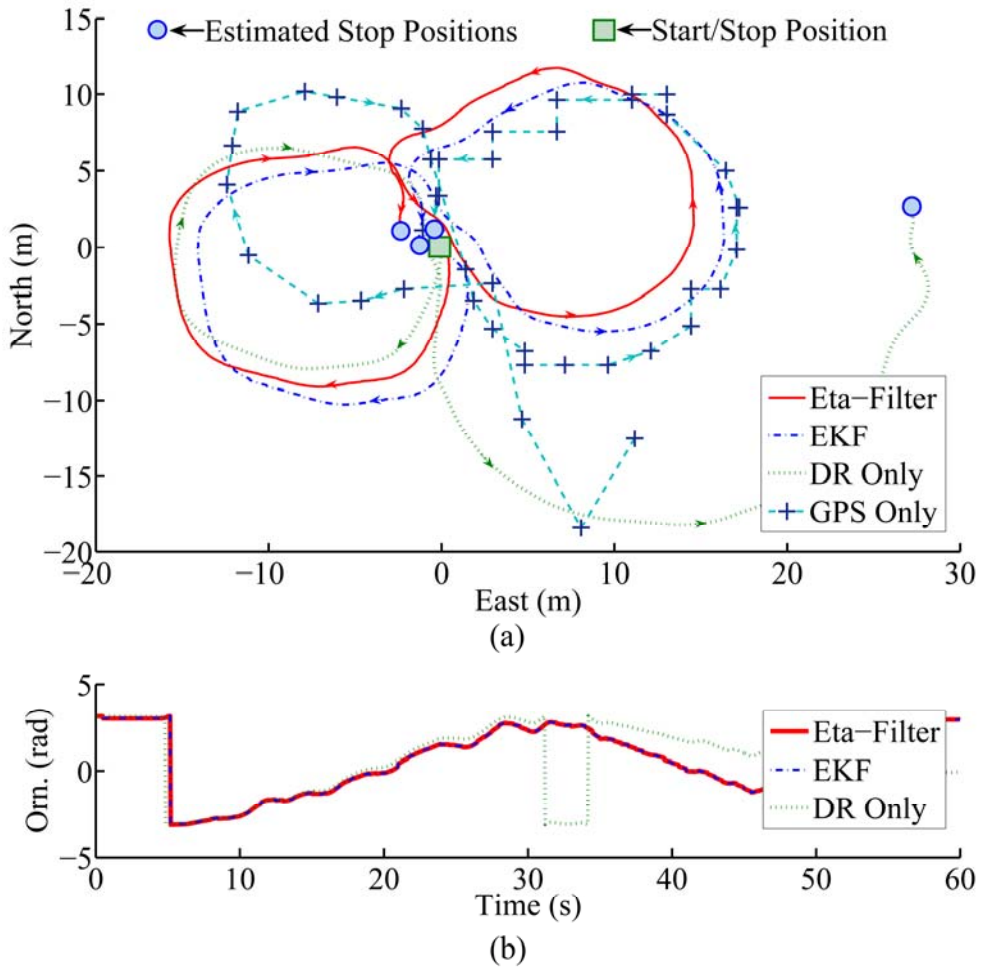

Figure A.25 The Path (a) and Orientation (b) Plots for Run Nine in the "normal" Scenario: There is no significant difference between the $\boldsymbol{\eta}$-Filter and the EKF.

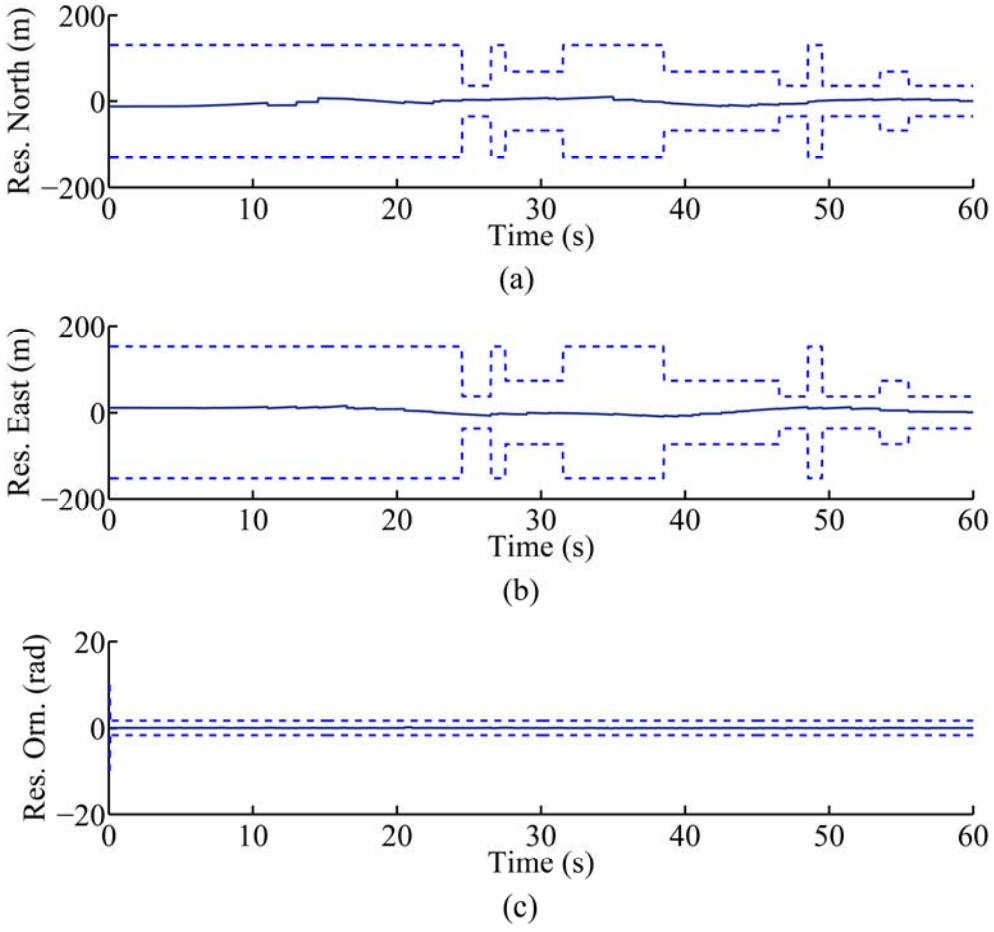

Figure A.26 The Residual Plots of North (a), East (b), and Orientation (c) for Run Nine: The residuals, marked as solid lines, are within their ±2σ bounds (95% confidence bounds), marked as dashed lines.

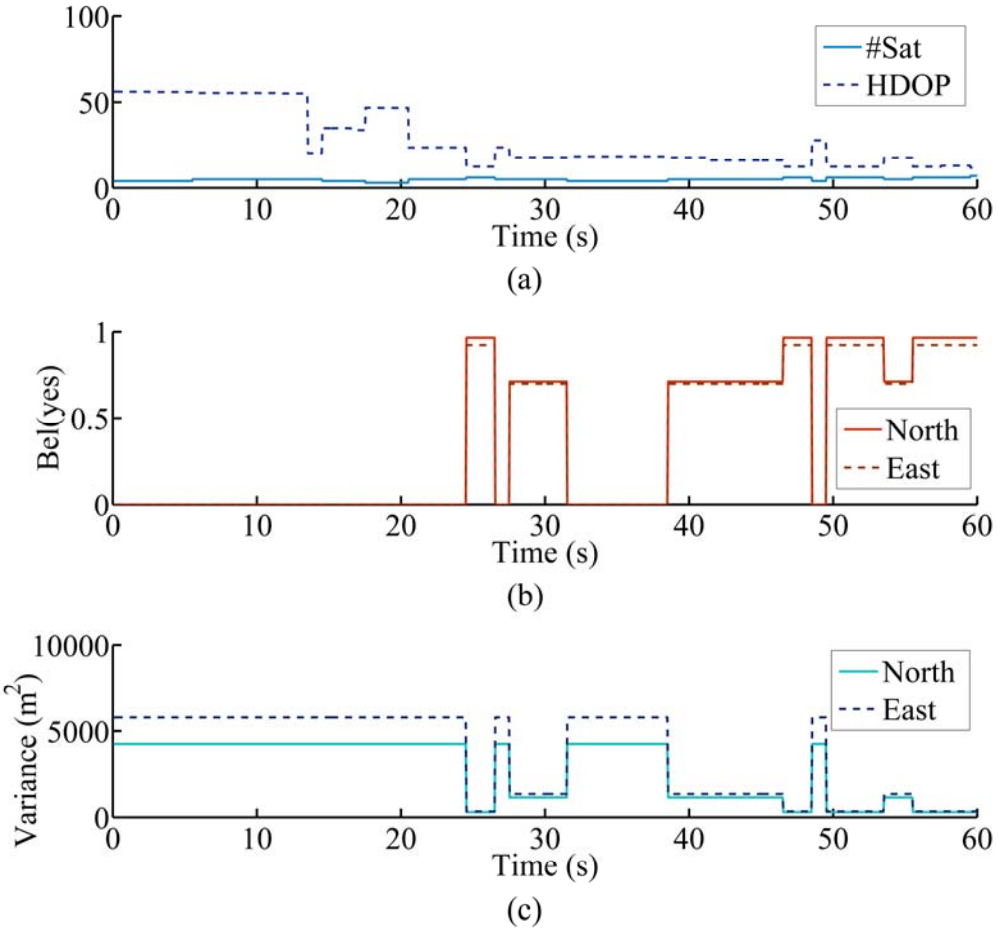

Figure A.27 GPS Sensor Goodness Plots for Run Nine: An increase in HDOP and a decrease in #Sat (a) lead to a decrease in the belief value for *yes* (the GPS is good) (b) and an increase in the north (*xx*) and the east (*yy*) components of the measurement error covariance matrix **R** (c).

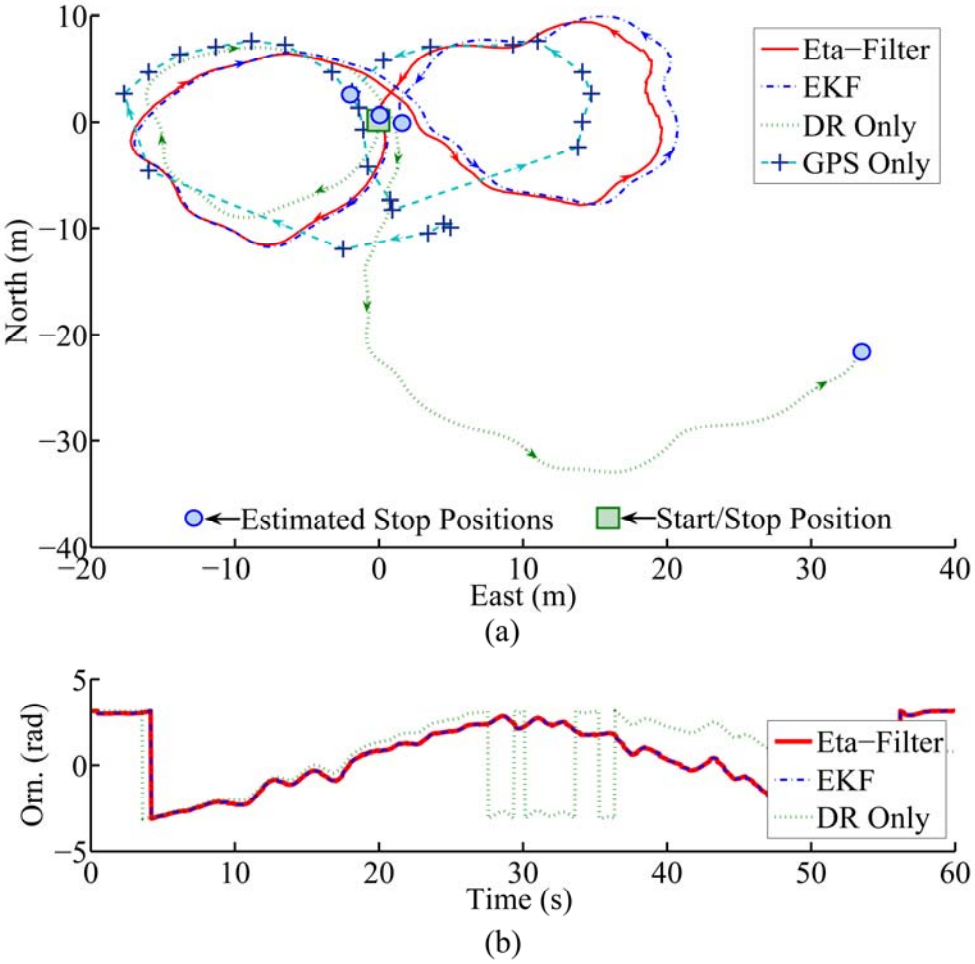

Figure A.28 The Path (a) and Orientation (b) Plots for Run Ten in the "normal" Scenario: There is no significant difference between the $\boldsymbol{\eta}$-Filter and the EKF.

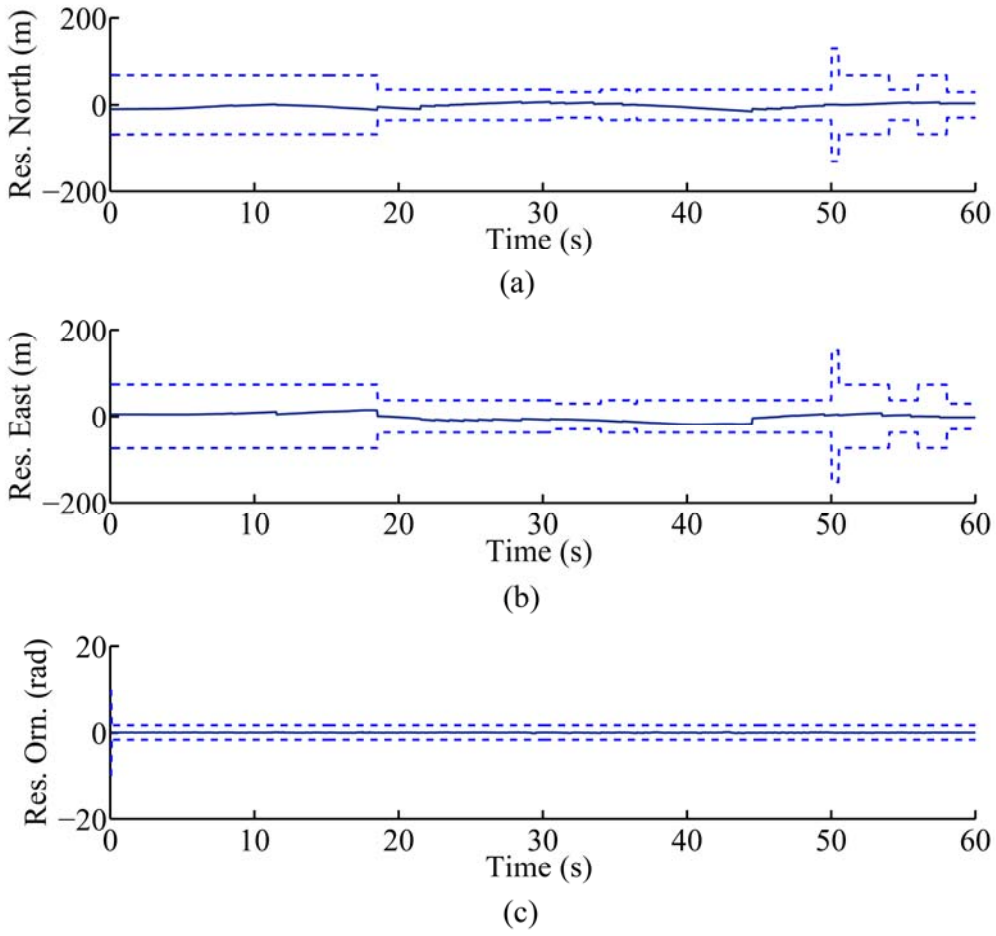

Figure A.29 The Residual Plots of North (a), East (b), and Orientation (c) for Run Ten: The residuals, marked as solid lines, are within their ±2σ bounds (95% confidence bounds), marked as dashed lines.

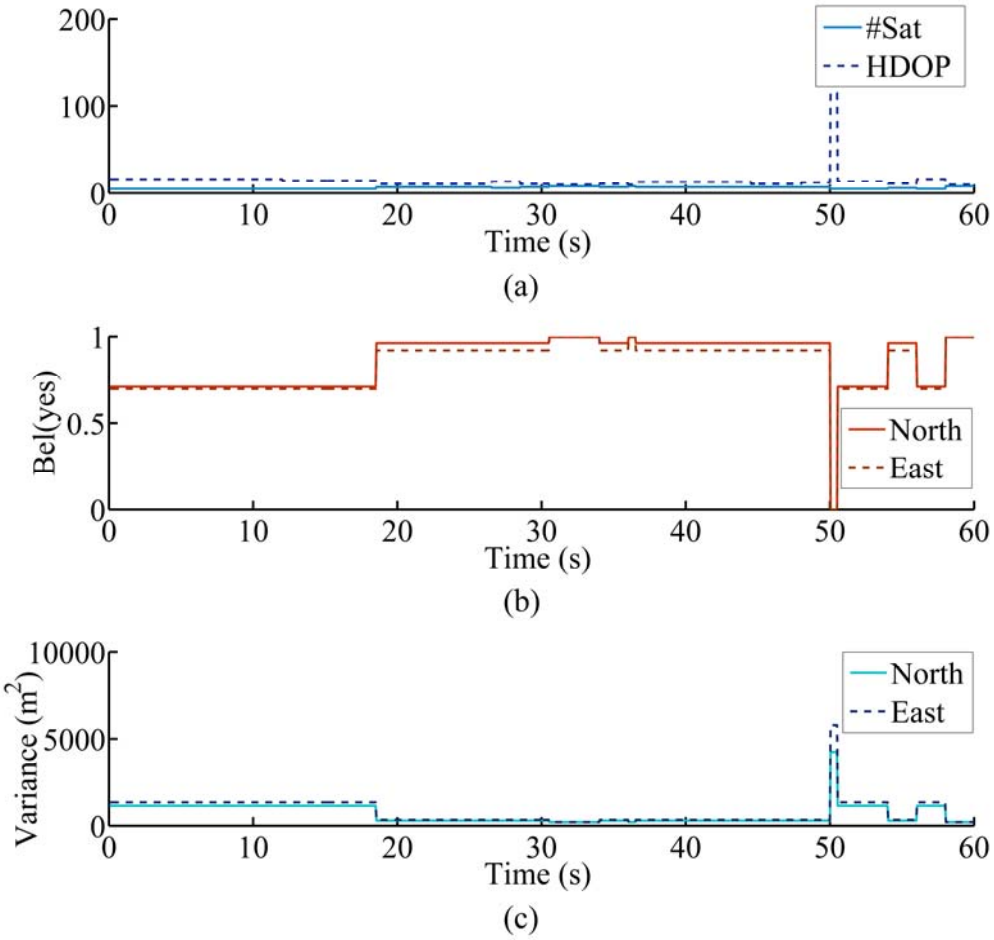

Figure A.30 GPS Sensor Goodness Plots for Run Ten: An increase in HDOP and a decrease in #Sat (a) lead to a decrease in the belief value for *yes* (the GPS is good) (b) and an increase in the north (*xx*) and the east (*yy*) components of the measurement error covariance matrix **R** (c).

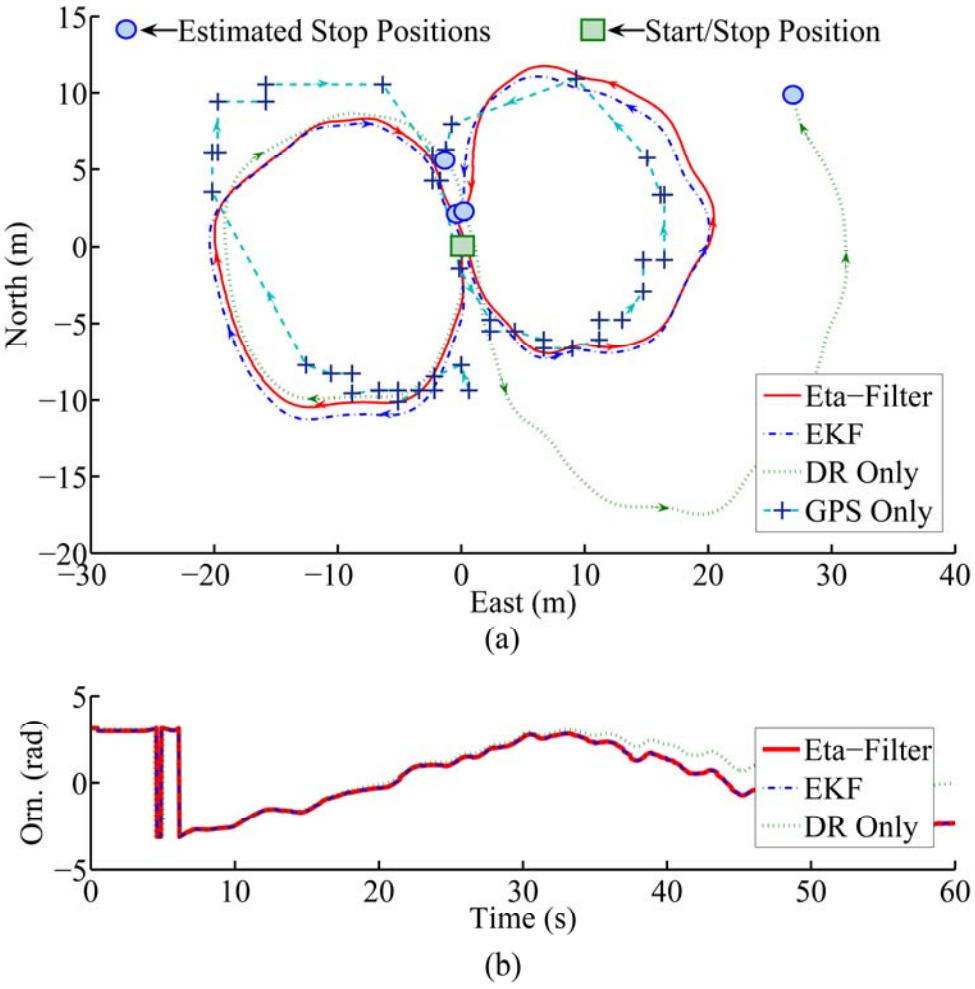

Figure A.31 The Path (a) and Orientation (b) Plots for Run Eleven in the "normal" Scenario: There is no significant difference between the $\boldsymbol{\eta}$-Filter and the EKF.

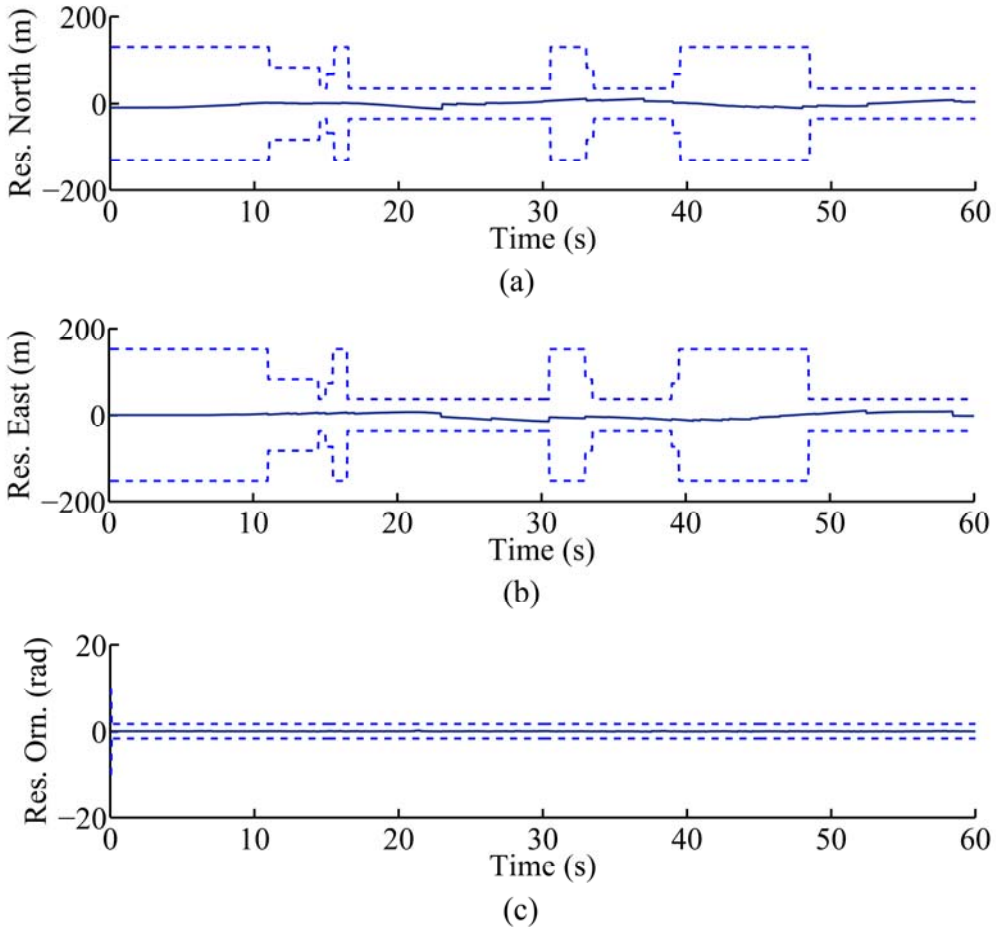

Figure A.32 The Residual Plots of North (a), East (b), and Orientation (c) for Run Eleven: The residuals, marked as solid lines, are within their ±2σ bounds (95% confidence bounds), marked as dashed lines.

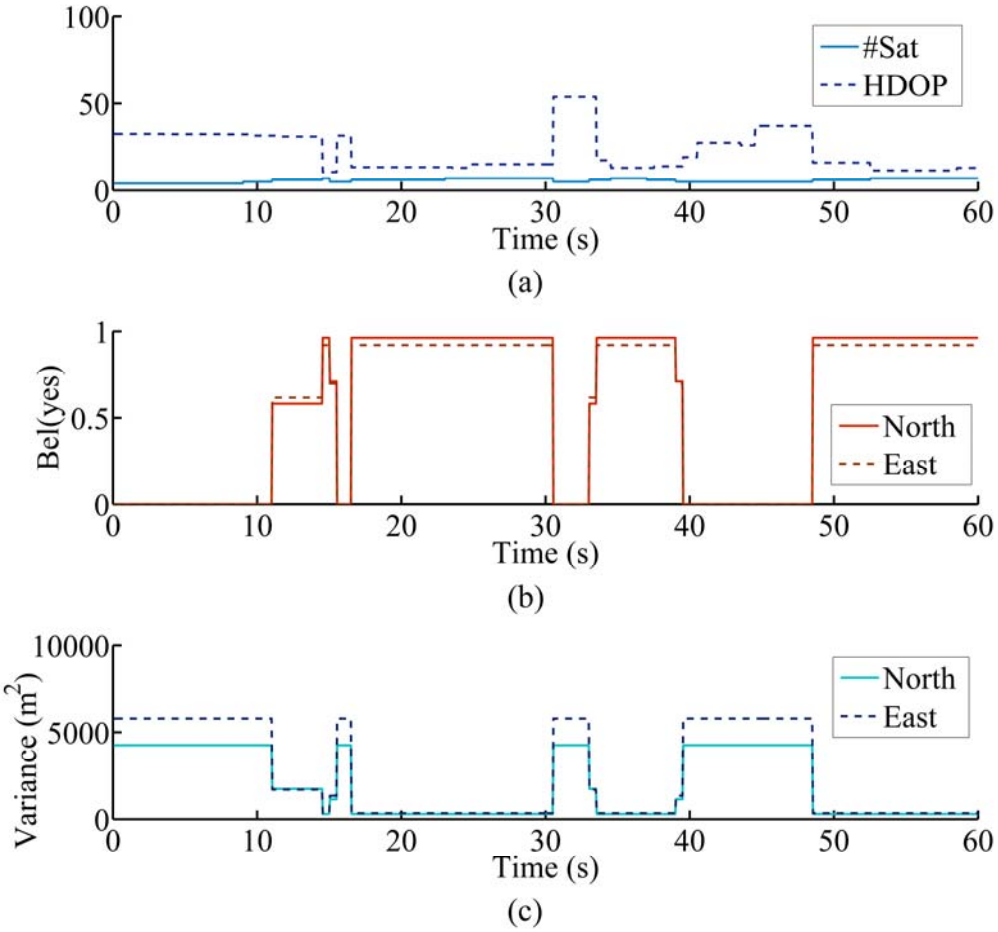

Figure A.33 GPS Sensor Goodness Plots for Run Eleven: An increase in HDOP and a decrease in #Sat (a) lead to a decrease in the belief value for *yes* (the GPS is good) (b) and an increase in the north (*xx*) and the east (*yy*) components of the measurement error covariance matrix **R** (c).

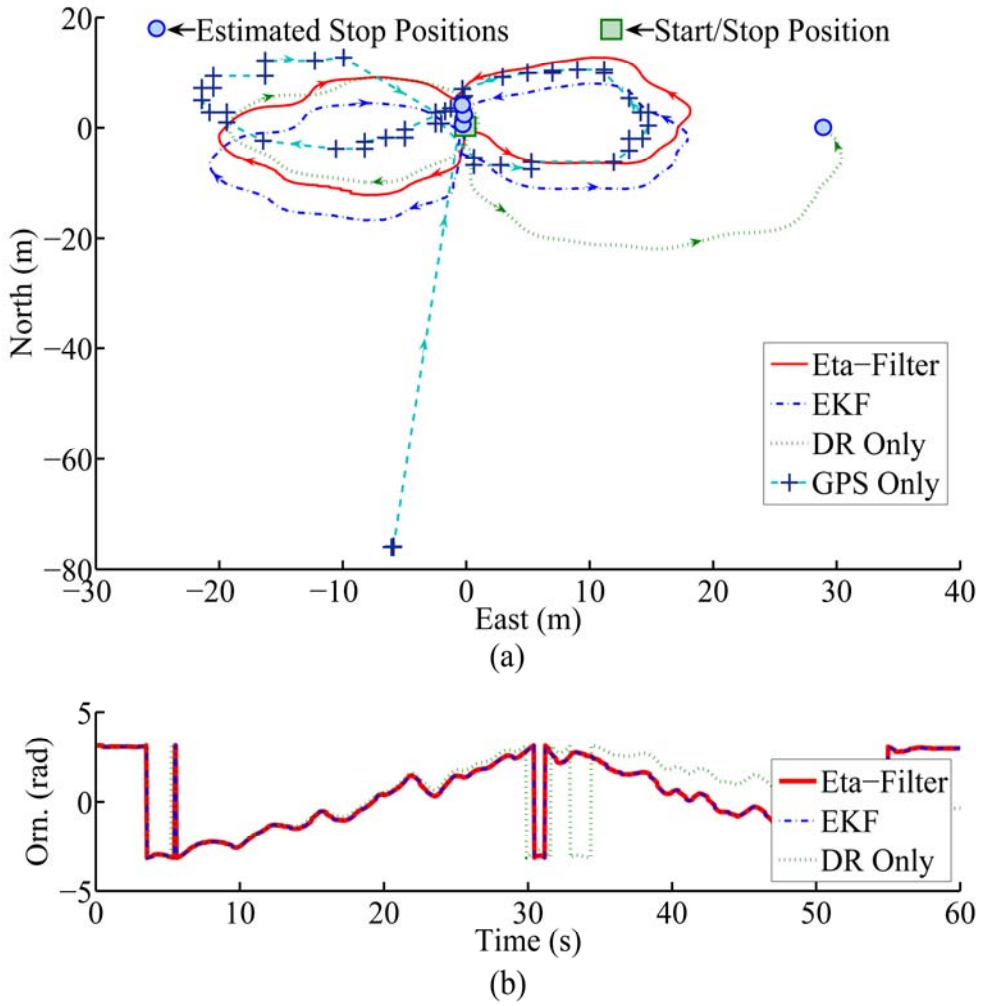

Figure A.34 The Path (a) and Orientation (b) Plots for Run Twelve in the "normal" Scenario: An erratic GPS measurement is present. There is no significant difference between the $\boldsymbol{\eta}$-Filter and the EKF.

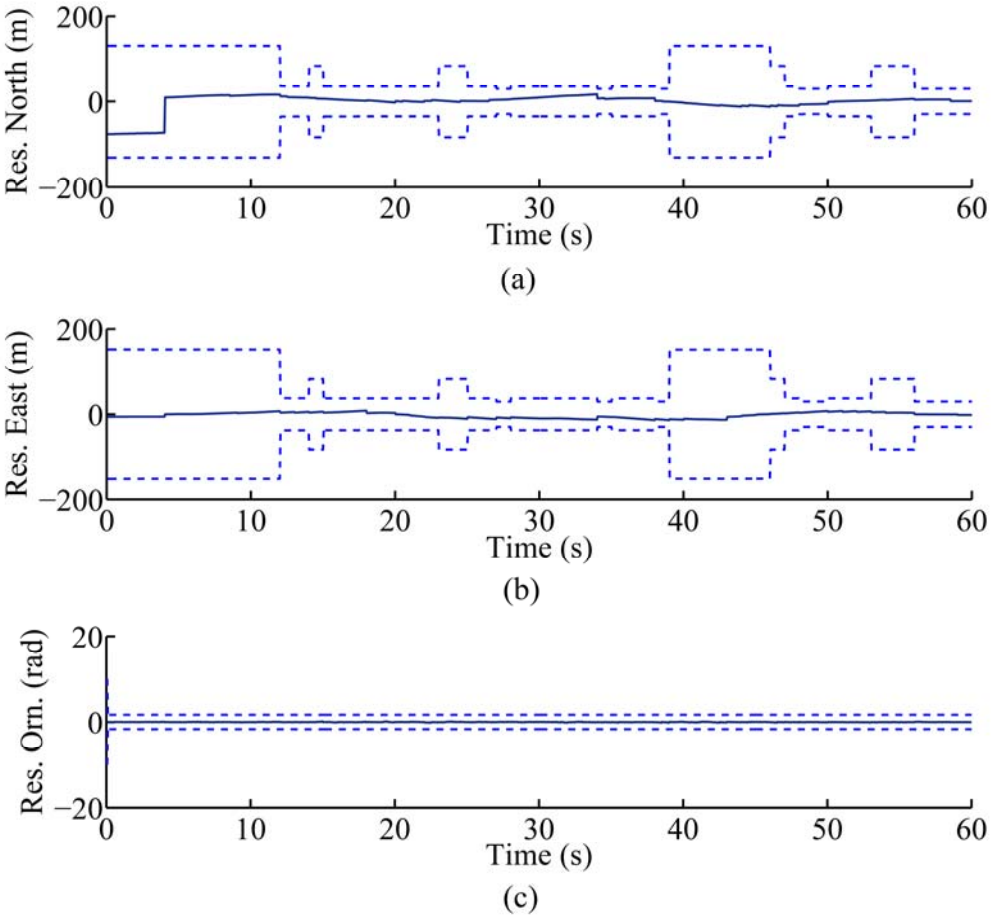

Figure A.35 The Residual Plots of North (a), East (b), and Orientation (c) for Run Twelve: The residuals, marked as solid lines, are within their ±2σ bounds (95% confidence bounds), marked as dashed lines.

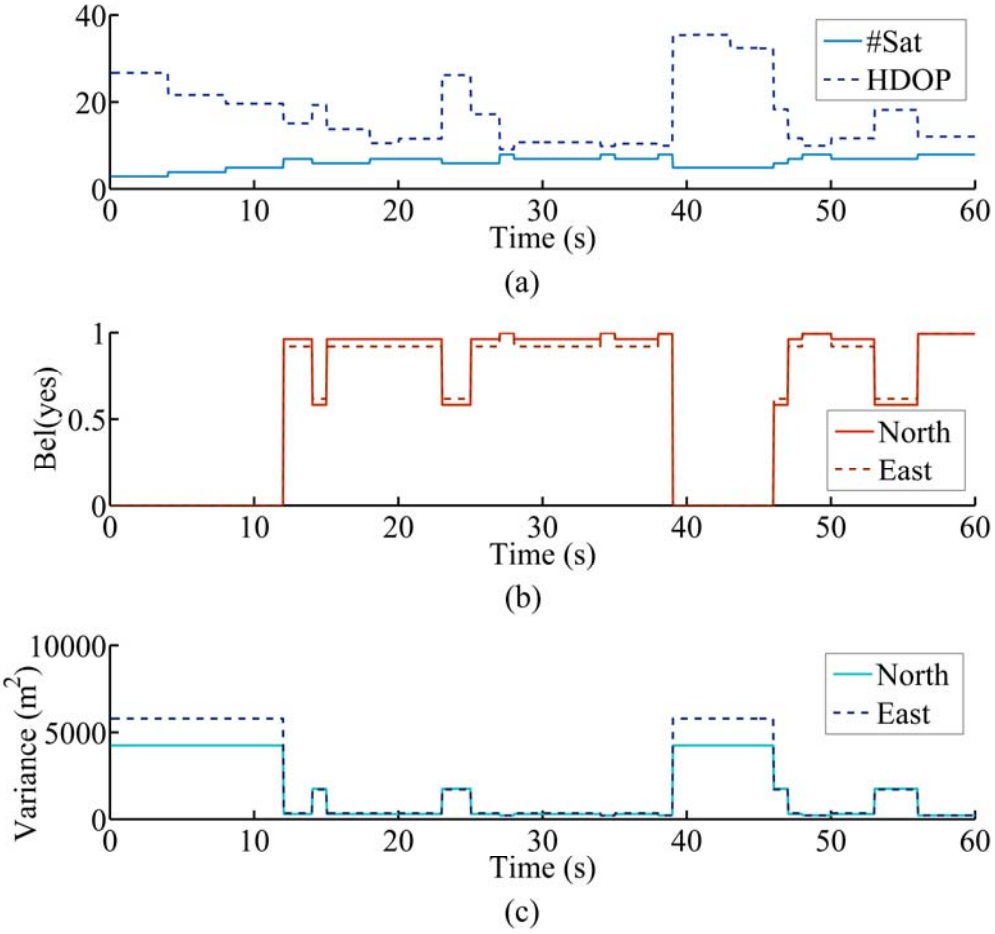

Figure A.36 GPS Sensor Goodness Plots for Run Twelve: An increase in HDOP and a decrease in #Sat (a) lead to a decrease in the belief value for *yes* (the GPS is good) (b) and an increase in the north (*xx*) and the east (*yy*) components of the measurement error covariance matrix **R** (c).

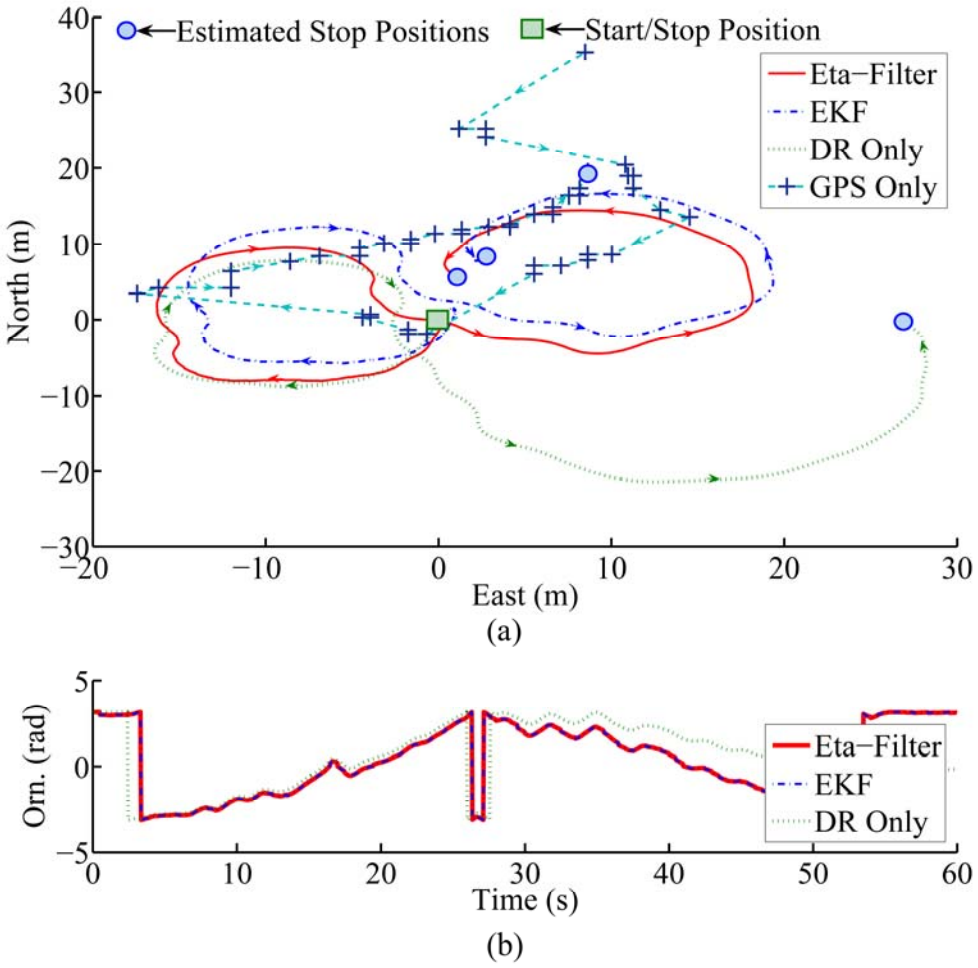

Figure A.37 The Path (a) and Orientation (b) Plots for Run Thirteen in the "normal" Scenario: There is no significant difference between the $\boldsymbol{\eta}$-Filter and the EKF.

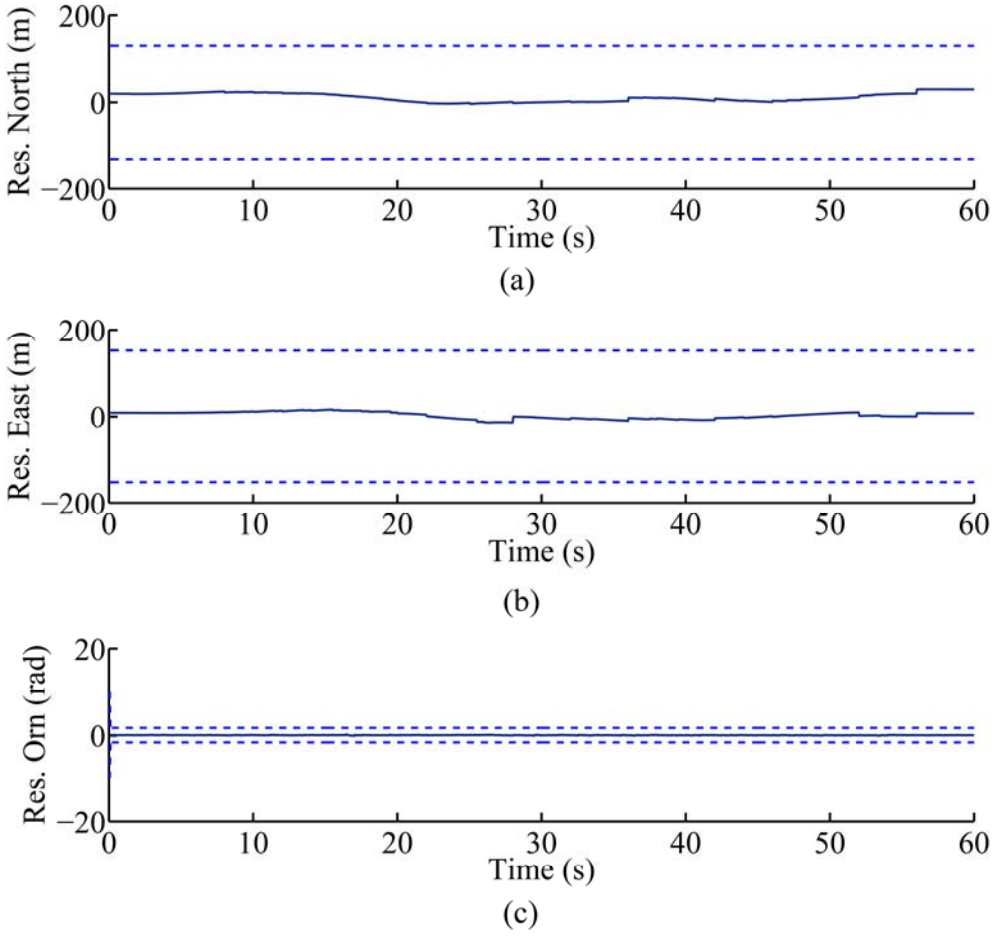

Figure A.38 The Residual Plots of North (a), East (b), and Orientation (c) for Run Thirteen: The residuals, marked as solid lines, are within their ±2σ bounds (95% confidence bounds), marked as dashed lines.

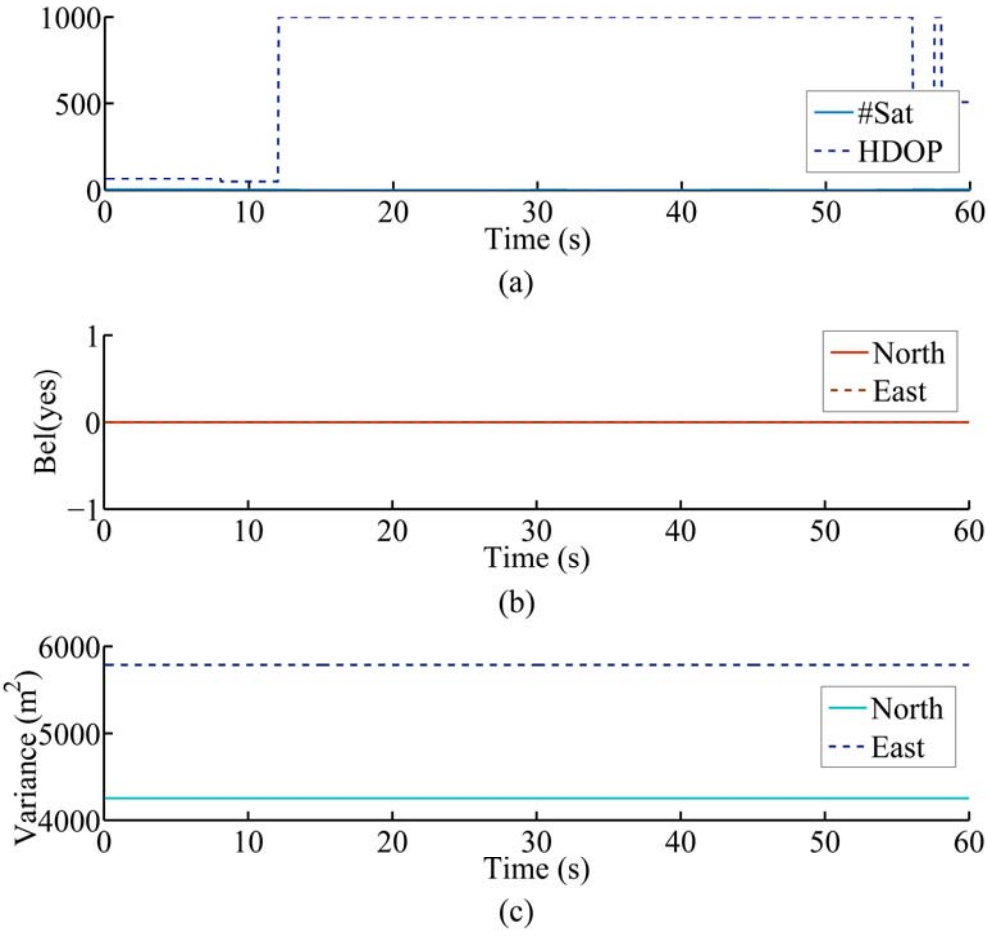

Figure A.39 GPS Sensor Goodness Plots for Run Thirteen: An increase in HDOP and a decrease in #Sat (a) lead to a decrease in the belief value for *yes* (the GPS is good) (b) and an increase in the north (*xx*) and the east (*yy*) components of the measurement error covariance matrix **R** (c).

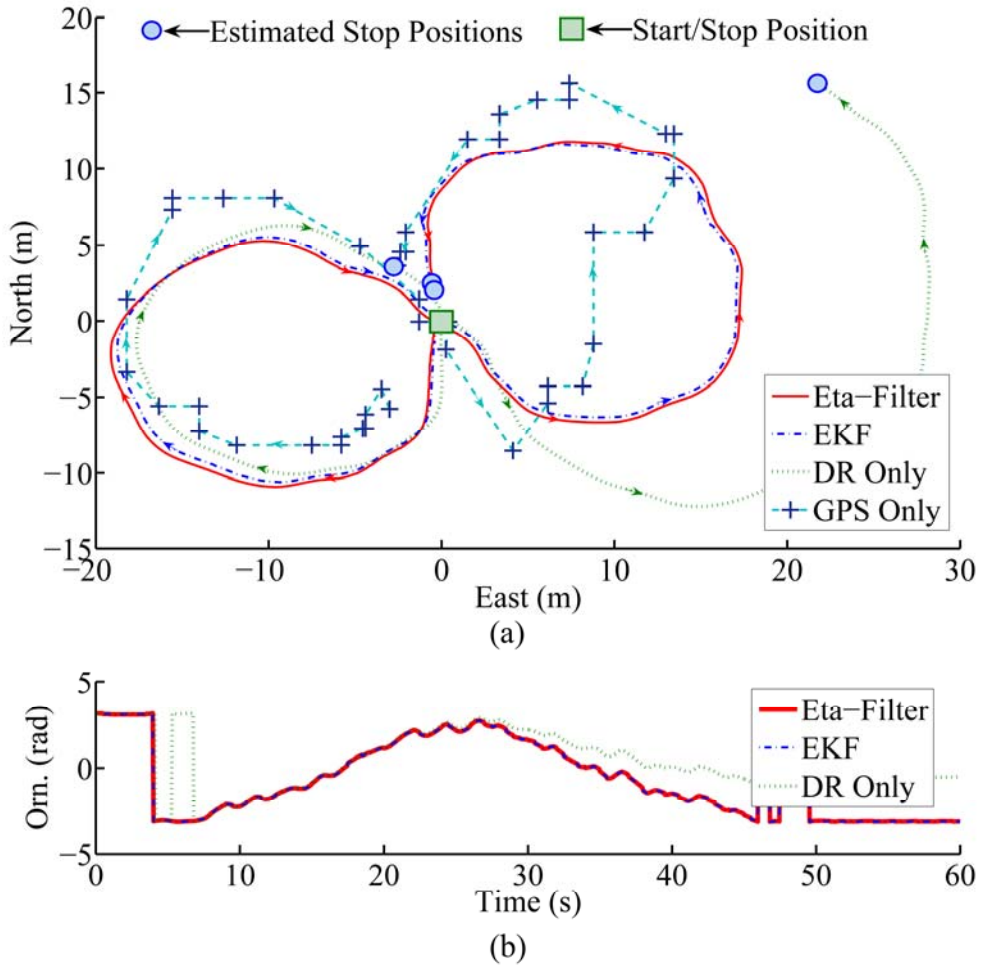

Figure A.40 The Path (a) and Orientation (b) Plots for Run Fourteen in the "normal" Scenario: There is no significant difference between the $\boldsymbol{\eta}$-Filter and the EKF.

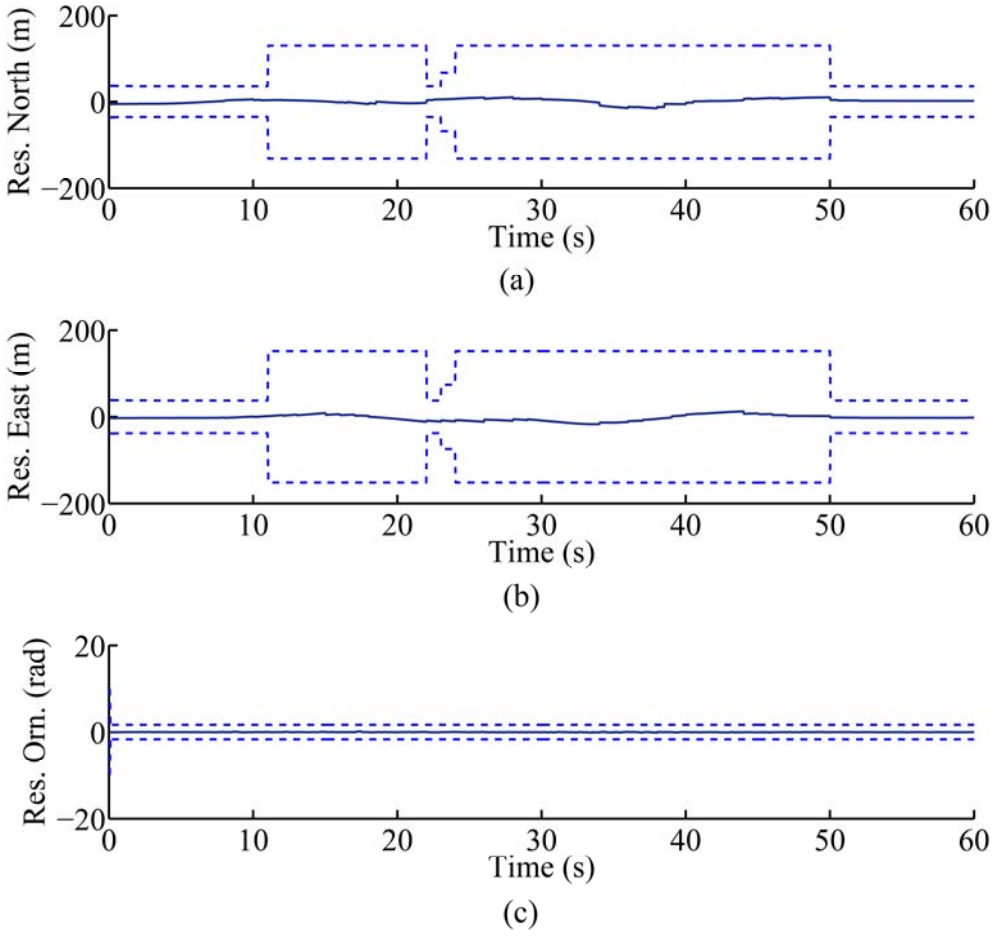

Figure A.41 The Residual Plots of North (a), East (b), and Orientation (c) for Run Fourteen: The residuals, marked as solid lines, are within their ±2σ bounds (95% confidence bounds), marked as dashed lines.

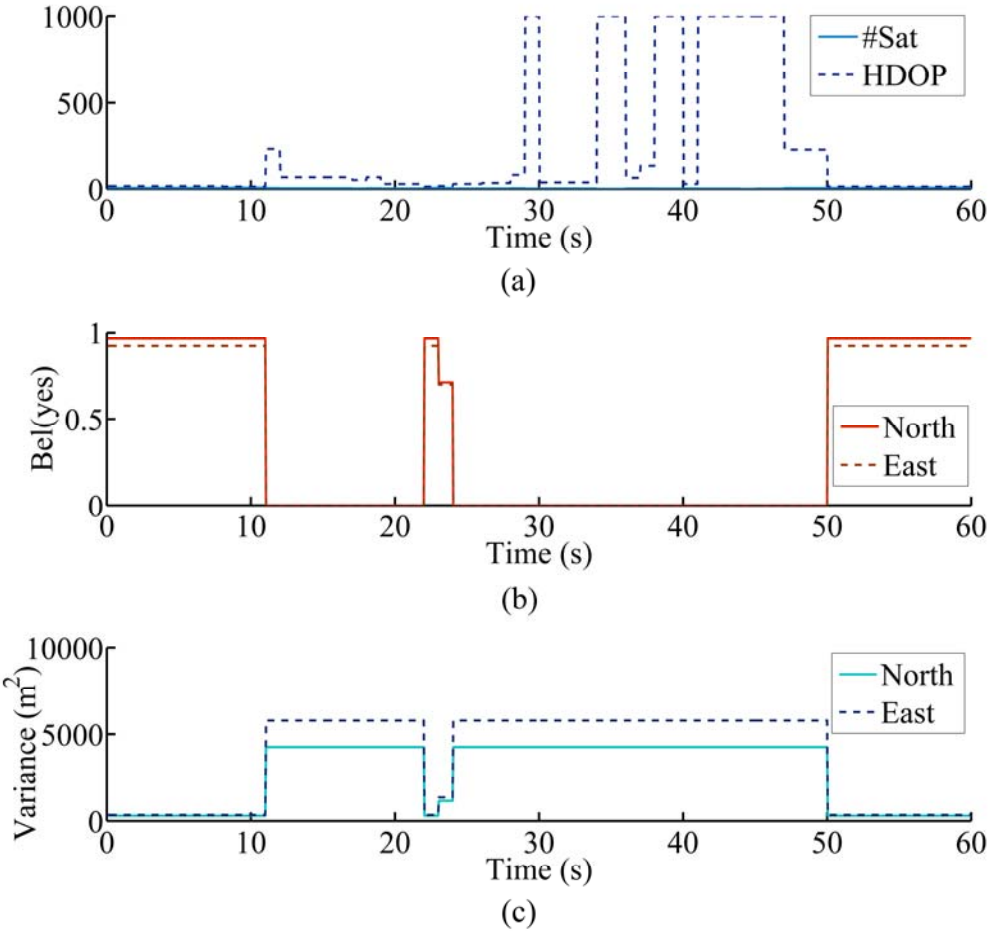

Figure A.42 GPS Sensor Goodness Plots for Run Fourteen: An increase in HDOP and a decrease in #Sat (a) lead to a decrease in the belief value for *yes* (the GPS is good) (b) and an increase in the north (*xx*) and the east (*yy*) components of the measurement error covariance matrix **R** (c).

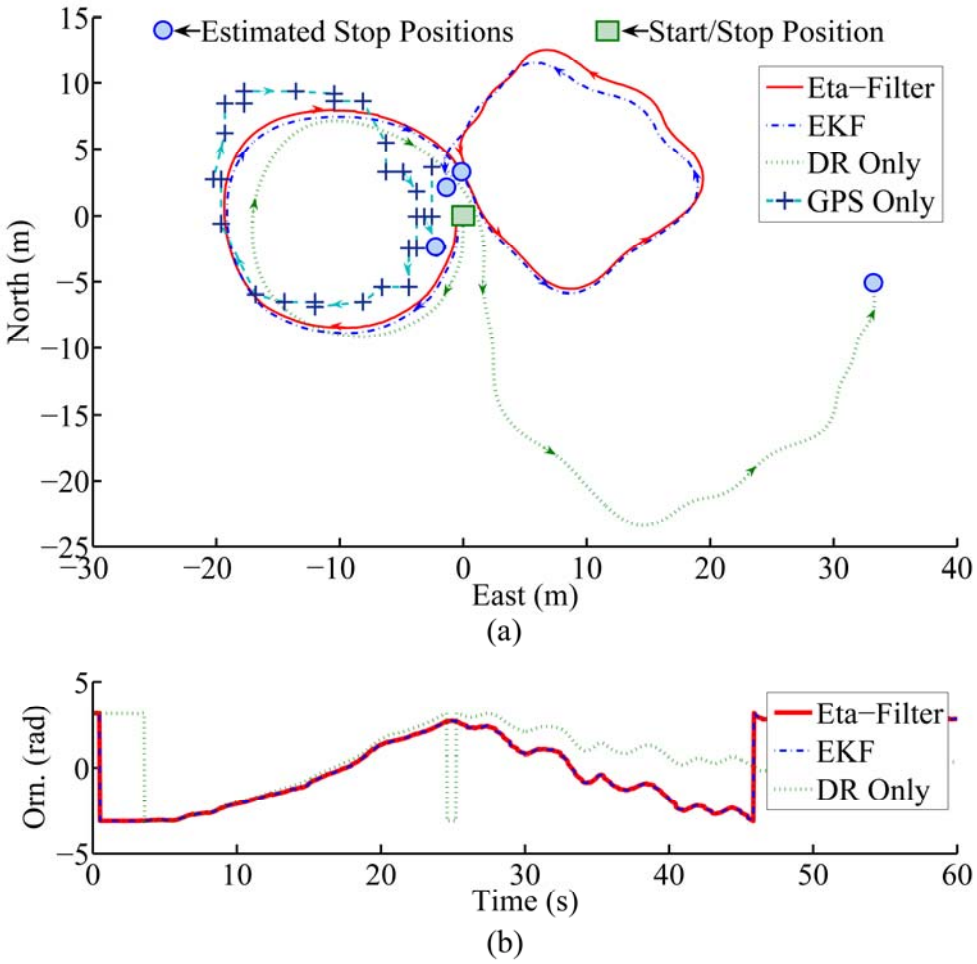

Figure A.43 The Path (a) and Orientation (b) Plots for Run Fifteen in the "normal" Scenario: There is no significant difference between the $\boldsymbol{\eta}$-Filter and the EKF.

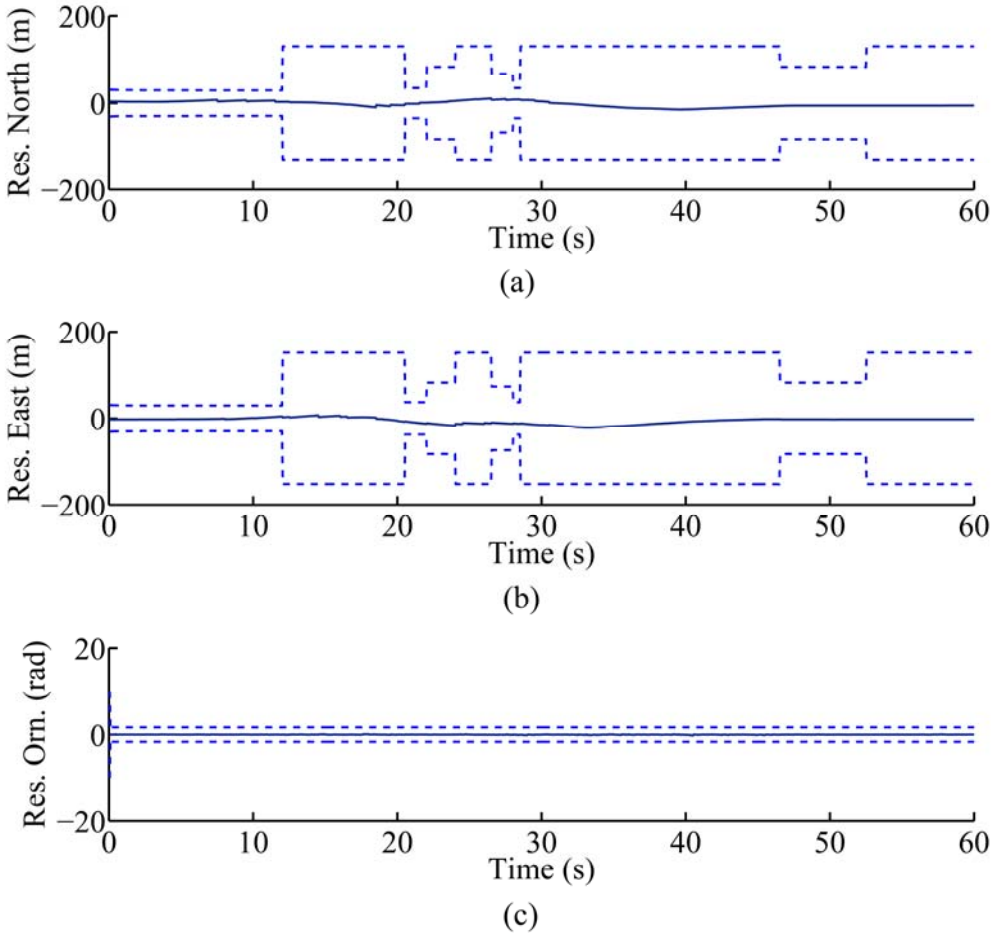

Figure A.44 The Residual Plots of North (a), East (b), and Orientation (c) for Run Fifteen: The residuals, marked as solid lines, are within their ±2σ bounds (95% confidence bounds), marked as dashed lines.

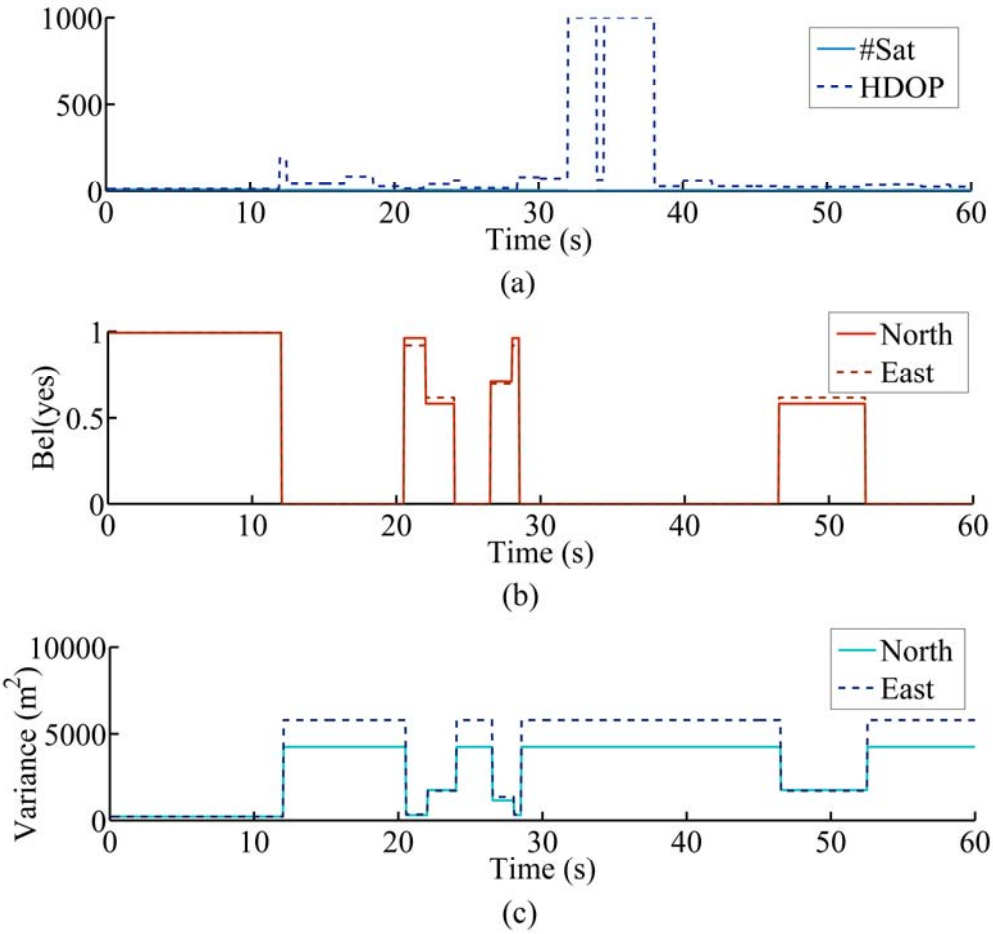

Figure A.45 GPS Sensor Goodness Plots for Run Fifteen: An increase in HDOP and a decrease in #Sat (a) lead to a decrease in the belief value for *yes* (the GPS is good) (b) and an increase in the north (*xx*) and the east (*yy*) components of the measurement error covariance matrix **R** (c).

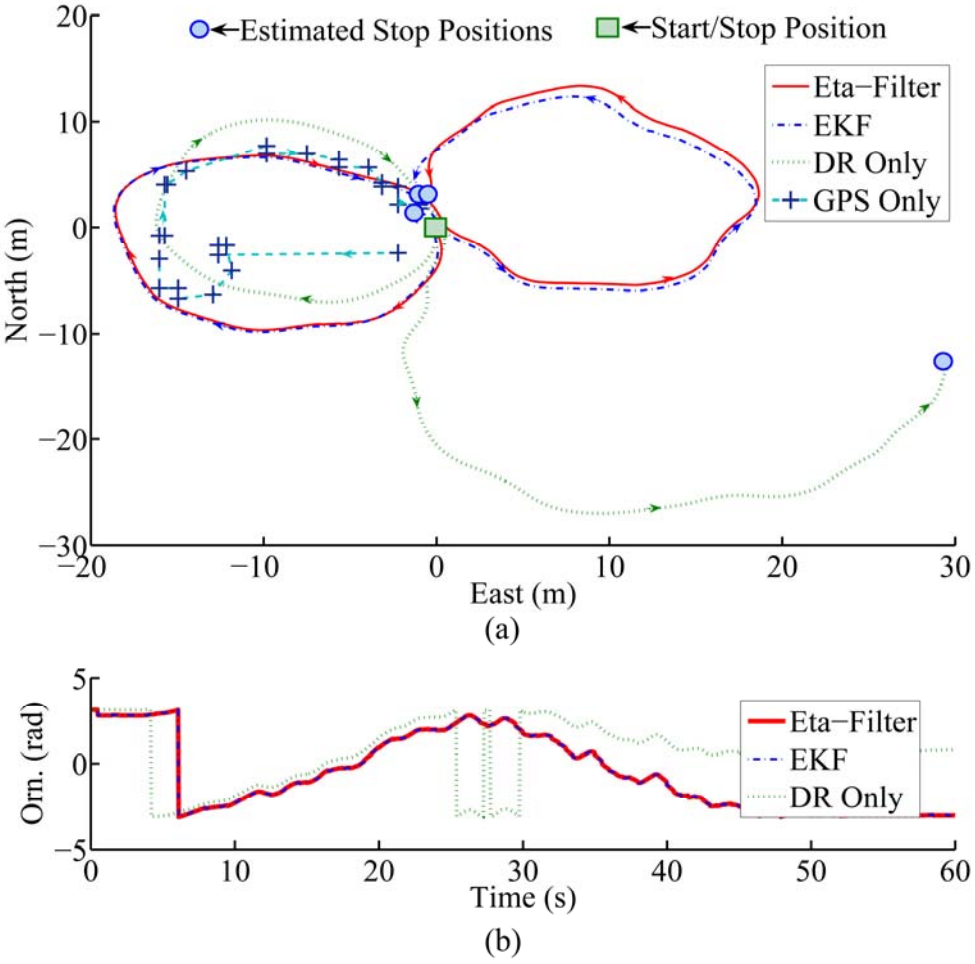

Figure A.46 The Path (a) and Orientation (b) Plots for Run Sixteen in the "normal" Scenario: There are no GPS measurements during the second half of the run. Figure A.48 shows belief values. There is no significant difference between the $\boldsymbol{\eta}$-Filter and the EKF.

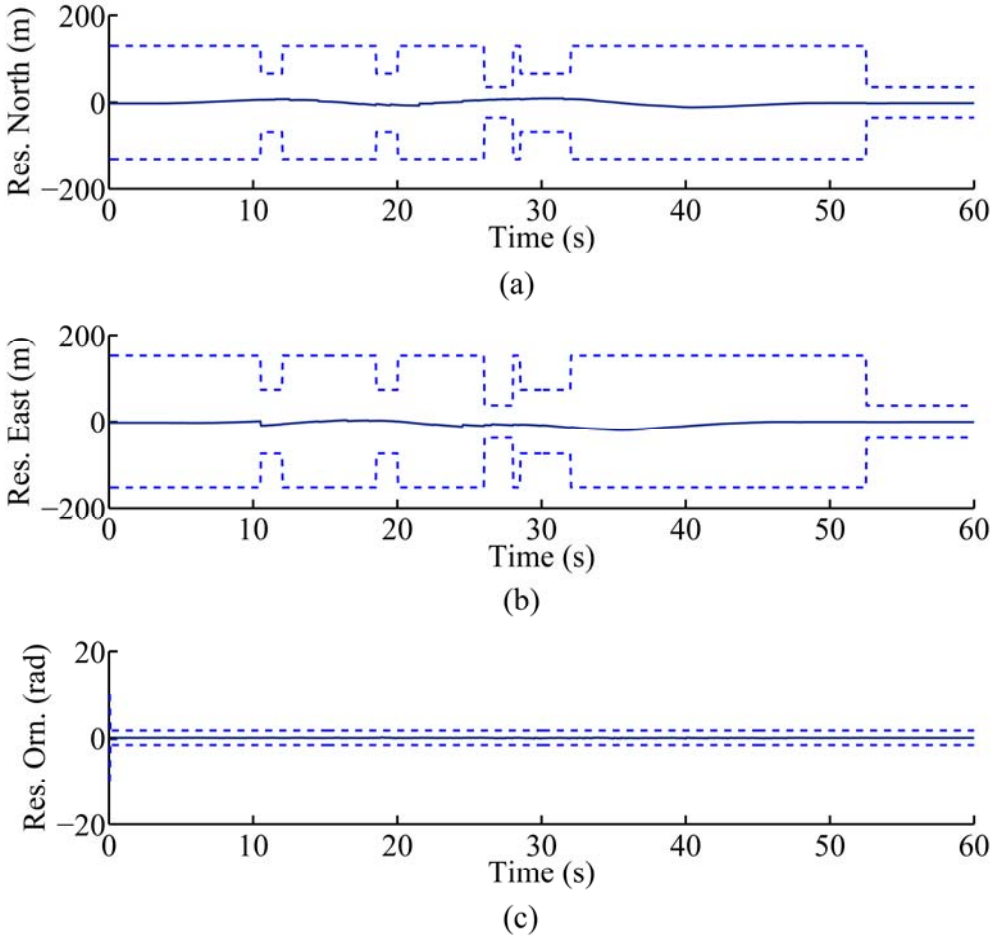

Figure A.47 The Residual Plots of North (a), East (b), and Orientation (c) for Run Sixteen: The residuals, marked as solid lines, are within their ±2σ bounds (95% confidence bounds), marked as dashed lines.

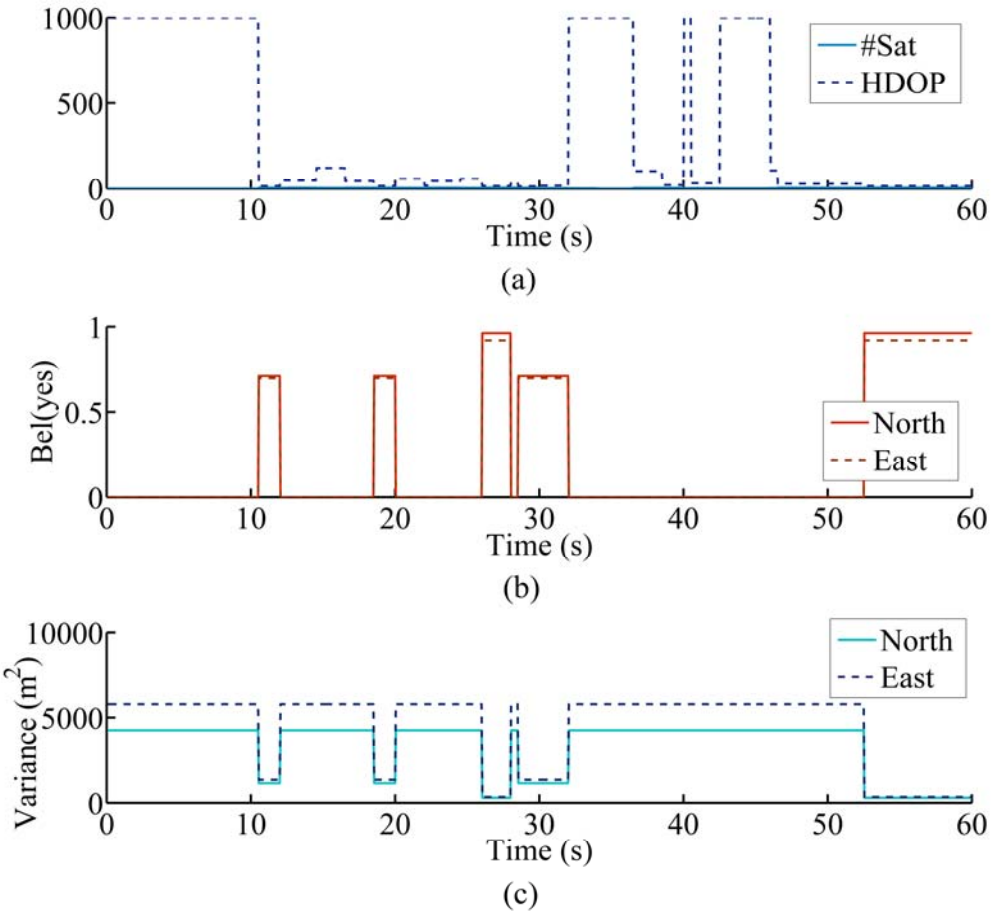

Figure A.48 GPS Sensor Goodness Plots for Run Sixteen: An increase in HDOP and a decrease in #Sat (a) lead to a decrease in the belief value for *yes* (the GPS is good) (b) and an increase in the north (*xx*) and the east (*yy*) components of the measurement error covariance matrix **R** (c).

APPENDIX B

DESIGNED EXPERIMENT FOR η-FILTER

B.1 OVERVIEW

A designed experiment was conducted to determine the effects of *filter* and *location* on the final position errors. A 2x2 balanced complete factorial experiment was conducted with the following hypotheses:

H_0: The mean final position errors are same. (B.1)

H_1: the mean final position errors are different. (B.2)

Here, H_0 and H_1 are the null hypothesis and alternate hypothesis respectively. The response variable is the final position error in meters. There are two factors of interest. Factor A is "*filter*" with levels 1 = $\boldsymbol{\eta}$-Filter and 2 = EKF. Factor B is "*location*" with levels 1 = L1 and 2 = L2. Locations L1 and L2 are defined in Section 3.4.1. Eight repetitions were performed. The goal was to determine whether the final position error depended on the filter used for estimation and also to see if there was a variation due to change in location. The data collection procedure and the method for computing the final position errors in meters are described in Section 3.4.2. Table B.1 shows the Treatment Combinations (TCs) for each level of the two factors.

Based on the box-plots shown in Figure B.1, location L2 appears to have a lower mean final error when compared to location L1. There does not seem to be any major difference in mean final error between the $\boldsymbol{\eta}$-Filter and the EKF. The significance of the differences in mean final error in position was tested by using ANOVA.

SS is the Sum of Squares, DF is the Degrees of Freedom, Pr is the Probability, Coeff. Var. is the Coefficient of Variation, r is the number of repetitions, n is sample size, a is the number of Factor-A levels, b is the number of Factor B levels, and $v = ab$.

Table B.1 *Filter-Location* Treatment Combinations

TC	*Filter*	*Location*
1	$\boldsymbol{\eta}$-Filter	L1
2	$\boldsymbol{\eta}$-Filter	L2
3	EKF	L1
4	EKF	L2

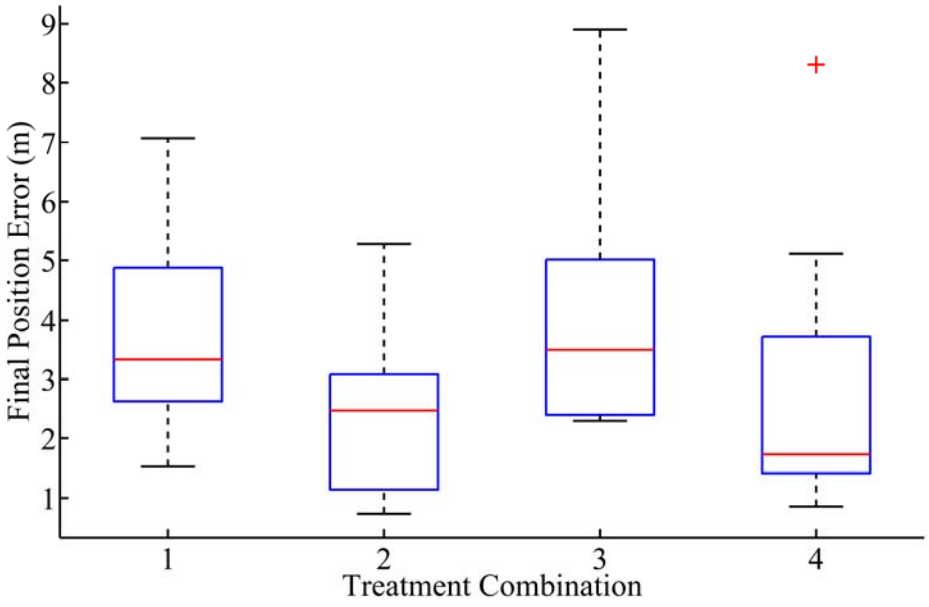

Figure B.1 Box-Plot of Final Position Errors: Location L2 (2, 4) appears to have a lower mean final position error than location L1 (1, 3). There is only a minor difference between the $\boldsymbol{\eta}$-Filter (1, 2) and the EKF (3, 4). Also, the presence of an outlier is indicated by the plus sign.

Table B.2 Mean Position Errors for Treatments

Filter (*i*)	*Location* (*j*)		Mean (*i*)
	j = 1	*j* = 2	
i = 1	3.783033	2.423602	3.493182
i = 2	4.126047	2.860318	3.103318
Mean (*j*)	3.95454	2.64196	3.29825

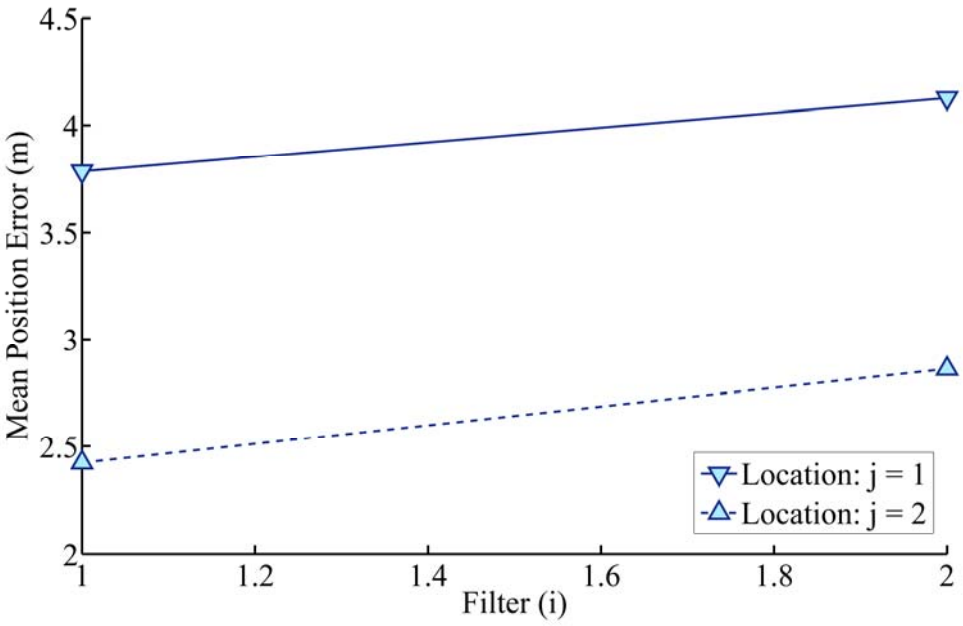

Figure B.2 The *Filter-Location* Interaction Plot: The lines are parallel. This indicates that there is no interaction between *filter* and *location*, *i.e.*, the difference in means between the two locations is the same for the two filters.

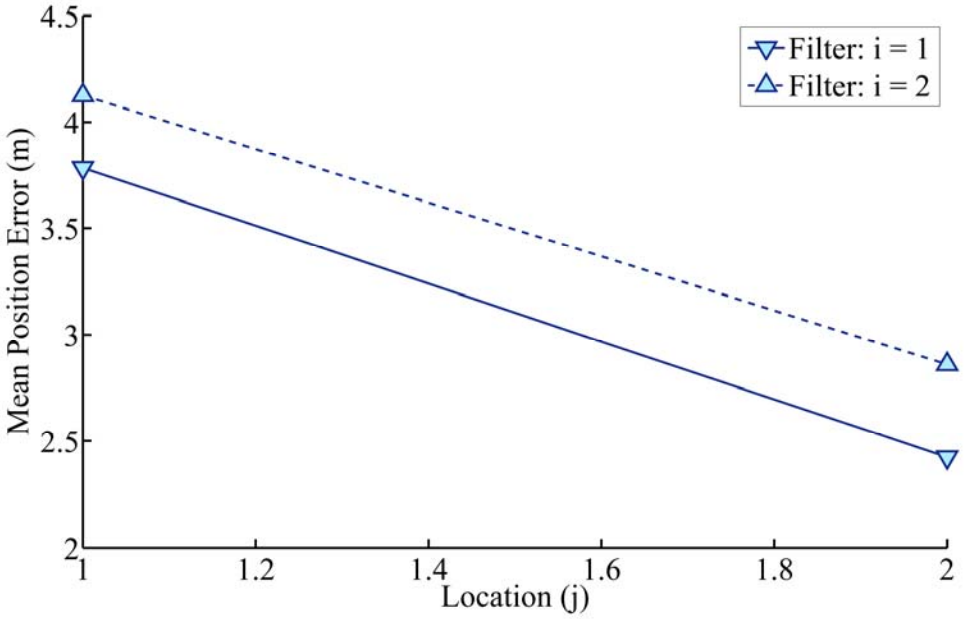

Figure B.3 The *Location-Filter* Interaction Plot: The lines are parallel. This indicates that there is no interaction between *filter* and *location*, *i.e.*, the difference in means between the two filters is the same for the two locations.

As the lines in Figures B.2 and B.3 are distinct, there appear to be main *filter* effects and main *location* effects. However, the lines are parallel. This indicates that there is no interaction between *filter* and *location*.

The appropriate two-way complete model for this experiment is as follows:

$$Y_{ijt} = \mu_{...} + \alpha_i + \beta_j + \in_{ijt}, \tag{B.3}$$

where $\in_{ijt}$ is the random error with $\in_{ijt} \sim N(0, \sigma^2)$ and $\in_{ijt}$'s mutually independent, i = 1, 2, j = 1, 2, t = 1, 2, 3, 4, 5, 6, 7, 8, $\mu_{...}$ is the overall mean, α_i is the effect of *filter* = i, β_j is the effect of *location* = j, and Y_{ijt} is the random variable representing the position error for repetition = t, *filter* = i, and *location* = j.

The main effects are estimated using information from Table B.2 as follows.

Main *filter* effects:

$$\alpha_1 = \overline{Y}_{1\bullet\bullet} - \overline{Y}_{\bullet\bullet\bullet} = 3.493182 - 3.29825 = 0.194932. \quad \text{(B.4)}$$

$$\alpha_2 = \overline{Y}_{2\bullet\bullet} - \overline{Y}_{\bullet\bullet\bullet} = 3.103318 - 3.29825 = -0.194932. \quad \text{(B.5)}$$

Main *location* effects:

$$\beta_1 = \overline{Y}_{\bullet 1\bullet} - \overline{Y}_{\bullet\bullet\bullet} = 3.95454 - 3.29825 = 0.65629. \quad \text{(B.6)}$$

$$\beta_2 = \overline{Y}_{\bullet 2\bullet} - \overline{Y}_{\bullet\bullet\bullet} = 2.64196 - 3.29825 = -0.65629. \quad \text{(B.7)}$$

B.2 RESULTS OF ANOVA

Table B.3 presents the ANOVA results. F-Tests for main effects are performed as follows.

For the main effect *filter*, the following hypotheses are considered:

$$H_0^{filter}: \text{Main effect } \textit{filter} \text{ is negligible} \leftrightarrow H_0^{filter}: \alpha_i = 0 \; \forall \, i. \quad \text{(B.8)}$$

$$H_1^{filter}: \text{Main effect } \textit{filter} \text{ is not negligible} \leftrightarrow H_1^{filter}: \text{Not all } \alpha_i = 0. \quad \text{(B.9)}$$

For a significance level of $\alpha = 0.05$, the decision rule is to reject H_0^{filter} if $p < 0.05$. Since $p = 0.5949$ from Table B.3, H_0^{filter} is not rejected. This implies that the main effect for *filter* is negligible, at the 5% significance level.

Table B.3 The ANOVA Results for the No-Interaction Model.

Source	DF	Sum of Squares	Mean Square	F-Value	Pr > F (*p*-value)
Model	2	14.99	7.49	1.78	0.1861
Error	29	121.99	4.21		
Corrected Total	31	136.99			
R-Square		Coeff. Var.		Root MSE	Position Error Mean
0.11		62.19		2.05	3.29
Source	DF	Type III SS	Mean Square	F-Value	Pr > F (*p*-value)
Filter	1	1.22	1.22	0.29	0.5949
Location	1	13.78	13.78	3.28	0.0807

For the main effect *location* the following hypotheses are considered:

$$H_0^{location}: \text{Main effect } location \text{ is negligible} \leftrightarrow H_0^{location}: \beta_j = 0 \,\forall\, j. \qquad \text{(B.10)}$$

$$H_1^{location}: \text{Main effect } location \text{ is not negligible} \leftrightarrow H_1^{location}: \text{Not all } \beta_j = 0\ . \quad \text{(B.11)}$$

For a significance level of $\alpha = 0.05$, the decision rule is to reject $H_0^{location}$ if $p < 0.05$. Since $p = 0.0807$ from Table B.3, $H_0^{location}$ is not rejected. This implies that the main effect for *location* is negligible, at the 5% significance level.

However, the mean final position errors are as follows: 3.10 m (***η***-Filter) and 3.49 m (EKF). The ***η***-Filter shows a 11.17% improvement over the EKF with respect to the mean final position error.

B.3 CHECKING MODEL ASSUMPTIONS

A modified *Levene's* test is performed for checking the equality of error variances. The following hypotheses are considered:

$$H_0 : \sigma_1^2 = \sigma_2^2 = ... = \sigma_4^2 . \quad \text{(B.12)}$$

$$H_1 : \text{Not all } \sigma_i^2\text{'s are same, } i = 1,\ldots, 4. \quad \text{(B.13)}$$

For a significance level of $\alpha = 0.05$, the decision rule is to reject H_0 if $p < 0.05$. Since $p = 0.8443$ from Table B.4, H_0 is not rejected. This implies that the constant error variance assumption is valid in this case, at the 5% significance level. Also, Figures B.4 and B.5 indicate that there is no major difference in error variances for the eight treatment combinations.

Table B.4 The ANOVA Results for the Modified Levene's Test.

Source	DF	Sum of Squares	Mean Square	F-Value	Pr > F (*p*-value)
Model	3	2.13	0.7095	0.27	0.8443
Error	28	72.76	2.5987		
Corrected Total	31	74.89			
R-Square		Coeff. Var.		Root MSE	Deviation from Medians Mean
0.03		115.63		1.61	1.39
Source	DF	ANOVA SS	Mean Square	F-Value	Pr > F (*p*-value)
TC	3	2.13	0.7095	0.27	0.8443

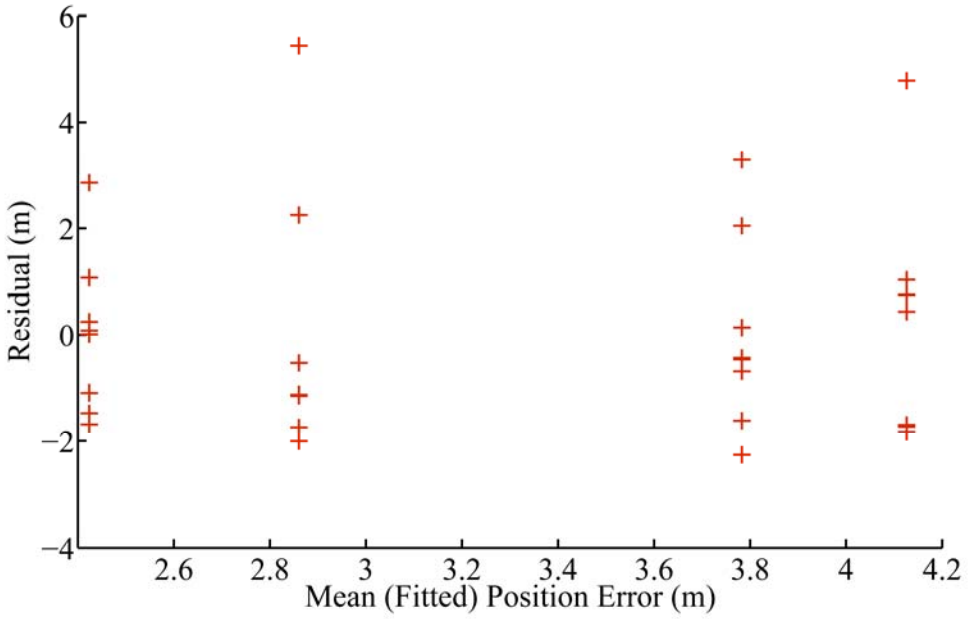

Figure B.4 The Residual as a Function of the Mean Position Error: There is no major difference in the variation of the residual.

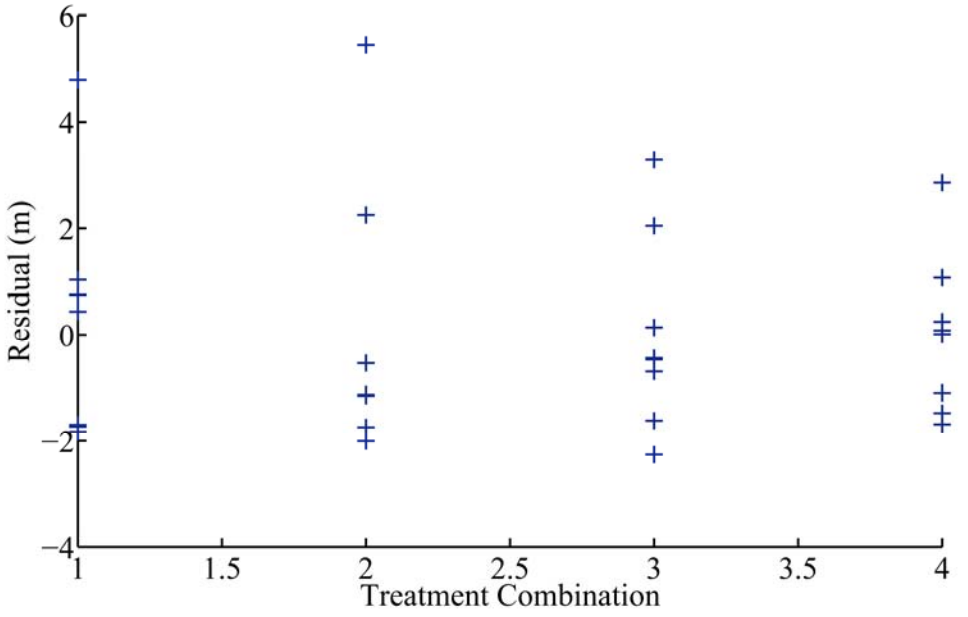

Figure B.5 The Residual as a Function of the Treatment Combination: There is no major difference in the variation of the residual.

The normality assumption is tested by checking for linearity of the normal probability plot (Figure B.6). The following hypotheses are considered:

$$H_0 : \text{Normality assumption is valid.} \tag{B.14}$$

$$H_1 : \text{Normality assumption is violated.} \tag{B.15}$$

For a significance level of $\alpha = 0.10$, the *Pearson's* correlation coefficient, $\hat{\rho} = 0.93288$. Critical value, C (0.10, 32) = 0.972 (From Table 1 in [Fil75]). Since $\hat{\rho} <$ critical value ($\alpha = 0.10$, $n = 32$), H_0 is rejected at the 10% significance level. So, it is concluded, at the 10% significance level, that there is a deviation from normality.

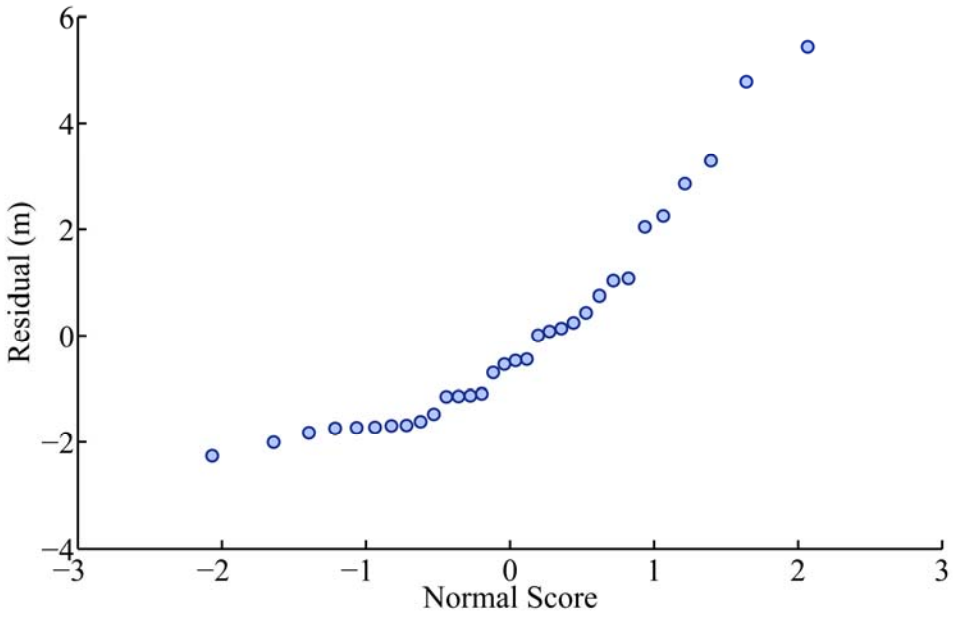

Figure B.6 Normal Probability Plot: There is lack of linearity. This indicates that the normality assumption is violated.

Outliers are detected using the *Bonferroni* outlier test. The following hypotheses are considered:

$$H_0 : \text{Observation is not an outlier.} \tag{B.16}$$

$$H_1 : \text{Observation is an outlier.} \tag{B.17}$$

For a significance level of $\alpha = 0.05$, the decision rule is to reject H_0, when $|t_{ij}| > t_{n-v-1,\alpha/2n} = t_{abr-ab-1,\alpha/2abr} = t_{27,0.00625} = 2.67626$. t_{ij} is the studentized deleted residual. Since $|t_{ij}| > 2.67626$ for observations 21 and 28, we reject H_0 for those observations, at the 5% significance level. So, observations 21 and 28 are outliers (Figure B.7).

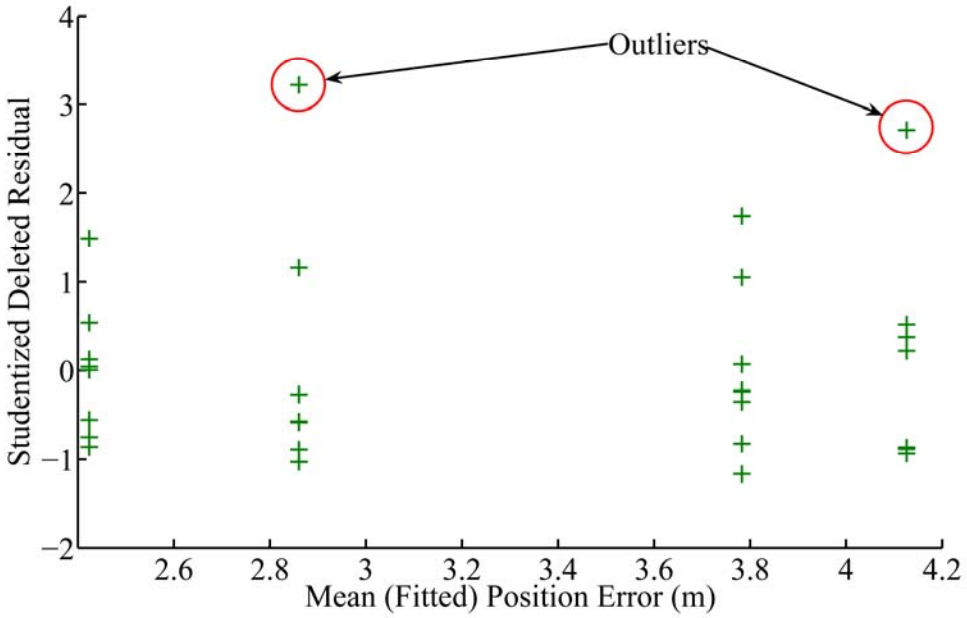

Figure B.7 Studentized Deleted Residuals as a Function of the Mean Position Error: There are two outliers, *i.e.*, observations corresponding to $|t_{ij}| > 2.67626$.

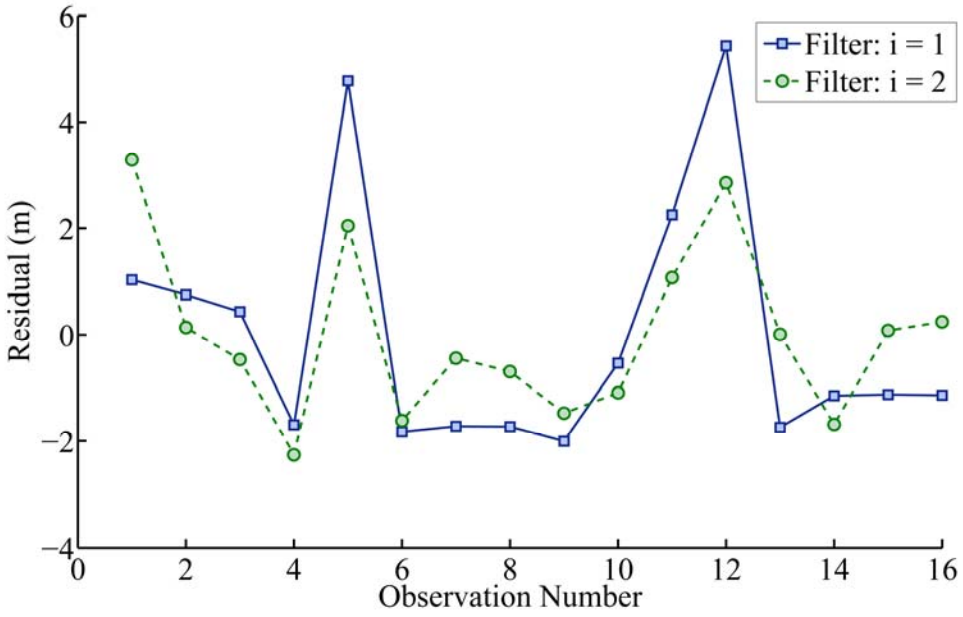

Figure B.8 Serial Correlation Plot: There is no strong pattern or trend, *i.e.*, there is no serial correlation of errors.

The power of detecting a difference is computed as follows [Che05]. Let Δ be the difference in position error that is to be detected, *i.e.*, the power of the test is the power to detect Δ due to factor effects. Let Δ = 1 m. Here, $r = 8$, $n = 32$, $v = ab = 4$, and MSE = 4.21 (from Table B.2).

$$\text{Treatment degrees of freedom} = \upsilon_1 = v - 1 = 4 - 1 = 3. \tag{B.18}$$

$$\text{Error degrees of freedom} = \upsilon_2 = n - v = 32 - 8 = 24. \tag{B.19}$$

$$\varphi^2 = \frac{r\Delta^2}{2v\sigma^2} \Rightarrow \varphi = \sqrt{\frac{r\Delta^2}{2v\sigma^2}} = 0.4873702. \tag{B.20}$$

Using *SAS*^{TM}, the power of the test = P [Rejecting H_0 | H_0 is false] = $1 - \beta = 0.10232$.

APPENDIX C

DESIGNED EXPERIMENT FOR CL

C.1 OVERVIEW

A designed experiment was conducted to determine the effects of *CL* and *UGV* on the final position errors. A 2x4 balanced complete factorial experiment was conducted with the following hypotheses:

H_0: The mean final position errors for CL and non-CL are same. (C.1)

H_1: The mean final position errors for CL and non-CL are different. (C.2)

The response variable is the final position error in meters. There are two factors of interest. Factor A is "*CL*" with levels 1 = CL system and 2 = non-CL system. Factor B is "*UGV*" with levels 1 = UGV-1, 2 = UGV-2, 3 = UGV-3, and 4 = UGV-4. Five repetitions were performed. Figure 4.7 in Chapter 4 shows the formation of UGV-1, UGV-2, UGV-3, and UGV-4. The goal was to determine whether the final position error depended on the localization system used (CL or non-CL) and also to see if there was a variation between the four UGVs. The data collection procedure and the method for computing the final position errors in meters are described in Section 4.4. Table C.1 shows the Treatment Combinations (TCs) for each level of the two factors.

Based on the box-plots shown in Figure C.1, the CL system appears to have a lower mean final position error than the non-CL system. Also, there is a variation in the mean final position error between *UGV* levels. The significance of the difference in the mean final position error was tested using ANOVA.

Table C.1 *CL-UGV* Treatment Combinations

TC	*CL*	*UGV*
1	CL system	UGV-1
2	CL system	UGV-2
3	CL system	UGV-3
4	CL system	UGV-4
5	Non-CL system	UGV-1
6	Non-CL system	UGV-2
7	Non-CL system	UGV-3
8	Non-CL system	UGV-4

Table C.2 Mean Position Errors for Treatments

CL (*i*)	*UGV* (*j*)				Mean (*i*)
	j = 1	*j* = 2	*j* = 3	*j* = 4	
i = 1	1.735380	0.601754	1.191490	3.39818	1.731701
i = 2	2.219516	1.115388	2.244080	5.99730	2.894071
Mean (*j*)	1.977448	0.858571	1.717785	4.69774	2.312886

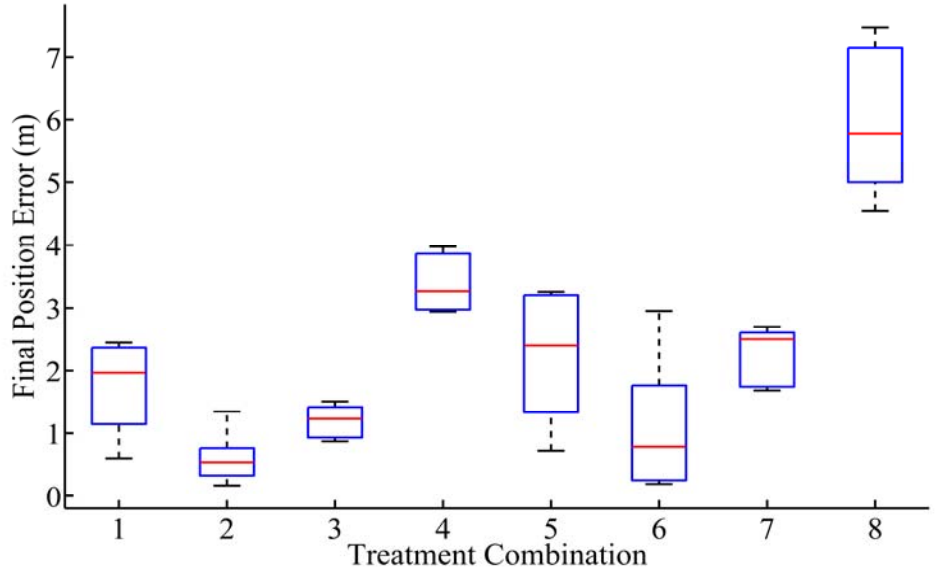

Figure C.1 Box-Plot of Final Position Errors: *CL* = 1 (1, 2, 3, 4) appears to have a lower mean final position error than *CL* = 2 (5, 6, 7, 8). Also, there are differences between *UGV* levels.

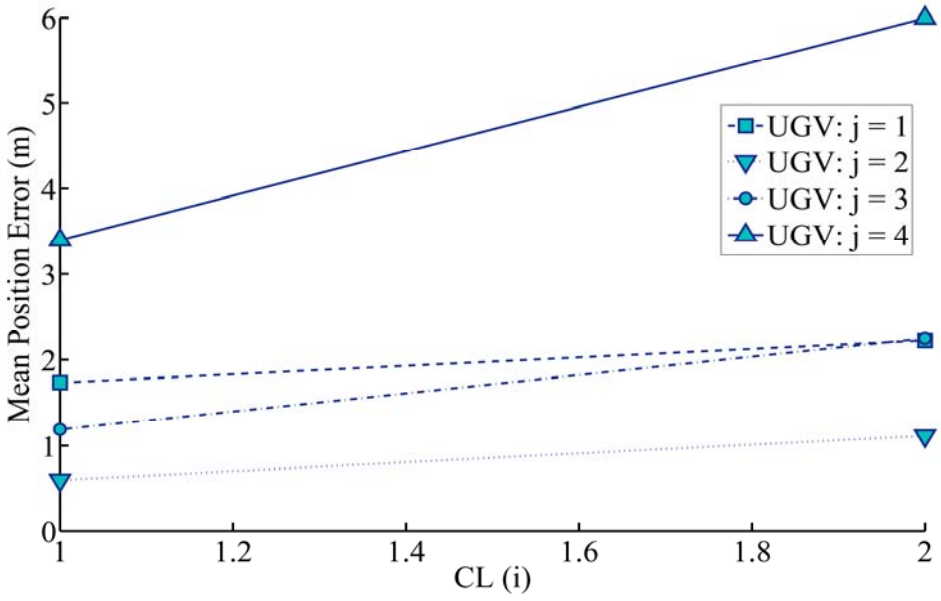

Figure C.2 The *CL*-*UGV* Interaction Plot: The lines are not parallel. This indicates that there may be an interaction between *CL* and *UGV*, *i.e.*, the difference in means between {UGV-1, UGV-2} and {UGV-3, UGV-4} is different for CL and non-CL.

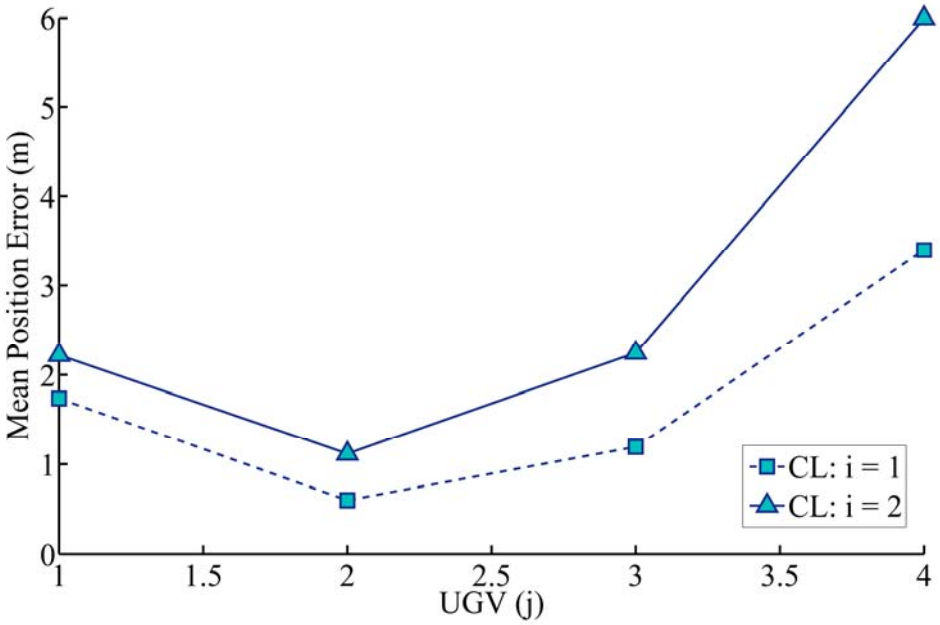

Figure C.3 The *UGV-CL* Interaction Plot: The lines are not parallel. This indicates that there may be an interaction between *UGV* and *CL*, *i.e.*, the difference in means between CL and non-CL is not the same for {UGV-1, UGV-2} and {UGV-3, UGV-4}.

As the lines in Figures C.2 and C.3 are distinct, there are main *CL* effects and main *UGV* effects. The lines are not parallel. This indicates that there may be interactions. So, a full-interaction model is used to test the interaction effect.

The appropriate two-way complete model for this experiment is as follows:

$$Y_{ijt} = \mu_{...} + \alpha_i + \beta_j + (\alpha\beta)_{ij} + \in_{ijt}, \tag{C.3}$$

where $\in_{ijt}$ is the random error with $\in_{ijt} \sim N(0, \sigma^2)$ and $\in_{ijt}$'s mutually independent, i = 1, 2, j = 1, 2, 3, 4, t = 1, 2, 3, 4, 5, $\mu_{...}$ is the overall mean, α_i is the effect of the $CL = i$, β_j is the effect of $UGV = j$, $(\alpha\beta)_{ij}$ is the interaction effect of $CL = i$ and $UGV = j$, and

Y_{ijt} is the random variable representing the position error for repetition = *t*, *CL* = *i*, and *UGV* = *j*.

The main and interaction effects are estimated using information from Table C.2 as follows.

Main *CL* effects:

$$\alpha_1 = \overline{Y}_{1\bullet\bullet} - \overline{Y}_{\bullet\bullet\bullet} = 1.731701 - 2.312886 = -0.581185. \quad \text{(C.4)}$$

$$\alpha_2 = \overline{Y}_{2\bullet\bullet} - \overline{Y}_{\bullet\bullet\bullet} = 2.894071 - 2.312886 = 0.581185. \quad \text{(C.5)}$$

Main *UGV* effects:

$$\beta_1 = \overline{Y}_{\bullet 1\bullet} - \overline{Y}_{\bullet\bullet\bullet} = 1.977448 - 2.312886 = -0.335438. \quad \text{(C.6)}$$

$$\beta_2 = \overline{Y}_{\bullet 2\bullet} - \overline{Y}_{\bullet\bullet\bullet} = 0.858571 - 2.312886 = -1.454315. \quad \text{(C.7)}$$

$$\beta_3 = \overline{Y}_{\bullet 3\bullet} - \overline{Y}_{\bullet\bullet\bullet} = 1.717785 - 2.312886 = -0.595101. \quad \text{(C.8)}$$

$$\beta_4 = \overline{Y}_{\bullet 4\bullet} - \overline{Y}_{\bullet\bullet\bullet} = 4.69774 - 2.312886 = 2.384854. \quad \text{(C.9)}$$

Interaction *CL*-*UGV* effects:

$$(\alpha\beta)_{11} = \overline{Y}_{11\bullet} - \overline{Y}_{1\bullet\bullet} - \overline{Y}_{\bullet 1\bullet} + \overline{Y}_{\bullet\bullet\bullet} =$$

$$1.735380 - 1.731701 - 1.977448 + 2.312886 = 0.339117. \quad \text{(C.10)}$$

$$(\alpha\beta)_{12} = \overline{Y}_{12\bullet} - \overline{Y}_{1\bullet\bullet} - \overline{Y}_{\bullet 2\bullet} + \overline{Y}_{\bullet\bullet\bullet} =$$

$$0.601754 - 1.731701 - 0.858571 + 2.312886 = 0.324368. \quad \text{(C.11)}$$

$$(\alpha\beta)_{13} = \overline{Y}_{13\bullet} - \overline{Y}_{1\bullet\bullet} - \overline{Y}_{\bullet 3\bullet} + \overline{Y}_{\bullet\bullet\bullet} =$$

$$1.191490 - 1.731701 - 1.717785 + 2.312886 = 0.05489. \quad \text{(C.12)}$$

$$(\alpha\beta)_{14} = \overline{Y}_{14\bullet} - \overline{Y}_{1\bullet\bullet} - \overline{Y}_{\bullet 4\bullet} + \overline{Y}_{\bullet\bullet\bullet} =$$

$$3.39818 - 1.731701 - 4.69774 + 2.312886 = -0.718375. \quad \text{(C.13)}$$

$$(\alpha\beta)_{21} = \overline{Y}_{21\bullet} - \overline{Y}_{2\bullet\bullet} - \overline{Y}_{\bullet 1\bullet} + \overline{Y}_{\bullet\bullet\bullet} =$$

$$2.219516 - 2.894071 - 1.977448 + 2.312886 = -0.339117. \quad \text{(C.14)}$$

$$(\alpha\beta)_{22} = \overline{Y}_{22\bullet} - \overline{Y}_{2\bullet\bullet} - \overline{Y}_{\bullet 2\bullet} + \overline{Y}_{\bullet\bullet\bullet} =$$

$$1.115388 - 2.894071 - 0.858571 + 2.312886 = -0.324368. \quad \text{(C.15)}$$

$$(\alpha\beta)_{23} = \overline{Y}_{23\bullet} - \overline{Y}_{2\bullet\bullet} - \overline{Y}_{\bullet 3\bullet} + \overline{Y}_{\bullet\bullet\bullet} =$$

$$2.244080 - 2.894071 - 1.717785 + 2.312886 = -0.05489. \quad \text{(C.16)}$$

$$(\alpha\beta)_{24} = \overline{Y}_{24\bullet} - \overline{Y}_{2\bullet\bullet} - \overline{Y}_{\bullet 4\bullet} + \overline{Y}_{\bullet\bullet\bullet} =$$

$$5.99730 - 2.894071 - 4.69774 + 2.312886 = 0.718375. \quad \text{(C.17)}$$

C.2 RESULTS OF ANOVA

Table C.3 shows the ANOVA results. F-Tests for interaction and main effects are performed as follows.

For the interaction effect the following hypotheses are considered:

$$H_0^{CL-UGV}: \textit{CL-UGV} \text{ interaction is negligible} \leftrightarrow H_0^{CL-UGV}: (\alpha\beta)_{ij} = 0 \; \forall \, i, j. \quad \text{(C.18)}$$

$$H_1^{CL-UGV}: \textit{CL-UGV} \text{ interaction is not negligible} \leftrightarrow H_1^{CL-UGV}: \text{Not all } (\alpha\beta)_{ij} = 0. \quad \text{(C.19)}$$

For a significance level of $\alpha = 0.01$, the decision rule is to reject H_0^{CL-UGV} if $p < 0.01$. Since $p = 0.0214$ from Table C.3, H_0^{CL-UGV} cannot be rejected. This implies that the interaction is negligible, at the 1% significance level.

Table C.3 The ANOVA Results for the Full-Interaction Model.

Source	DF	Sum of Squares	Mean Square	F-Value	Pr > F (*p*-value)
Model	7	103.59	14.79	22.25	<.0001
Error	32	21.28	0.67		
Corrected Total	39	124.88			
R-Square		Coeff. Var.		Root MSE	Position Error Mean
0.83		35.26		0.82	2.31
Source	DF	Type III SS	Mean Square	F-Value	Pr > F (*p*-value)
CL	1	13.51	13.51	20.32	<.0001
UGV	3	82.69	27.56	41.45	<.0001
*CL*UGV*	3	7.39	2.46	3.71	0.0214

For the main effect *CL* the following hypotheses are considered:

$$H_0^{CL}: \text{Main effect } CL \text{ is negligible} \leftrightarrow H_0^{CL}: \alpha_i = 0 \,\forall\, i. \qquad \text{(C.20)}$$

$$H_1^{CL}: \text{Main effect } CL \text{ is not negligible} \leftrightarrow H_1^{CL}: \text{Not all } \alpha_i = 0. \qquad \text{(C.21)}$$

For a significance level of $\alpha = 0.01$, the decision rule is to reject H_0^{CL} if $p < 0.01$. Since $p < 0.0001$ from Table C.3, H_0^{CL} is rejected. This implies that the main effect for *CL* is not negligible, at the 1% significance level. Therefore, a pair-wise comparison of the *CL* effects is performed (Table C.4).

For the main effect *UGV* the following hypotheses are considered:

$$H_0^{UGV}: \text{Main effect } UGV \text{ is negligible} \leftrightarrow H_0^{UGV}: \beta_j = 0 \,\forall\, j. \qquad \text{(C.22)}$$

$$H_1^{UGV}: \text{Main effect } UGV \text{ is not negligible} \leftrightarrow H_1^{UGV}: \text{Not all } \beta_j = 0. \qquad \text{(C.23)}$$

For a significance level of $\alpha = 0.01$, the decision rule is to reject H_0^{UGV} if $p < 0.01$. Since $p < 0.0001$ from Table C.3, H_0^{UGV} is rejected. This implies that the main effect for *UGV* is not negligible, at the 1% significance level. Therefore, a pair-wise comparison of the *UGV* effects is performed (Table C.5).

The 99% confidence limits are determined using the *Tukey's* pair-wise comparison test for factor level means on the full-interaction model (Tables C.4 and C.5).

Table C.4 LSMs for *CL* Effect.

CL = i	*CL = j*	Difference Between Means	Simultaneous 99% Confidence Limits for LSM(*i*) – LSM(*j*)
1	2	-1.162370	(-1.868560, -0.456180)

Table C.5 LSMs for *UGV* Effect.

UGV = i	*UGV = j*	Difference Between Means	Simultaneous 99% Confidence Limits for LSM(*i*) – LSM(*j*)
1	2	1.118877	(-0.111933, 2.349687)
1	3	0.259663	(-0.971147, 1.490473)
1	4	-2.720292	(-3.951102, -1.489482)
2	3	-0.859214	(-2.090024, 0.371596)
2	4	-3.839169	(-5.069979, -2.608359)
3	4	-2.979955	(-4.210765, -1.749145)

Table C.4 shows the *Tukey* 99% confidence interval for the difference between the means. As can be inferred, $0 \notin (-1.868560, -0.456180)$. Hence, the difference between $CL = 1$ and $CL = 2$ is statistically significant, at the 1% significance level. In other words, the final position error for the cooperative localization system is different from the final position error for the non-cooperative localization system. The mean final position errors are as follows: 1.7317 m (CL system) and 2.8941 m (non-CL system). The range-only CL system shows a 40% improvement in the mean final position error over a non-CL system.

C.3 CHECKING MODEL ASSUMPTIONS

A modified *Levene's* test is performed for checking the equality of error variances. The following hypotheses are considered:

$$H_0 : \sigma_1^2 = \sigma_2^2 = ... = \sigma_8^2 . \quad \text{(C.24)}$$

$$H_1 : \text{Not all } \sigma_i^2\text{'s are same, } i = 1,\ldots, 8. \quad \text{(C.25)}$$

For a significance level of $\alpha = 0.01$, the decision rule is to reject H_0 if $p < 0.01$. Since $p = 0.1898$ from Table C.6, H_0 is not rejected. This implies that the constant error variance assumption is valid in this case, at the 1% significance level.

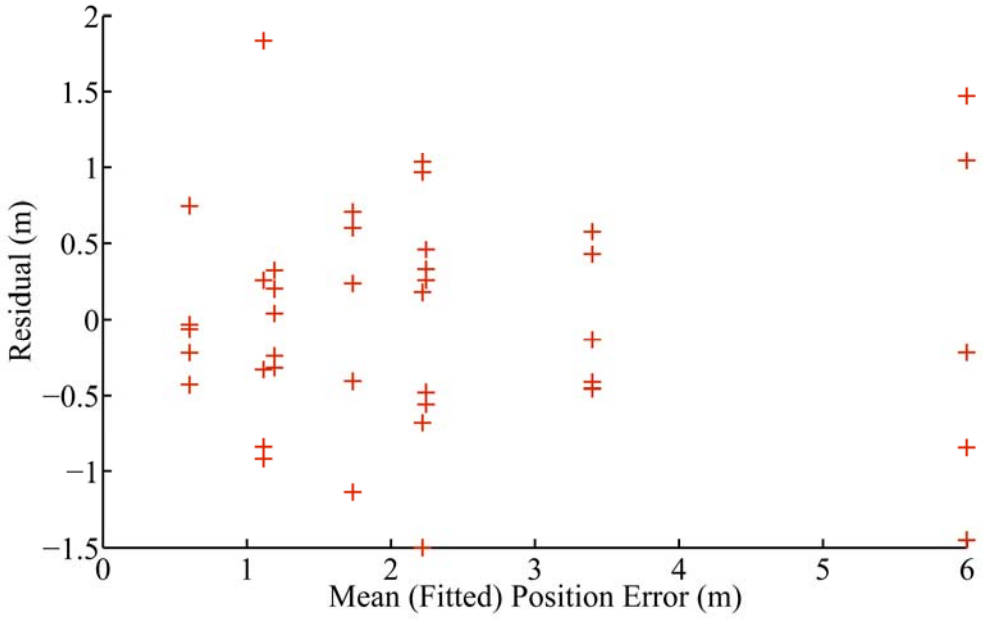

Figure C.4 The Residual as a Function of the Mean Position Error: There appears to be some difference in the variation of the residual.

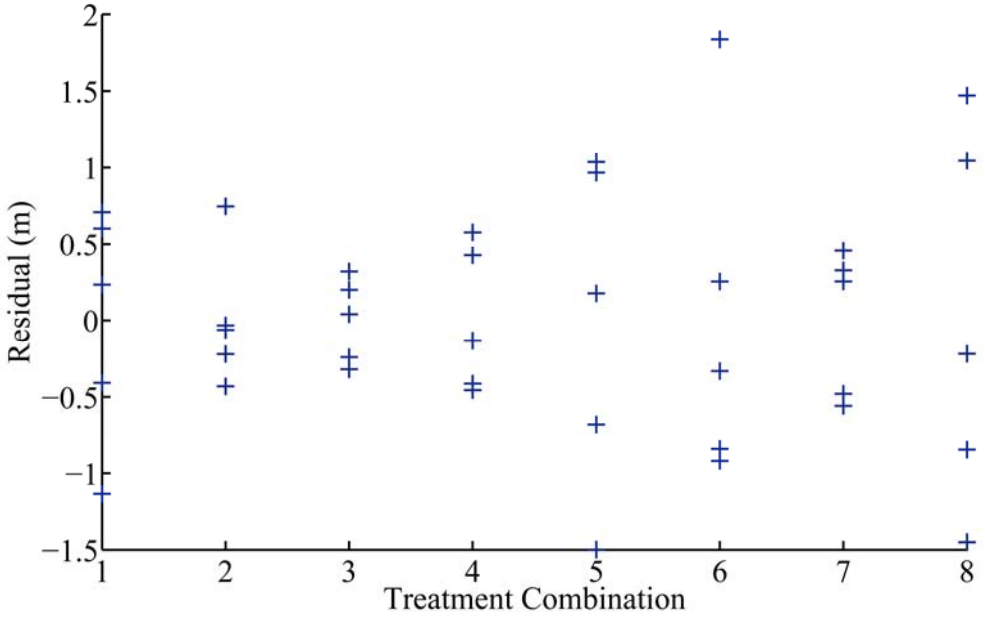

Figure C.5 The Residual as a Function of the Treatment Combination: There is more variation for higher treatment combinations.

The normality assumption is checked by a test for linearity of the normal probability plot (Figure C.6). The following hypotheses are considered:

$$H_0 : \text{Normality assumption is valid.} \tag{C.26}$$

$$H_1 : \text{Normality assumption is violated.} \tag{C.27}$$

For a significance level of $\alpha = 0.10$, the *Pearson's* correlation coefficient, $\hat{\rho} = 0.99457$. Critical value, C (0.01, 40) = 0.977 (From Table 1 in [Fil75]). Since $\hat{\rho} >$ critical value ($\alpha = 0.10$, $n = 40$), H_0 cannot be rejected, at the 10% significance level. So, it cannot be concluded, at the 10% significance level, that there is a deviation from normality.

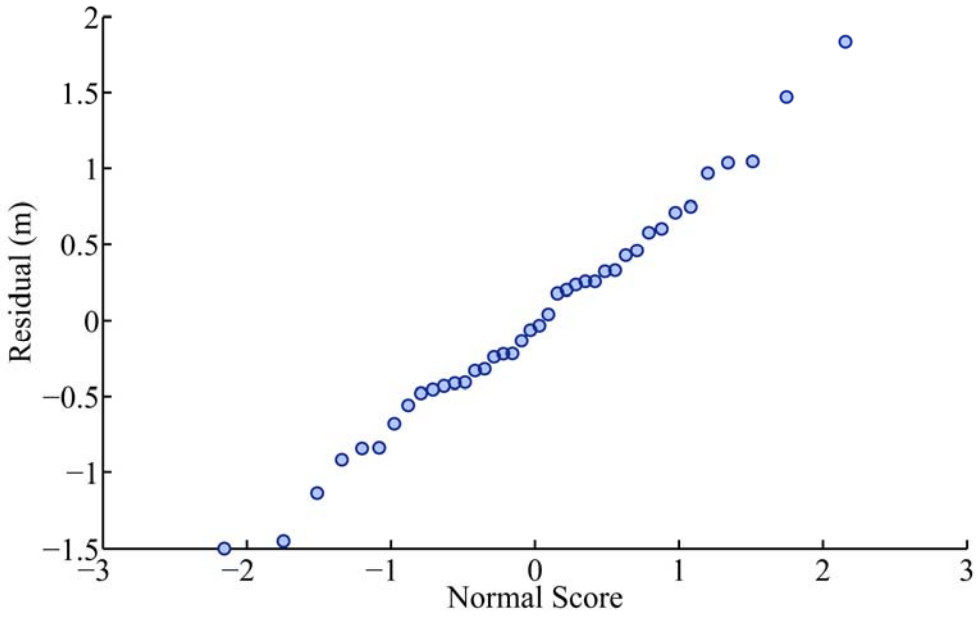

Figure C.6 Normal Probability Plot: A linear fit appears to be valid. This indicates that there is no violation of the normality assumption.

Table C.6 The ANOVA Results for the Modified Levene's Test.

Source	DF	Sum of Squares	Mean Square	F-Value	Pr > F (*p*-value)
Model	7	2.78	0.3964	1.54	0.1898
Error	32	8.24	0.2575		
Corrected Total	39	11.02			
R-Square		Coeff. Var.		Root MSE	Deviation from Medians Mean
0.25		92.96		0.51	0.55
Source	DF	ANOVA SS	Mean Square	F-Value	Pr > F (*p*-value)
TC	7	2.78	0.3964	1.54	0.1898

The *Bonferroni* outlier test is used to detect outliers. The following hypotheses are considered:

$$H_0 : \text{Observation is not an outlier.} \quad \text{(C.28)}$$

$$H_1 : \text{Observation is an outlier.} \quad \text{(C.29)}$$

For a significance level of α = 0.05, the decision rule is to reject H_0 when $|t_{ij}| > t_{n-v-1,\alpha/2n} = t_{abr-ab-1,\alpha/2abr} = t_{31,0.000625} = 3.55087$. Since $|t_{ij}| < 3.55087 \quad \forall\ i, j$, H_0 is not rejected, at the 5% significance level. So, there are no outliers (Figure C.7).

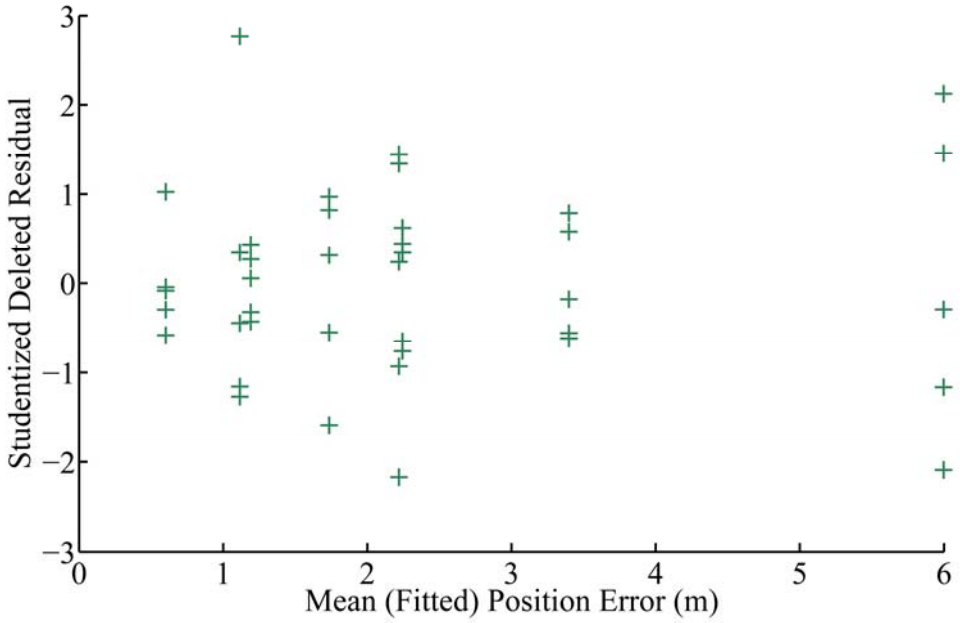

Figure C.7 Studentized Deleted Residuals as a Function of the Mean Position Error: There are no outliers, *i.e.*, $|t_{ij}| < 3.55087$ for all *i, j*.

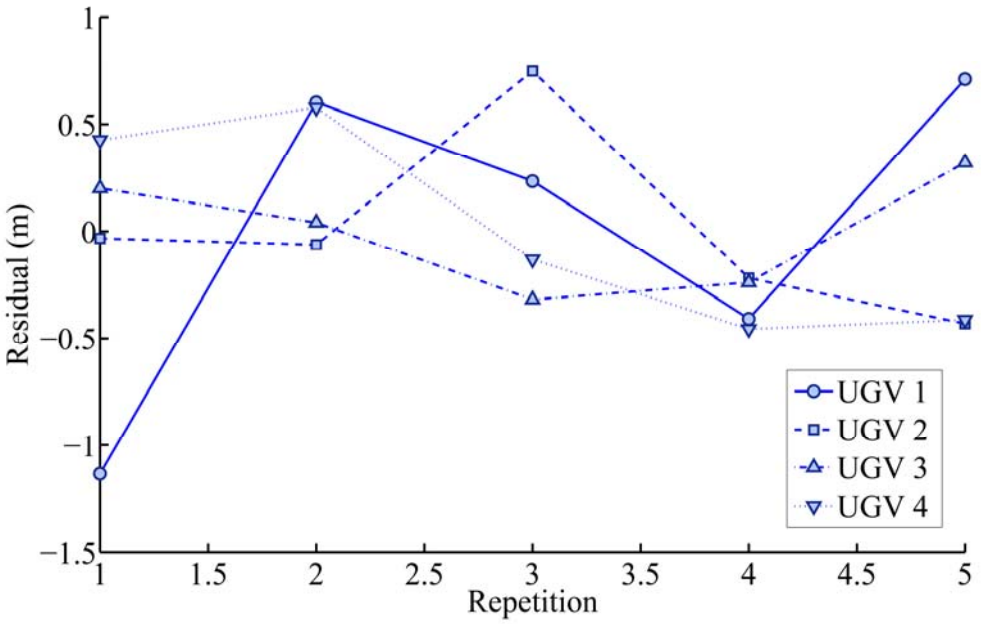

Figure C.8 Serial Correlation Plot for CL: There is no strong pattern or trend, *i.e.*, there is no serial correlation of errors.

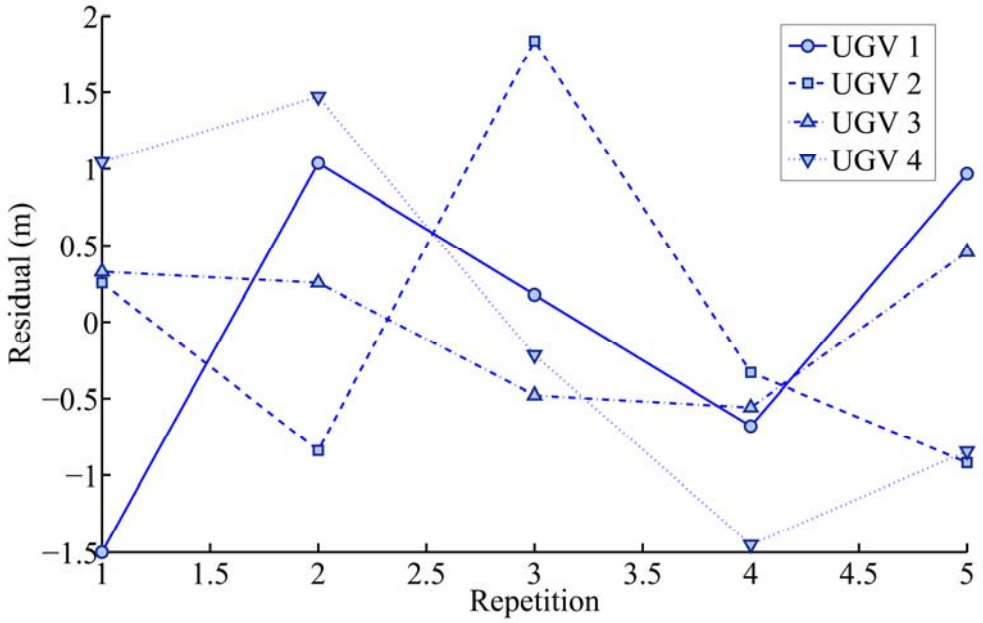

Figure C.9 Serial Correlation Plot for Non-CL: There is no strong pattern or trend, *i.e.*, there is no serial correlation of errors.

The power of detecting a difference is computed as follows [Che05]. Let Δ be the difference in position error that is to be detected, *i.e.*, the power of the test is the power to detect Δ due to factor effects. Let $\Delta = 1$ m. Here, $r = 5$, $n = 40$, $v = ab = 8$, and MSE = 0.67 (from Table C.2).

$$\upsilon_1 = v - 1 = 8 - 1 = 7. \tag{C.30}$$

$$\upsilon_2 = n - v = 40 - 8 = 32. \tag{C.31}$$

$$\varphi^2 = \frac{r\Delta^2}{2v\sigma^2} \Rightarrow \varphi = \sqrt{\frac{r\Delta^2}{2v\sigma^2}} = 0.682948. \tag{C.32}$$

Using SAS^{TM}, the power of the test = P [Rejecting H_0 | H_0 is false] = $1 - \beta = 0.19512$.

REFERENCES

[Ant05] G. Antonelli, S. Chiaverini, and G. Fusco, "A Calibration Method for Odometry of Mobile Robots based on the Least-Squares Technique: Theory and Experimental Validation," *IEEE Transactions on Robotics*, vol. 21, no. 5, pages 994-1004, October 2005.

[Ara02] T. Arai, E. Pagello, and L. E. Parker, "Editorial: Advances in Multi-Robot Systems," *IEEE Transactions on Robotics and Automation*, vol. 18, no. 5, pages 655-661, October 2002.

[Att00] S. Attouche, S. Hayat, and M. Staroswiecki, "A Prediction System Based On Vehicle Sensor Data in Automated Highway," *Proceedings of the 2000 IEEE Intelligent Transportation Systems Conference*, Dearborn, MI, pages 494-499, October 2000.

[Bal94] T. Balch and R. C. Arkin, "Communication in Reactive Multiagent Robotic Systems," *Autonomous Robots*, vol. 1, no. 1, pages 27-52, 1994.

[Bal03] H. Baltzakis and P. Trahanias, "A Hybrid Framework for Mobile Robot Localization: Formulation Using Switching State-Space Models," *Autonomous Robots*, vol. 15, no. 2, pages 169-191, 2003.

[Bar01] Y. Bar-Shalom, X. R. Li, and T. Kirubarajan, "Estimation with Applications to Tracking and Navigation," New York: John Wiley & Sons, 2001.

[Bar95] B. Barshan and H. F. Durrant-Whyte, "Inertial Navigation Systems for Mobile Robots," *IEEE Transactions on Robotics and Automation*, vol. 11, no. 3, pages 328-342, June 1995.

[Bon01] P. Bonnifait, P. Bouron, P. Crubille, and D. Meizel, "Data Fusion of Four ABS Sensors and GPS for an Enhanced Localization of Car-Like Vehicles," *Proceedings of the 2001 IEEE International Conference on Robotics & Automation*, Seoul, Korea, vol. 2, pages 1597-1602, May 2001.

[Bor94] J. Borenstein and L. Feng, "UMBmark – a Method for Measuring, Comparing, and Correcting Dead-Reckoning Errors in Mobile Robots," The University of Michigan, Technical Report: UM-MEAM-94-22, December 1994.

[Bor95] J. Borenstein and L. Feng, "Correction of Systematic Odometry Errors in Mobile Robots," *Proceedings of the 1995 IEEE International Conference on Intelligent Robots and Systems*, Pittsburgh, PA, vol. 3, pages 569-574, August 1995.

[Bor96] J. Borenstein, H. R. Everett, and L. Feng (May 2, 2007), "Where am I: Sensors and Methods for Mobile Robot Positioning," The University of Michigan, April 1996. Available: http://www-personal.umich.edu/~johannb/shared/pos96rep.pdf.

[Bor97] J. Borenstein, H. R. Everett, L. Feng, and D. Wehe, "Mobile Robot Positioning: Sensors and Techniques," *Journal of Robotic Systems*, vol. 14, no. 4, pages 231-249, 1997.

[Bou00] D. Bouvet and G. Garcia, "GPS Latency Identification by Kalman Filtering," *Robotica*, vol. 18, no. 5, pages 475-485, September 2000.

[Bra03] T. Braunl, "Embedded Robotics: Mobile Robot Design and Applications with Embedded Systems," New York: Springer, 2003.

[Byc03] V. Bychkovskiy, S. Megerian, D. Estrin, and M. Potkonjak, "A Collaborative Approach to In-Place Sensor Calibration," *Proceedings of the Second International Workshop on Information Processing in Sensor Networks*, Palo Alto, CA, vol. 2364 of Lecture Notes in Computer Science, pages 301-316, Springer-Verlag, 2003.

[Cag06] V. Caglioti, A. Citterio, and A. Fossati, "Cooperative Distributed Localization in Multi-Robot Systems: A Minimum Entropy Approach," *IEEE Workshop on Distributed Intelligent Systems: Collective Intelligence and Its Applications*, Prague, Czech Republic, pages 25-20, June 2006.

[Cao97] Y. U. Cao, A. S. Fukunaga, and A. B. Kahng, "Cooperative Mobile Robotics: Antecedents and Directions," *Autonomous Robots*, vol. 4, pages 1-23, 1997.

[Car90] N. A. Carlson, "Federated Square Root Filter for Decentralized Parallel Processes," *IEEE Transactions on Aerospace and Electronic Systems*, vol. 26, no. 3, pages 517-525, May 1990.

[Car96] N. A. Carlson, "Federated Filter for Computer-Efficient Near-Optimal GPS Integration," *Proceedings of the IEEE Position Location and Navigation Symposium*, Atlanta, GA, pages 306-314, April 1996.

[Car04] R. Carrasco and A. Cipriano, "Fuzzy Logic Based Nonlinear Kalman Filter Applied to Mobile Robots Modelling," *Proceedings of the 2004 IEEE International Conference on Fuzzy Systems*, Budapest, Hungary, vol. 3, pages 1485-1490, 2004.

[Che05] V. C. P. Chen, IMSE Department, The University of Texas at Arlington, Design of Experiments, IE-6308, Class Handouts, 2005.

[Che04] K. C. Cheok, G. E. Smid, G. R. Hudas, and J. L. Overholt, "An Ultra-Wideband RF Method for Localizing an Autonomous Mobile Robot," *Proceedings of the Twenty-Fourth Army Science Conference*, Orlando, FL, November/December 2004.

[Cle02] A. Clerentin, L. Delahoche, E. Brassart, and C. Cauchois, "Mobile Robot Localization Based on Multi Target Tracking," *Proceedings of the 2002 IEEE International Conference on Robotics and Automation*, Washington, DC, vol. 1, pages 13-18, May 2002.

[Cox90] I. J. Cox and G. T. Wilfong, "Autonomous Robot Vehicles," New York: Springer-Verlag, 1990.

[Cox91] I. J. Cox, "Blanche – An Experiment in Guidance and Navigation of an Autonomous Robot Vehicle," *IEEE Transactions on Robotics and Automation*, vol. 7, no. 2, pages 193-204, April 1991.

[Cra89] J. J. Craig, "Introduction to Robotics: Mechanics and Control," Reading, MA: Addison-Wesley, 1989.

[Cra04] J. L. Crassidis and J. L. Junkins, "Optimal Estimation of Dynamic Systems," Boca Raton, FL: Chapman & Hall/CRC, 2004.

[Cro95] J. L. Crowley, "Mathematical Foundations of Navigation and Perception for an Autonomous Mobile Robot," *Proceedings of the International Workshop on Reasoning with Uncertainty in Robotics*, Amsterdam, The Netherlands, pages 9-51, December 1995.

[Das02] A. Das, J. Spletzer, V. Kumar, and C. Taylor, "Ad Hoc Networks for Localization and Control," *Proceedings of the Forty-First IEEE Conference on Decision and Control,* Las Vegas, NV, vol. 3, pages 2978-2983, December 2002.

[Dav00] A. J. Davison and N. Kita, "Active Visual Localisation for Cooperating Inspection Robots," *Proceedings of the 2000 IEEE/RSJ International Conference on Intelligent Robots and Systems*, Takamatsu, Japan, vol. 3, pages 1709-1715, 2000.

[deC03] M. de Cecco, "Sensor Fusion of Inertial-Odometric Navigation as a Function of the Actual Manoeuvres of Autonomous Guided Vehicles," *Measurement Science and Technology*, Institute of Physics Publishing, vol. 14, no. 5, pages 643-653, May 2003.

[Del99] F. Dellaert, D. Fox, W. Burgard, and S. Thrun, "Monte Carlo Localization for Mobile Robots," *Proceedings of the IEEE International Conference on Robotics and Automation*, Detroit, MI, vol. 2, pages 1322-1328, 1999.

[Dju01] G. M. Djuknic and R. E. Richton, "Geolocation and Assisted GPS," *IEEE Computer*, vol. 34, no. 2, February 2001.

[Dou01] A. Doucet, N. de Freitas, and N. Gordon, "Sequential Monte Carlo Methods in Practice," New York: Springer-Verlag, 2001.

[Dur90] H. F. Durrant-Whyte, B. Y. S. Rao, and H. Hu, "Toward a Fully Decentralized Architecture for Multi-Sensor Data Fusion," *Proceedings of the IEEE International Conference on Robotics and Automation*, Cincinnati, OH, pages 1331-1336, May 1990.

[Dur01] H. F. Durrant-Whyte, "A Critical Review of the State-of-the-Art in Autonomous Land Vehicle Systems," Sandia National Laboratories, Sandia Report: SAND2001-3685, November 2001.

[Eco00] J. T. Economou and R. E. Colyer, "Modelling of Skid Steering and Fuzzy Logic Vehicle Ground Interaction," *Proceedings of the American Control Conference*, Chicago, IL, vol. 1, no. 6, pages 100-104, June 2000.

[ElM00] A. El-Mowafy, "Performance Analysis of the RTK Technique in an Urban Environment," *The Australian Surveyor*, vol. 1, no. 45, pages 47-54, June 2000.

[ElN05] M. E. El-Najjar and P. Bonnifait, "A Road-Matching Method for Precise Vehicle Localization Using Belief Theory and Kalman Filtering," *Autonomous Robots*, vol. 19, no. 2, pages 173-191, 2005.

[Eva05] C. P. Evans, III, "Development of a Geospatial Data-Sharing Method for Unmanned Vehicles based on the Joint Architecture for Unmanned Systems,"

MS Thesis, Department of Mechanical and Aerospace Engineering, University of Florida, 2005.

[Eve95] H. R. Everett, "Sensors for Mobile Robots: Theory and Applications," Wellesley, MA: A. K. Peters, February 1995.

[Fen04] J. Feng, G. Qu, and M. Potkonjak, "Sensor Calibration Using Nonparametric Statistical Characterization of Error Models," *Proceedings of the IEEE Sensors Conference*, Vienna, Austria, vol. 3, pages 1456-1459, October 2004.

[Fer98] C. Ferrari, E. Pagello, J. Ota, and T. Arai, "Multirobot Coordination in Space and Time," *Robotic Autonomous Systems*, vol. 25, no. 3, pages 219-229, November 1998.

[Fil75] J. J. Filliben, "The Probability Plot Correlation Coefficient Test for Normality," *Technometrics*, vol. 17, no. 1, February 1975.

[Fon02] R. J. Fontana and S. J. Gunderson, "Ultra-Wideband Precision Asset Location System," *Proceedings of the 2002 IEEE Conference on Ultra Wideband Systems and Technologies*, Baltimore, MD, pages 147-150, May 2002.

[Fon03] R. J. Fontana, E. Richley, and J. Barney, "Commercialization of an Ultra-Wideband Precision Asset Location System," *Proceedings of the 2003 IEEE Conference on Ultra Wideband Systems and Technologies*, Baltimore, MD, pages 369-373, November 2003.

[Fox00] D. Fox, W. Burgard, H. Kruppa, and S. Thrun, "Collaborative Multi-Robot Localization," *Autonomous Robots*, vol. 8, no. 3, 2000.

[Fra04] J. Fraden, "Handbook of Modern Sensors: Physics, Designs, and Applications," New York: AIP Press/Springer, 2004.

[Fri91] J. H. Friedman, "Multivariate Adaptive Regression Splines," *The Annals of Statistics*, vol. 19, no. 1, pages 1-67, 1991.

[Gag95] D. W. Gage, "A Brief History of Unmanned Ground Vehicle (UGV) Development Efforts," *Unmanned Systems Magazine*, vol. 13, no. 3, 1995.

[Gao93] Y. Gao, E. J. Krakiwsky, M. A. Abousalem, and J. F. McLellan, "Comparison and Analysis of Centralized, Decentralized, and Federated Filters," *Journal of the Institute of Navigation*, vol. 40, no. 1, pages 69-86, 1993.

[Goe99] P. Goel, S. I. Roumeliotis, and G. S. Sukhatme, "Robust Localization Using Relative and Absolute Position Estimates," *Proceedings of the IEEE/RSJ International Conference on Intelligent Robots and Systems*, Kyongju, Korea, vol. 2, pages 1134-1140, October 1999.

[Gra01] R. Grabowski and P. Khosla, "Localization Techniques for a Team of Small Robots," *Proceedings of the IEEE/RSJ International Conference on Intelligent Robots and Systems*, Maui, HI, vol. 2, pages 1067-1072, October/November 2001.

[Gus02] F. Gustafsson, F. Gunnarsson, N. Bergman, U. Forssell, J. Jansson, R. Karlsson, and P. Nordlund, "Particle Filters for Positioning, Navigation and Tracking," *IEEE Transactions on Signal Processing*, vol. 50, no. 2, pages 425-437, February 2002.

[Gut98] J. S. Gutmann, W. Burgard, D. Fox, and K. Konolige, "An Experimental Comparison of Localization Methods," *IEEE/RSJ International Conference on Intelligent Robotics and Systems (IROS'98)*, Victoria, Canada, vol. 2, pages 736-743, 1998.

[Hal03] J. Y. Halpern, "Reasoning about Uncertainty," Cambridge, MA: MIT Press, 2003.

[Han98] P. D. Hanlon and P. S. Maybeck, "Multiple-Model Adaptive Estimation Using a Residual Correlation Kalman Filter Bank," *Proceedings of the Thirty-Seventh IEEE Conference on Decision and Control*, Tampa, FL, vol. 36, no. 2, pages 393-406, December 1998.

[Has88] H. R. Hashemipour, S. Roy, and A. J. Laub, "Decentralized Structures for Parallel Kalman Filtering," *IEEE Transactions on Automatic Control*, vol. 33, no. 1, pages 88-94, January 1988.

[How03] A. Howard, M. J. Mataric, and G. S. Sukhatme, "Putting the 'I' in the Team: An Ego-Centric Approach to Cooperative Localization," *Proceedings of the IEEE International Conference on Robotics and Automation*, Taipei, Taiwan, vol. 1, pages 868-874, September 2003.

[Hya99] J. Hyams, M. W. Powell, and R. Murphy, "Cooperative Navigation of Micro-Rovers Using Color Segmentation," *Proceedings of the IEEE International Symposium on Computational Intelligence in Robotics and Automation*, Monterey, CA, pages 195-201, November 1999.

[Joi04] Joint Architecture for Unmanned Systems (May 2, 2007), "Reference Architecture Specifications," vol. 2, part 2, ver. 3.2, August 2004. Available: http://www.jauswg.org/baseline/refarch.html.

[Kal60] R. E. Kalman, "A New Approach to Linear Filtering and Prediction Problems," *Transactions of the ASME – Journal of Basic Engineering*, vol. 82, series D, pages 35-45, 1960.

[Kam97] M. Kam, X. Zhu, and P. Kalata, "Sensor Fusion for Mobile Robot Navigation," *Proceedings of the IEEE*, vol. 85, no. 1, pages 108-119, 1997.

[Kat99] K. Kato, H. Ishiguro, and M. Barth, "Identifying and Localizing Robots in a Multi-Robot System Environment," *Proceedings of the 1999 IEEE/RSJ International Conference on Intelligent Robots and Systems*, Kyongju, Korea, vol. 2, pages 966-971, October 1999.

[Kou06] D. Koutsonikolas, S. M. Das, Y. C. Hu, Y. H. Lu, and C. S. G. Lee, "CoCoA: Coordinated Cooperative Localization for Mobile Multi-Robot Ad Hoc Networks," *Proceedings of the Twenty-Sixth IEEE International Conference on Distributed Computing Systems Workshops*, Lisboa, Portugal, July 2006.

[Kur94] R. Kurazume, S. Nagata, and S. Hirose, "Cooperative Positioning with Multiple Robots," *Proceedings of the IEEE International Conference on Robotics and Automation*, vol. 2, pages 1250-1257, San Diego, CA, May 1994.

[Kur98] R. Kurazume and S. Hirose, "Study on Cooperative Positioning System – Optimum Moving Strategies for CPS III," *Proceedings of the IEEE*

International Conference on Robotics and Automation, Leuven, Belgium, vol. 4, pages 2896-2903, May 1998.

[Kur00] R. Kurazume and S. Hirose, "An Experimental Study of a Cooperative Positioning System," *Autonomous Robots*, vol. 8, no. 1, pages 43-52, 2000.

[Lin05] Y. Lin, P. Vernaza, J. Ham, and D. D. Lee, "Cooperative Relative Robot Localization with Audible Acoustic Sensing," *Proceedings of IEEE/RSJ International Conference on Intelligent Robots and Systems*, Edmonton, Canada, pages 3764-3769, August 2005.

[Liu01] H. H. S. Liu and G. K. H. Pang, "Accelerometer for Mobile Robot Positioning," *IEEE Transactions on Industry Applications*, vol. 37, no. 3, pages 812-819, May/June 2001.

[Lop00] J. A. Lopez-Orozco, J. M. de la Cruz, E. Besada, and P. Ruiperez, "An Asynchronous, Robust, and Distributed Multisensor Fusion System for Mobile Robots," *The International Journal of Robotics Research*, vol. 19, no. 10, pages 914-932, October 2000.

[Mad04] R. Madhavan, K. Fregene, and L. E. Parker, "Distributed Cooperative Outdoor Multirobot Localization and Mapping," *Autonomous Robots*, vol. 17, no. 1, pages 23-39, 2004.

[Man96] D. E. Manolakis, "Efficient Solution and Performance Analysis of 3-D Position Estimation by Trilateration," *IEEE Transactions on Aerospace and Electronic Systems*, vol. 32, no. 4, pages 1239-1248, 1996.

[Mar05] A. Martinelli, F. Pont, and R. Siegwart, "Multi-Robot Localization Using Relative Observations," *Proceedings of the 2005 IEEE International Conference on Robotics and Automation*, Barcelona, Spain, pages 2797-2802, April 2005.

[Mas03] R. L. Mason, R. F. Gunst, and J. L. Hest, "Statistical Design and Analysis of Experiments," Hoboken, NJ: John Wiley & Sons, 2003.

[Mat94] M. J. Mataric, "Interaction and Intelligent Behavior," PhD Dissertation, Department of Electrical Engineering and Computer Science, Massachusetts Institute of Technology, Cambridge, MA, 1994.

[May79] P. S. Maybeck, "Stochastic Models, Estimation and Control," vol. 1, New York: Academic Press, 1979.

[May85] P. S. Maybeck and R. I. Sulzu, "Adaptive Tracker Field-of-View Variation Via Multiple Model Filtering", *IEEE Transactions on Aerospace and Electronic Systems*, vol. AES-21, no. 4, pages 529-539, July 1985.

[McL04] S. McLean, S. Maus, D. Dater, S. Macmillan, V. Lesur, and A. Thomson, "The US/UK World Magnetic Model for 2005-2010," NOAA Technical Report: NESDIS/NGDC-1, 2004.

[Mil05] A. Milella, F. Pont, and R. Siegwart, "Model-Based Relative Localization for Cooperative Robots using Stereo Vision," *Proceedings of the Twelfth Annual Conference on Mechatronics and Machine Vision in Practice*, Manila, Philippines, 2005.

[Mon05] L. Montesano, J. Gaspar, J. Santos-Victor, and L. Montano, "Cooperative Localization by Fusing Vision-Based Bearing Measurements and Motion," *Proceedings of the IEEE/RSJ International Conference on Intelligent Robots and Systems*, Edmonton, Canada, pages 2333-2338, August 2005.

[Mou06] A. I. Mourikis and S. I. Roumeliotis, "Performance Analysis of Multirobot Cooperative Localization," *IEEE Transactions on Robotics*, vol. 22, no. 4, pages 666-681, August 2006.

[Mur98] R. R. Murphy, "Dempster-Shafer Theory for Sensor Fusion in Autonomous Mobile Robots," *IEEE Transactions on Robotics and Automation*, vol. 14, no. 2, pages 197-206, April 1998.

[Mut00] A. G. O. Mutambara and H. F. Durrant-Whyte, "Fully Decentralized Estimation and Control for a Modular Wheeled Mobile Robot," *The International Journal of Robotics Research*, vol. 19, no. 6, pages 582-596, June 2000.

[Neb97] E. Nebot, S. Sukkarieh, and H. Durrant-Whyte, "Inertial Navigation Aided with GPS Information," *Proceedings of the Fourth Annual Conference on Mechatronics and Machine Vision in Practice*, Toowoomba, Australia, pages 169-174, September 1997.

[Neb99] E. Nebot and H. F. Durrant-Whyte, "Initial Calibration and Alignment of Low-Cost Inertial Navigation Units for Land Vehicle Applications," *Journal of Robotic Systems*, vol. 16, no. 2, pages 81-92, 1999.

[Oje00] L. Ojeda and J. Borenstein, "Experimental Results with the KVH C-100 Fluxgate Compass in Mobile Robots," *Proceedings of IASTED International Conference on Robotics and Applications*, Honolulu, HI, August 2000.

[Pat05] N. Patwari, J. N. Ash, S. Kyperountas, A. O. Hero, III, R. L. Moses, and N. S. Correal, "Locating the Nodes: Cooperative Localization in Wireless Sensor Networks," *IEEE Signal Processing Magazine*, vol. 22, no. 4, July 2005.

[Pea05] M. Peasgood, C. Clark, and J. McPhee, "Localization of Multiple Robots with Simple Sensors," *International Conference on Mechatronics and Automation*, Niagara Falls, Canada, vol. 2, pages 671-676, July 2005.

[Pel98] M. R. Peltier, C. J. Wilcox, and D. C. Sharp, "Technical Note: Application of the Box-Cox Data Transformation to Animal Science Experiments," *Journal of Animal Science*, vol. 76, no. 3, pages 847-849, 1998.

[Pre90] S. Premvuti and S. Yuta, "Consideration on the Cooperation of Multiple Autonomous Mobile Robots," *IEEE International Workshop on Intelligent Robots and Systems*, Ibaraki, Japan, vol. 1, pages 59-63, 1990.

[Rac05] M. Y. Rachkov, L. Marques, and A. T. de Almeida, "Multisensor Demining Robot," *Autonomous Robots*, vol. 18, no. 3, May 2005.

[Rek98] I. M. Rekleitis, G. Dudek, and E. E. Milios, "Accurate Mapping of an Unknown World and Online Landmark Positioning," *Proceedings of Vision Interface*, Vancouver, Canada, pages 455-461, June 1998.

[Rek02] I. M. Rekleitis, G. Dudek, and E. E. Milios, "Multi-Robot Cooperative Localization: A Study of Trade-Offs Between Efficiency and Accuracy," *Proceedings of the 2003 IEEE/RSJ International Conference on Intelligent Robots and Systems*, Lausanne, Switzerland, vol. 3, pages 2690-2695, October 2002.

[Reu00] J. Reuter, "Mobile Robot Self-Localization Using PDAB," *Proceedings of the IEEE International Conference on Robotics and Automation*, San Francisco, CA, vol. 4, pages 3512-3518, April 2000.

[Rou97] S. I. Roumeliotis and G. A. Bekey, "An Extended Kalman Filter for Frequent Local and Infrequent Global Sensor Data Fusion," *Proceedings of the SPIE (Sensor Fusion and Decentralized Control in Autonomous Robotic Systems)*, Pittsburgh, PA, pages 11-22, October 1997.

[Rou02] S. I. Roumeliotis and G. A. Bekey, "Distributed Multirobot Localization," *IEEE Transactions on Robotics and Automation*, vol. 18, no. 5, pages 781-795, October 2002.

[Ryd05] J. Ryde and H. Hu, "Laser Based Simultaneous Mutual Localisation for Multiple Mobile Robots," *Proceedings of the IEEE International Conference on Mechatronics and Automation*, Niagara Falls, Canada, vol. 1, pages 404-409, July 2005.

[Saa05] J. Saarinen, S. Heikkila, M. Elomaa, J. Suomela, and A. Halme, "Rescue Personnel Localization System," *Proceedings of the 2005 IEEE International*

Workshop on Safety, Security and Rescue Robotics, Kobe, Japan, pages 218-223, June 2005.

[Sai95] M. Saitoh, Y. Takahashi, A. Sankaranarayanan, H. Ohmachi, and K. Marukawa, "A Mobile Robot Testbed with Manipulator for Security Guard Application," *Proceedings of the 1995 IEEE International Conference on Robotics and Automation*, Nagoya, Japan, vol. 3, pages 2518-2523, May 1995.

[Sas00] J. Z. Sasiadek and P. Hartana, "Sensor Data Fusion Using Kalman Filter," *Proceedings of the Third International Conference on Information Fusion*, Paris, France, vol. 2, pages WED5/19-WED5/25, 2000.

[Sch04] F. E. Schneider and D. Wildermuth, "Using an Extended Kalman Filter for Relative Localization in a Moving Robot Formation," *Proceedings of the Fourth International Workshop on Robot Motion and Control*, Puszczykowo, Poland, pages 85-90, June 2004.

[Sch98] M. Schneider-Fontan and M. J. Mataric, "Territorial Multi-Robot Task Division," *IEEE Transactions on Robotics and Automation*, vol. 4, no. 5, pages 815-822, October 1998.

[Sha76] G. Shafer, "A Mathematical Theory of Evidence," Princeton, NJ: Princeton University Press, 1976.

[Sol04] E. Solda, R. Worst, and J. Hertzberg, "Poor Man's Gyro-Based Localization," *Proceedings of the Fifth IFAC/EURON Symposium on Intelligent Autonomous Vehicles*, Lisboa, Portugal, July 2004.

[Spl01] J. Spletzer, A. K. Das, R. Fierro, C. J. Taylor, V. Kumar, and J. P. Ostrowski, "Cooperative Localization and Control for Multi-Robot Manipulation," *Proceedings of the 2001 IEEE/RSJ International Conference on Intelligent Robots and Systems*, Maui, HI, vol. 2, pages 631-636, October/November 2001.

[Spl03] J. R. Spletzer, "Sensor Fusion Techniques for Cooperative Localization in Robot Teams," PhD Dissertation, CIS Department, University of Pennsylvania, Philadelphia, PA, 2003.

[Sti06] J. Stipes, R. Hawthorne, D. Scheidt, and D. Pacifico, "Cooperative Localization and Mapping," *Proceedings of the 2006 IEEE International Conference on Networking, Sensing and Control*, Fort Lauderdale, FL, pages 596-601, April 2006.

[Sto00] T. Stork, "Note: Electronic Compass Design using KMZ51 and KMZ52," Systems Laboratory Hamburg, Philips Semiconductors, Hamburg, Germany, Application Note: AN00022, March 2000.

[Sug93] H. Sugiyama, "A Method for an Autonomous Mobile Robot to Recognize its Position in the Global Coordinate System When Building a Map," *Proceedings of the 1993 IEEE/RSJ International Conference on Intelligent Robots and Systems*, vol. 3, pages 2186-2191, Yokohama, Japan, 1993.

[Suk99] S. Sukkarieh, E. M. Nebot, and H. F. Durrant-Whyte, "A High Integrity IMU/GPS Navigation Loop for Autonomous Land Vehicle Applications," *IEEE Transactions on Robotics and Automation*, vol. 15, no. 3, June 1999.

[Tay94] B. N. Taylor and C. E. Kuyatt, "Guidelines for Evaluating and Expressing the Uncertainty of NIST Measurement Results," National Institute of Standards and Technology (NIST), Gaithersburg, MD, Technical Note: 1297, September 1994.

[Tay01] B. N. Taylor, "The International System of Units (SI)," Physics Laboratory, National Institute of Standards and Technology (NIST), Gaithersburg, MD, Special Publication: 330, July 2001.

[Thr01] S. Thrun, D. Fox, W. Burgard, and F. Dellaert, "Robust Monte Carlo Localization for Mobile Robots," *Artificial Intelligence*, vol. 128, no. 1, pages 99-141, May 2001.

[Thr05] S. Thrun, W. Burgard, and D. Fox, "Probabilistic Robotics," Cambridge, MA: MIT Press, 2005.

[Tri99] J. S. Tripp and P. Tcheng, "Uncertainty Analysis of Instrument Calibration and Application," Langley Research Center, National Aeronautics and Space Administration (NASA), Hampton, VA, NASA/TP: 1999-209545, 1999.

[Tsu78] T. Tsumura and N. Fujiwara, "An Experimental System for Processing Movement Information of Vehicle," *Proceedings of the Twenty-Eighth IEEE Vehicular Technology Conference*, Denver, CO, vol. 28, pages 163-168, March 1978.

[Tsu82] T. Tsumura, N. Fujiwara, T. Shirakawa, and M. Hashimoto, "Automatic Vehicle Guidance – Commanded Map Routing," *Proceedings of the Thirty-*

Second IEEE Vehicular Technology Conference, San Diego, CA, pages 62-67, May 1982.

[Vib06] V. J. Vibeeshanan, "The Eta-Filter Concept," IMSE Department, The University of Texas at Arlington, Technical Report: UTA/IMSE/MFG-2006-01, October 2006.

[Vib07a] V. J. Vibeeshanan, K. Subbarao, and B. L. Huff, "A Sensor Calibration Methodology for Evidence Theoretic Unmanned Ground Vehicle Localization," *Proceedings of the 2007 IEEE International Symposium on Computational Intelligence in Robotics and Automation*, Jacksonville, FL, June 2007.

[Vib07b] V. J. Vibeeshanan, K. Subbarao, and B. L. Huff, "Eta-Filter: An Evidence Theoretic Approach to Unmanned Ground Vehicle Localization," *Proceedings of the 2007 IEEE International Symposium on Computational Intelligence in Robotics and Automation*, Jacksonville, FL, June 2007.

[von98] H. J. von der Hardt, R. Husson, and D. Wolf, "An Automatic Calibration Method for a Multisensor System: Application to a Mobile Robot Localization System," *Proceedings of the 1998 IEEE International Conference on Robotics and Automation*, Leuven, Belgium, vol. 4, pages 3141-3146, 1998.

[Wal03] K. J. Walchko, "Embedded Low Cost Inertial Navigation System," *Proceedings of the Florida Conference on Recent Advances in Robotics*, Dania Beach, FL, May 2003.

[Wei98] H. Weinberg and C. Lemaire, "Using the ADXL202E as a Multifunction Sensor (Tilt, Vibration and Shock) in Car Alarms," Technical Note: 781/329-4700, Analog Devices, Norwood, MA, 1998.

[Wil76] D. Willner, C. B. Chang, and K. P. Dunn, "Kalman Filter Algorithms for a Multi-Sensor System," *Proceedings of the IEEE International Conference on Decision and Control including the 15th Symposium on Adaptive Processes*, Clearwater, FL, vol. 15, pages 570-574, December 1976.

[Wu02] H. Wu, M. Siegel, R. Stiefelhagen, and J. Yang, "Sensor Fusion Using Dempster-Shafer Theory," *Proceedings of the 2002 IEEE Instrumentation and Measurement Technology Conference*, Anchorage, AK, vol. 1, pages 7-12, May 2002.

BIOGRAPHICAL INFORMATION

Veera Jawahar Vibeeshanan is a native of Karur, Tamil Nadu (India). He received the Bachelor of Engineering degree in Mechanical Engineering in 1996 from College of Engineering, Guindy, Anna University, Chennai, India. He received the Master of Science degree in Industrial Engineering in 2001 and the Doctor of Philosophy degree in Industrial Engineering in 2007 both from the University of Texas at Arlington. He was awarded the First Place in the Engineering Model Contest at the National Convention on Mechanical Engineering held in Chennai, India in 1996 for a prototype of his undergraduate project. He won the Best Paper Award at the IEEE International Symposium on Computational Intelligence in Robotics and Automation held in Jacksonville, Florida in 2007 for a paper based on his Ph.D. research.